Fault detection and diagnosis (FDD) for multiple-dependent faults of chillers

Hongwen Dou

A Thesis
In the Department
of
Building, Civil, and Environmental Engineering

Presented in Partial Fulfillment of the Requirements

For the Degree of

Doctor of Philosophy (Building Engineering) at

Concordia University

Montreal, Quebec, Canada

March 2023

CONCORDIA UNIVERSITY

SCHOOL OF GRADUATE STUDIES

This is to certify that the thesis prepared

By: Hongwen Dou

Entitled: Fault detection and diagnosis (FDD) for multiple-dependent faults of chillers

and submitted in partial fulfillment of the requirements for the degree of

Doctor Of Philosophy Building Engineering

complies with the regulations of the University and meets the accepted standards with respect to originality and quality.

Signed by the final examining committee:

______________________________ Chair
Dr. Andrea Schiffauerova

______________________________ Thesis Supervisor
Dr. Radu Grigore Zmeureanu

______________________________ Thesis Supervisor
Dr.

______________________________ Thesis Supervisor
Dr.

______________________________ Examiner
Dr. Luiz Lopes

______________________________ Examiner
Dr. Liangzhu Wang

______________________________ Examiner
Dr. Andreas Athienities

______________________________ Examiner
Dr.

______________________________ External Examiner
Dr. Micheal Kummert

Approved by ______________________________
Dr. Mazdak Nik-Bakht , Graduate Program Director

«March 29th, 2023» ______________________________
Dr. Mourad Debbabi , Dean

Abstract

Fault detection and diagnosis (FDD) of multiple-dependent faults of chillers

Hongwen Dou, Ph.D.
Concordia University, 2023

As an indispensable system in modern buildings, the heating, ventilation, and air conditioning (HVAC) system usually takes a large proportion of building energy usage. However, faults of HVAC system in modern buildings are becoming a growing issue. These faults can aggravate equipment degradation or even damage equipment, and sequentially lead to the increase of maintenance cost and the significant energy waste. Therefore, it is paramount for the HVAC system to run as effectivity and fault free as possible; as a result, research and development into HVAC faults turns to an effective approach to improve building energy efficiency. This dissertation is a contribution to the research of fault detection and diagnosis with a new topic of chiller multiple dependent faults in a real building.

The forward fault detection model and the backward fault diagnosis model are developed to identify and isolate chiller system-level and component-level faults respectively, based on the measurement data from an institutional building. The second law of thermodynamics is applied to analyse the energy flow over an electric chiller, for the purpose of selecting target variables. Benchmarking grey-box models are developed to predict target variables, and sequentially to estimate the impacts of regressor variable faults on target variables. A fault symptom is detected when the residual of a target variable, the difference between the measured value and the predicted value, exceeds the corresponding threshold. Then, a backward rule-based approach is presented to identify if (i) the fault symptom is correct (i.e., a variable has abnormal values), or (ii) the fault symptom is incorrect (i.e., the symptom of target variable is caused by impacts generated by other faulty variables due to the dependency between variables), or (iii) both target and regressor variables are abnormal. The proposed model for chiller multiple-dependent faults is validated by a case study with a cooling plant serving an institutional building, where some faults are artificially inserted into the measurement data file. This dissertation also explored the effectiveness of transfer learning method in the application of improving deep learning model performance.

Acknowledgements

Foremost and sincerely, I would like to thank my supervisor, Dr. Radu Grigore Zmeureanu, without whom this thesis would not have been possible. I am so lucky to have him as my supervisor for my PhD program. I am grateful for his patience, guidance, criticism, and suggestions throughout this study. His passion, vision, and attitude as a scholar, both in academia and life, would affect and encourage me forever.

A special acknowledgement goes to Dr. Yaolin Lin for his suggestions and generous help when I got lost. I will never forget.

Thank my friends and colleagues (Jason Runge, Behrad Bezyan, Pedro Rafael Guaraldi da Silva, Zihan Xie, Chen Liu, etc.) at Concordia, who have enriched my experiences in exploring local life at Montreal and interesting cultures worldwide. I am also grateful to Mr. Zihan Xie, it is always comfortable and enjoyable to talk with you. Extended thanks to Dr. Jason Runge for your considerate and continuous help and assistant in both daily lives and discussing.

Lastly, I here thank my big family (my parents, my uncles, my aunts, my brothers and sisters) for ever accompanying my growth with happiness and loves, and supporting my every choice. I will always love you!

For my beloved grandfather, Lin Ya Dou (窦林亚),
who is a funny friend and a respectable elder,
loving and dedicating to this big family without rewards.

Table of contents

List of figures

List of tables

Nomenclature

BAS: building automation system

BU: bias uncertainty

COP: coefficient of performance

c_p: specific heat capacity at constant pressure, kJ/(kg · K)

E: electric power, kW

FN: false negative

FP: false positive

h_{dis}: compressor discharge enthalpy, kJ/kg

h_{ll}: refrigerant liquid line enthalpy, kJ/kg

h_{suc}: compressor suction enthalpy, kJ/kg

m_{refr}: refrigerant mass flow rate, kg/s

$m_{refr,ref}$: the reference value of refrigerant mass flow rate, kg/s

OU: overall uncertainty

P_{cd}: refrigerant absolute pressure at the condenser, kPa

P_{ev}: refrigerant absolute pressure at the evaporator, kPa

PLR: part load ratio

Q_{cd}: condenser heat load, kW

$Q_{cd,cdw}$: condenser heat transfer rate on condenser-water side, kW

$Q_{cd,ref}$: condenser heat transfer rate on refrigerant side, kW

Q_{ev}: evaporator cooling load, kW

$Q_{ev,chw}$: evaporator heat transfer rate on chilled water side, kW

$Q_{ev,ref}$: evaporator heat transfer rate on refrigerant side, kW

RU: random uncertainty

Res: residual

RH_{oa}: outdoor air relative humidity, %

T_{cd}: saturated refrigerant temperature at the condenser, °C

T_{cdwl}: condenser-water leaving temperature, °C

T_{cdwr}: condenser-water return temperature, °C

$T_{cd,appr}$: condenser approach temperature, °C

T_{chwl}: chilled water leaving temperature, °C

T_{chwr}: chilled water return temperature, °C

T_{dis}: compressor discharge refrigerant temperature, °C

T_{ev}: saturated refrigerant temperature at the evaporator, °C

$T_{ev,appr}$: evaporator approach temperature, °C

T_{ll}: refrigerant liquid line temperature, °C

T_{oa}: outdoor air temperature, °C

T_{suc}: compressor suction refrigerant temperature, °C

TN: true negative

TP: true positive

U_m: measurement uncertainty

U_p: prediction uncertainty

V_{cdw}: condenser water volumetric flow rate, m^3/s

V_{chw}: chiller water volumetric flow rate, m^3/s

ΔT_{suc}: superheating, °C

ΔT_{ll}: sub-cooling, °C

ΔT_{cdw}: temperature difference between condenser-water leaving temperature and condenser-water return temperature, °C

ΔT_{chw}: temperature difference between chilled water leaving temperature and chilled water return temperature, °C

Greek symbols

ε: threshold

ρ: water density, kg/m^3

γ: heat capacity ratio

Subscript

chw: chilled water

b: benchmarking

cd: condenser

cdw: condensing water

comp: compressor

ev: evaporator

m: measured value of a variable

p: predicted value of a variable

ref: reference

refr: refrigerant

Chapter 1: Introduction

The concerns of rising energy usage are becoming a serious issue worldwide. The global primary energy consumption raised to 583.90 EJ in 2020 with an average growth rate of 2.09% per year for the past decade [1]. As an energy leader, Canada consumed 13.63 EJ (3% of the global energy consumption) in 2020 [2]. The energy used for buildings reached to 2.79 EJ in 2018, accounting for 28.78% of Canada's overall energy usage [3]. The percentage for energy consumption of buildings is greater inside Quebec, accounting for 30% of Quebec's overall energy consumption in 2016 [4]. According to Natural Resources Canada, 63.20% of secondary energy in the building sector is used for space heating and cooling across Canada [3]. In the USA, 70% of electricity is primarily used for heating, cooling, and lighting [5].

As an indispensable system, the heating, ventilation, and air conditioning (HVAC) system in modern buildings may consume roughly 50% of a building's energy to keep the indoor environment within a certain level [6]. Faults of HVAC system are responsible for part of energy waste and impacts. It is reported that building faults lead to (1) energy waste, 0.4-1.8EJ of energy for commercial buildings in USA is squandered [7], (2) increased maintenance cost [8], and (3) the degradation or even possible damage to equipment [9,10]. Hence, maintaining HVAC system at optimum working status becomes one of the most important approaches to improve energy efficiency, especially when faults could occur in HVAC systems [11]. But faults of HVAC systems are becoming increasingly frequent. A study about building maintenance reported there were 11 fault cases every year per 1,000 m^2 floor area, for both chillers and boilers [12]. Worse, these faults might occur simultaneously, interact with each other, or even induced new faults, which may be aggravated due to the building automation system. As such, the ever-changing conditions are making fault detection and diagnosis (FDD) a challenging endeavor, especially for the topic of multiple faults (MFs).

As the core component, chillers account for around 40% of the service resources and around 25% of the repair costs [13]. However, the research on chiller FDD has mainly focused on single fault (SF) problems to date. Only a small number of papers were found to study chiller MFs or multiple-dependent faults (MDFs), which is in-sufficient and deserves more attentions. This dissertation contributes to the study of FDD for chiller MDFs.

Chapter 2: Literature review

The literature review in this dissertation starts with the definition of common terms of FDD (e.g., multiple dependent faults) in the field of HVAC, followed by the research on single fault. Then, publications with the topic of multiple/simultaneous faults are reviewed to conclude on the research gaps, to indicate the research goals.

2.1. Term definitions and a classification scheme for multiple faults

2.1.1. Definitions for fault, simultaneous fault, fault detection, and fault diagnosis

This section defines the terms used in the FDD field for HVAC systems, including fault, simultaneous faults, fault detection, fault diagnosis, etc. The sources of these definitions are from published work and the author.

Two definitions for a fault are found from published papers:

I. A departure from an acceptable range on an observed variable or calculated parameter associated with the equipment [14].
II. An abnormal condition or defect at the component, equipment, or sub-system level which may lead to a failure [15].

Simultaneous faults were defined as two or more faults occurring at the same time, but at different locations [16]. The key characteristic of this definition is that faults that occur simultaneously within a system. However, it lacks the specified scope or location, for instance, a study for FDD within an air handling unit (AHU) also treated faults as simultaneous faults [17]. Hence, this dissertation defines simultaneous faults as two or more faults occurring at the same time with respect to a component or a system.

Collins Dictionary illustrates the word detection as the act of discovering or the fact of being discovered [18]. Thus, the act of identifying a symptom that is/was occurring in a system/component is termed as fault detection.

Fault diagnosis can be defined as a search for the causal origin of an observed pattern of abnormal system behavior [14].

2.1.2. Definition for multiple faults and a classification scheme

MFs can be defined as more than two faults that happen simultaneously or sequentially, and they can be classified as the following four categories [19]:

I. *Induced fault*: a fault is induced by another fault.
II. *Independent multiple faults*: different faults have effects on different variables.
III. *Masked multiple faults*: some faults from fault group A can explain all symptoms from another fault group B.
IV. *Dependent multiple faults*: these are the faults that interact with each other, resulting in mixed symptoms.

This definition [19] comes from the industry of chemical processes. It describes MFs from the view of causal relationship between a fault source and corresponding symptoms. However, this definition limits the number of faults to more than two faults, which might contradict to many publications [20–22]. Besides, though masked multiple faults are treated as a separate category, rare case in HVAC systems fall into this group.

This dissertation terms MFs as two or more faults that occur simultaneously or sequentially with respect to a system/component. As MFs consists of, at least, two faults, the joint effect on a target variable may act as an accumulative impact or not. The case of MFs differs to another one if the condition that the interaction effect exists holds. Therefore, cases of MFs can be generally classified based on whether the impact of one (or more) fault could propagate to other variable(s), which is described as dependency relationship and used to distinguish independent faults from dependent faults. For instance, within a system (e.g., chiller system), the case of sensor fault is under the category of independent fault and the case of variable fault is under the category of dependent fault, as a sensor normally does not propagate to other variables, but only shows abnormal measurement values. An experimental study shows the case of independent fault, where no connection was found between supply air temperature sensor fault and supply fan pressure sensor fault [17]. Dependent faults are those in which one variable fault (abnormal value) could propagate to other variables. Another experimental study of fault impacts of a vapor compression rooftop unit reveals the dependent relation, where a physical artificial variable fault usually led to abnormal values of other multiple variables [23].

Further, dependent faults can be categorized by the consequence of dependency relationship, when the impact of one variable (called a regressor variable) was assessed on the other subsequent variable(s) (called the target variable) that are measured or simulated. Apart from the dependency relation between a regressor and a target variable, the following discussion applies when the impact between regressor variables exist.

I. *General dependent faults*: the fault on a target variable depends on the fault of a regressor variable.

II. *Aggravated faults*: faults of multiple regressor variables have the same impact trend on a target variable, as a result, the joint-impact on the target variable is aggravated, regardless of relation (independent or dependent) between individual regressor variables. For example, simultaneous outdoor air damper fault and supply air damper fault together could aggravate the heating power fault. Therefore, the sum of two individual faults is nearly the same with a joint impact on the heating power [17]. Author clarifies that a new fault might occur due to the aggravated effect, thus, such cases (new fault occurs) should be classified into this category.

III. *Counteracted faults*: faults of multiple regressor variables have different impact trends on a target variable. As a result, the joint-impact on the target variable is counteracted, regardless the relation (independent or dependent) between individual regressor variables. For example, condenser fouling fault of the chiller leads to the decrease of T_{cdwl}; and valve stuck of condenser water loop rises T_{cdwl}. If both the faults occur simultaneously, the counteracted impact might lead to a 'normal' state of T_{cdwl}.

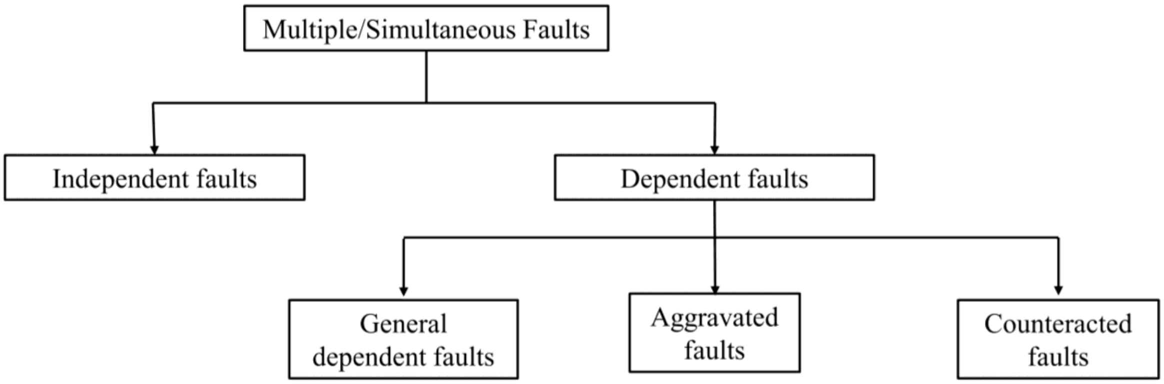

Figure 2-1. Classification scheme of multiple faults.

Thus, a classification scheme is proposed to summarize the relationship between each fault in the case of multiple simultaneous faults (MSFs), as shown in Figure 2-1.

From this paragraph on, literature review about SF and MSFs is presented. In terms of research models for FDD, Katipamula and Brambley [24] proposed a classification scheme (see Figure 2-2) for building systems, which is well acknowledged in this field and used to classify the reviewed publications in this dissertation. The reviewed articles on each topic are discussed in a chronological order.

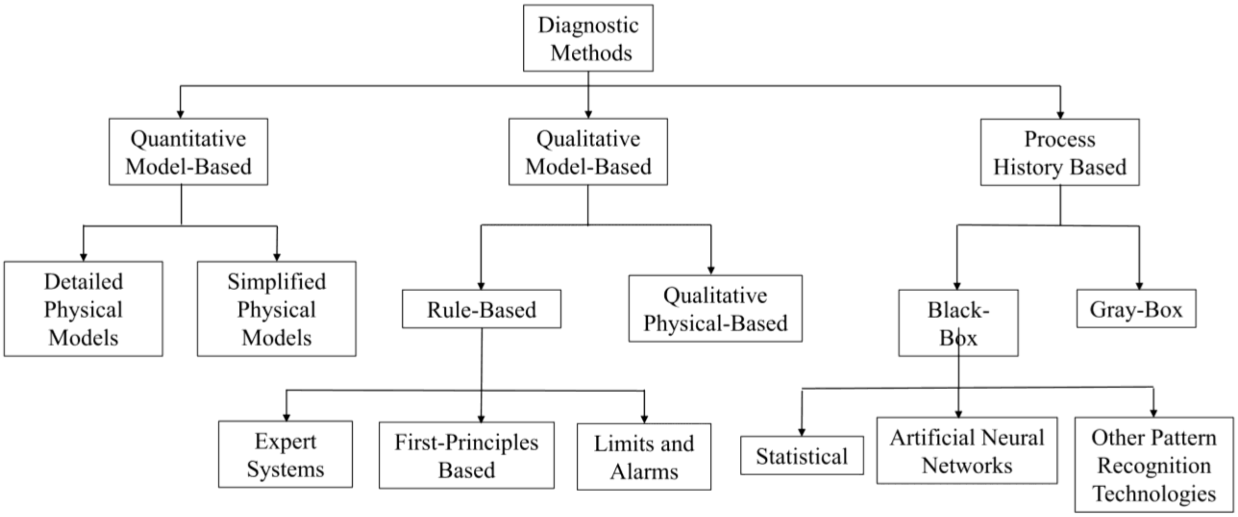

Figure 2-2. The classification scheme for FDD methods [24].

2.2. Literature review for single fault

The review for SF was conducted over a period spanning twenty-four years, from 1998 to 2022, with key words of HVAC, building system, fault detection and diagnosis.

2.2.1. Quantitative model-based method

Keir and Alleyne [25] developed a detailed physical-based model to describe the vapor compression system (VCS), and applied it with experiment data to calculate the residual. When the residual exceeds a threshold, a fault symptom is detected.

Weimer et al. [26] proposed a thermodynamic model, derived through a spatial discretization of heat transfer equation for a room, to evaluate indoor air temperature. After the calibration with experiment data, case study results indicated this model was accurate and robust for FDD.

2.2.2. Qualitative model-based method

Initially, a rule-based method was presented to research the common refrigerator SF by experiments [27]. Comparisons of data derived from experiments under fault and fault-free conditions was used for FDD.

Fernandez et al. [28] generated rules to detect and isolate faults of sensor, controller, and damper, based on laboratory tests of a HVAC system. The work was adopted by [29] to study economic impacts due to faults for the VAV system and AHU. Coupled with self-correcting controls, results indicated that the packaged HVAC system realized 15% energy savings per year [29].

An expert rule system was presented based on the on-site survey for eighteen AHUs, operating under fault or fault-free status, to improve the energy efficiency [30]. Case study reported that over €104,000 per year of energy savings were achieved.

In summary, the qualitative model-based method relies on expert knowledge. Though the qualitative model-based method is computationally effective and easy to use, its universality is limited as each system is case-independent. A review paper indicated that the rule-based approach accounts for 78% of all the 52 pieces of research within qualitative model-based methods after they went through 197 publications [31].

2.2.3. Process history-based method

The literature review for SF problems finds that research utilizing the black-box model takes most studies among the category of process history-based methods. Therefore, this section starts with the grey-box models (a type of process history-based method) and ends with black box models.

A grey-box model is a data-driven model that couples a physical model, and then identifies important parameters representative of certain key or aggregated physical parameters by statistical analysis [32]. The research, using the grey-box model for FDD, includes publications focusing on the evaporator and the condenser fouling fault for a heat pump system [33], root top unit (RTU) equipment faults [34], and the gradual and the sudden fault of chiller and cooling tower [35], etc. For instance, Yu et al. [34] selected input variables identified by experimental analysis and the coefficients identified by genetic algorithm to build a grey-box for a RTU, which was applied for the detection of RTU dirty indoor filter fault and slipping supply fan belt fault.

A black-box method is a data-driven model, derived from the mathematical relationship, between inputs and outputs with a strict parameter tuning process [32]. Ren et al. [36] proposed a multi-class support vector machine (SVM) model, where each of eight features was assigned with a specific fault [37,38]. The model was applied to perform FDD to a refrigerant system with the experiment data, and reported a high diagnostic accuracy of 98%.

Youming and Lili [39] presented a principal component analysis (PCA) model to detect condenser fouling fault for an air-source heat pump. The data, collected from experiments under faulty and fault-free conditions, was projected into PCA space to generate the residual for fault detection. Results indicated that condensing fouling fault with 20% and 60% levels was identified successfully.

FDD model developed with artificial neural network (ANN), focusing on HVAC, has received much attention [40–42]. For instance, [42] established ANN models to detect the total electricity consumption fault and as a diagnostic tool to isolate the fault of a subsystem.

2.2.4 Summary of literature review for single fault

To summarize, the literature review for FDD covers the application from whole-building-level fault to component-level or sensor-level fault. Research on the whole building system attracts the least attention (6.25%), and research on HVAC equipment take the largest proportion (46.25%) [43]. Apart from the HVAC system, application of FDD has been expanded to improve the quality and throughput in industrial processes [44], robot work systems [45], nuclear power plants [46], etc.

2.3. Literature review for multiple/simultaneous faults

A single fault is usually much simpler to deal with, compared with the multiple/simultaneous faults that occur at the same time but at different locations [16,47]. Detection and diagnosis of multiple/simultaneous faults in HVAC systems is still a challenge, since the combination of several faults makes it difficult to separate the individual faults. MFs and MDFs are two related but distinct topics. Both refer to multiple faults, but differ in whether dependency among faults exists. A fault symptom might not reveal a real fault, but could be the result of another fault in the system.

The review for multiple/simultaneous faults and MDFs was conducted over a period spanning eighteen years, from 2004 to 2022, with key words of HVAC, building system, fault detection and diagnosis, and multiple/simultaneous faults.

2.3.1. *Quantitative model-based method*

Li and James [48] presented a decoupling-based approach, between target variable and potential source of fault, to detect and diagnose MDFs. They used an air-cooled roof top unit, installed in a laboratory-controlled environment, as a case study. Based on the theoretical analysis of physical processes in the system and within each equipment (e.g., compressor, condenser), and the experimental measurements, they proposed a decoupling-based method. The decoupling-based method simplifies the diagnosis by assuming that abnormal target variable (e.g., the discharge refrigerant temperature T_{dis}) is caused exclusively by one regressor variable, while the role of all other possible regressor variables is neglected. For instance, they concluded that the abnormal deviation of T_{dis} is only caused by the compressor valve leakage. The situation of a faulty target variable (e.g, faulty sensor of T_{dis}) was not considered. This method is applied to research MFs for packaged air conditioners [49], and air conditioners [50,51].

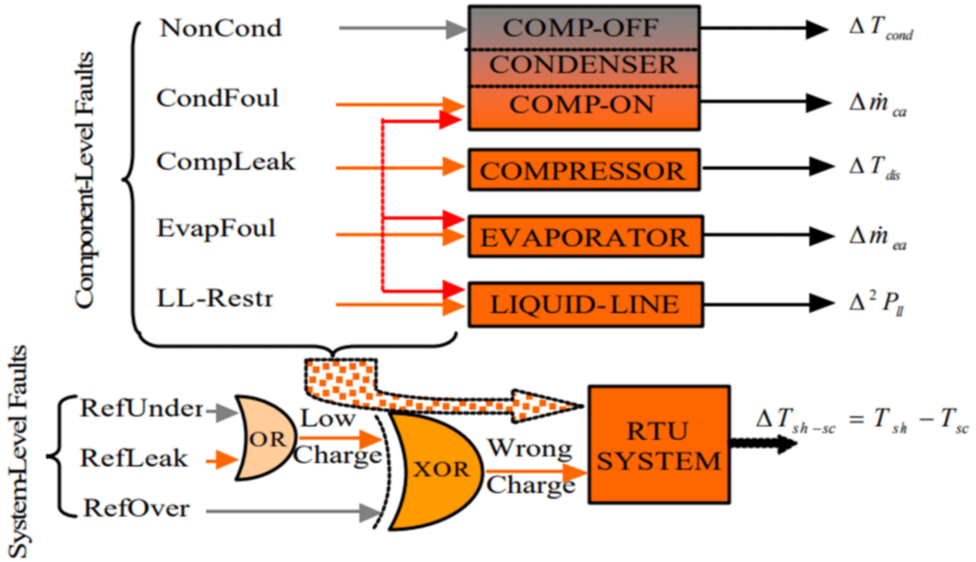

Figure 2-3. Decoupling scheme of rooftop system faults [48].

Thumati et al. [52] utilized the time-discrete HVAC model [53] to investigate a simultaneous cooling coil degradation fault and insulation leakage fault for an AHU, using measurement data. The faults could be diagnosed if the residual between the outputs of the developed models and system states exceeded a pre-defined threshold, which was identified by the system uncertainties and fault magnitudes [54].

Subramaniam et al. [55] presented a physical model to estimate zone temperature to study

VAV damper lock-in-place MFs. Cases studies were introduced to study multiple faults occurring sequentially and simultaneously in different zones, using SIMBAD simulation toolbox [56].

Kim and Braun [57] expanded previous work on FDD methods [48–51] and developed a MDFDD system that decouples the impacts of individual faults to estimate multiple faults that occur simultaneously. They developed virtual sensors for the compressor, expansion valve, condenser, evaporator, and refrigerant charge, using measurements from a four-ton rooftop unit in a laboratory-controlled environment, and the compressor map. When two simultaneous faults occur (e.g., the reduction of airflow rate due to condenser fouling, and compressor valve leakage), the impact ratio of each fault on the system performance (e.g., COP) degradation is isolated.

In summary, the physical-based model is built based on first principles and applied to topics of multiple/simultaneous faults and MDFs. Physical models show strength to capture the transients in a dynamic system [31]. However, the model relies on rich and deep physical knowledge. For large and complex systems, the detailed quantitative model could be quite complex or could not be solved.

2.3.2. Qualitative model-based method

Breuker and Braun [23] used measurements from a three-ton packaged rooftop unit along with polynomial models to develop a statistical, rule-based classifier for faults. Such rules show whether a particular measurement increases or decreases in response to a particular fault at steady-state conditions. For instance, the compressor valve leakage generally increases the discharge refrigerant temperature (T_{dis}) from the compressor above the normal value under steady-state condition. If measurements in a real rooftop units show the increase of T_{dis}, the detection rule indicates that the fault is caused by the compressor valve leakage, whereas all other possible causes are neglected.

Qin and Wang [20] integrated performance indexes with expert rules to study the multiple/simultaneous faults for the VAV system terminal. Following the working sequence of VAV system, to ensure a fault has no impact on the subsequential fault, a rule was set for a component (e.g., coil) fault. The method was limited to the condition that independent fault holds.

Wang and Chen [58] developed expert rules to diagnose MSFs of AHU, where the residual-based exponential weighted moving average chart was used to detect the fault.

Apart from the application above, the expert rule was also used as an assistant tool to a prediagnose fault [21,59].

To summarize, the expert rule is the only method that can be found in the literature review applied for the topic of multiple/simultaneous faults among qualitative model-based methods and usually is combined with other models (e.g., black-box model). Though rule-based model has some limitations, such as it requires prior expert knowledge, expert rule is interpretable, computational-efficient, and easy to use.

2.3.3. Process history-based method

A multiple-level FDD system was built based on PCA and joint angle analysis (JAA) algorithms to solve MFs of an AHU, under the assumption that multiple faults could not occur simultaneously in one subsystem (e.g., supply air control loop) [21]. Another two papers integrate PCA with fisher discriminant analysis (FDA) [59] and joint angle plot analysis [60] to diagnose the faults in two subsystems of an AHU. Combined with cluster analysis, another application of PCA model for MSFs was FDD for sensor faults of an AHU [61], where PCA model served as a feature extraction tool to select features.

Han et al. [62] proposed a SVM model to detect and diagnose multiple chiller faults, based on the conclusion of [63] where each chiller fault was assigned with a unique feature. The model was trained with several datasets (each dataset included one fault) and tested with one dataset with MSFs. Case study results indicated high accuracy of FDD for MSFs. As the author claimed, however, the model was not feasible to deal with MDFs.

To summarize, as an effective dimension-reduction algorithm, PCA was widely used to perform fault detection for MFs. But it is weak in diagnosing faults, as the orthogonal relationship disconnects the principal components. To apply PCA model for FDD, additional algorithms are usually required to isolate the fault source [31].

To author’s best knowledge, ANN was first used to study MFs in 2005 [17]. To estimate dynamic system operation, recurrent neural network was established to study multiple sensor and actuator faults for AHU and VAV box based on experiments [64]. Later in 2020, Elnour et al. [65] used an auto-associative neural network to solve multiple sensor faults in a HVAC system. Case study results with data from TRNSYS program indicated the proposed model successfully diagnosed multiple-sensor faults and outperformed PCA-based model by an improvement of 40% in terms of FDD accuracy. However, the model may fail to detect simultaneous sensor and actuator faults, as they lead to a very similar fault symptom.

In summary, ANN is a mathematical model and capable of dealing with complex and non-linear systems. It is highly modulable, and convenient researchers or engineers to flexibly shape ANN architecture based on the need.

2.3.4. Conclusion of literature review for multiple/simultaneous faults

To summarize the literature review for MSFs in the field of HVAC, Table 2-1 lists the main information for the reviewed publications in a chronological order. Process-history based methods (data-driven models) take the most proportion of 76.9% during the reviewed publications and mainly focus on black-box models because of simplicity. Other methods of MDFDD includes rule-based approaches, physical model-based approach, etc.

Table 2-1. Details of MSFs research literature review.

Method	Target system	Target component	Data source	Ref.
Expert Rule	RTU	Variable	Laboratory data	[23]
First principles	RTU	Variable	Laboratory data	[48]
First principles	AC	Variable	Laboratory data	[49]
ANN	AHU	Variable and sensor	Laboratory data	[17]
Expert rule	VAV system	Variable and sensor	Simulation	[20]
First principles	AC	Variable	Laboratory data	[51]
First principles	AC	Variable	Laboratory data	[50]
PCA and JAA	VAV system	Variable and sensor	Simulation	[21]
PCA, FDA	AHU	Sensor	Simulation	[59]
SVM and ML	Chiller	Variable	Laboratory data	[62]
First principles	AHU	Variable	Simulation	[52]
PCA and JAP	VAV system	Sensor	Simulation	[60]
Expert Rule	VAV system	Variable and sensor	On-site data	[58]
PCA and cluster analysis	AHU	Sensor	Simulation	[61]
Recurrent ANN	AHU and VAV box	Actuator and Sensor	Laboratory data and On-site data	[64]
Auto-associative ANN	HVAC system	Sensor	Simulation	[65]
First principles	VAV system	Variable	Simulation	[55]
First principles and Bayesian classifier	RTU	Variable	Laboratory data	[57]

Figure 2-4 shows the findings of multiple/simultaneous faults in terms of system, target component, and data source. Six papers focus on MSFs of the VAV system [20,21,55,58,60,64] among the eighteen papers. By comparison, there is only one paper focusing on chiller MSFs [62]. As for data type, the research based on laboratory experiment data takes a proportion of 47%

[17,48–51,57,62,64]. Seven papers [20,21,52,55,59,61,65] are found to utilize simulation data to study MSFs. By comparison, the research based on on-site measurements takes the least: only two papers used measured data [58,65], as Figure 2-4(c) shows.

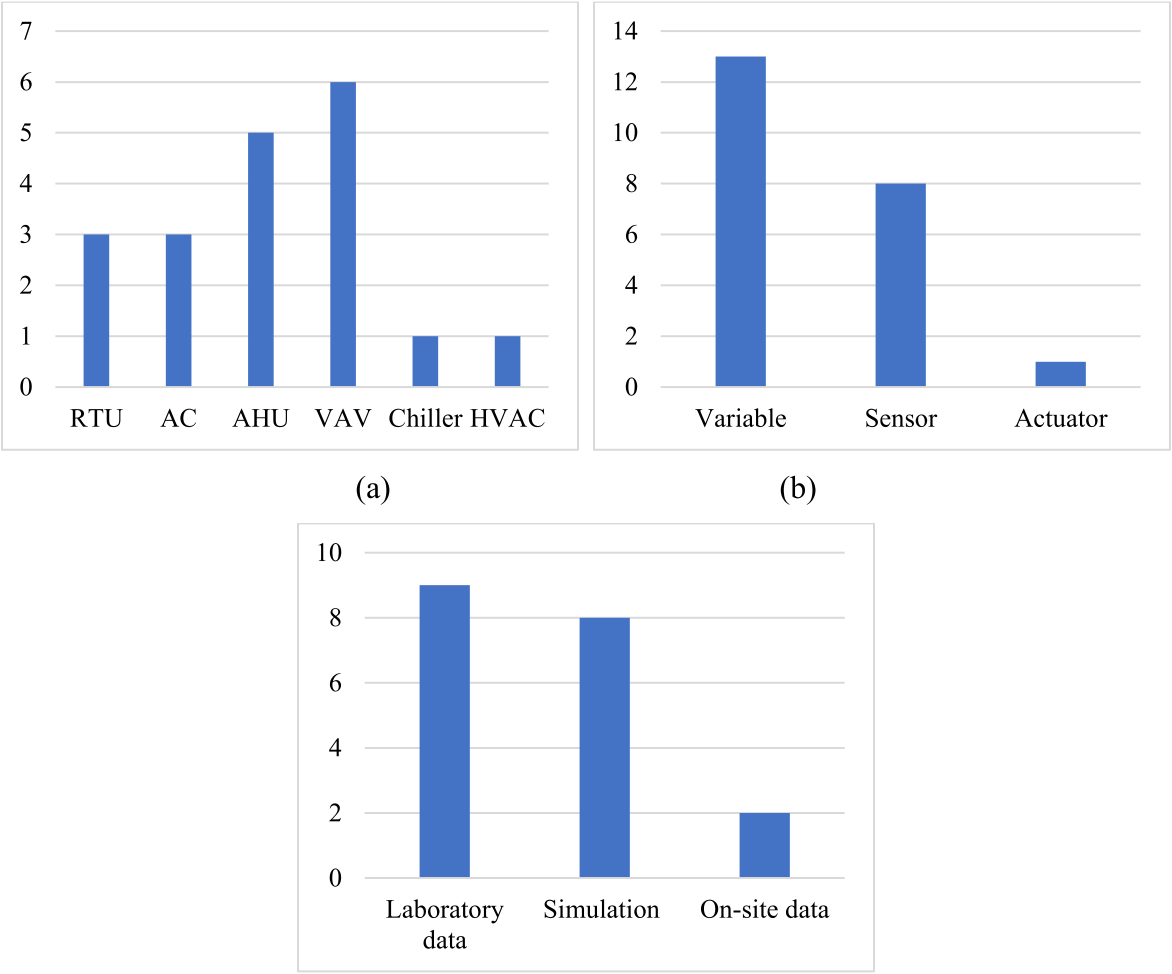

(a) (b)

(c)

Figure 2-4. Summary for the literature review of multiple/simultaneous faults. (a) target system; (b) target component; (c) data type.

Some publications ignore the dependency of multi-faults. For example, [21] assumed the case when independent faults occur simultaneously in two separate loops of a variable air volume (VAV) system: (i) the sensor of supply air temperature control loop, and (ii) the sensor of outdoor air control loop. Reference [66] proposed a set of 26 rules for the isolation of multiple single faults of air handling units. For instance, faults of mixed air temperature, chilled water circulating pump, and cooling coil valve controller can be detected. However, the interactions between the individual faults are not analyzed in this work.

Only a small number of publications deal with methods for MDFs in HVAC systems [23,50,51,57,67]. Based on the literature review, one can conclude that methods presented by [23,50,51,57,67] are forward methods, which detect the impact of some faults (e.g., compressor valve leakage) on the next sensors or equipment performance (e.g., chiller *COP*). These methods could be used as reference rules for the reverse detection of single faults. However, such rules can be applied only to an HVAC equipment used in the laboratory-controlled environment. The level of detailed measurements of all variables used in laboratory work is not feasible for an HVAC equipment in existing buildings. Additional research is needed for the generalization of decoupling-based method to HVAC systems with limited information.

The literature review concludes the research on chiller multiple dependent faults using measurement data is lacking. The research on multiple/simultaneous faults is still in its infancy, due to the natural nonlinear property of multiple faults, which makes it challenging to be solved and deserves more attention [47,68].

2.4. Literature review for chiller grey-box models

Table 2-1 indicates that the FDD research on multiple/simultaneous faults utilizing grey-box models is rare. However, as a type of model derived from physical principles, grey-box models have several advantages: (1) robust [24], (2) require less data and are fast to train [31], (3) physically traceable parameters [32], and (4) the grey-box model extrapolates well to operating conditions outside the range of training dataset. The critical literature review in this section presents existing chiller grey-box models, aiming to explore potential models for the application of chiller MDFDD. This review investigates publications spanning from 1980 to 2021 with key words of chiller, fault detection and diagnosis, and grey-box model. Generally, the existing grey-box models can be classified into two groups: physical-based models (Table 2-2), and correlation-based models (Table 2-3).

Table 2-2. Physical-based grey-box models for chillers, extracted from literature review spanning from 1980 to 2021.

Equation Number	Equation	Order	Parameter identification	Data source	Ref.
(2-1)	$\frac{1}{COP}=-1+\frac{T_{cdwr}}{T_{chwl}}+\frac{1}{Q_{ev}}(a_0+a_1T_{cdwr}+a_2\frac{T_{cdwr}}{T_{chwl}})$	1	Linear regression	Laboratory data	[69]
(2-2)	$\frac{1}{COP}=-1+\frac{T_{cdwr}}{T_{chwl}}+\frac{1}{Q_{ev}}(b_0+b_1\frac{T_{cdwr}}{T_{chwl}})+b_2$	1	NA	Laboratory data	[70]
(2-3)	$\frac{1}{COP}=-1+\frac{T_{cdwr}}{T_{chwr}}+\frac{1}{Q_{ev}}\left(-c_0+c_1T_{cdwr}-c_2\frac{T_{cdwr}}{T_{chwr}}\right)$	1	Regression analysis	Laboratory data	[71]
(2-4)	$\begin{cases} \mathrm{Y}= X_1\Delta S_T+X_2R \\ Y=\frac{T_{chwr}}{T_{cdwr}}\left(1+\frac{1}{COP}\right)-1 \\ X_1=\frac{T_{chwr}}{Q_{ev}}, X_2=\frac{Q_{ev}}{T_{cdwr}}\left(1+\frac{1}{COP}\right) \end{cases}$	1	Linear regression	Laboratory data	[72]

Table 2-3. Correlation-based grey-box models for chiller, extracted from literature review spanning from 1980 to 2021.

Equation Number	Equation	Order	Parameter identification	Data source	Ref.
(2-5)	$COP=d_0+d_1Q_{ev}+d_2T_{chwr}+d_3T_{cdwr}+d_4Q_{ev}^2+d_5T_{chwr}^2+d_6T_{cdwr}^2+d_7Q_{ev}T_{chwr}+d_8Q_{ev}T_{cdwr}+d_9T_{chwr}T_{cdwr}$	2	NA	NA	[73]
(2-6)	$\begin{cases} \frac{E}{E_{des}}=e_0+e_1A+e_2A^2+e_3B+e_4B^2+e_1AB \\ A=PLR, B=\frac{T_{cdwl}-T_{chwl}}{T_{cdwl,des}-T_{chwl,des}} \end{cases}$	2	Least square	NA	[74]
(2-7)	$\frac{E}{E_{des.}}=f_0+f_1PLR+f_2PLR^2+f_3T_{cdwr}+f_4T_{cdwr}^2+f_5PLRT_{cdwr}+f_6PLR^2T_{cdwr}+f_7PLRT_{cdwr}^2+f_8PLR^2T_{cdwr}^2$	4	Regression analysis	Manufacturer data	[75]
(2-8)	$COP=g_1Q_{ev}+g_2T_{chwr}+g_3T_{cdwr}$	1	Least square	On-site data	[76]
(2-9)	$EIR=2.208266+0.009742T_{cdwr}-5.14097PLR+5.428211PLR^2-1.78486PLR^3$	3	NA	On-site data	[77]
(2-10)	$\begin{cases} PLR=h_0+h_1T_{chwl}+h_2T_{chwl}^2+h_3T_{cdwr}+h_4T_{cdwr}^2+h_5T_{chws} \\ EIR=i_0+i_1PLR+i_2PLR^2 \end{cases}$	2	NA	NA	[78]
(2-11)	$\begin{cases} E=j_1PLR+j_2T_{cdwl}+j_3T_{oa} \\ COP=k_1\frac{1}{PLR}+k_2T_{cdwl}+k_3T_{oa} \\ E=l_0+l_1PLR+l_2PLR^2+l_3T_{cdwl}+l_4T_{cdwl}^2+l_5T_{oa} \\ COP=m_1PLR+m_2PLR^2+m_3T_{cdwl}+m_4T_{cdwl}^2+m_5T_{oa} \end{cases}$	1,2	Least square	On-site data	[79]
(2-12)	$COP=1.1760+1.2843\times\Delta T_{chw}-0.7216\Delta T_{cdw}$	1	Recursive least-squares	On-site data	[80]

2.4.1. Physical-based grey-box models

Gordon and Ng [69] built a thermodynamic model to evaluate the performance of the reciprocating chiller, as shown in Equation 2-1 (Table 2-2). T_{cdwr} and T_{chwl} are in *K*, and Q_{ev} is in *kW*. Compared with data from eighty reciprocating chillers (including 897 experimental data samples and data from two manufacturers), the model achieved the maximum *RMSE*= 0.0066. The model was later extended to centrifugal chillers, and it turned out to work well [81].

Gordon et al. [70] proposed another thermodynamic model to describe the chiller operation based on first principles, shown in Equation 2-2 (Table 2-2). T_{cdwr} and T_{chwl} are in *K*, and Q_{ev} is in *kW*. The heat energy balance between the refrigerant loop and the water loop, heat leakage, and entropy produced in VCS was taken into consideration. This model could estimate the chiller performance over a wide range of operating conditions and is the source of many studies, such as a study focusing on chiller efficiency versus ambient wet bulb temperature [82], regression models development [71,72], etc. Besides, it serves as the main model in many research topics, including the control of ground source heat pump [83], thermal energy storage [84], optimal sequencing control for chiller [85], etc.

Lee [71] investigated the chiller energy and entropy balance relation [86], and proposed a grey-box model to estimate chiller *COP* with T_{cdwr}, T_{chwr}, and Q_{ev}, as shown in Equation 2-3 (Table 2-2). T_{cdwr} and T_{chwr} are in *℃,* and Q_{ev} is in kW. The model was validated by the experiment data and achieved a high correlation with $R^2 = 98.87\%$.

Jayaprakash and Kim [72] introduced a grey-box model-based approach to study the fault of a centrifugal chiller, as shown in Equation 2-4 (Table 2-2). T_{cdwr} and T_{chwr} are in *K*, and Q_{ev} is in *kW*. ΔS_T (*kW/K*) and *R (K/kW)* are coefficients representing expansion valve and compressor, and heat exchangers, respectively. To apply this model, ΔS_T (*kW/K*) and *R (K/kW)* need to be identified first.

2.4.2. Correlation-based grey-box models

The first correlation-based model, to the author's knowledge, came from the DOE-2 reference manual in 1980 [73], which is listed in Equation 2-5 (Table 2-3). T_{cdwr} and T_{chwr} are in *K*, and Q_{ev} is in *kW*. If this model is used for fault diagnosis, additional target variables, rather than *COP*, are required, as *COP* is only an index representing system-level performance.

Braun [74] developed a correlation-based model to predict *E*, as shown in Equation 2-6 (Table 2-3). T_{cdwl}, T_{chwl}, $T_{cdwl,des}$, and $T_{chwl,des}$ are in *℉,* and *E* is in *kW*. The coefficients of the model could be identified by the least square algorithm.

Yik and Lam [75] presented a bi-quadratic equation to predict the normalized power input to a chiller, as shown in Equation 2-7 (Table 2-3). *E* is in *kW*, and T_{cdwr} is in *℃*. The utilization of normalized variables for *E* and Q_{ev} enlarges *E* prediction range regardless of the chiller capacity.

Swider [76] proposed a linear regression model, as shown in Equation 2-8 (Table 2-3). Here, T_{chwr} and T_{cdwr} are in *K*, and Q_{ev} is in *kW*. Experimental measurements of two vapor compression chillers were used for model validation, along with another three *COP* models: DOE-2 regression model [73], bi-quadratic regression model [75], and physical-based model [81]. The results indicated that DOE-2 regression model Equation 2-5 (Table 2-3) was the most accurate model with $R^2 = 99.11\%$ and $RMSE = 0.0806$.

Chan [77] proposed a cubic regression model with two input variables (PLR and T_{cdwr}) to predict the chiller efficiency, as shown in Equation 2-9 (Table 2-3). EIR is in *kW/ton* and T_{cdwr} is in *℃*.

The EnergyPlus program provided a bi-quadratic regression model [78] to predict the PLR using T_{chwl} and T_{cdwr}, as listed in Equation 2-10 (Table 2-3). T_{chwl} and T_{cdwr} is in *℃*. The model was validated by Shrestha and Maxwell [87] using the manufacture's data for an air-cooled chiller, which covered PLR within a range of 25% to 100%. The results reported a high R^2 value of 0.9962.

Monfet and Zmeureanu [79] proposed correlation-based models to predict E and COP of water-cooled electric chillers, as listed in Equation 2-11 (Table 2-3). T_{cdwl} and T_{oa} are in *℃*, E and Q_{ev} are in *kW*. The work used the measurements from building automation system (BAS) to train and test models. The model is capable of *COP*-oriented or *E*-oriented fault detection at system-level.

Zhao et al. [80] developed an online predictive model to predict the global COP of a cooling plant, as listed in Equation 2-11 (Table 2-3). ΔT_{chw} and ΔT_{cdw} are in *℃*. The model was built, starting from the energy balance equation, and used Pearson correlation coefficients to eliminate the redundant input variables. The coefficients are identified by the recursive least-square approach with measurement data recorded every 5 minutes.

2.4.3. Summary for chiller grey-box literature review

In summary, physically-based grey-box models [69–72] are derived from first principles, while correlation-based grey-box models [73–80] usually select input variables related to a physical process. These models are proposed to predict chiller system-level performance (e.g., *COP*) [69–80], and validated by the data either from experiments or manufactures. Such models derived from experiments or manufacturer's data can be very powerful to predict the behavior of a chiller, but they might not be practical when it is desired to apply them in real buildings, where BAS only cover very limited information for monitoring or control purpose [88]. Furthermore, the information of design conditions with respect to a HVAC system or a component (e.g., chiller) might not always be available for existing buildings. Thus, new grey-box models that are based on the research purpose should be developed, using only the parameters available in the databases collected from BAS.

2.5. Literature review for artificial faults

The literature review was conducted with the scope of how to insert artificial faults in the field of HVAC systems. The literature survey covers thirty-six publications covering chiller, AHU, VCS (including RTU, HP and AC) and HVAC systems. The number of publications with respect to each research target is listed in Table 2-4.

Table 2-4. Number of publications in the literature review for different systems, based on both measurements and simulation.

System	Chiller	AHU	HVAC system	VCS	Summary
Number of publications	12	5	15	6	36

2.5.1 Fault insertion methods

The literature review finds HVAC systems attract the most research with eighteen publications [17,20,21,52,55,60,64,65,68,89–94], followed by chillers with ten publications [22,72,95–104], six papers for VCS [33,39,48,51,57,67], and four papers for AHU [59,66,104–106]. It was observed that experimental data from ASHRAE project 1043-RP [107] is the source of other seven papers [22,72,95–99] for the chiller fault studies. A few examples of fault insertion approaches are shown in Table 2-5, where NM means not mentioned in the publication.

Table 2-5. Approaches to generate faults in the reviewed publications.

System	Data source	Ways to generate faults	Ref.

HVAC system	Laboratory experiment	Measurement signals are replaced with errors for supply flow rate and supply fan.	[17]
	Field measurement	Mechanically tighten up the actuator mechanism of a VAV box. Manually add bias to measurement data for VAV flow rate.	[21]
	TRNSYS simulation	Integrate a fault generator into simulation for VAV box.	[60]
	TRNSYS simulation	Integrate a fault generator in the HVAC simulator.	[91]
	Field measurement	Add bias to sensor measurements	[93]
	TRNSYS simulation	Insert fault into the normal operation data	[65]
	Experiment	Insert fault into the normal measurement data	[64]
	Field measurement	Add bias to sensor measurements	[108]
AHU	Field measurement	Replace sensor reading in SQL server artificially	[66]
	TRNSYS simulation	Apply a sensor reading bias generator	[61]
	Field measurement	Inject a constant voltage to a damper driver to keep its position unchanged	[104]
Chiller	DeST simulation	NM	[103]
	Synthetic data and measurement data	Add bias to the measurements data	[109]
	Laboratory experiment	1. Reduce pressure head of chilled water pump 2. Remove refrigerant 3. Block tubes in the condenser 4. Add nitrogen to the refrigerant	[107]
	DeST simulation	Reduced CT fan speed in DeST program	[103]
	Measurement data	Add bias error via software to chiller control panel	[104]

Note*: NA means not available.

2.5.2 Fault levels

The inserted faults levels for chiller studies, found in the literature review, are summarized in Table 2-6. The maximum amplitude of fault is 68% for excess oil fault [72,97,99], while the minimum amplitude with 1% is found for non-condensable gas fault [72,95,97,99].

As for sensor faults studies, HVAC system attracts most attentions [17,20,21,60,64,65,91–94]. In addition, chiller sensor faults [103,109] and AHU sensor faults [61] are also noticed in the literature review. The levels of artificial sensor faults are listed in Table 2-7. Here, V_{sa} is the supply air flow rate in m^3/s, V_{oa} is the outdoor air flow rate in m^3/s, V_{ra} is the return air flow rate in m^3/s, T_{chws} is the chilled water supply temperature in ℃, T_{chwr} is the chilled water return temperature in ℃, T_{oa} is the outdoor air temperature in ℃, T_{sa} is the supply air temperature in ℃, T_{room} is the room temperature in ℃, V_{chw} is the chilled water flow rate in L/s.

Table 2-6. Common chiller variable faults in the literature review.

Chiller variable faults	Fault level
Reduced chilled water flow rate (V_{chw})	Reduction by 10% to 40% [22,95–97,99]
Reduced condenser water flow rate (V_{cdw})	Reduction by 10% to 40% [22,72,95–99]
Refrigerant undercharge	Reduction by 10% to 40% [22,95,97–99]
Refrigerant overcharge	Addition of 10% to 40% [22,72,95,97,99]
Excess oil	Addition of 14% to 68% [72,97,99]
Condenser fouling	Addition of 12% to 45% [22,72,95,97,99]
Non-condensable gas	Addition of 1% to 5.7% [72,95,97,99]
Reduced air follow rate for CT	Reduction by 10% [103]

Table 2-7. Artificial sensor faults insertion in the literature review.

System	Faults			
	Sensor	Bias fault	Drifting fault	Complete failure
HVAC system	V_{sa}	Addition of +10% [17], reduced by -20% [21]		[20]
	V_{ra}	Reduced by -20% [60]		
	T_{chws}	Addition of 7% [21], 1℃[91], 1℃ [93]	0.3℃/h [65]	
	T_{chwr}	Addition of 7% [21], 1℃[91], with a range of (1℃, 30℃) [65], reduced by -1℃ [93]	0.3℃/h [65]	
	T_{oa}	Addition with a range of (1℃, 30℃) [65]	0.3℃/h [65]	
	T_{sa}	Addition of 8% [21,60], and 2.8℃ [64], reduced by -8% [60], and -1.5℃ [91]	-0.004℃/min [91]	[91]
	T_{room}	Addition with a range of (1%, 20%) [66], Addition with a range of (1℃, 30℃) [65]	0.3℃/h [65]	[20]
AHU	V_{sa}	Reduced by 20% [60], and 10%[61]	0.004(kg/s)/min [60]	
	V_{oa}	Addition of 20% [59,60] and 25% [59]		[59,60]
	T_{sa}	Addition 5% [66]		[59,66]
	T_{chws}	Addition of 7.1%[61]		
	T_{chwr}	Addition of 7% [60], 4.2% [61]		
	V_{chw}	Reduced by -10%[61]		
Chiller	T_{cdwr}		1℃ per month [103]	
	T_{chwl}	Random bias with a range of (-0.54℃, 0.81℃)		

The complete failure means sensor reading keeps constant in Table 2-7. The maximum injected bias faults for T_{chws} and T_{chwr} sensor are 30 ℃ for cooling coil of a HVAC system [65]. Sun et, al. [103] investigated the gradual degradation fault of chiller capacity in an 1800-hour period, and a drifting fault of 1℃ per month for T_{cdwr} sensor.

Literature review finds diverse approaches to inserting faults with no standard, guideline, or general rule for how/where to inject a fault. Injecting a fault in the reviewed publications is case-independent.

2.6. Conclusions from literature review

Literature review finds most studies have used experimental data or synthetic data, and applied different machine learning models to detect and diagnose faults in the field of HVAC. Three gaps are found including:

1. Lack of research for chiller FDD based on measurement data from a real building.
2. Lack of research for chiller MSFs study. As the core component of the HVAC system, chiller accounted for 42% of service resources and 26% repair cost [110], which deserves more attentions. Though dependent relationships exist in most HVAC system which increases the complexity of faults and their respective symptoms [111], there are no publications that focus directly on chiller MDFs.
3. Lack of grey-box models to predict the behavior of chiller components in a real building. Existing grey-box models of chiller, derived from laboratory experiments, are powerful to predict target variables, since laboratory experiments can provide very strict conditions and enough information required by a specific research project. But they are not practical when it is desired to apply them in real buildings, where the instrumentation is the minimum needed to monitor and control the building process [88].

2.7. Dissertation scope

First, we clarify the difference between sensor fault and variable fault. The fault of a sensor normally does not propagate to other variables, but only shows abnormal measurement values. The variable fault (abnormal value) could propagate to other variables.

This dissertation focuses on detecting and diagnosing dependent variable faults of a water-cooled chiller, using a grey-box model-based approach with measurements from a real building. The study of independent sensor fault(s) is beyond the scope of this dissertation. Grey-box models are time-efficient (fast to be trained) and resource-efficient. Such merits are beneficial for implementation, therefore, can easily be integrated with BAS to provide automated/online FDD.

FDD can be coupled with many different approaches as it underpins many applications for the decision/strategy-making of operators, energy-efficient improvements, system maintenance plan etc. Furthermore, there are many additional task/applications which could incorporate this work; however, they are beyond the scope of this dissertation.

Chapter 3: Evidence-based assessment of energy performance of two large centrifugal chillers over nine cooling seasons

The evaluation of energy performance changes of large centrifugal chillers over long-term periods is seldom presented in the literature. This chapter assesses the variation of energy performance over nine years of two identical (at design conditions) vapor-compression water-cooled large capacity centrifugal chillers. Both chillers serve the cooling system of a university campus, where measurements are recorded at 15-min time intervals and data was extracted over a period from 2009 to 2017 [112]. The measurement uncertainty estimation of direct and derived variables, extracted form BAS during the summer of 2016, are presented as an example. First, the hypothesis that weekly values of coefficient of performance (*COP*) of these large chillers does not change significantly over the summer of 2016 is verified. Second, the t-test also verifies the hypothesis of no significant change of seasonal *COP* values from 2009 to 2017. Third, a linear correlation-based model shows a variation of *COP* values by 1-2% per year between 2009 and 2017. The results show that the seasonal variation of *COP* is not statistically significant.

3.1. Introduction of long-term performance analysis of large centrifugal chillers

Vapor-compression electric centrifugal chillers, installed in commercial and institutional buildings, have an important contribution to the whole building energy use. Chillers of capacities of 264 to 2640 kW (75- to 750-ton refrigeration) have a median service life of more than 25 years [113]. They are usually designed for a lifetime of 40 years or more [114], and they can exceed this lifetime if operations, maintenance, service water, and operating environment are properly managed and controlled. For comparison, window-type air conditioners have a lifetime of 10 years, residential single or split package 15 years, residential and commercial air-to-air heat pumps 15 years, and commercial water-to-air heat pumps have more than 24 years [113].

The long-term performance of such large capacity chillers used in heating, ventilation, and air-conditioning (HVAC) systems plays a major role on the energy costs over the equipment lifetime. Long-term energy performance could change from the design performance due to the degradation with time, faults, and failures. Relevant information about degradation with time can help for (i) setting preventive maintenance plans, (ii) proper sizing of required cooling capacity at the design stage, and (iii) estimation of lifetime energy consumption and cost. However, such information is rarely available as it depends on many factors such as chiller type and cooling capacity, manufacturer, operation and maintenance conditions.

3.*2. Information of the cooling plant and maintenance strategy*

3.2.1. Cooling plant information

This cooling plant is composed of two water-cooling centrifugal chillers at design conditions and serves, with chilled and hot water, several AHUs and fan coils installed in building of Concordia Loyola Campus, Montreal, Canada. The two centrifugal chillers, EarthWise^{TM} CenTraVacTM Water Chillers (TRANE), Model CVHF910, use low-pressure R-123 refrigerant, and are identical at design conditions (Table 3-1) [115]. They are named as CH#1 and CH#2 in this dissertation, and cooled down by two cross flow cooling towers (B.A.C.), CT-1 and CT-2, having a capacity of 4540 kW (1290 tons) each, at design conditions.

Table 3-1. Design conditions.

Description of variable	Symbol of variable	Value	Unit
Evaporator cooling load at design condition	$Q_{ev,des}$	3,165	*kW*
Chiller *COP* at design condition	COP_{des}	5.76	NA
Electric power input to chiller at design condition	E_{des}	549.5	*kW*
Chilled water leaving temperature at design condition	$T_{chwl,des}$	5.6	*°C*
Chilled water return temperature at design condition	$T_{chwr,des}$	13.3	*°C*
Condenser-water leaving temperature at design condition	$T_{cdwl,des}$	35.0	*°C*
Condenser-water return temperature at design condition	$T_{cdwr,des}$	29.4	*°C*
Cooling tower load at design condition	$Q_{CT, des}$	4,540	*kW*
Volumetric flow rate of chilled water at design condition	$V_{chw,des}$	72.6	*L/s*
Volumetric flow rate of condenser-water at design condition	$V_{cdw,des}$	131.5	*L/s*

The cooling plant operates in three different scenarios: (1) Scenario 1: only chiller 1 works (CH#1); (2) Scenario 2: only Chiller 2 works (CH#2); and (3) Scenario 3: both CH#1 and CH#2 work simultaneously (CH#1+CH#2). When the first chiller starts, the corresponding chilled-water and condenser-water pumps start too. The fans of the cooling towers start when the condenser pumps start. The second chiller starts only if the first chiller cannot meet the chilled-water demand, and therefore it cannot keep the set point of the supply chilled water temperature. Chiller CH#1 or CH#2 starts first by rotation, in order to balance the number of operating hours over the life span for each chiller.

Figure 3-1 presents a schematic of the cooling plant and main measurements, where the blue line represents the condenser-water loop, red line represents the refrigerant loop, and green line represents the chilled-water loop. BAS records the cooling plant operation every 15 minutes, and the raw measurements are assigned into three groups based on the three-scenario status. The measured variables from BAS are listed in Table 3-2. Each of the three data groups is further divided into two datasets, i.e., working days (WD) and weekend/holidays (WH).

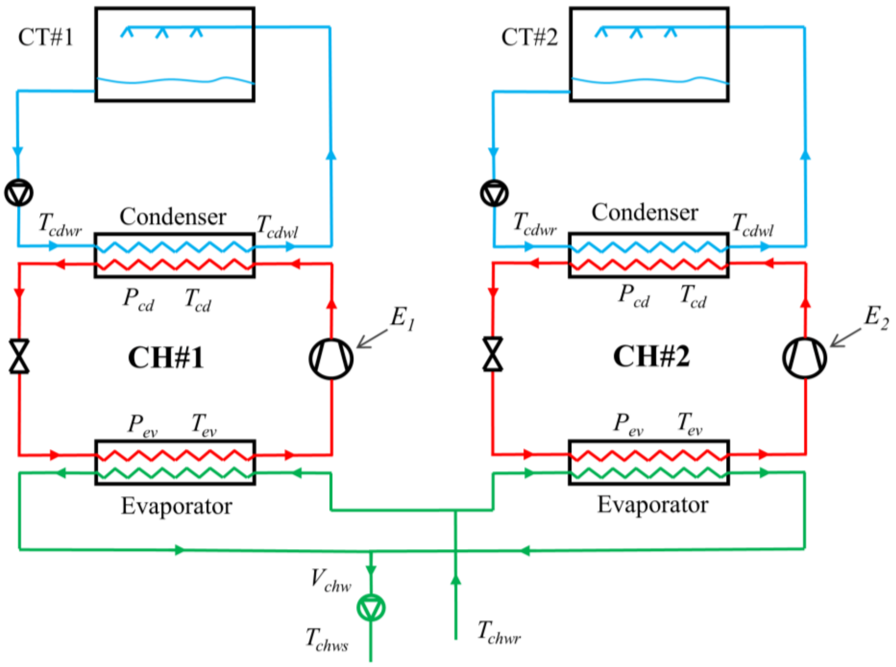

Figure 3-1. Schematic of the cooling plant.

Table 3-2. Available variables from measurements for the cooling plant in BAS.

Variable type	Description of points	Symbol	Unit	Reliability
Directly measured variables from BAS	Relatively humidity of outdoor air	RH_{oa}	%	✓
	Outdoor air temperature	T_{oa}	℃	✓
	Chilled water return temperature	T_{chwr}	℃	✓
	Chilled water leaving temperature	*T_{chwl}	℃	×
	Condenser-water return temperature	T_{cdwr}	℃	✓
	Condenser-water leaving temperatures	*T_{cdwl}	℃	✓
	Chilled water volumetric flow rate	V_{chw}	gpm	✓
	Power input to chiller	*E	kW	✓
	Saturated refrigerant temperature in evaporator	T_{ev}	℃	✓
	Refrigerant pressure in evaporator	P_{ev}	kPa	✓
	Saturated refrigerant temperature in condenser	T_{cd}	℃	✓
	Refrigerant pressure in condenser	P_{cd}	kPa	✓
Derived variables	Refrigerant temperature at compressor suction	T_{suc}	℃	✓
	Refrigerant temperature at compressor discharge	T_{dis}	℃	✓
	Refrigerant liquid line temperature	T_{ll}	℃	✓
	Coefficient of performance	*COP	~	✓
	Refrigerant mass flow rate	*$m_{ev,refr}$	kg/s	×
	Delta-T of chilled water	*ΔT_{chw}	℃	✓
	Delta-T of condenser water	*ΔT_{cdw}	℃	✓

3.2.2. Maintenance strategy

Regular maintenance of chillers is composed of annual maintenance and 5-year verifications. Annual maintenance, which is performed during the fall, is composed of the following tasks.

1. When the system is shut down:
    a. Cleaning of condenser tubes.
    b. Testing for refrigerant leaks in compliance with the provincial regulation on halocarbons.
    c. Revision and cleaning of primary and secondary electric connections of chillers.
2. When the system is turned on:
    a. Spectrographic oil analysis.

   b. Measurement of pressure loss in the evaporator and condenser for the validation of water flow with the manufacturer's design specifications.
   c. Measurement of operation pressure of evaporator, and the evaporator approach.
   d. Measurement of electric current for the validation with the manufacturer's design specifications.
   e. Measurement of oil pressure.
   f. Test of vibration.
   g. Measurement of temperature of major electric components.
   h. Verification of refrigerant and oil levels.
   i. Verification of warning and alarm signals from the controller.
3. Every five years, the following tasks are undertaken.
   a. Cleaning of condenser and evaporator tubes.
   b. Eddy current (Foucault) testing of all tubes of condenser and evaporator.

3.3. Analysis of energy performance of two chillers during the summer of 2016

3.3.1. Uncertainty analysis of measurements

The uncertainty of a measured variable (U_m) is consisted of bias uncertainty (BU_m) and random uncertainty (RU_m) [116,117], as described by Equation 3-1:

$$U_m = \sqrt{BU_m^2 + RU_m^2} \tag{3-1}$$

Where BU_m is the bias uncertainty, and RU_m is the random uncertainty. The author clarifies that for a measured variable without the information of bias error, the uncertainty only contains the random uncertainty.

The bias uncertainty of direct variables of T_{chwl}, T_{chwr}, and V_{chw} are:

$$BU_{T_{chwl}} = \overline{T_{chwl}} \times 0.005 + 0.3 \tag{3-2}$$

$$BU_{T_{chwr}} = \overline{T_{chwr}} \times 0.005 + 0.3 \tag{3-3}$$

$$BU_{V_{chw}} = \overline{V_{chw}} \times 0.05 \quad (3\text{-}4)$$

The random uncertainty, due to random fluctuations in measurements of a variable x, is:

$$RU_x = \frac{t \cdot S_x}{\sqrt{n}} \quad (3\text{-}5)$$

Where t-statistic value = 1.96, for a 95% confident level, for two-sided interval, and S_x is the standard deviation.

As for the derived variables, they are affected by the errors propagated from directly measured variables. An example for the measurement uncertainty of $Q_{ev,chw}$ ($U_{Qev,chw}$) is presented here to show the error propagation. Based on the calculation of $Q_{ev,chw}$ (Equation 3-8) with multiplication algorithm, $Q_{ev,chw}$ is derived based on three direct measurements, T_{chwl}, T_{chwr}, and V_{chw}. Hence, $U_{Qev,chw}$ is calculated by Equation 3-6, and such a method is also applied for the derived variable with division algorithm:

$$\frac{U_{Q_{ev,chw}}}{Q_{ev,chw}} = \sqrt{\left(\frac{U_{T_{chwr}}}{T_{chwr}}\right)^2 + \left(\frac{U_{T_{chwl}}}{T_{chwl}}\right)^2 + \left(\frac{U_{V_{chw}}}{V_{chw}}\right)^2} \quad (3\text{-}6)$$

3.3.2 Measurement data of the summer of 2016

Before comparing the energy performance of those two chillers over nine seasons of operation (section 3.4), the author opted for the discussion of results from measurements recorded at 15 min time intervals during the summer of 2016. That summer had the greatest cooling load among the last three years of data collected. This section presents the uncertainty of direct and derived measurements, and discusses some relationships of interest extracted from measurements: (a) change of weekly *COP* values; (b) variation of *COP* versus cooling load Q_{ev}; (c) variation of *COP* versus outdoor air temperature T_{oa}; and (d) variation of power input ratio to compressor versus part load ratio at evaporator.

Dataset extracted from BAS contains measurements of 14 weeks from May 30, 2016 until August 28, 2016, recorded at 15 min time intervals. There are three operation scenarios: (1) only chiller CH#1 is on, (2) only chiller CH#2 is on, and (3) both chillers CH#1 and CH#2 are on. Only measurements recorded during chillers operations were extracted from BAS and used for the long-term chiller operational analysis. The authors used BAS trend data collected over nine years. The issue of periodic recalibration of thousands of sensors on a large campus is beyond the authors' control.

The cooling load of evaporator(s) is calculated for the three scenarios using the measurements at the exit of central plant. The chilled water volumetric flow rate (V_{chw}) is the summation of chilled water flow rates from both chillers. The mean value of V_{chw} is 88 *L/s* when only one chiller is on, and 156 *L/s* when both chillers are on. The average difference between the measurements of chilled water supply temperature at the exit of central plant and corresponding values measured at chiller CH#1 is negligible, while at chiller #2 is about 0.5°C. The *COP* value is calculated separately for CH#1 and CH#2 respectively, for scenarios (1) and (2). The average *COP* of both chillers working simultaneously is calculated for scenario (3).

The entire dataset is divided into three different datasets according to the three scenarios. Chiller CH#1 worked 51.3% of the total operation time, chiller CH#2 worked 19.8% of time, and both chillers CH#1 and CH#2 worked together 28.9% of time.

The cooling plant serves with chilled and hot water several air-handling units and fan coils installed in buildings of this campus. This thesis presents the *COP* of chillers. The analysis of *COP* of whole system that should take into account the electric power input to supply and return fans, circulating pumps, and controls, is beyond the scope of this dissertation. The data processing follows the approaches presented in Chapter 5.

Cooling load at evaporator $Q_{ev,chw}$, in kW, is calculated at each time step (Equation 3-8):

$$Q_{ev,chw} = c\rho V_{chw}(T_{chwr} - T_{chwl}) \quad (3\text{-}8)$$

Where $Q_{ev,chw}$ is the evaporator cooling load on chilled water side in *kW*, *c* is water heat capacity in kJ/(kg·℃*)*, ρ is water density in kg/m^3, V_{chw} is the volumetric flow rate of chilled water in m^3/s, T_{chwr} is the chilled water return temperature in ℃, T_{chwl} is the chilled water leaving temperature in ℃,

The mean value of *COP* is calculated over the selected time interval (e.g. day, week, season) with Equation 3-9:

$$COP = \frac{1}{n}\sum_{i=1}^{n}\frac{Q_{ev,i}}{E_i} \tag{3-9}$$

3.3.3. *Change of weekly COP values during the summer 2016*

This section presents the use of classical method of statistical inference, in the area of tests of hypotheses [118] to verify if the weekly *COP* values of scenarios 1 and 3 change over the summer of 2016. Section 4 applies the method to seasonal *COP* values over nine years. Table 3-3 presents as an example the weekly values (mean ± uncertainty) from the simultaneous operation of chillers CH#1 and CH#2 (scenario 3) over the summer of 2016. For completeness of data presentation, Table B1 of Appendix B presents the measurements from the operation of chiller CH#1 (scenario 1). Measurements from the operation of chiller CH#2 in the summer of 2016 are not presented because only four weeks of data are available.

Table 3-3. Weakly values (mean ± uncertainty) of direct and derived measurements from the simultaneous operation of chillers CH#1 and CH#2 (scenario 3) over 13 weeks, from May 30 to August 28, 2016.

Week	T_{chwl} (℃)	T_{chwr} (℃)	V_{chw} (L/s)	E (kW)	$Q_{ev,chw}$ (kW)	COP (-)
1	6.88±0.33	11.70±0.39	156.48±7.86	557.87±32.31	3144.82±243.98	5.64±0.55
4	7.18±0.37	12.33±0.47	156.06±7.90	607.79±43.93	3351.92±273.54	5.51±0.60
5	6.58±0.33	12.00±0.40	155.97±7.85	614.47±36.78	3525.63±277.72	5.74±0.57
6	6.58±0.33	11.84±0.39	156.39±7.85	602.15±34.55	3422.99±268.99	5.68±0.55
7	6.71±0.34	12.69±0.40	157.40±7.89	696.11±39.92	3916.21±304.51	5.63±0.54
8	6.58±0.33	11.94±0.39	155.79±7.81	617.12±35.88	3479.03±272.84	5.64±0.55
9	6.58±0.33	11.86±0.37	156.18±7.83	605.84±32.79	3436.13±267.86	5.67±0.54
10	6.58±0.33	11.76±0.37	155.16±7.77	595.67±32.04	3351.33±261.21	5.63±0.53
11	6.57±0.33	12.40±0.39	157.37±7.87	674.86±38.01	3812.01±296.75	5.65±0.54
12	6.58±0.33	11.43±0.37	155.60±7.80	566.23±30.95	3145.41±246.60	5.56±0.53
13	6.58±0.33	12.24±0.38	157.74±7.90	649.36±35.45	3708.80±288.05	5.71±0.54

The method is first presented for the operation under scenario 3 (Table 3-3). Two populations of weekly *COP* values, calculated from 15 min time intervals data, are considered. The first population is generated by assuming that the *COP* value (*COPwk1*) of first week of data set does not change over the following weeks (from week 2 to 13). The second population is composed of derived weekly *COP* values of weeks *j*=2 to 13 (Table 3-3). Since the measurements came from the same chiller, the two populations are interdependent or paired. In this case, the t-test applies for testing the mean of differences of these two paired-populations, rather than testing the differences of means as in the case of independent populations [117].

The null hypothesis H_0 states that the weakly COP values do not change over time:

$$H_0\colon d_{mean} = 0 \tag{3-10}$$

where d_{mean} is the mean of the individual differences dj between the weekly COP values of two populations; and $dj = COPwk1 - COPwkj$, with j=2 to 13.

The alternative hypothesis H_1 states that weekly COP values change with time:

$$H_1\colon d_{mean} \neq 0 \tag{3-11}$$

The t-statistic is calculated as follows (Equation 3-12):

$$t = d_{mean}/(s/\sqrt{n}) \tag{3-12}$$

where d_{mean} and s are random variables that represent the mean and standard deviations of dj values; and n is the number of paired COP values [117].

The critical region of the Student's t-distribution for the two-tailed test is defined as: $t > t_{CR,\alpha/2,n-1}$, and $t < - t_{CR,\alpha/2,n-1}$. The critical value t_{CR} is selected by using the significance level $\alpha/2 = 0.025$ (2.5% probability of committing a Type I error, or rejection of null hypothesis when it is true); and number of degrees of freedom $d.f. = n - 1$. The null hypothesis is rejected if t is in the critical region of the Student's t-distribution.

Table 3-4. Results of t-test for comparison of weekly COP values during the summer 2016.

Dataset	d_{mean}	s	$d.f.$	t	Critical region	
					$t > t_{CR,\alpha/2,n-1}$	$t < - t_{CR,\alpha/2,n-1}$
Scenario 1 CH#1	-0.112	0.059	8	-0.635	2.306	-2.306
Scenario 3 CH#1+CH#2	-0.002	0.067	9	-0.10	2.262	-2.262

The results from scenarios 1 and 3 (Table 3-4) show that the null hypothesis is true because t-statistic is not in the critical region. In conclusion, there is not significant statistical evidence to say that the weekly *COP* values have changed from the *COP* value of the first week of available data during the summer of 2016, for the operation under scenarios 1 and 3.

3.3.4. COP versus cooling load $Q_{ev,chw}$ at evaporator using 15 min time intervals data

Since the t-test concluded that the weekly *COP* values of chillers have not changed during the summer of 2016, Section 3.4 uses the whole data set of 15 min time intervals of summer 2016 for the subsequent analysis.

Under normal operation conditions, *COP* increases with the rise of Part Load Ratio ($PLR=Q_{ev,chw}/Q_{des}$), and has the maximum value at *PLR*=1.0. As shown by from the measurements of a cooling plant with four chillers rated at 1758 kW each, the highest degree of correlation was obtained between the chiller *COP* and *PLR*, and less degree of correlation with other operation variables [119].

The measurements of chillers of this study show that the maximum *COP* values of CH#1 and CH#2 are recorded in the flat region of cooling load curves between 2,000 kW and 2,500 kW, which corresponds to *PLR* between 0.63 and 0.79 (Figure 3-2.a), and decreases after. When both chillers are used simultaneously, their maximum *COP* corresponds to 3,000 kW to 5,000 kW cooling load $Q_{ev,chw}$, or *PLR* between 0.47 and 0.79, and slightly decreases after. Other operation variables, not measured in this study, and the uncertainty of measurements could be the reason of such a variation of *COP* versus $Q_{ev,chw}$.

The results of other studies support the results of this paper. The measurements by [120] of a cooling plant, composed of five air-cooled chillers of rated cooling capacity of 1,400 kW each, revealed also that the majority of *COP* values were significantly below the manufacturer's curve in the *PLR* range above 0.5. The reduction in chilled water flow rate from the rated value could be the main reason for the degradation in chiller performance. In another study, [121] showed that the Part Load Factor ($PLF=COP/COP_{des}$) of a centrifugal chiller has the maximum value in an almost flat region of *PLR* between 0.6 and 0.9.

Chillers CH#1 and CH#2 reached maximum cooling load of about 3,000 kW each or *PLR* = 0.95 (Figure 3-2.a and 3-2.b). When both chillers work in parallel, they do not reach the maximum capacity; they work at *PLR* of about 0.87 each.

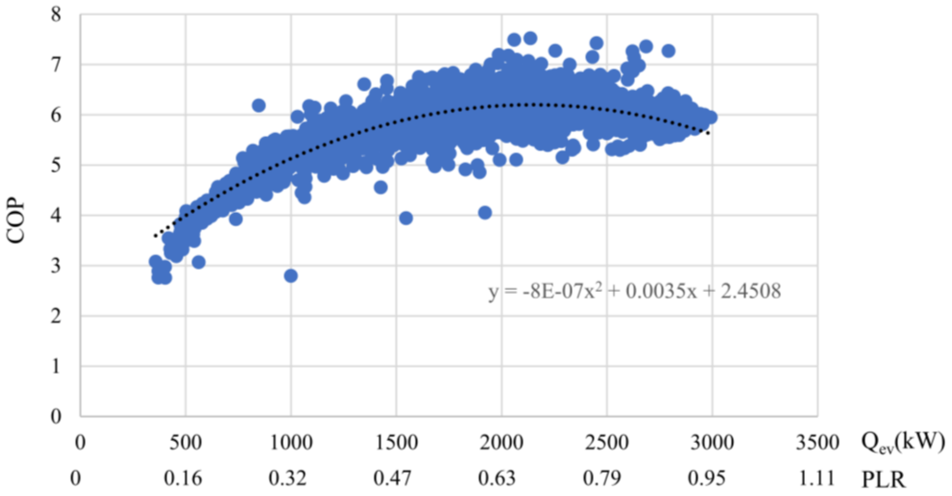

(a) Chiller CH#1

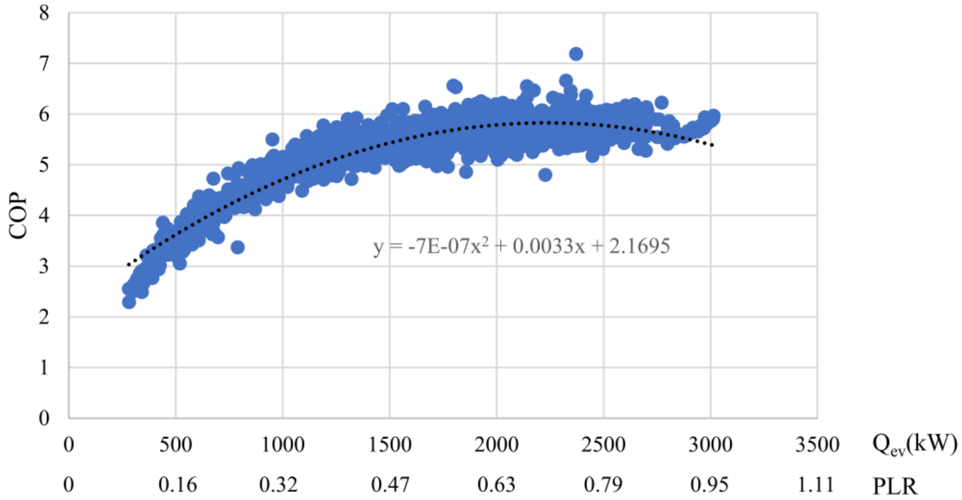

(b) Chiller CH#2

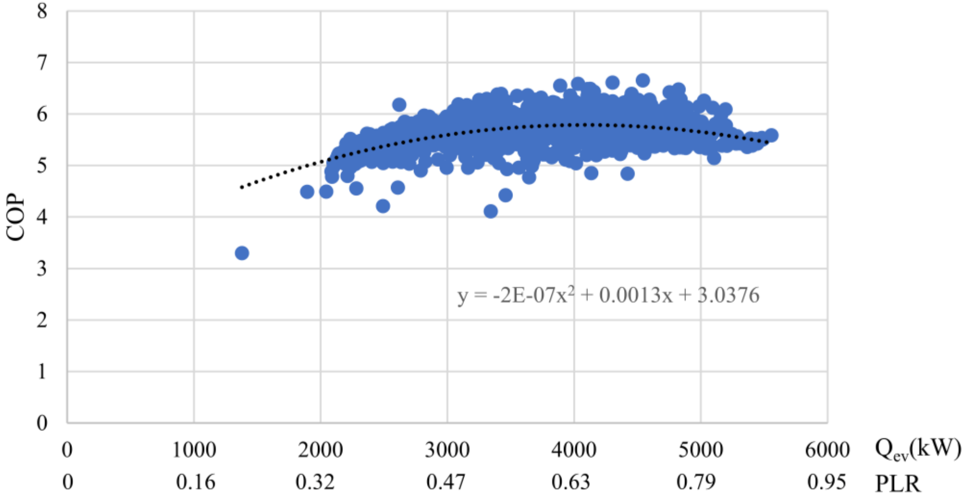

(c) Chillers CH#1 + CH#2

Figure 3-2. Variation of *COP* versus chiller cooling load (Q_{ev}) using 15 min time intervals data recorded during the summer of 2016. (a) Chiller CH#1, (b) Chiller CH#2, (c) Chillers CH#1+CH#2.

Let us take some data from the operation of chiller CH#1 alone (scenario 1) on two operation periods of the summer 2016 to explain the variance presented in Figure 3-2.a (same comments apply to Figure 3-2.b and 3-2.c). Data extracted correspond to almost constant $PLR = 0.51 \pm 0.01$ (Table 3-5).

1. Direct measured variables (E, T_{chwl}, T_{chwr}) have variations around the mean values, which can be observed in Table 3-5, and Figure 3-3 where E/E_{des} is plotted against $Q_{ev,chw}/Q_{des}$.
2. The uncertainties of direct measurements propagate through the corresponding defining formulas of the derived measurements ($Q_{ev,chw}$, PLR, COP) (Appendix A). To simplify the explanation, Table 3-5 shows only the mean and standard deviation of each variable. At constant PLR value, the derived measurements show variation about the mean value.
3. As an example, by considering the COP uncertainty of 0.57 (Table 3-3) the maximum COP value calculated for July 4-10, 2016 is 6.54, which is within the range of Figure 3-2.a.

Table 3-5. Mean and standard deviation of direct and derived measurements when $PLR = 0.51 \pm 0.01$.

Time interval	P, kW	T_{chwl}, °C	T_{chwr}, °C	$Q_{ev,chw}$, kW	COP (-)
July 4-10, 2016	271.95±10.13	6.85±0.07	11.33±0.13	1621.16±38.36	5.97± 0.27
July 25-31, 2016	271.96± 9.01	6.84±0.09	11.30±0.13	1610.328±42.37	5.93± 0.19

4. Another situation that adds variance to normal pattern is when the operation changes from one chiller (CH#1) to two chillers (CH#1+CH#2). This is due to the difference between the system response time and recording data of variables change. In this case study, measurements are recorded at 15 min time intervals. For instance, on July 5, 2016 at 13:15:00, only chiller CH#1 was on, and T_{chwr} was too high (15.75°C). The chiller was unable to maintain the T_{chwl} setpoint, and the control system turned on the second circulating pump. The effect of second chiller on T_{chwl} was not yet noticed. As a consequence, at that time interval T_{chwl} was almost equal with T_{chwr}, and the cooling load $Q_{ev,chw}$ was small, which led to low calculated PLR. At 13:30:00 when the operation was recorded again, the operation of two chillers (CH#1 + CH#2) was recorded, and T_{chwl} was within the control range, and $PLR=0.71$. This kind of situation occurs only for short recording time intervals, of 15-30 min. When the integration of results is carried out for longer time periods of days, weeks or cooling season, this kind of variation is unnoticeable, and has no effect on the long-term variation of COP.

3.3.5. COP versus outdoor air temperature using 15 min time intervals data

When the outdoor air temperature T_{oa} is between 20°C and 40°C, the mean *COP* value of each operation scenario does not vary with T_{oa}: mean *COP* = 5.9 when CH#1 is on, 5.8 when CH#2 is on, and 5.7 when both CH#1 and CH#2 are on. When T_{oa} is between 15°C and 20°C, the *COP* value increases by about 0.37 per 1°C of increase of outdoor air temperature.

3.3.6. Power input ratio (PIR) versus part load ratio (PLR) at evaporator

Since the operation at part load ($PLR= Q_{ev,chw}/Q_{ev,des}$) at evaporator has an important impact on the electric power input ratio ($PIR= E/E_{des}$) at the compressor, this section evaluates their relationship from measurements at 15 min time intervals over summer 2016. Any abnormal pattern between these two normalized variables could bring the attention on some possible operation issues, before the long-term analysis is carried out.

The quadratic form of correlation-based model of *PIR*= f(*PLR*) used by two well-known building energy analysis programs, eQUEST and EnergyPlus, is used in this section as the starting point (Equation 3-13). The coefficients B_1, B_2 and B_3 are identified by using 15 min time intervals data of summer 2016 (Table 3-6).

$$PIR = B_1 + B_2 \cdot PLR + B_3 \cdot PLR^2 \tag{3-13}$$

Table 3-6. Coefficients *B1, B2* and B3 of Equation 3-13 from measurements at 15 min time intervals of summer 2016.

Model	B_1	B_2	B_3
CH#1, Measurements	0.1951	0.3464	0.4577
CH#2, Measurements	0.157	0.6248	0.2233
CH#1+CH#2, Measurements	0.2167	0.3065	0.5544
eQUEST	0.1715	0.5882	0.2374
EnergyPlus	0.2229	0.3134	0.4637

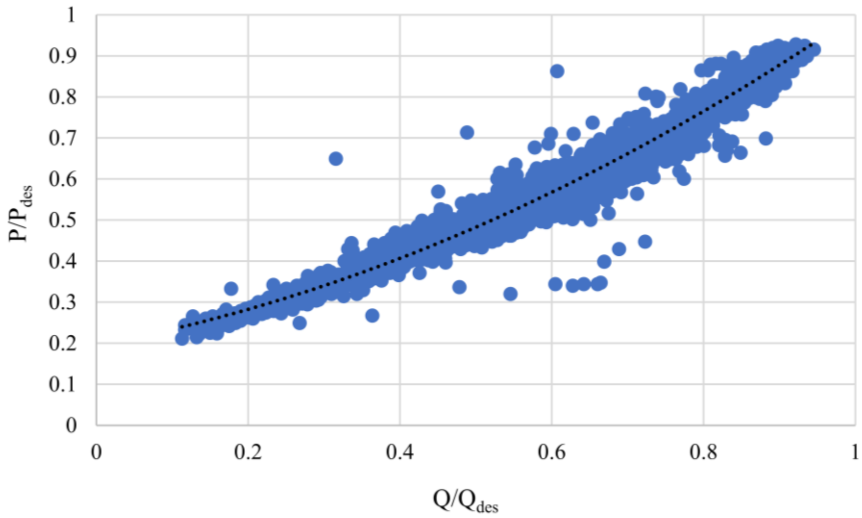

(a) Chiller CH#1

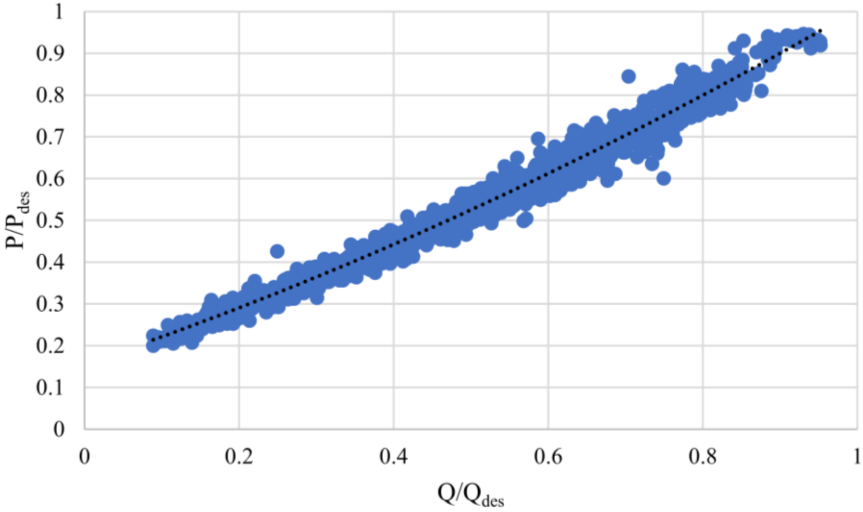

(b) Chiller CH#2

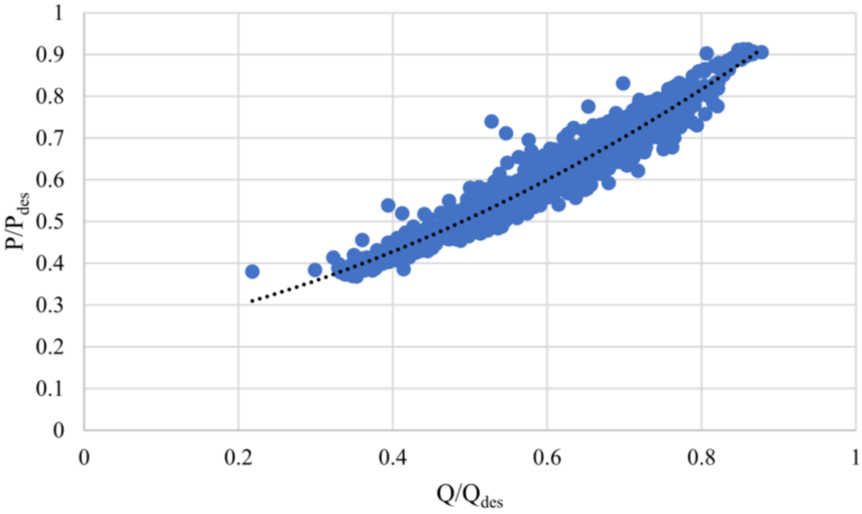

(c) Chillers CH#1 + CH#2

Figure 3-3. Variation of PIR=P/P_{des} versus PLR = Q/Q_{ev} from measurements of 15 min.

Figures 3-3.a to 3-3.c show the data points distribution from the three scenarios, and reveal normal pattern of operation. There is good agreement between the correlation-based models obtained from the measurements and two defaults models from eQuest and EnergyPlus programs (Figure 3-4), with some minor differences of values of coefficients B_1, B_2 and B_3 (Table 3-6). The coefficients B_1, B_2 and B_3 that are identified from the operation of CH#1 alone, and those from the simultaneous operation of chillers CH#1+CH#2 are close to the default coefficients used by EnergyPlus; while the coefficients identified from the operation of CH#2 alone are close to the default values of eQUEST.

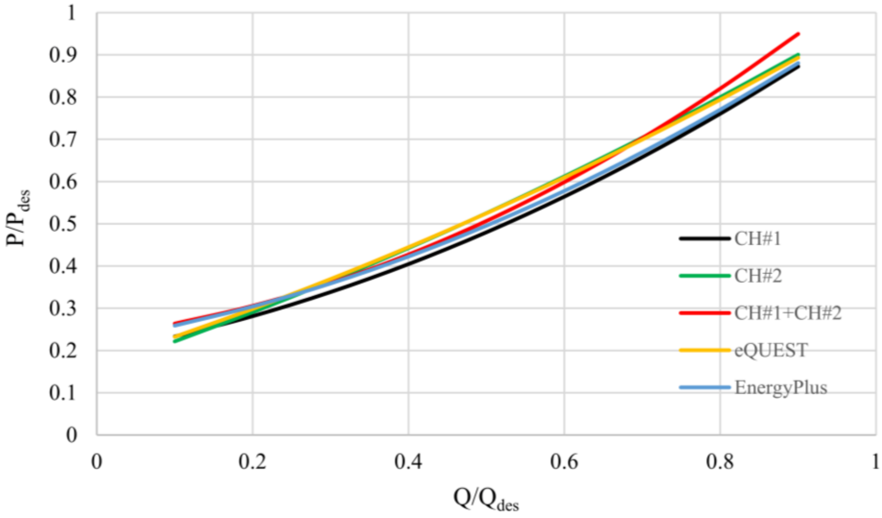

Figure 3-4. Variation of PIR=P/P_{des} versus PLR = Q/Q_{ev}. Comparison of correlation-based models from measurements of 15 min time interval of summer 2016 with default models from eQUEST and EnergyPlus programs.

3.4. Change of seasonal COP values from 2009 to 2017

Figure 3-5 reveals a small increasing trend of the seasonal average *COP* of chillers over nine years from 2009 until 2017, which was not presented so far in any publication. Tables B2 to B4 show detailed data.

Since results presented in Figure 3-5 contradict the literature, additional investigation was carried out to support the conclusions, and results are presented in this section (from Figure 3-6 to Figure 3-12). Measurements on the refrigerant loop were available from 2013 (Figure 3-6 and Figure 3-7). The average refrigerant pressure in the condensers of CH#1 and CH#2 was smaller in

2016-2017. The average refrigerant pressure in both evaporators was almost constant over five years, with the exception of CH#1 in 2013. Since chillers use low-pressure refrigerant R123, the pressure in the evaporator is lower that the atmospheric pressure.

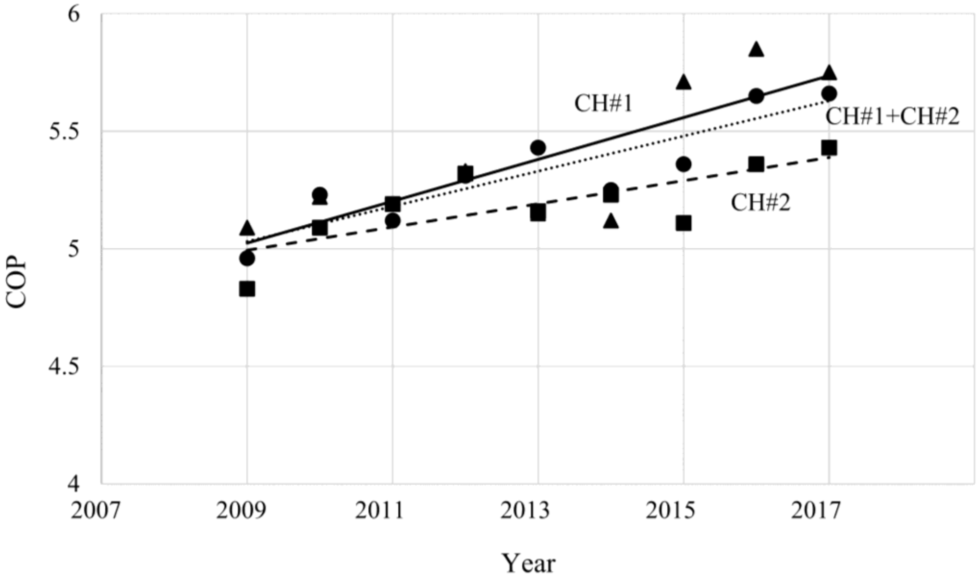

Figure 3-5. Seasonal average *COP* of chillers versus year of measurements.

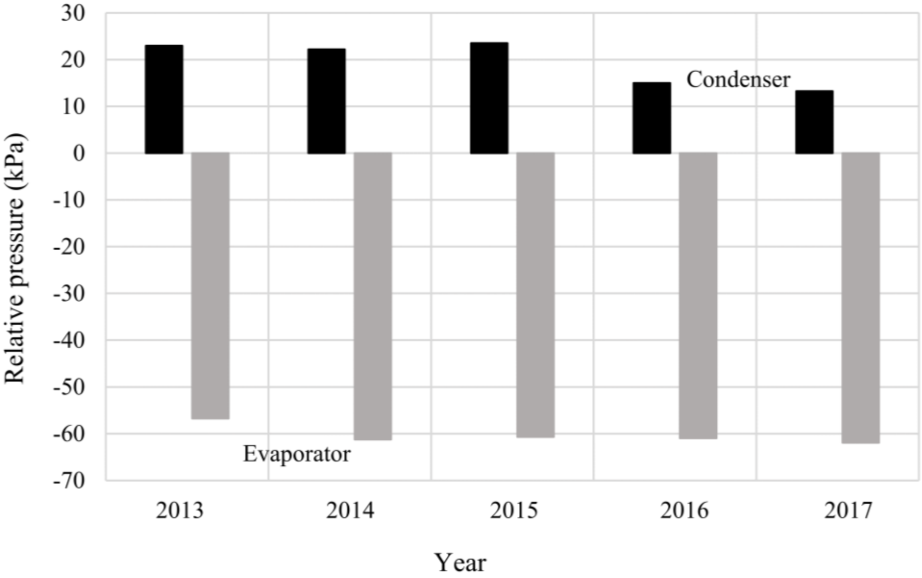

Figure 3-6. Seasonal average pressures of condenser and evaporator of chiller CH#1 versus year of measurements.

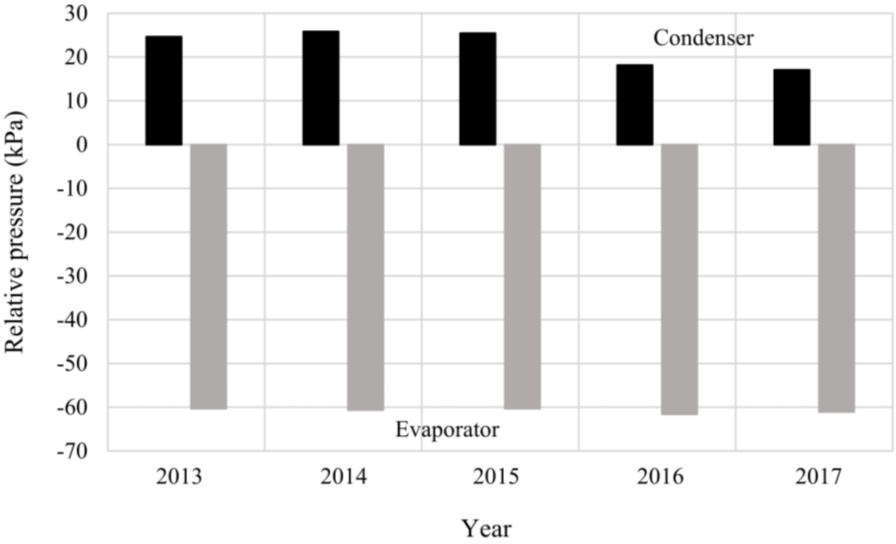

Figure 3-7. Seasonal average pressures of condenser and evaporator of chiller CH#2 versus year of measurements

One useful metric for assessing the chiller operation is the compressor lift or head pressure, which is calculated as the difference between the condenser and evaporator refrigerant pressures. Under the conditions presented in this paper, the compressor lift was smaller by about 10% in CH#1 and CH#2 in 2016-2017 compared with 2014-2015 (Figure 3-8). This reduction is expected to increase the *COP*, because of smaller compressor work, if other variables of interest remain constant (e.g., evaporator load, water temperature to and from the cooling towers, etc.).

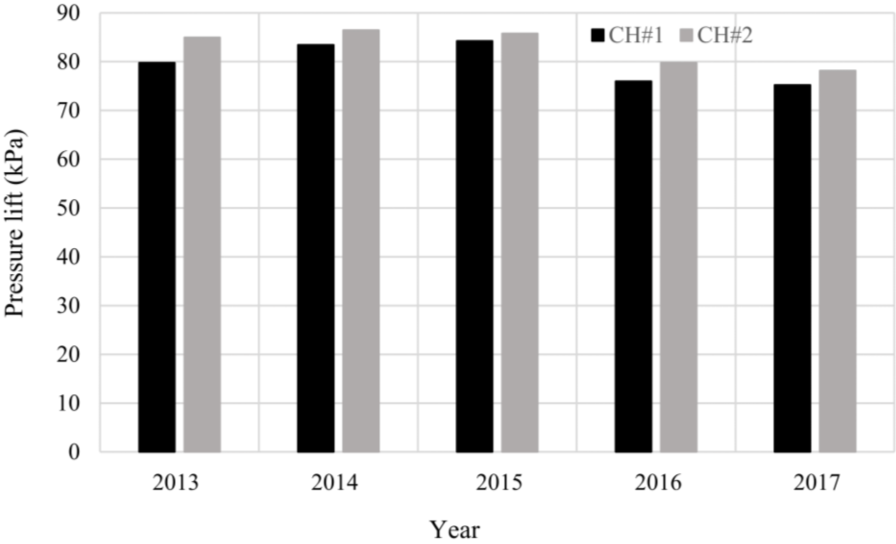

Figure 3-8. Seasonal average compressor lift versus year of measurements.

However, measured values of other variables also changed: (1) the evaporators load slightly increased since 2013 (Tables B2 to B4); and (2) the average temperature difference of water through condensers was about 4.3°C in both chillers (Figure 3-9 and Figure 3-10), compared with design temperature difference of 5.6°C.

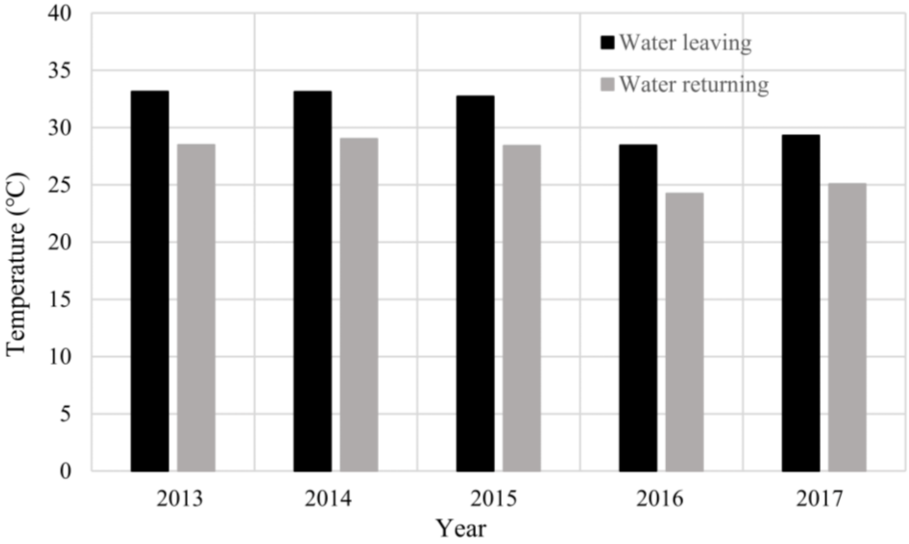

Figure 3-9. Water temperature leaving the condenser of chiller CH#1 and returning from the cooling tower CT-1.

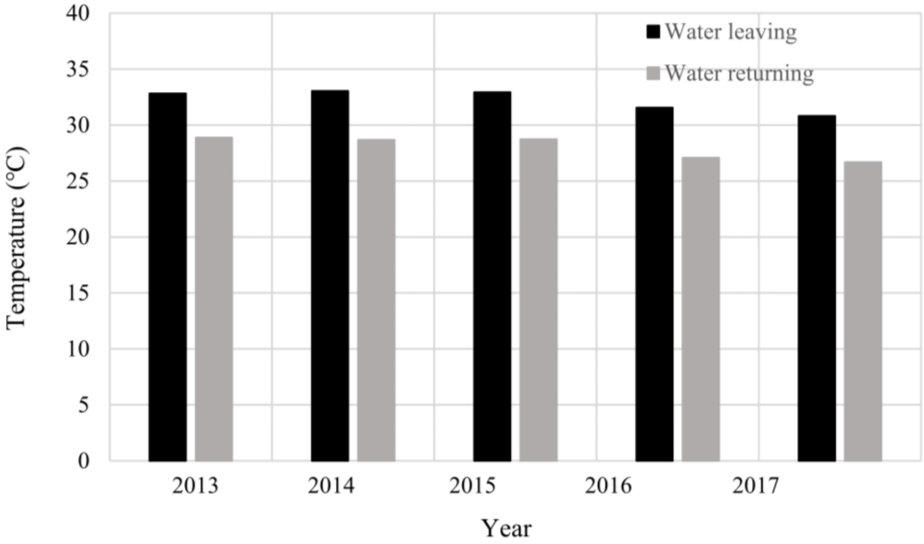

Figure 3-10. Water temperature leaving the condenser of chiller CH#2 and returning from the cooling tower CT-2.

Additionally, the average T_{chwl} was about 7.0°C, that is higher than the design temperature of 5.6°C; and the chilled water temperature difference through the evaporators was about 4.1°C, that is smaller than 7.7°C at design conditions.

The second useful metric is the condenser approach that is calculated as the difference between the liquid refrigerant (measured on the liquid line) and leaving condenser water temperature. The condenser approach in this study (Figure 3-11) has values between 0°C and 2.09°C for CH#1, and between 0°C and 0.35°C for CH#2, compared with practical recommendations of 0°C-3°C for water-cooled chillers [122].

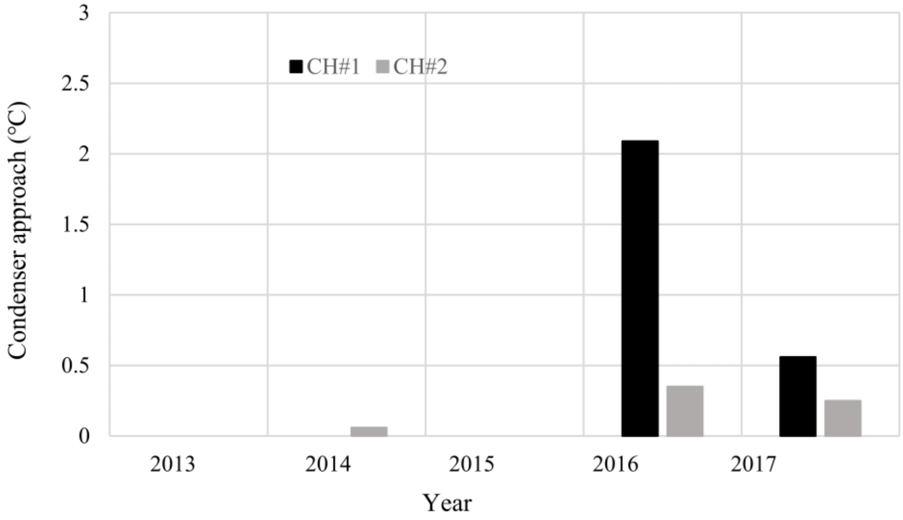

Figure 3-11. Seasonal average condenser approach versus year of measurements.

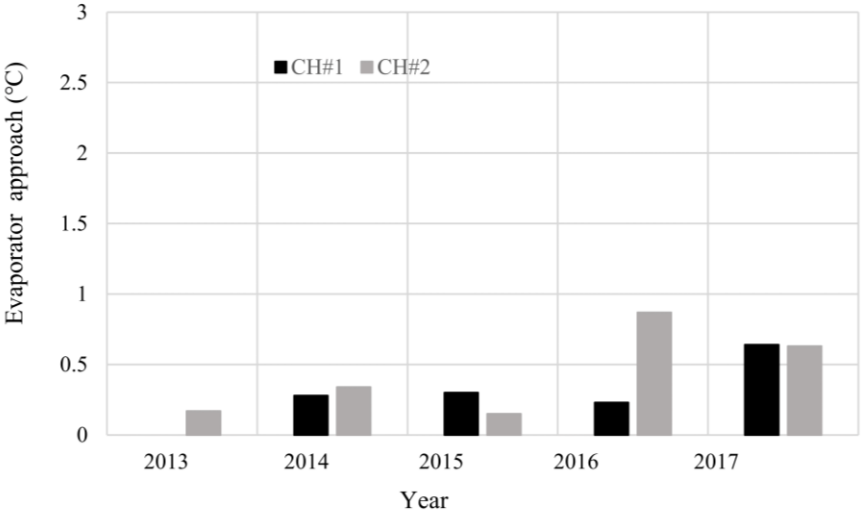

Figure 3-12. Seasonal average evaporator approach versus year of measurements.

The third useful metric is the evaporator approach that is calculated as the difference between the leaving chilled water temperature and saturated refrigerant temperature leaving the evaporator. The evaporator approach in this study (Figure 3-12) has values between 0°C and 0.64°C for CH#1, and between 0.15°C and 0.87°C for CH#2, compared with practical recommendations of 0°C-2°C for water-cooled chillers [123].

One can conclude that the condenser and evaporator approaches, calculated from measurements of 2013-2017, are within the acceptable limits.

The analysis of measurements indicates that the reduction of the compressor lift, variation of evaporator cooling load, and operation of chilled and condenser water temperatures at different values compared with design conditions, along with regular maintenance of chillers at the beginning of a cooling season, might be the reason of offsetting the chillers ageing. The authors do not have other information about chillers design and operation variables that possibly contributed to the trend of Figure 3-5.

Only the visual display of *COP* variation over nine years (Figure 3-5) cannot prove the paper hypothesis that the seasonal energy performance of these two centrifugal chillers does not change significantly over nine seasons of operation. Section 3.4.1 and Section 3.4.2 present two different approaches to conclude if the change of *COP* is statistically significant or not: (1) using the hypothesis testing as discussed in section 3, and (2) using linear correlation-based model between seasonal *COP* values and time.

3.4.1. Hypothesis testing

The t-test presented in section 3.3.3 is also used in this section to verify if the seasonal *COP* values of each scenario have changed significantly from 2009 to 2017. Although the operation of chillers started in 2007, the measurements of electric power input *E*, required for *COP* calculations, became available only in 2009. Tables B2 to B4 (Appendix B) present direct and derived measurements of summers of 2009 to 2017 under the three scenarios, displayed as the seasonal mean value ± uncertainty.

The null hypothesis H_0 states that the seasonal COP_s values do not change over time from 2009 to 2017:

$$H_0\colon D_{mean} = 0 \qquad (3\text{-}14)$$

The alternative hypothesis H_1 states that seasonal COP_s values change with time:

$$H_1 : D_{mean} \neq 0 \tag{3-15}$$

where D_{mean} is the mean of the individual differences dj between the seasonal COP_{s2009} value of summer 2009 and the seasonal COP_{sj} value of each subsequent year j (from 2010 to 2017); and $d_j = COP_{s2009} - COP_{sj}$, *with* j=2010 to 2017.

The t-statistic is calculated as (Equation 3-16):

$$t = D_{mean} / \left(s / \sqrt{n} \right) \tag{3-16}$$

where D_{mean} and s are random variables that represent the mean and standard deviations of dj values; and n is the number of paired *COP* values [117].

The results (Table 3-7) prove that the null hypothesis is true because t-statistic is not in the critical region of Student t-distribution (as selected for the two-sided test, and the significance level $\alpha/2 = 0.025$). In conclusion, there is not significant statistical evidence to say that the seasonal *COP* values have changed from 2009 to 2017 for all three scenarios of operation.

Table 3-7. Results of t-test for comparison of seasonal COP values between 2009 and 2017

Data set	D_{mean}	s	*d.f.*	t	Critical region	
					$t > t_{CR,\alpha/2,n-1}$	$t < -t_{CR,\alpha/2,n-1}$
Scenario 1: CH#1	-0.357	0.312	5	-0.443	2.571	-2.571
Scenario 2: CH#2	-0.406	0.123	6	-1.253	2.447	-2.447
Scenario 3: CH#1+CH#2	-0.416	0.195	6	-0.080	2.447	-2.447

3.4.2. Linear correlation-based model

A linear trend model is assumed for the relationship between the seasonal COP_{sj} of year j (with j = 1 to 9) and year that is counted from 2007 (Equation 3-17):

$$COP_s = a \cdot (Year - 2007) + b \tag{3-17}$$

The regression coefficient *a* shows the slope of variation of COP_s with the number of years, while *b* shows the *COPs* value at *year* = 2007 (Table 3-8).

Table 3-8. Regression coefficients a and b of correlation-based model COP_s = f(year) under three scenarios.

	Scenario	a	b	R^2
COP_s	(1) CH#1	0.02	0.85	0.63
	(2) CH#2	0.01	0.85	0.58
	(3) CH#1+CH#2	0.01	0.85	0.80

When chillers CH#1 and CH#2 work separately, the slope of linear regression of COP_s is 0.02 per year (for scenario CH#1), and 0.01 per year (for scenario 2) from 2009 to 2017. The coefficient of determination R^2 of 0.63 and 0.58, respectively, indicates a moderate positive linear relationship between COP_s and time (year).

When both chillers work in parallel (scenario 3), the slope of linear regression of COP_s is 0.01 per year from 2009 to 2017. The coefficient of determination R^2 = 0.80 indicates a strong positive linear relationship.

The results of this case study show that the seasonal COP_s value increased slightly by 1% per year for scenarios 2 and 3, and by 2% per year for scenario 1. This result over nine years contradicts all publications that conclude on the annual reduction of COP_s.

The results of this study of 1-2% of seasonal change of COP_s per year are 25 to 50 times smaller than the calculated measurement uncertainty of *COP* of about 0.5 (Tables B2 to B4). Therefore, one can easily conclude that the seasonal change of COP_s is negligible.

The results of sections 3.4.1 and 3.4.2 converge on the same conclusion: there is not evidence to prove that the seasonal *COP* values of two chillers of this case study, working under three different scenarios, have significantly changed from 2009 until 2017. Annual changes of *COP* of 1% to 2% do not have a statistical significance.

3.4.3. Conclusions of long-term chiller energy performance assessment

This chapter concludes that there is not evidence to prove that the seasonal *COP* values of two chillers of this case study, working under three different scenarios, have changed over nine years (from 2009 to 2017). Though other operation and control variables, not measured in this study, might be source of such in-significant degradation of long-term energy performance, in the absence of other explanations, the authors concluded that the reduction of the compressor lift, variation of evaporator cooling load, and operation of chilled and condenser water temperatures at different values compared with design conditions, along with regular maintenance at the beginning of cooling season, have offset the chillers ageing. As a result, the *COP* value has not changed significantly over the nine cooling seasons of measurements.

3.5. Experience learnt about the need of FDD

As the chiller energy performance can keep unchanged over a long-term, one of the most likely explanations for a malfunction of chiller system is a fault occurs due to various reasons, which calls for the need to detection the fault and finally isolate the source of fault, if possible.

Measurements of this cooling plant were obtained directly from building automation system, without authors' participation in sensors calibration. Authors have doubts that on a large campus most sensors are periodically re-calibrated, when other urgent actions are needed for proper operation of HVAC systems. In an ideal world, a dedicated monitoring system periodically re-calibrated should be installed, and results of analysis, over many years of data, should be compared with those obtained from using BAS trend data.

However, in a real world, noise, inaccuracy, etc., are the intrinsic properties of measurements, which reduces the performance of a derived model, or even add barriers to formulate a model. Therefore, measurement data of this cooling plant should be well calibrated to assess its feasibility in the application of model development. A study for the same cooing plant [124] dispels this concern, where the default EnergyPlus model was calibrated with measurements, and compared with measurement data and TRNSYS simulation data. The study indicated it is possible to develop a calibrated model using measurement data without modifying by trial-and-error some variables or using stochastic approaches. Thus, measurements, extracted from BAS for this cooling plant, are readily feasible for model development.

Chapter 4: Methodology for the development of MDFDD models

This dissertation focuses on the development of benchmarking grey-box model-based method to detect and diagnose chiller MDFs, using measurement data from a real building. The monitored variables from BAS were extracted as the input of benchmarking grey-box models. The forward fault detection model and the backward diagnosis model underpin the main structure of MDFDD model in this dissertation. Different from the experiment data from laboratory in a controlled environment or the synthetic data from simulation programs, measurements from BAS in a real building usually cover limited information. Thus, establishing grey-box models with measurement data to achieve good performance requires many endeavors. If the benchmarking grey-box models are successfully developed, they are then integrated into the forward model to detect a fault symptom, when the difference between measurements and predictions of a target variable exceeds a threshold value. Once the fault symptom is detected, the rule-based backward fault diagnosis model is applied. The proposed method can be generalized by updating the model parameters with measurements from other chillers. Such an alternative method can be integrated in BAS for continuous commissioning of HVAC equipment.

4.1. Measurement data

This dissertation used the monitored variables from the available trend data of BAS (Table 3-2) and applied the data preprocessing steps prior to the model development stage and the model application stage. Data preprocessing includes corrective actions and the removing actions. Missing recordings are replaced by the publicly available sources or removed. Outliers identified by a commonly recognized criteria are also removed. Apart from the direct variables (directly measured variables), derived variables are also used in this dissertation.

4.2. Forward residual-based model for fault detection

The feedforward fault detection model works in a way following three sequential steps: (1) establish benchmarking grey-box models to predict target variables, (2) calculate the residual between the predicted variable and the measured variable, and (3) compare the residual with a corresponding threshold. If the residual of a variable exceeds the corresponding threshold, a fault symptom is detected. The strategy, using forward-sequential steps to finalize the identification of fault symptoms, underpins the feedforward structure of the fault detection model. To fully describe the chiller operation, target variables representing both the system-level behaviors and local-level behaviors are selected for model development.

4.2.1. Benchmarking grey-box models

The grey box model contains many benefits similar to physical based models; however, such models differ in that the parameters of grey-box models can be identified through statistical analysis. Thus, grey-box models tend to be robust [24]. Compared with other data-driven models, grey-box models can provide limited extrapolation outside the range of training data [24]. Besides, the form of grey-box model is usually simple, and are, therefore, scrutable, and easy to use.

Within this dissertation, grey-box models are developed with input variables (called regressor variables) that show impacts on subsequential variables (called target variables), which are available in BAS measurements and presented in Chapter 5. A grey-box model is regarded as a benchmarking grey-box model if results of model training and testing, due to both the static window approach and the dynamic window approach, verify the accuracy and robustness of the proposed grey-box model. Thus, a benchmarking grey-box model characterizes for accurate and robust, and could provide reference values for the corresponding target variable.

Benchmarking grey-box models are then applied within this dissertation for the following three purposes:

I. Predict the chiller operation status under normal conditions (e.g., E and T_{cdwl}).

II. Predict the refrigerant enthalpy at three key points in a refrigerant loop within the vapor compression system, using the information only from the refrigerant side (e.g., T_{ev} and P_{ev}). Consequently, the predicted enthalpy are used to estimate some derived variables (e.g., $Q_{ev,chw}$).

III. After benchmarking grey-box models are validated by measurement data under normal conditions, artificial faults are inserted into the testing dataset. Then, the benchmarking grey-box models are applied to generate the impact on target variables due to artificial regressor faults.

4.2.2. Symptom models

Symptom models are developed to detect faults within the chiller. As defined in Chapter 2, a fault means this deviation/difference exceeds an acceptable tolerance of a variable in terms of the research target; herein, this toleration is estimated by the threshold. Several target variables are selected for the symptom model development.

This dissertation establishes symptom models for the purpose of detecting MDFs. The symptom models are defined as residuals, describing the deviation/difference between the predicted variables and the measured variables. If this deviation/difference falls out of a threshold, a fault symptom is identified.

4.2.3 Insertion of artificial fault

As measurement data with faults are not available, in this dissertation, some faults are manually inserted in the measurement dataset (e.g., 5°C increase bias for T_{chwl}), after the model validation with fault-free data is completed. Sequentially, the impact on a target variable is generated by the corresponding benchmarking grey-box model.

4.3. Backward rule-based model for fault diagnosis

After fault symptoms are detected, the backward rule-based approach is applied to diagnose the fault source. Since the fault diagnosis model needs and relies on the detected fault symptoms to trace the fault source, it follows a backward process.

Figure 4-1 summarizes the workflow of MDFDD model, where three main modules are included: (1) model validation module, (2) forward fault detection module, and (3) backward fault diagnosis module. Processes in black blocks are with respect to normal conditions, while processes in red blocks are related to the conditions with faults. The workflow of MDFDD model follows six sequential steps:

I. Extract data from BAS, preprocess them, and split training and testing datasets.
II. Key target variables that give essential information about the chiller system-level and component-level status are selected.
III. Grey-box models that predict the expected operation values of selected target variables, under normal operation conditions, are developed. Validate the accuracy and robustness of grey-box models with both the static window approach and the dynamic window approach

to identify whether these models can be regarded as benchmarking grey-box models. These models use measurements from input variables (regressor variables) that could be the source of abnormal performance of target variables.

IV. Insert artificial faults into the dataset, and calculate the impacts using benchmarking grey-box models. If the residual between a measured variable and a predicted variable exceeds the threshold, the fault symptom is detected.

V. A fault symptom might not reveal a real fault, but could be the result of abnormal values of regressors, which are in the loop prior to the target variable. The backward fault diagnosis method looks for the diagnosis of regressor faults. Thus, the target variable could be dependent of regressors. The faulty target variable itself can also generate the fault symptom.

VI. The MDFDD method concludes with three possible outcomes: (1) the target variable is faulty, (2) the regressor variables are faulty, and (3) both target and regressor variables are faulty.

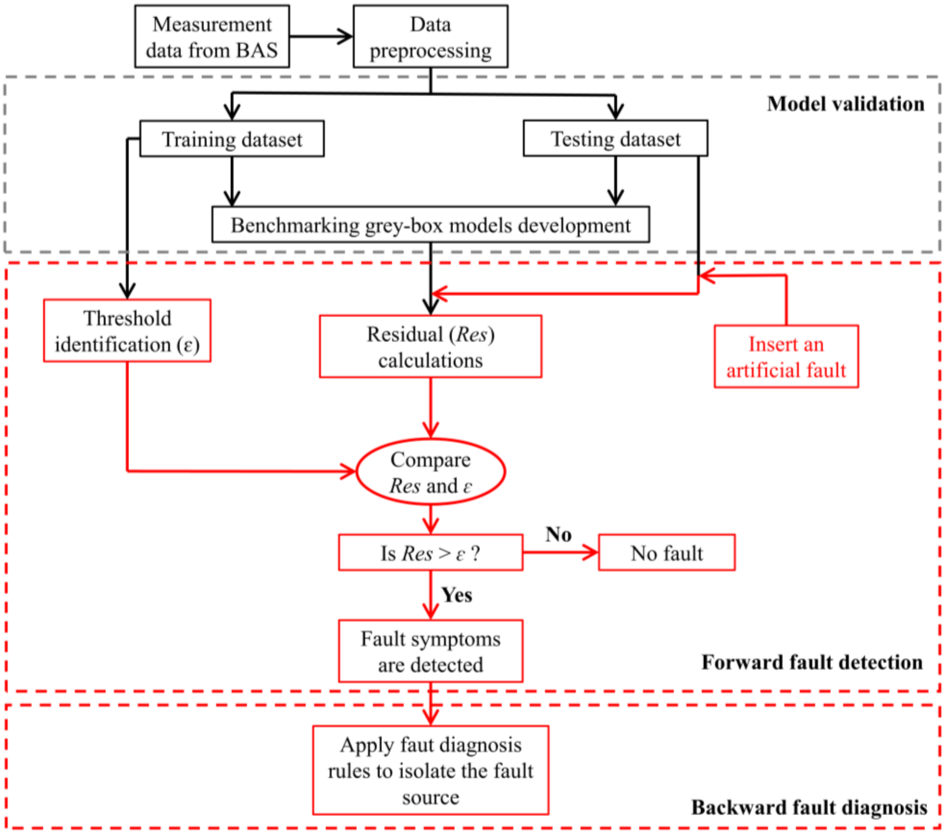

Figure 4-1. Workflow chart of dependent fault detection and diagnosis model.

4.4. Transfer learning

Transfer learning (TL) can be defined as the ability of a system to recognize and apply knowledge and skills learned in previous tasks to novel tasks [125]. TL is an efficient approach to a new task without developing new models, which is a time-efficient and resource-saving approach utilized by many studies in the field of HVAC [126–129].

Within this dissertation, Deep neural network (DNN) models are developed to predict chiller target variables with the application of different TL strategies. A DNN model, learnt on one chiller (called source chiller), is transferred to another chiller (called target chiller) with weights fine-tuned. The model performance is evaluated on the target chiller. The derived DNN models with different TL strategies are examined under diverse chiller operation conditions and different data distribution characters (e.g., small size of training dataset and large size of testing dataset) of the target chiller. This transfer is the generalized methodology that will be applied to all DNN models. The application of TL is conducted for the purpose of identifying the best TL strategy in improving DNN model performance on the target chiller.

Chapter 5: Development of the multiple dependent fault detection and diagnosis models

This chapter presents the model development for the feedforward fault detection models and the backward fault diagnosis models. The MDFDD model is established with the available variables extracted from BAS, including water-side and refrigerant-side information. Grey-box models are developed to predict system-level and component-level chiller operation status, for the purpose of generating residuals once predictions are compared with measurements, which are used for fault detection. Based on the results of fault symptom detection and dependency of target variables and regressor variables, backward fault diagnosis models are developed to isolate the fault source.

5.1 Data preprocessing

Due to the inaccuracy, incompleteness, and inconsistency of real-world databases, it is necessary to verify and, if needed, correct raw data quality [130]. The preprocessing of data includes corrective and removing actions of raw measurements. For the corrective action, the missed data for T_{oa} and RH_{oa} are replaced by values recorded by Environment Canada [131]. Due to possible factors of the sensor itself, the recording system, and/or the periodic maintenance [132], the noise and other abnormal data are unavoidable, which should be removed. For the removing actions, it follows the three sequential steps listed below.

Step 1: Samples with missing data (related cells in Excel file are filled with 'No Data') are removed. The variables with obviously abnormal values (e.g., negative values of V_{chw}) are also removed, when the cooling plant was operating in the normal condition.

Step 2: For the data rejection, measurements under transient conditions (start-up and shut-down periods of a chiller) are eliminated.

Step 3: Erase outliers. Chauvenet's criterion [116] is used to identify outliers. Any measurement will be eliminated if the value of deviation from the mean value divided by the standard deviation exceeds the criterion determined by Equation 5-1.

$$\frac{d_{max}}{S} = 0.819 + 0.544In(n) - 0.02346In(n^2) \tag{5-1}$$

Where d_{max} is the deviation from the mean of a variable, S is the standard deviation, and n is the number of data points.

5.2. Development of benchmarking grey-box models

The second law of thermodynamics reveals how energy flows through a chiller, from building to the outdoor environment, which follows the three sequential steps: (1) the building heat flows to the chiller evaporator, which is represented by the process that the chilled water is cooled down and the refrigerant evaporates. (2) the energy of evaporator flows to the condenser, driven by the work of a compressor, which is represented by the process that the low-pressure and low-temperature refrigerant is compressed to the high-pressure and high-temperature refrigerant. (3) the heat flows to the condenser water and is rejected to the outdoor environment through a cooling tower, which is represented by the process that the temperature of condenser water increases.

The above energy flow analysis indicates the subsequential variables (e.g., E, T_{cdwl}, etc.) can be affected by variables like T_{chwl}, V_{chw}, etc. As this dissertation focuses on dependent faults, the subsequential variables are preferred to be selected as target variables to describe system-level operation status of chiller. As for the local-level status, delta-T of chilled water (ΔT_{chw}) and delta-T of condenser water (ΔT_{cdw}) are two derived variables to describe the operation status of evaporator and condenser, respectively. Thus, variables of E, COP, and T_{cdwl} are selected to describe system-level status, and variables of ΔT_{chw}, and ΔT_{cdw} are selected to describe local-level status (evaporator and condenser). T_{chwl} and $m_{ev,refr,ref}$ are also selected as target variables. All these target variables are marked with *'*'* in Table 3-2. The primary unit for V_{chw} (gpm) is transferred to *L/s* in this dissertation with a conversion factor of 0.063.

5.2.1. Model of the electric power input to a chiller

The grey-box model for electric power input to the chiller (E) development starts with the analysis for the estimation of refrigerant mass flow rate, which is used as a regressor variable for the grey-box model of E_b. In most examples, the electric power input to the compressor, but not the electric power input to a chiller, is used to estimate the refrigerant mass flow rate. Li and Braun [50] proposed a virtual sensor to estimate the mass flow rate of refrigerant, where the power input to compressor was used in calculations; they assumed that 5% of electric power input is lost through heat exchange with environment and results reported that 93.33% of prediction fell within a range of ±3% of experiment data. Furthermore, references [133–136] also estimated the refrigerant mass flow rate of chiller with respect to electric power input to compressor.

The estimation of refrigerant mass flow rate, using electric power input to the chiller may ignore factors like the heat exchange between the compressor and environment, motor efficiency, etc [137]. However, the information of these factors is rarely available in real buildings. Therefore, it is necessary to develop a model to estimate the refrigerant mass flow rate, using only the available variables in the BAS trend data.

This dissertation assumes the refrigeration cycle starts with the heat removed from the chilled water loop at the evaporator, where the refrigerant mass flow rate is controlled by expansion valve. For most chillers in real buildings, T_{chwl} is a controlled variable and used as the reference for sizing equipment of the secondary HVAC system (AHU, fan coil, etc.). The measurements of case study indicate T_{chwl} varies around a setpoint temperature within a very limited variance (Section 6.3, Chapter 6). As the information of setpoint temperature of T_{chwl} is not available in BAS, it is replaced by the mean value of T_{chwl} over the training dataset ($\overline{T_{chwl}}$). Thus, Equation 5-2 is proposed to estimate the reference cooling load of evaporator ($Q_{ev,chw,ref}$) on water side with respect to $\overline{T_{chwl}}$. Correspondingly, $m_{ev,refr,ref}$ is the reference refrigerant mass flow rate at the evaporator (Equation 5-3).

$$Q_{ev,chw,ref} = c\rho V_{chw}(T_{chwr} - \overline{T_{chwl}}) \tag{5-2}$$

$$m_{ev,refr,ref} = \frac{Q_{ev,chw,ref}}{h_{suc} - h_{ll}} \tag{5-3}$$

The chiller compressor consumes electricity and compresses the refrigerant vapor to the super-heated status, for this reason, variable of $m_{ev,refr,ref}$ is selected as one regressor for the grey-box model of E_b. Another two variables, T_{chwl} and V_{chw}, also show potential impact on E, thus, a correlation based grey-box model is proposed to predict the electric power input to a chiller:

$$E_b = \alpha_1(T_{chwr} - \overline{T_{chwl}}) + \alpha_2 V_{chw} + \alpha_3 m_{ev,refr,ref} + \alpha_0 \tag{5-4}$$

5.2.2. Model of the coefficient of performance (COP)

A correlation-based benchmarking grey-box model is proposed with regressors showing potential impact on the *COP*.

$$COP_b = \beta_1 T_{chwl} + \beta_2 V_{chw} + \beta_3 PLR + \beta_4 m_{ev,refr,ref} + \beta_0 \tag{5-5}$$

Where β_i ($i = 0, 1,\ldots,4$) are the parameters to be identified during the training phase.

5.2.3. Model of the condenser-water leaving temperature

The development of grey-box models for T_{cdwl} starts with a chiller energy balance equation, which is introduced by Equation 5-6:

$$Q_{ev,chw} + E = Q_{cd,cdw} \tag{5-6}$$

$$Q_{cd,cdw} = c\rho V_{cdw}(T_{cdwl} - T_{cdwr}) \tag{5-7}$$

Where $Q_{cd,cdw}$ is the condenser load on condenser water side in kW, V_{cdw} is the volumetric flow rate of condenser water in m^3/s, T_{cdwr} is the condenser-water return temperature in ℃, T_{cdwl} is the condenser-water leaving temperature in ℃.

Based on Equation 3-8, Equation 5-6, and Equation 5-7, T_{cdwl} can be derived from:

$$T_{cdwl} = \frac{V_{chw}}{V_{cdw}}(T_{chwr} - T_{chwl}) + \frac{E}{c\rho V_{cdw}} + T_{cdwr} \tag{5-8}$$

Equation 5-8 is affected by the following three factors: (1) heat leakage, from the compressor to the environment, (2) the heat exchanger efficiency of the condenser, and (3) the heat exchanger efficiency of the evaporator. However, the information for the three factors is not available in measurements. To integrate the three factors, a grey-box model for T_{cdwl} can be developed with independent input variables in Equation 5-8. Besides, an experiment study found the refrigerant mass level has a direct impact on T_{cdwl} [138]. Thus, $m_{ev,refr,ref}$ is added as another independent variable for the grey-box model of T_{cdwl}. Therefore, a grey-box model for T_{cdwl} is proposed as Equation 5-9:

$$T_{cdwl,b} = \delta_1(T_{chwr} - T_{chwl}) + \delta_2 V_{chw} + \delta_3 m_{ev,refr,ref} + \delta_4 E + \delta_5 T_{cdwr} + \delta_0 \qquad (5\text{-}9)$$

Where δ_i (i = 0, 1, …5) are the parameters to be identified during the training phase.

5.2.4. Model of the delta – T of chilled water

The heat exchange, between chilled water and refrigerant, in the evaporator is separated by the evaporator tubes and complies with the forced heat convection process [139]: (1) the refrigerant absorbs the heat from chilled water (separated by evaporator tubes) and evaporates at a constant temperature, while (2) the chilled water, returning from the building (T_{chwr}), releases the heat to the evaporator tube and is cooled down. Then chilled water leaves the evaporator at a lower temperature (T_{chwl}). Figure 5-1 provides a schematic for the temperature distribution within a general evaporator.

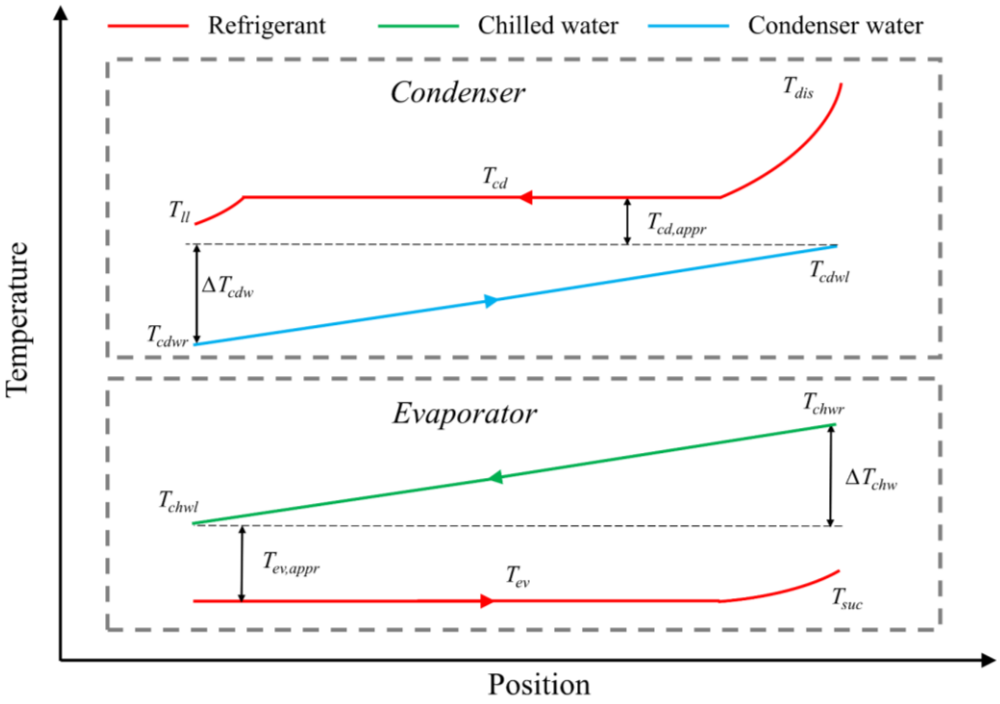

Figure 5-1. Schematic for temperature distributions of refrigerant loop and water loop in evaporator and condenser.

As refrigerant usually goes through the evaporating process within an evaporator, the evaporating temperature keeps constant and the subsequential surface temperature of evaporator tubes is constant, which generates a temperature difference, between the refrigerant in evaporator and chilled water temperature, as $T_{chwr} - T_{ev}$ (ignoring the thermal resistance of evaporator tubes). On the chilled water side, water properties related to heat convection like thermal diffusivity, dynamic viscosity depend on the chilled water velocity (u_{chw}).

Though u_{chw} is not available in measurements, the normalized $u_{chw,norm}$ can be approximated. Equation 5-10 indicates u_{chw} is proportional to V_{chw}, where A_{sec} is the cross-sectional area of chilled water flow in the evaporator. In the absence of the information of A_{sec}, $u_{chw,norm}$ is calculated by Equation 5-11:

$$u_{chw} = \frac{V_{chw}}{A_{sec}} \tag{5-10}$$

$$u_{chw,norm} = \frac{u}{u_{max}} = \frac{V_{chw}}{V_{chw,max}} \tag{5-11}$$

Where $V_{chw,max}$ is the maximum chilled-water flow rate in measurements.

The above analysis indicates u_{chw} can be used to estimate the un-available variables related to the forced heat convection process. Coupling with another term, T_{chwr} - T_{ev}, a grey-box model is proposed to estimate the delta-T of chilled water, where a multiplication algorithm is assumed:

$$\Delta T_{chw,b} = (\epsilon_1 u_{norm} + \epsilon_2)(T_{chwr} - T_{ev}) \tag{5-12}$$

Where ϵ_1 and ϵ_2 are parameters to be identified during the training phase. Equation 5-12 can be transformed to predict other variables (e.g., T_{chwr}), if needed.

5.2.5. Model of the delta-T of condenser-water

The general process for the condenser water circulating via the condenser follows the temperature increase, as the chiller rejects the heat to the condenser-water. The heat exchange, between condenser water and refrigerant, in the condenser is separated by the condenser tube and complies with the forced heat convection process: (1) the refrigerant releases the heat to the condenser tube, while (2) the condenser water absorbs this heat via the condenser tube. Then condenser water leaves the condenser with a higher temperature. The temperature distribution within a general water-cooled condenser and a schematic for the corresponding heat exchange process is displayed in Figure 5-1.

Heat transfer on the water side in a condenser complies with forced convection processes. The temperature difference between condenser tube ($T_{cd,tube}$) and condenser water return temperature (T_{cdwr}) is the driving force of heat transfer, as $T_{cd,tube}$ - T_{cdwr}. As the mass flow rate of condenser water is always set as a constant value in a common water-cooled chiller system, therefore, let's assume variables affecting heat transfer rate, like condenser configurations (condenser tube area, characteristic length, etc.) and condenser water properties (thermal diffusivity, dynamic viscosity, etc.), can be integrated into coefficients of a grey-box model.

Thus, the temperature difference of $T_{cd,tube}$ - T_{cdwr} turns to the most important term affecting the heat transfer rate of the condenser, which subsequently determines the delta-T of condenser water, $\Delta T_{cdw} = T_{cdwl} - T_{cdwr}$. The refrigerant status in a condenser can be divided into three sequential processes [140]: (1) the superheated refrigerant vapor at a temperature of T_{dis}, discharged by the compressor, is cooled to the saturated vapor, (2) the saturated vapor condenses to the saturated liquid (T_{cd}), and (3) the saturated liquid is sub-cooled (T_{ll}). Hence, a grey-box model is proposed to estimate $T_{cd,tube}$ considering the three processes:

$$T_{cd,tube} = c_1 T_{dis} + c_2 T_{cd} + c_3 T_{ll} + c_0 \tag{5-13}$$

Where:

$$T_{ll} = T_{cd} - \Delta T_{ll} \tag{5-14}$$

Here, T_{ll} is refrigerant liquid line temperature in °C, and ΔT_{ll} is 1°C [141]. Then, T_{ll} can be represented by T_{cd} by integrating it into the coefficient of T_{cd} and the bias term of the grey-box model, presented by Equation 5-15:

$$\Delta T_{cdw,b} = \theta_1 T_{dis} + \theta_2 T_{cd} - \theta_3 T_{cdwr} + \theta_0 \tag{5-15}$$

Where θ_i (i = 0, 1,…3) are the parameters to be identified during the training phase. Equation 5-15 can be transformed to predict other variables (e.g., T_{cdwl}), if needed.

5.2.6. Grey-box models for enthalpy at key points of the chiller refrigerant loop

Figure 5-2 maps four key points of the refrigerant cycle, where Point 1 is at the compressor suction manifold, Point 2 is at the compressor discharge, Point 3 is at the liquid line after the condenser, and Point 4 is after the expansion valve at the entrance of the evaporator. The refrigerant enthalpy keeps unchanged when it flows through the expansion valve: the refrigerant enthalpy at Point 3 equals to that at Point 4 ($h_4 = h_3$). In this dissertation, $h_{suc} = h_1$ in kJ/kg, $h_{dis} = h_2$ in kJ/kg, and $h_{ll} = h_3$ in kJ/kg. The state equation indicates refrigerant enthalpy is defined by state variables of refrigerant pressure and temperature, as described by:

$$h_{suc} = f(P_{ev}, T_{suc}) \tag{5-16}$$

$$h_{dis} = f(P_{cd}, T_{dis}) \tag{5-17}$$

$$h_{ll} = f(P_{cd}, T_{ll}) \tag{5-18}$$

Where P_{ev} in kPa is the refrigerant absolute pressure at the evaporator, P_{cd} in kPa is the refrigerant absolute pressure at the condenser. The superheating, $\varDelta T_{suc} = 2$ °C, and sub-cooling, $\varDelta T_{ll} = 1$ °C [141]. T_{suc} is defined by Equation 5-19, and T_{ll} is defined by Equation 5-14:

$$T_{suc} = T_{ev} + \varDelta T_{suc} \tag{5-19}$$

The compressor discharge temperature (T_{dis} in °C) is estimated by Equation 5-20 [142]:

$$T_{dis} = T_{suc}(\frac{P_{cd}}{P_{ev}})^{\frac{\gamma-1}{\gamma}} \tag{5-20}$$

Where γ is the heat capacity ratio. The thermodynamic property of the refrigerant in ideal conditions is only affected by state variables like temperature and pressure [32]. Refer to the PREFPROP program [143], the value of γ, within the range of refrigerant state in this work, has only very small variations. Thus, $\gamma = 1.1$ is used in this study.

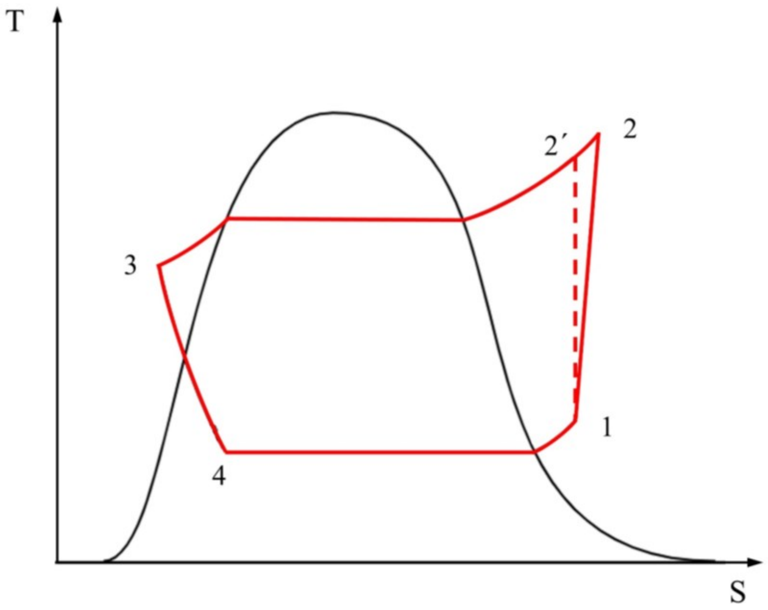

Figure 5-2. T-S diagram of the refrigeration cycle.

Then, the PREFPROP program are used to calculate the refrigerant enthalpy, since case study of this dissertation contains two R-123 electric chillers. PREFPROP, developed by the National Institute of Standards and Technology (NIST) [144], is a program to calculate the thermodynamic and transport properties of industrial fluids, and has been proven to be an extremely useful tool used by industry, government, and academia [145]. Enthalpy values derived from the PREFPROP program are used as the measurements for the grey-box model development of enthalpy at three key locations (h_{suc}, h_{dis}, and h_{ll}).

Since refrigerant enthalpy is mainly affected by the refrigerant temperature and pressure, this dissertation proposes the following three modes to estimate the refrigerant enthalpy of R-123 at three key locations:

$$h_{suc,b} = \vartheta_1 P_{ev} + \vartheta_2 T_{suc} + \vartheta_0 \tag{5-21}$$

$$h_{dis,b} = \tau_1 P_{cd} + \tau_2 T_{dis} + \tau_0 \tag{5-22}$$

$$h_{ll,b} = \varphi_1 P_{cd} + \varphi_2 T_{ll} + \varphi_0 \tag{5-23}$$

Where ϑ_i, τ_i, and φ_1 ($i = 0, 1, 2$) are the parameters to be identified during the training phase. Enthalpy values derived from PREFPROP program are used as the ground truth data for model training and testing.

5.2.7. Summary of grey-box models

To summarize, eight grey-box models are proposed to predict chiller operation status at system level and local level, which are listed in Table 5-1. These grey-box models with coefficients in Table 5-1 are trained with three model training approaches that are introduced in Section 5.6 of this chapter.

Table 5-1. Summary of grey-box models.

Variables	Grey-box models	Equation
E_b	$E_b = \alpha_1(T_{chwr} - \overline{T_{chwl}}) + \alpha_2 V_{chw} + \alpha_3 m_{ev,refr,ref} + \alpha_0$	5-4
COP_b	$COP_b = \beta_1 T_{chwl} + \beta_2 V_{chw} + \beta_3 PLR + \beta_4 m_{ev,refr,ref} + \beta_0$	5-5
$T_{cdwl,b}$	$T_{cdwl,b} = \delta_1(T_{chwr} - T_{chwl}) + \delta_2 V_{chw} + \delta_3 m_{ev,refr,ref} + \delta_4 E + \delta_5 T_{cdwr} + \delta_0$	5-9
$\Delta T_{chw,b}$	$\Delta T_{chw,b} = (\epsilon_1 u_{norm} + \epsilon_2)(T_{chwr} - T_{ev})$	5-12
$\Delta T_{cdw,b}$	$\Delta T_{cdw,b} = \theta_1 T_{dis} + \theta_2 T_{cd} - \theta_3 T_{cdwr} + \theta_0$	5-15
$h_{suc,b}$	$h_{suc,b} = \vartheta_1 P_{ev} + \vartheta_2 T_{suc} + \vartheta_0$	5-21
$h_{dis,b}$	$h_{dis,b} = \tau_1 P_{cd} + \tau_2 T_{dis} + \tau_0$	5-22
$h_{ll,b}$	$h_{ll,b} = \varphi_1 P_{cd} + \varphi_2 T_{ll} + \varphi_0$	5-23

5.3. Forward residual-based fault detection model

A fault symptom is detected when the residual, calculated as the difference between the measured value and predicted value, of a variable is greater than the corresponding threshold (ε). The following seven fault symptoms are considered in this dissertation. The threshold, used for fault symptom detection, equals to the measurement uncertainty of the corresponding variable. The discussion for measurement uncertainty analysis is presented in Section 5.5 of this chapter.

5.3.1. Symptom model for chilled water leaving temperature

A fault symptom is detected for the chilled water leaving temperature, if the following condition holds:

If $Res\ (T_{chwl}) = abs(T_{chwl,m} - \overline{T_{chwl}}) > \varepsilon(T_{chwl})$, then $Symp(T_{chwl}) = 1$

Otherwise: $Symp(T_{chwl}) = 0$

5.3.2. Symptom model for electric power input to the chiller

A fault symptom is detected for the electric power input, if the following condition holds:

If $Res(E) = abs(E_m - E_b) > \varepsilon(E)$, then $Symp(E) = 1$

Otherwise: $Symp(E) = 0$

5.3.3. Symptom model for coefficient of performance

A fault symptom is detected for the derived measurement of *COP*, if the following condition holds:

If $Res(COP) = abs(COP_m - COP_b) > \varepsilon(COP)$, then $Symp(COP) = 1$

Otherwise: $Symp(COP) = 0$

5.3.4. Symptom model for condenser water leaving temperature

A fault symptom is detected for the condenser water leaving temperature, if the following condition holds:

If $Res\ (T_{cdwl}) = abs(T_{cdwl,m} - T_{cdwl,b}) > \varepsilon(T_{cdwl})$, then $Symp(T_{cdwl}) = 1$

Otherwise: $Symp(T_{cdwl}) = 0$

5.3.5. Symptom model for delta-T of chilled water

A fault symptom is detected for the delta-T of chilled water, if the following condition holds:

If $Res\ (\Delta T_{chw}) = abs(\Delta T_{chw,m} - \Delta T_{chw,b}) > \varepsilon(\Delta T_{chw})$, then $Symp(\Delta T_{chw}) = 1$

Otherwise: $Symp(\Delta T_{chw}) = 0$

5.3.6. Symptom model for delta-T of condenser water

A fault symptom is detected for the delta-T of condenser water, if the following condition holds:

If $Res\ (\Delta T_{cdw}) = abs(\Delta T_{cdw,m} - \Delta T_{cdw,b}) > \varepsilon(\Delta T_{cdw})$, then $Symp(\Delta T_{cdw}) = 1$

Otherwise: $Symp(\Delta T_{cdw}) = 0$

5.3.7. Symptom model for refrigerant

A fault symptom of refrigerant flow rate, $Symp(m_{ev,refr})$, at the evaporator is detected, if the following condition holds:

If $Res(m_{ev,refr}) = \text{abs}(\Delta m_{ev,refr}) > \varepsilon(m_{ev,refr})$, then $Symp(m_{ev,refr}) = 1$

Otherwise: $Symp(m_{ev,refr}) = 0$

Where $\Delta m_{ev,refr}$ is the derived variation of refrigerant mass flow rate around a reference value (Equation 5-3), which is calculated with respect to the mean value of T_{chwl} (or $\overline{T_{chwl}}$). $\varepsilon(m_{ev,refr})$ is the threshold of $m_{ev,refr,ref}$.

$$\Delta m_{ev,ref} = \frac{\rho V_{chw}(\overline{T_{chwl}} - T_{chwl})}{h_{suc} - h_{ll}} \tag{5-24}$$

5.3.8. Analysis for the forward dependent fault detection model

The dependency between regressor variables and target variables, or even between only regressor variables, makes the fault detection complex. Figure 5-3 elaborates the dependency relation and the structure of forward fault detection model.

As shown in Figure 5-3, the variable dependency between Column *Direct variables* and Column *Target variables* is defined, including (1) the relationship between direct variables and target variables, and (2) the relationship between direct variables and derived variables (e.g., *COP*, $m_{ev,refr,ref}$, etc.). Please note that as the regressor variable $m_{ev,refr,ref}$ of three grey-box models (E_b, COP_b, and $T_{cdwl,b}$), they are connected on the other side in Figure 5-3. For instance, three regressor variables T_{chwl}, V_{chw}, and $m_{ev,refr,ref}$ of the grey-box model for electric power input are connected to the E_b (marked with an orange dot ●) with arrowed lines.

The fault detection model, as shown in Figure 5-3, follows a forward process: (1) establish grey-box models to predict target variables, (2) calculate residuals between measurements and predictions of grey-box models, (3) compare the residual with the corresponding threshold, and (4) a fault system is detected if the residual exceeds the corresponding threshold. Thus, the fault detection model is called the forward model.

This forward 'map' (Figure 5-3) navigates how one regressor variable fault propagates to a target variable and potentially trigs a fault symptom. Let's take the impact of T_{chwl} fault on *Symp(E)* as an instance: T_{chwl} fault propagates to E_b, and sequentially leads to the increases of *Res(E)*, which results in *Symp(E)* might be detected potentially. Following another path in Figure 5-3, T_{chwl} fault propagates to the derived variable of ΔT_{chw}, and sequentially leads to the increases of $Res(\Delta T_{chw})$, which results in $Symp(\Delta T_{chw})$ might be detected potentially. Thus, this forward fault detection 'map' illustrates well the dependency between regressor and target variables, and gives an overall view of fault propagation from regressor variables to target variables.

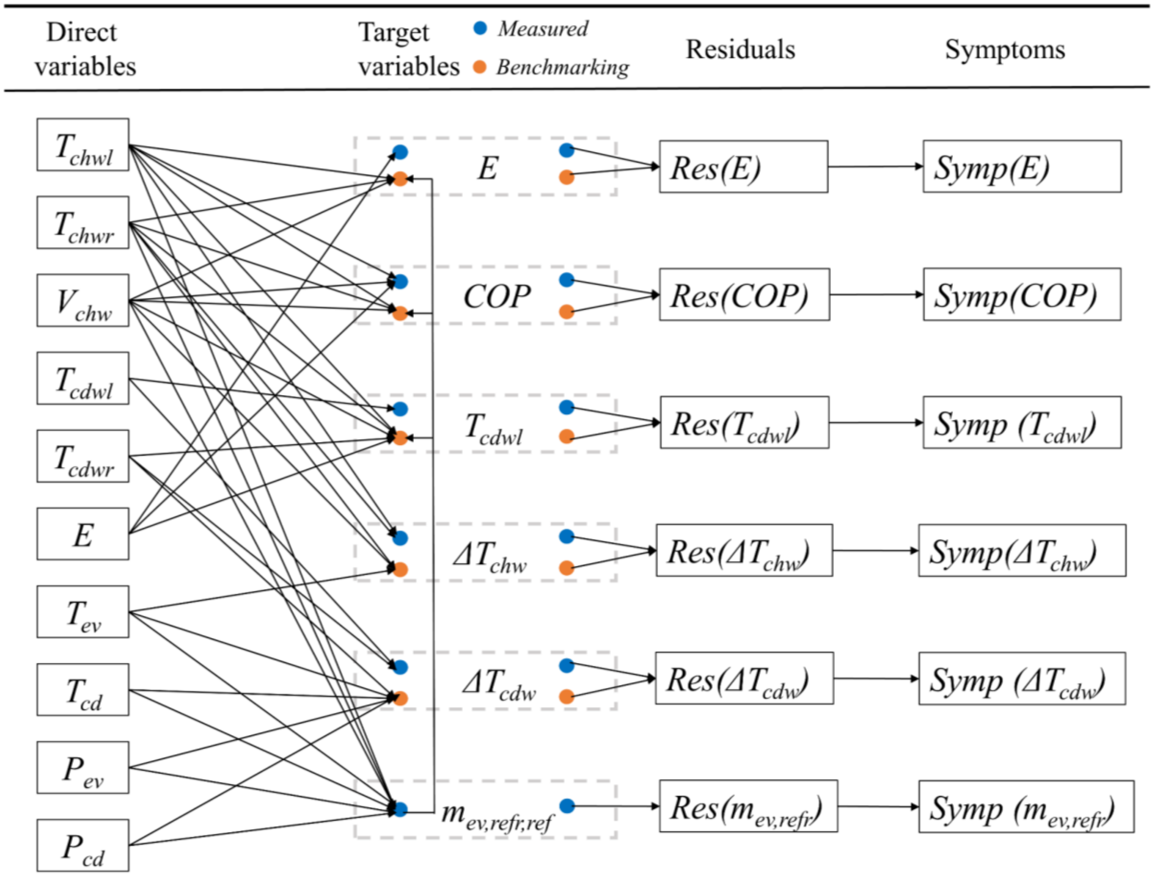

Figure 5-3. Dependency of variables and flowchart of forward fault detection model, mapping from measured variables to fault symptoms.

Within this dissertation, a fault symptom only indicates the possibility of a real fault, as fault symptoms on target variables might depend on regressor variables. Therefore, it requires the fault diagnosis. A question naturally comes up: when a fault symptom is detected, is the target variable faulty or regressor variable faulty, or both are faulty? To respond this question, the backward fault diagnosis model is presented in Section 5.4.

5.4. Backward rule-based fault diagnosis model

Diagnosis of MDFs is an even more difficult task than the diagnosis of a single fault. This dissertation proposes a backward rule-based approach to diagnose multi-dependent faults (MDFs).

To simplify the explanation of the rule-based backward approach, only the diagnosis of fault symptom with respect to a target variable (e.g., E) is discussed. The analysis discusses the relationship between target variable (E) and regressor variable (T_{chwl}). All other regressor variables are assumed normal.

Rule A. If the fault symptom is detected, i.e., $Symp(E) = 1$, the status of regressor variables used in Equation 5-4 should be verified.

> Rule A1. If, for instance, the variable of T_{chwl} is not faulty, i.e., it does not exceed its threshold of normal operation ($Symp(T_{chwl}) = 0$), $Res(T_{chwl}) < \varepsilon(T_{chwl})$, then the target variable E is faulty. Thus, $Symp(E)$ is independent of regressor variables.
>
> Rule A2. If, for instance, the variable of T_{chwl} is faulty, i.e., it exceeds its threshold of normal operation ($Symp(T_{chwl}) = 1$), $Res(T_{chwl}) > \varepsilon(T_{chwl})$, then faults could occur with the regressor variable of T_{chwl} and/or the target variable E. Thus, additional investigation is required to verify the dependence between E and T_{chwl}, because the fault symptom of E could be induced (i) by abnormal operation of regressor variable of T_{chwl}, (ii) by target variable E itself, or (iii) by both.

To explicit the fault diagnosis model well, this section takes the case study results from Chapter 8 as an instance. Two cases could occur here:

- For instance, at 14:00 on July 26, T_{chwl} is 12.25°C instead of 7.25°C under normal operation (Figure 8-1); the predicted benchmark value $E_b = 562.18$ kW instead of measured value $E_m = 440$ kW, with $Res(E) = 122.18$ kW that is greater than the threshold of 19.02 kW (Table 6-5). Thus, both variables T_{chwl} and E appear to be faulty. Additional investigation by the operation team is needed.
- However, if $E_b = 562.18$ kW and the measured value $E_m = 560$ kW, the residual of $E = 2.18$ kW is smaller than the threshold of 19.02 kW. The measurement error of T_{chwl} propagates through Equation 5-4, and $E_b = 562.18$kW is almost equal with E_m. Thus, only T_{chwl} is faulty. The false fault symptom of E is dependent of T_{chwl}. Thus, the electric power E is not faulty.

Rule B. If the fault symptom is not detected $Symp(E) = 0$, then variable E is normal.

This method for developing fault diagnosis rules can be generalized to create rules for the case of another regressor variable $m_{ev,refr,ref}$, which are not presented here because of space limitation.

5.5. Threshold identification with measurement uncertainty and prediction uncertainty

This dissertation applies forward residual-based model to detect faults, when the residual of a variable exceeds the threshold. The threshold should be well defined. Generally, the residual of a variable includes two parts: one is a measured variable, and the other is a predicted variable by a benchmarking model.

5.5.1. Uncertainty of a measured variable

The measurement uncertainty (U_m) of direct variable (e.g., E) and derived variable (e.g., ΔT_{chw}) follows the method presented in Section 3.3 of Chapter 3. Here, an example for the measured uncertainty of ΔT_{chw} ($U_{\Delta Tchw}$) is presented to show the uncertainty calculation for a derived variable with respect to the subtraction/summation algorithm:

$$U_{\Delta T_{chw}} = \sqrt{(U_{T_{chwr}})^2 + (U_{T_{chwl}})^2} \tag{5-25}$$

Appendix B presents the calculation of U_m for all other direct measurements and derived variables used in this dissertation.

5.5.2. Evaluation of prediction uncertainty of a grey-box model

The prediction uncertainty (U_p) refers to the variability in model predictions due to plausible alternative input values (input uncertainty) and plausible alternative model structures (structural uncertainty) [146] . A simple way to estimate the variance of prediction is the usual propagation-of-error method, which is based on the first order expansion of Taylor series [146]. This method is also adopted by Reddy [117] to estimate the prediction variance.

$$MSE(y_p) = \sum_i \left(\frac{\partial y(x)}{\partial x_i}\right)^2 MSE(x_i) \tag{5-26}$$

Where MSE is the mean square error, y_p is the output of a prediction model.

Relate this method to the grey-box model, the term $\frac{\partial y(x)}{\partial x_i}$ represents a parameter of a grey-box model.

The uncertainty of a predicted variable (U_p) can be calculated by:

$$U_p = t\frac{S_{y_p}}{\sqrt{n}} \tag{5-27}$$

$$S_{y_p} = \sqrt{MSE(y_p)} \tag{5-28}$$

Where U_p is the uncertainty of a predicted variable, S_{yp} is the standard deviation of the predicted y_p, and t is the t-value at the specified confident level. Within this dissertation, 95% confidence level is selected for every predicted variable and $t = 1.96$.

5.5.3. Identification of threshold for the fault detection model

I. Method A

The residual of a variable determines whether a status is identified as a fault symptom or not as described by the fault detection model. A common way to evaluate the threshold is to define it as the measurement uncertainty (Method A):

$$\varepsilon = U_m \tag{5-29}$$

II. Method B

As a residual is defined as the difference between the predicted value and the measured value of a variable. Naturally, the threshold should be estimated with the information from both the measurement side and the prediction sild, where the latter is usually ignored in most studies. This dissertation proposes another method to identify the threshold (Method B), covering both prediction and measurement sides uncertainty information. Method B calculates the overall uncertainty (OU) of a variable (measured and predicted) according to the approach of measurement uncertainty calculation with respect to the subtraction algorithm [117]:

$$\varepsilon = OU \tag{5-30}$$

$$OU = \sqrt{U_m^2 + U_p^2} \tag{5-31}$$

Where *OU* is the overall uncertainty with respected to the measurement and prediction of a variable.

This dissertation presents the case study results mainly with Method A, results based on Method B are also presented for comparison.

5.6. Model training, testing, and evaluation

5.6.1. Strategy for model training and testing

To start a modelling project, one of the first decisions is how to utilize the existing data. One common way is to split the data into two groups typically referred as the training dataset and the testing dataset. Estimating parameters is one of the main activities in terms of the training dataset. Besides, the training dataset is also used for model comparison, feature sets development, and all the other needs to reach a final model. While testing dataset is used only to assess the performance of a final model. It is critical that testing dataset not be used prior to this point [147].

Decision making for the division of the training and testing dataset is affected by many factors like the size of original samples and the total number of predictors. For this reason, there is not a uniform guideline to split datasets. The most common strategy is to use the straightforward random sampling. However, this strategy could be problematic when (1) the response is not evenly distributed, or (2) if there is time stamp since it may fail to grasp the inherent patterns of trend data. Hence, this dissertation uses sequential splitting to divide the time series measurement data and the following three approaches are presented:

I. Single split approach (SSA) divides the time-series dataset into one training dataset and one testing dataset, without the actions of model retaining. Hence, the model development solely by single split approach (SSA) may lead to the biased model [148,149].

II. Augmented window approach (AWA) adds the new data to the initial dataset before the model is retrained. The models are then retrained with the larger historical dataset and applied for testing. Thus, the window size increases periodically for this method.

III. For the sliding window approach (SWA), the window size is kept constant throughout the whole training dataset. As new data become available, the oldest training data of equal length are dropped before the model is retrained. Then, the models are retrained periodically with the newest available data.

The three approaches are adopted by [79,106,108,149,150], which successfully validated the robustness of correspondingly proposed models. Model robustness usually represents the prediction of a model are consistently accurate even if one or more of regressors changes drastically [151,152]. In general, the performance metric derived from AWA and SWA is more robust than SSA [153,154]. This dissertation utilizes the three approaches (SSA, AWA, and SWA), aiming to avoid underfitting or overfitting of models, and validate the model robustness and generalization.

5.6.2. Evaluation of benchmarking grey-box models

Reddy [117] recommended five metrics to evaluate the performance of a model, which are coefficient of determination (R^2), root mean square error (*RMSE*), coefficient of variation of the *RMSE* (*CV*), mean bias error (*MBE*), and normalized MBE (*NMBE*). R^2 is unitless, which eases the comparison between different models. Another benefit of R^2 is the straightforward interpretation since it is the proportion of total variability in the outcome that can be explained by the model. However, R^2 could be a deceiving metric when used to evaluate a model with multiple regressors, since it tends to increase when a new regressor (regardless of the correlation to model outcome) is added to the model. Another disadvantage of R^2 is it ignores the model number of degree of freedom [117]. Hence, this work replaces R^2 with Pearson coefficient (r) to evaluate the correlation between the prediction and ground truth. The value of r is less than or equal to 1. $r = 1$ implies a perfect correlation, while $r < 0$ usually means a weak correlation [117].

$$r = \frac{Cov(y,\hat{y})}{S(y)\cdot S(\hat{y})} \tag{5-32}$$

$$RMSE = \sqrt{\frac{\sum_{i=1}^{n}(\hat{y}_i - y_i)^2}{n}} \tag{5-33}$$

$$CV(RMSE) = \frac{\sqrt{\frac{\sum_{i=1}^{n}(\hat{y}_i - y_i)^2}{n}}}{\bar{y}} \times 100\% \tag{5-34}$$

$$MBE = \frac{\sum_{i=1}^{n}(\hat{y_i} - y_i)}{n} \tag{5-35}$$

$$NMBE = \frac{\frac{\sum_{i=1}^{n}(\hat{y_i} - y_i)}{n}}{\bar{y}} \tag{5-36}$$

Where y_i is the measured value, $\hat{y_i}$ is the predicted value, $\bar{y}$ is the mean value of measurements, $Cov(y,\ \hat{y})$ is the covariance of y and $\hat{y}$, and S is the standard deviation, n is the number of samples.

5.6.3. Evaluation of MDFDD models

In statistics, confusion matrix is a synthetic approach to fully evaluate a classifier, which assesses both the correctly classified side and misclassified side [130]. This matrix is widely used to evaluate the FDD models in the field of HVAC system [155,156]. Figure 5-4 illustrates the compositions of a confusion matrix in terms of a binary classifier [130].

I. True positives (TP): These points are the positive points that are correctly labeled by the classifier. In this dissertation, TP represents the number of true positives.
II. False positives (FP): These points are the negative points that are incorrectly labeled by the classifier. In this dissertation, TP represents the number of false positives.
III. False negatives (FN): These points refer to the positive points that are incorrectly labeled by the classifier. In this dissertation, FN represents the number of false negatives.
IV. True negatives (TN): These points refer to the negative points that are correctly labeled by the classifier. In this dissertation, TN represents the number of true negatives.

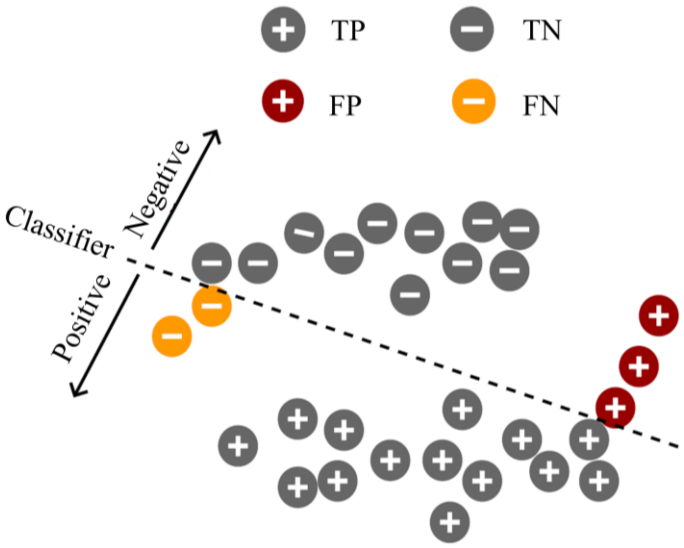

Figure 5-4. Schematic of confusion matric compositions [157].

The application of forward fault detection model returns a binary result: whether a condition is normal or faulty. Thus, to differentiate a fault from a normal condition of a variable is a classification problem. As illustrated by Figure 5-5, there are four classes of results (points): true positive (TP), false positive (FP), false negative (FN), and true negative (TN). TP and FN show the points when a system operates with a fault. Here, TP indicates the points above a threshold, and FN indicates the points below a threshold. TN and FP show the situation when a system operates with fault-free status; TN indicates the points below a threshold, and FP indicates the points above a threshold.

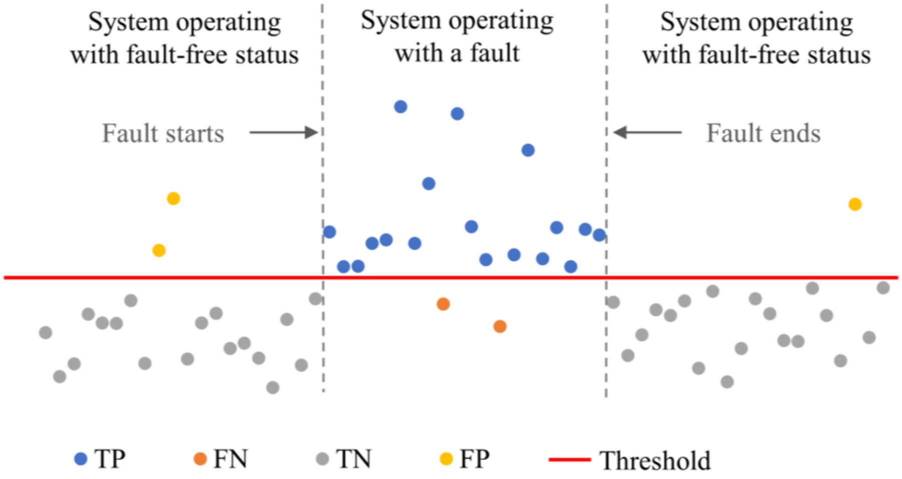

Figure 5-5. Confusion matric compositions in the field of fault detection and diagnosis.

Three metrics are usually applied to evaluate fault detection models [158,159]: accuracy (*AC*) (Equation 5-37), hit rate (*HR*) (Equation 5-38), and false alarm rate (*FAR*) (Equation 5-39), which corresponds to accuracy, precision, and sensitivity in the confusion matrix [130]. *AC* is defined as the percentage of points that are correctly classified by the model over the whole testing dataset, during both faulty time and fault-free time. *HR* is defined as the percentage of fault points that are successfully detected when a system is operating with a fault during only faulty time. *FAR* indicates the percentage of points that are misclassified during only fault-free time. Therefore, the three metrics cover all the time intervals over the test dataset. *AC* gives an overall view of the model, *HR* focuses on the intervals when faults are injected to a system, and *FAR* considers the time when a system operates under fault-free condition.

$$\mathrm{AC} = \frac{TP+TN}{TP+TN+FP+FN} \tag{5-37}$$

$$\mathrm{HR} = \frac{TP}{TP+FN} \tag{5-38}$$

$$\mathrm{FAR} = \frac{FP}{FP+TN} \tag{5-39}$$

Chapter 6: Case study datasets for multiple-dependent fault detection and diagnosis

6.1. A short dataset with one month cooling period – July 2013

The short dataset consists of measurements of the cooling plant for approximately one month, from June 24 to July 28, 2013. A summary of the raw measurements and results after data preprocessing is listed in Table 6-1.

Following the data preprocessing presented in Chapter 5, missing data corresponded to "No data" for T_{oa} and RH_{oa} were replaced by data recorded by Environment Canada [131]. Obvious abnormal values (e.g., negative values of V_{chw} when the chiller operates normally), as well as data under transient condition (e.g., chiller start-up) were removed. Outliers that exceed Chauvenet's criterion [32] were removed. Measurements numbers after dataset preprocessing are listed in Table 6-1. As more measurements are available from the chiller CH#2 under working days, it is selected for model development.

Table 6-1. Measurement summary over five weeks recorded at 15-min interval, from June 24, 2013, to July 28, 2013.

Year 2013	Raw measurements						After preprocessing					
	CH#1		CH#2		CH#1+ CH#2		CH#1		CH#2		CH#1+ CH#2	
	WD	WH	WD	WH	WD	WH	WD	WH	WD	WH	WD	WH
6/24-6/30	106	177	0	0	319	0	100	168	0	0	315	0
7/1-7/7	144	96	0	0	240	192	141	95	0	0	239	190
7/8-7/14	107	0	102	59	267	106	94	0	100	0	181	100
7/15-7/21	1	0	51	108	422	84	0	0	44	154	385	79
7/22-7/28	0	0	313	159	83	33	0	0	301	155	79	31
Summary	358	273	466	326	1331	415	335	263	445	309	1199	400

The selected dataset (CH#2) expands from July 11 to July 26, 2013, under working days, where its distribution is displayed in Figure 6-1. Totally, there are 445 data points. Three distribution characters of this dataset are summarized as the following:

I. Measurements distribution on each day is not homogenous in terms of the data number: For example, there are 96 points on July 12, 2013, but only 11 points on July 17, 2013.

II. Gaps exist due to (1) shunt-down period of Chiller CH#2 and (2) the removed data that are on weekends and holidays.

III. Missing points: For example, the data during 19:15 and 21:30 on 25 July 2013 are missing.

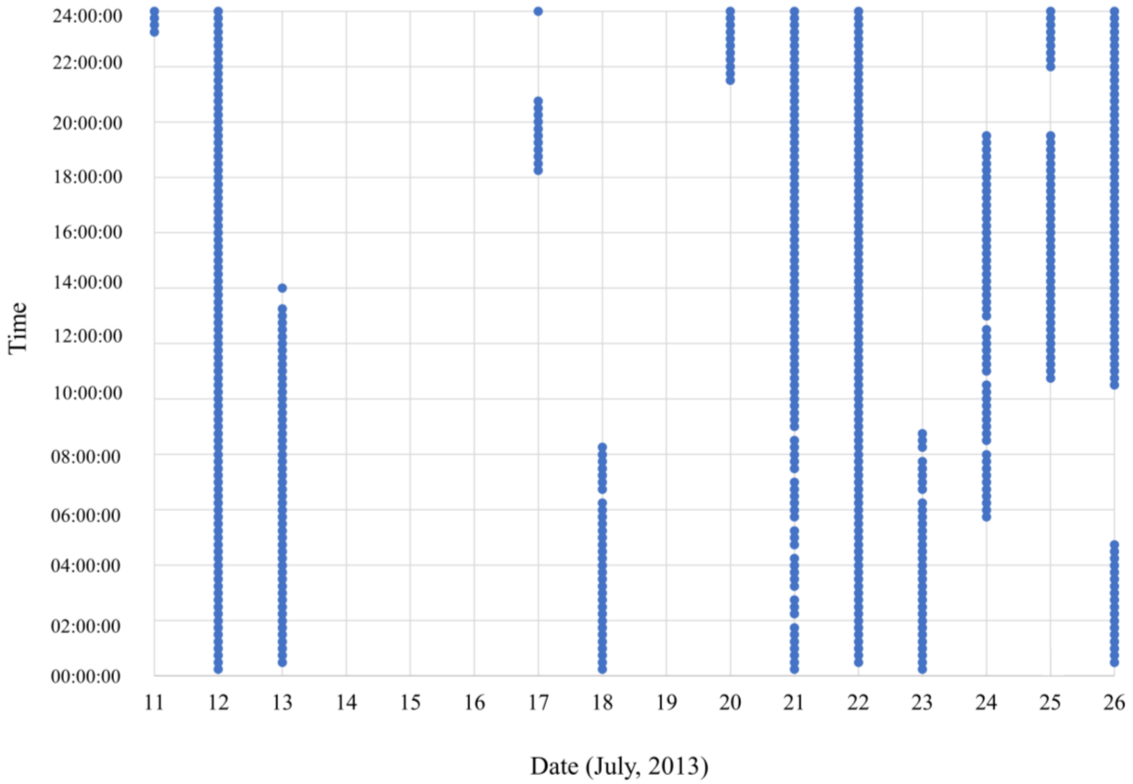

Figure 6-1. Data distribution of Chiller CH#2 under working days of July 2013.

6.2. A long dataset with the cooling season of 2016

The long dataset is composed of measurements of the cooling plant for a whole cooling season, from May 23 to September 04, 2016. A summary of the raw measurements and results after data preprocessing is listed in Table 6-2. The data preprocessing follows the approach presented in Chapter 5. As more measurements are available from the chiller CH#1, the dataset of chiller CH#1 under working days is selected for model development.

The selected dataset (CH#1) expands from May 23 to September 4, 2013, under working days, where its distribution is displayed in Figure 6-2. Totally, there are 2,876 data points.

Table 6-2. Measurement summary over fifteen weeks recorded at 15-min interval, from May 23 to September 04, 2016.

Year 2016	Raw measurements						After preprocessing					
	CH#1		CH#2		CH#1+ CH#2		CH#1		CH#2		CH#1+ CH#2	
	WD	WH	WD	WH	WD	WH	WD	WH	WD	WH	WD	WH
5/23-5/29	192	142	152	2	105	48	186	141	143	0	94	46
5/30-6/05	0	0	368	192	95	0	0	0	364	192	91	0
6/6-6/12	0	0	213	99	0	0	0	0	212	96	0	0
6/13-6/19	0	0	365	192	0	0	0	0	357	192	0	0
6/20-6/26	142	268	172	0	50	7	138	260	152	0	39	6
6/27-7/03	225	267	0	0	159	0	222	267	0	0	155	0
7/04-7/10	341	192	0	0	139	0	330	192	0	0	133	0
7/11-7/17	184	192	0	0	296	0	174	192	0	0	265	0
7/18-7/24	285	136	1	0	193	56	280	136	0	0	187	55
7/25-7/31	192	192	0	0	288	0	183	192	0	0	280	0
8/01-8/07	179	145	0	0	301	47	170	145	0	0	294	46
8/08-8/14	239	156	0	0	241	0	233	155	0	0	239	0
8/15-8/21	291	84	1	0	187	50	282	84	0	0	179	47
8/22-8/28	271	158	0	0	209	34	265	157	0	0	205	30
8/29-9/04	420	192	0	0	60	0	413	192	0	0	57	0
Summary	2961	2124	1272	485	2323	242	2876	2113	1228	480	2218	230

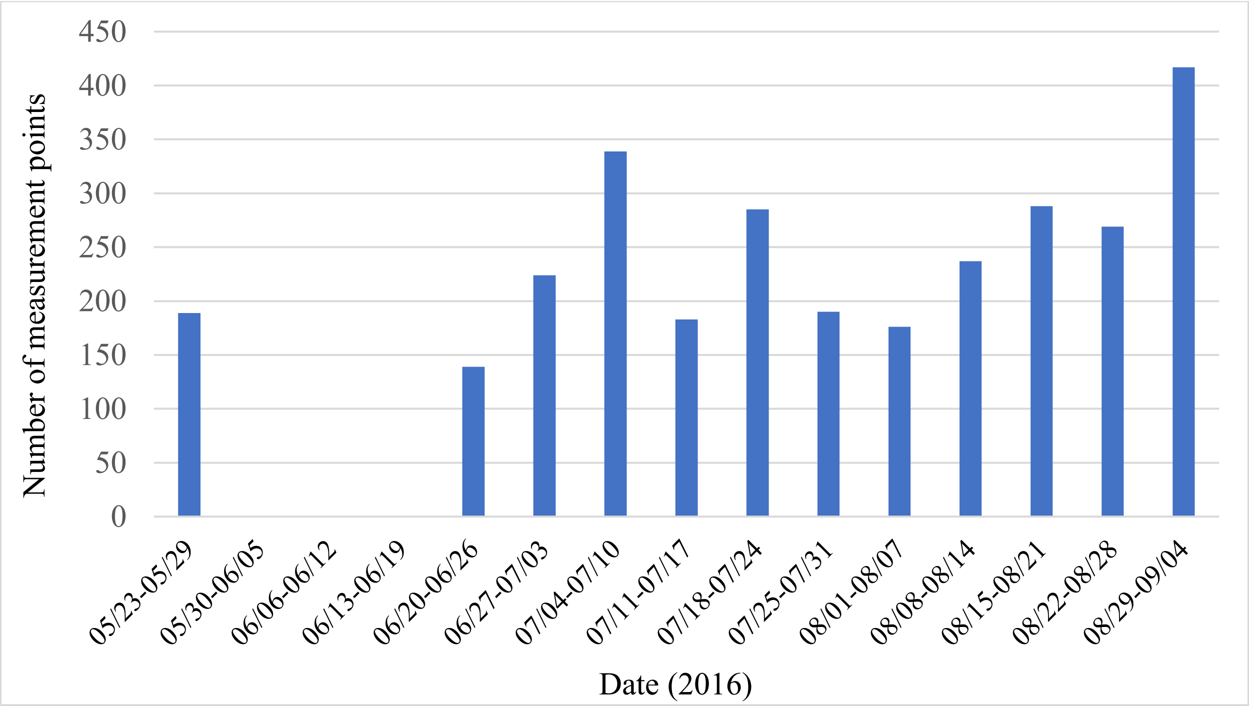

Figure 6-2. Distribution of measurement data from the chiller CH#1 during the cooling season of 2016.

6.3. Comparison of chilled water temperature measured at two positions

Temperatures of the chilled water loop are measured at two positions: (i) the common exit of central cooling plant (POS1), where the total chilled water flow from two chillers is measured, and (ii) at each chiller (POS2). This section verifies whether significant difference of measurements for the same variable (e.g., chilled water leaving temperature) collected at two positions, exists, using measurements of chiller CH#2 of July 2013.

The chilled water leaving temperature measured at POS1 is marked as T_{chwl}, while the variable measured at POS2 of chiller CH#2 is marked as $T_{chwl,\#2}$. Similarly, chilled water return temperature measured at POS1 is marked as T_{chwr}, and measured at POS2 of chiller CH#2 is marked as $T_{chwr,\#2}$. Delta-T of chilled water at POS1 is marked as ΔT_{chw}, while this variable measured at POS2 of chiller CH#2 is marked as $\Delta T_{chw,\#2}$. Table 6-3 lists the statistical information and measurement uncertainty of variables related to the chilled water, using measurement data of chiller CH#2, derived from July 11 to July 26, 2013.

Table 6-3. Statistical information of T_{chwl}, $T_{chwl\#2}$, T_{chwr} and $T_{chwr\#2}$.

Variables	Mean (℃)	Standard deviation (℃)	Overall uncertainty (℃)
T_{chwl}	7.17	0.34	±0.34
$T_{chwl,\#2}$	6.71	0.08	±0.33
T_{chwr}	11.58	1.84	±0.40
$T_{chwr,\#2}$	11.26	1.70	±0.39
ΔT_{chw}	4.42	1.76	±0.52
$\Delta T_{chw,\#2}$	4.56	1.71	±0.66

Besides, the derived variables of refrigerant mass flow rate at three main components (evaporator, compressor and condenser) of a chiller are also compared using measurements at two positions:

$$m_{ev,refr} = \frac{c\rho V_{chw}(T_{chwr}-T_{chwl})}{h_{suc}-h_{ll}} \tag{6-1}$$

$$m_{comp,refr} = \frac{E}{h_{dis}-h_{suc}} \tag{6-2}$$

$$m_{cd,refr} = \frac{c\rho V_{cdw}(T_{cdwl}-T_{cdwr})}{h_{dis}-h_{ll}} \tag{6-3}$$

Where V_{cdw} is the volumetric flow rate of condenser-water in m^3/s, T_{cdwr} is the condenser-water return temperature in ℃, T_{cdwl} is the condenser-water leaving temperature in ℃, $m_{ev,refr}$ is the refrigerant mass flow rate in evaporator in *kg/s*, $m_{comp,ref}$ is the refrigerant mass flow rate in compressor in *kg/s*, $m_{cd,ref}$ is the refrigerant mass flow rate in condenser in *kg/s*. Author clarifies that Equation 6-1, Equation 6-2, and Equation 6-3 are derived from the energy balance of three components of a chiller, and ignore the factors that affect energy balance, like the energy exchange between a component (e.g., condenser) with environment. The calculations are conducted with measurements of chiller CH#2, from July 11 to July 26, 2013, and results are listed in Table 6-4. Since the uncertainty information for V_{cdw} is not available in case study, it is not included in the calculation for measurement uncertainty of $m_{cd,ref}$.

Table 6-4. Estimation of refrigerant mass flow rate at evaporator, condenser, and compressor.

Refrigerant mass flow rate		$m_{ev,refr}$	$m_{comp,refr}$	$m_{cd,refr}$
POS1	Mean *(kg/s)*	11.11	15.52	11.01
	Standard deviation *(kg/s)*	4.85	3.8	4.14
	Measurement uncertainty *(kg/s)*	±0.87	±0.95	±0.30
POS2	Mean *(kg/s)*	11.45	15.52	11.01
	Standard deviation *(kg/s)*	4.73	3.8	4.14
	Measurement uncertainty *(kg/s)*	±0.91	±0.95	±0.30

Table 6-3 indicates that the mean value of ΔT_{chw} and that of $\Delta T_{chw,\#2}$ are very close, and fall into the range of measurement uncertainty. As for refrigerant mass flow rate at three components (evaporator, compressor and condenser), the results (Table 6-4) indicate an obvious difference between $m_{comp,refr}$ and $m_{ev,refr}$ (or $m_{cd,refr}$). The greater value of $m_{comp,refr}$ is caused by the electric power input E, which ignores the efficiency of electric motor and energy loss through the compressor envelope. Values of $m_{ev,refr}$, based on measurements at two positions, are very close and within the uncertainty.

Thus, one can conclude there is no significant difference of variables, collected at the central exist and entrance of cooling plant and at the evaporator of chiller CH#2. The same conclusion is drawn with respect to the dataset of whole cooling season of 2016. This dissertation selects measurement at the central exist and entrance of cooling plant for model development.

6.4. Threshold identification

Based on threshold identification Method A (measurement uncertainty) in Chapter 5, the threshold ε values derived from the dataset of 2013 is listed in Table 6-5, and threshold ε values with respect to the dataset of 2016 is listed in Table 6-6.

Table 6-5. Statistic information of direct/derived variables and measurement uncertainty of these variables, derived from the training dataset of 2013 with respect to the chiller CH#2 (Method A).

Variables	Average	Bias error	Standard deviation	Random error	Overall Uncertainty	Threshold ε
E (kW)	324.67	16.23	106.68	9.91	19.02	19.02
COP	5.02	NA	0.68	0.06	0.48	0.48
T_{cdwl} (°C)	32.70	0.46	1.58	0.15	0.49	0.49
T_{chwl} (°C)	7.19	0.34	0.08	0.01	0.34	0.34
ΔT_{chw} (°C)	4.31	NA	1.76	NA	0.52	0.52
ΔT_{cdw} (°C)	4.07	NA	1.56	NA	0.66	0.66
$m_{ev,refr,ref}$ (kg/s)	10.83	NA	4.93	NA	0.68	0.68

Table 6-6. Statistic information of direct/derived variables and measurement uncertainty of these variables, derived from the training dataset of 2016 with respect to the chiller CH#1 (Method A).

Variables	Average	Bias error	Standard deviation	Random error	Overall Uncertainty	Threshold ε
E (kW)	311.91	15.59	100.34	4.71	16.29	16.29
COP	5.77	NA	0.62	NA	0.53	0.53
T_{cdwl} (°C)	28.63	0.44	2.11	0.10	0.45	0.45
T_{chwl} (°C)	6.88	0.33	0.19	0.01	0.33	0.34
ΔT_{chw} (°C)	4.96	NA	1.67	NA	0.50	0.50
ΔT_{cdw} (°C)	4.53	NA	1.64	NA	0.62	0.62
$m_{ev,refr,ref}$ (kg/s)	11.73	NA	4.38	NA	0.91	0.69

Chapter 7: Grey-box models derived with both a short dataset and a long dataset

This chapter presents the grey-box model development with both the short dataset (July 2013) and the long dataset (whole cooling season of 2016), for the purpose of validating these grey-box models. Then, these grey-box models would be used for the subsequential application of fault detection and diagnosis. Eight grey-box models for E_b, COP_b, $T_{cdwl,b}$, $\Delta T_{chw,b}$, $\Delta T_{cdw,b}$, $h_{suc,b}$, $h_{dis,b}$, and $h_{ll,b}$ are trained and tested by the static window strategy. The dynamic window approach, including augmented window approach and sliding window approach, is applied to validate robustness of five grey-box models of E_b, COP_b, $T_{cdwl,b}$, $\Delta T_{chw,b}$, and $\Delta T_{cdw,b}$. The benchmarking grey-box models are developed using Python (version 3.9.12) [160] with open-source libraries (e.g., Scikit-learn [161]).

7.1. Grey-box models derived with static window regarding the dataset of July 2013

7.1.1. Dataset splitting using single split approach

The single split approach (SSA) divides the time-series data into training dataset and testing dataset, based on sequential splitting [147]. Specifically, measurements collected at first seven days (326 data points), starting at 23:00 on July 11, 2013, and ending at 19:15 on July 24, 2013, are used for model training. Measurements collected at last two days (119 data points), starting at 10:30 on July 25, 2013, and ending at 23:45 on July 26, 2013, are used for model testing.

7.1.2. Results of model training and testing

7.1.2.1. Model training

The eight grey-box models are developed from measurements of normal operation without known problems. Parameters of these grey-box models are identified by least-square algorithm using the training dataset of SSA with respect to the measurements of July 2013.

Grey-box model of the electric power input to the chiller

$$E_b = 22.60(T_{chwl} - \overline{T_{chwl}}) - 0.92\, V_{chw} + 22.09\, m_{ev,refr,ref} + 162.49 \quad (7\text{-}1)$$

Grey-box model of the coefficient of performance (COP)

$$COP_b = 0.80\, T_{chwl} + 0.03\, V_{chw} + 37.81\, PLR - 1.64\, m_{ev,refr,ref} - 5.02 \quad (7\text{-}2)$$

Grey-box model of the condenser-water leaving temperature

$$T_{cdwl,b} = 0.47\,(T_{chwr} - T_{chwl}) + 0.02\, V_{chw} - 0.09\, m_{ev,refr,ref} + 0.01\, E + 0.90\, T_{cdwr} + 0.63 \quad (7\text{-}3)$$

Grey-box model of Delta-T of chilled water

$$\Delta T_{chw.b} = (0.70 u_{norm} + 0.02)(T_{chwr} - T_{ev}) \quad (7\text{-}4)$$

Grey-box model of Delta-T of condenser-water

$$\Delta T_{cdw,b} = 0.19 T_{dis} + 0.48 T_{cd} - 0.46 T_{cdwr} - 6.55 \quad (7\text{-}5)$$

Grey-box model of suction enthalpy of refrigerant

$$h_{suc,b} = -0.03 P_{ev} + 0.66 T_{suc} + 379.29 \quad (7\text{-}6)$$

Grey-box model of discharge enthalpy of refrigerant

$$h_{dis,b} = -0.02 P_{cd} + 0.71 T_{dis} + 378.47 \quad (7\text{-}7)$$

Grey-box model of liquid line enthalpy of refrigerant

$$h_{ll,b} = 0.01 P_{cd} + 1.01 T_{ll} + 199.93 \quad (7\text{-}8)$$

7.1.2.2. Model testing results

The measured T_{chwl}, over the testing dataset, fluctuates around chilled water setpoint temperature as shown in Figure 7-1. Equations 7-1 to 7-5 are used to predict other target variables over the test dataset. The comparison between measured values and predicted values, over testing dataset, for other predicted variables (E_b, COP_b, $T_{cdwl,b}$, $\Delta T_{chw,b}$, and $\Delta T_{cdw,b}$) are displayed from Figure 7-2 to Figure 7-6. The performance metrics of grey-box models, over both the training and testing datasets of July 2013 is listed in Table 7-1, where values of performance metrics are rounded.

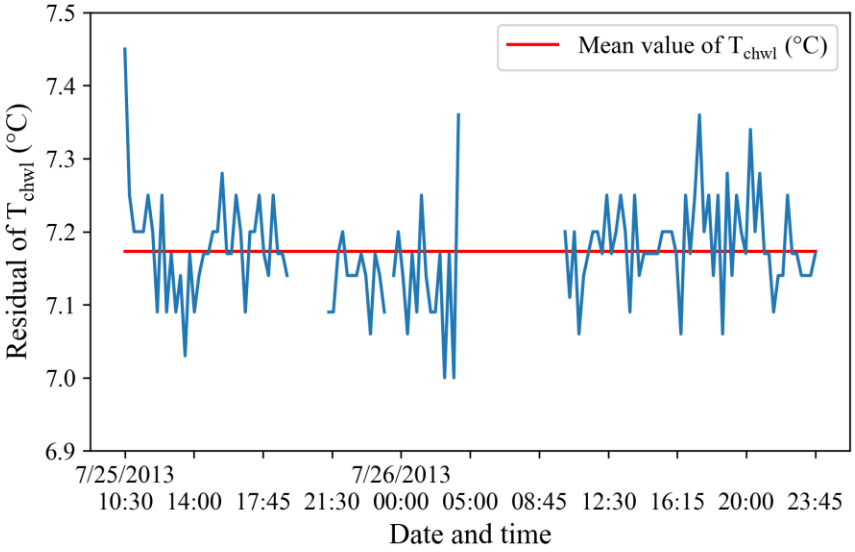

Figure 7-1. T_{chwl} VS time, derived from testing dataset of July 2013 under normal operation conditions.

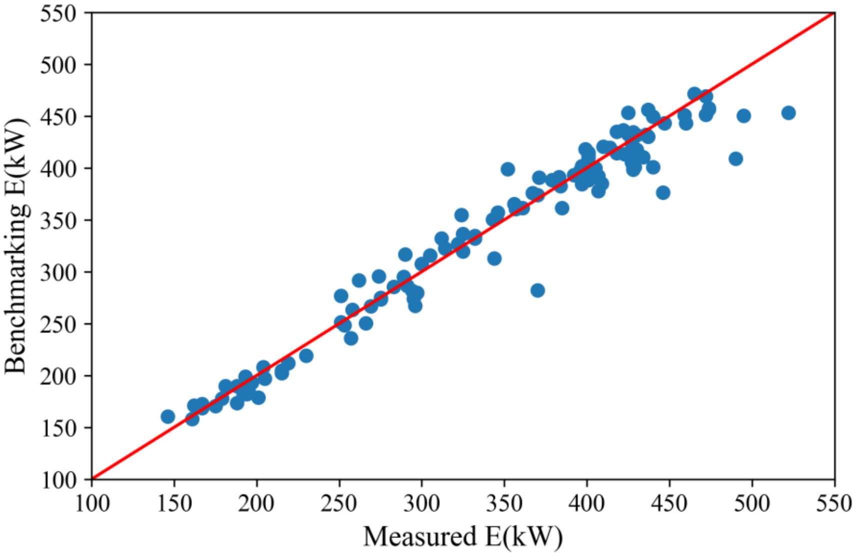

Figure 7-2. Benchmarking values of the electric power input E versus measured values over testing data of July 2013 under normal operation conditions.

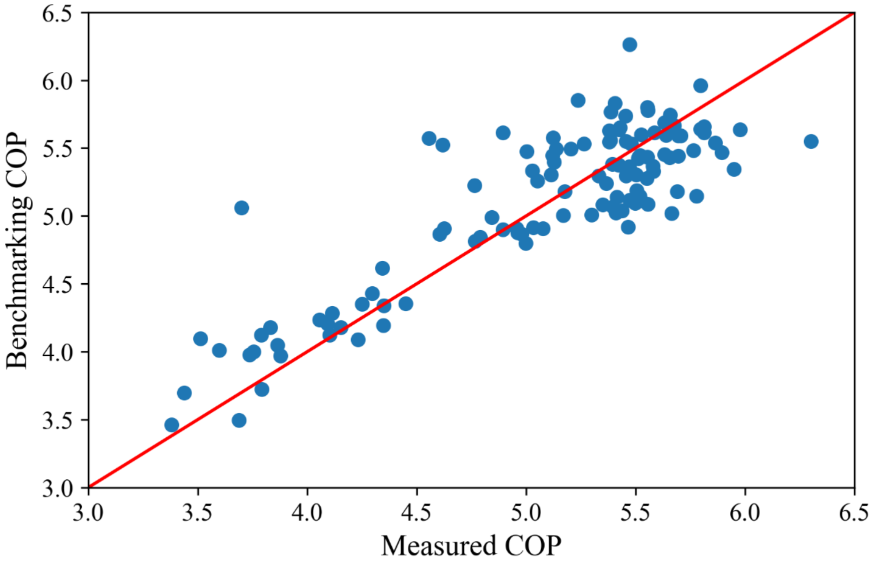

Figure 7-3. Benchmarking values of the coefficient of performance *COP* versus measured values over testing data of July 2013 under normal operation conditions.

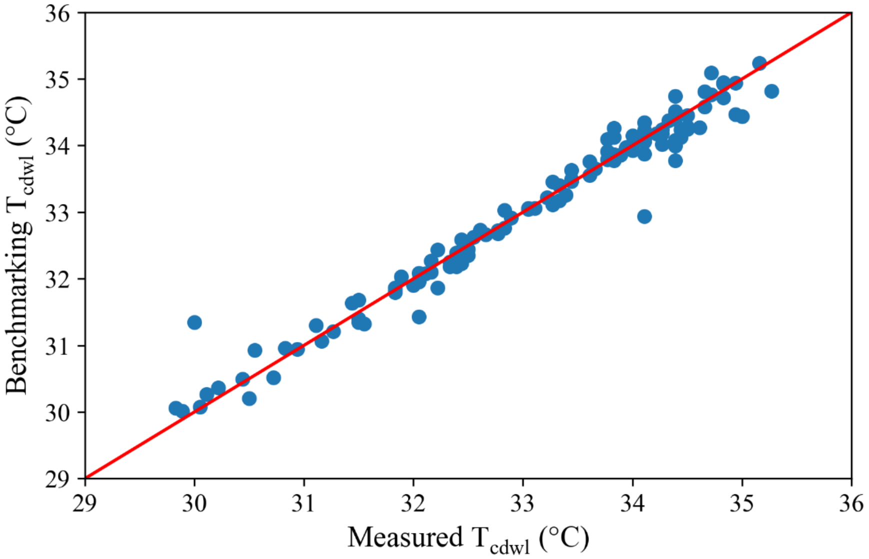

Figure 7-4. Benchmarking values of the condenser water leaving temperature T_{cdwl} versus measured values over testing data of July 2013 under normal operation conditions.

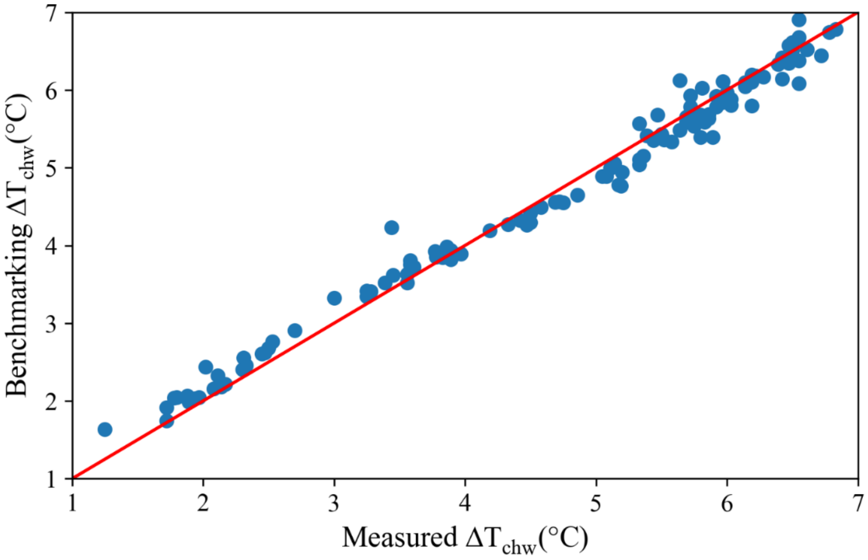

Figure 7-5. Benchmarking values of the delta-T of chilled water ΔT_{chw} versus measured values over testing data of July 2013 under normal operation conditions.

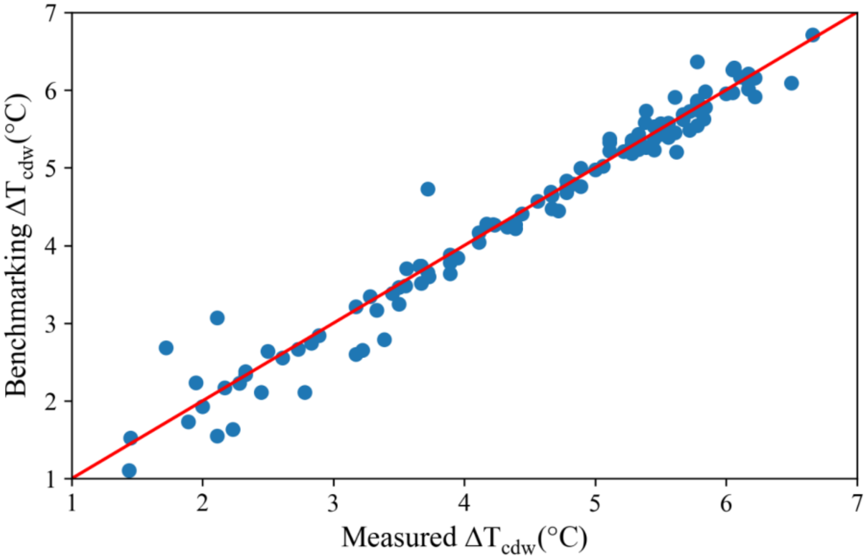

Figure 7-6. Benchmarking values of the delta-T of condenser water ΔT_{cdw} versus measured values over testing data of July 2013 under normal operation conditions.

Table 7-1. Performance metrics of grey-box models regarding the dataset of July 2013.

Model	Training dataset					Testing dataset				
	r	*RMSE*	*CV (%)*	*MBE*	*NMBE*	*r*	*RMSE*	*CV (%)*	*MBE*	*NMBE*
E (kW), Equation 5-4	0.99	16.67	5.24	0	0	0.98	20.13	5.89	2.40	0.01
COP (-), Equation 5-5	0.92	0.29	5.77	0	0	0.86	0.34	6.69	-0.02	0
T_{cdwl}(°C), Equation 5-9	0.99	0.23	0.70	0	0	0.98	0.25	0.76	0.02	0.00
ΔT_{chw} (°C) Equation 5-12	1.00	0.20	4.56	-0.04	-0.01	0.99	0.21	4.38	0.02	0.00
ΔT_{cdw} (°C) Equation 5-15	0.98	0.29	7.12	0.00	0.00	0.98	0.30	6.80	0.01	0.00
h_{suc}(kJ/kg), Equation 5-21	1.00	2.60×10^{-3}	0	0	0	1.00	2.90×10^{-3}	0	3.74×10^{-4}	0
h_{dis}(°C), Equation 5-22	1.00	6.42×10^{-3}	0	0	0	1.00	8.33×10^{-3}	0	-2.01×10^{-3}	0
h_{ll} (kJ/kg), Equation 5-23	1.00	3.34×10^{-3}	0	0	0	1.00	3.29×10^{-3}	0	-5.50×10^{-4}	0

Evaluation metrics values for the grey-box model of *E* (Equation 5-4) indicate good performance. Though the *RMSE* of 20.13kW, over the testing dataset, is slightly greater than the measurement uncertainty of *E* (19.91kW), one can still conclude the grey-box model of *E* (Equation 5-4) is accurate.

The comparison between the measured *COP* and the predicted *COP* (Equation 5-5), over the testing dataset, shows that *RMSE* value is less than the measurement uncertainty of *COP* (0.48), indicating Equation 5-5 can predict *COP* well.

As for the grey-box model for T_{cdwl}, evaluation metrics show *RMSE* = 0.25, over testing dataset, which is less than the measurement uncertainty of T_{cdwl} (0.49°C). Besides, with high Pearson Coefficient value, $r = 0.98$, one can conclude Equation 5-9 is reliable to predict T_{cdwl}.

Evaluation metrics of the grey-box model of ΔT_{chw} (Equation 5-12) indicate good performance, over both training and testing datasets. Besides, the *RMSE* value of 0.21 is less than half of the measurement uncertainty of ΔT_{chw} (0.52°C), and take 3.58% of the testing dataset range. A study for statistics model evaluation regards a model is accurate if *RMSE* value takes a proportion of less than 10% of testing dataset range [162]. In addition, high Pearson Coefficient values, $r = 1.00$ for Equation 5-12 (Table 7-1), are observed for the grey-box model of *E*. By comparison, a previous study, predicting the chilled water return temperature setpoint using a general regression neural network model, reported $r = 0.98$ on training dataset and $r = 0.95$ on testing dataset [163]. As a result, one can conclude that the proposed grey-box model for ΔT_{chw} are accurate.

As for the grey-box model of ΔT_{cdw} (Equation 5-15), over the testing dataset, $r = 0.98$ indicating the model fits well. The *RMSE* value of Equation 5-15 is 0.30°C, which is less than half of the measurement uncertainty of ΔT_{cdw} (0.66°C), and accounts for 5.37% over the testing dataset range. Hence, the prediction model for ΔT_{cdw} is accurate.

For the enthalpy prediction models of h_{suc}, h_{dis}, and h_{ll}, all r values equal to 1 indicating high correlation. Besides, small *RMSE* values for the three enthalpy models (Equation 5-21, Equation 5-22, and Equation 5-23), over the testing dataset, prove they are accurate.

The grey-box models derived with the dataset of July 2013 are summarized in Table 7-2.

Table 7-2. Summary of benchmarking grey-box models with single split approach based on the dataset of July 2013.

Variables	Benchmarking grey-box models
E	$E_b = 22.60(T_{chwl} - \overline{T_{chwl}}) - 0.92\, V_{chw} + 22.09\, m_{ev,refr,ref} + 162.49$
COP	$COP_b = 0.80\, T_{chwl} + 0.03\, V_{chw} + 37.81\, PLR - 1.64\, m_{ev,refr,ref} - 5.02$
T_{cdwl}	$T_{cdwl,b} = 0.47\, (T_{chwr} - T_{chwl}) + 0.02\, V_{chw} - 0.09\, m_{ev,refr,ref} + 0.01\, E + 0.90\, T_{cdwr} + 0.63$
ΔT_{chw}	$\Delta T_{chw.b} = (0.70 u_{norm} + 0.02)(T_{chwr} - T_{ev})$
ΔT_{cdw}	$\Delta T_{cdw,b} = 0.19 T_{dis} + 0.48 T_{cd} - 0.46 T_{cdwr} - 6.55$
h_{suc}	$h_{suc,b} = -0.03 P_{ev} + 0.66 T_{suc} + 379.29$
h_{dis}	$h_{dis,b} = -0.02 P_{cd} + 0.71 T_{dis} + 378.47$
h_{ll}	$h_{ll,b} = 0.01 P_{cd} + 1.01 T_{ll} + 199.93$

7.1.2.3. Comparison of residual and threshold

Figures 7-7 to 7-13 display residuals, with respect to seven symptoms (Section 5.3, Chapter5), over the testing dataset, under fault-free conditions. It is noticed that some measurements exceed the threshold under fault-free time for the five variables: E, T_{cdwl}, COP, ΔT_{chw}, and ΔT_{cdw}. These singular points might be due to the following factors, concluded from the investigation of the measurement trend data and grey-box models.

I. *Rotation of chiller working status*

Since this cooling plant consists of two chillers, the control system is designed to start one chiller when there is the cooling demand, and start the second chiller only if the first chiller cannot meet the chilled water demand. The recording system may sample at this rotation period, which adds variance to measurements. In this case study, measurements are recorded at a 15-min time interval. For instance, the cooling plant started working at 10:00 on July 26, 2013, after it stopped for a few hours and T_{chwr} was high (14.09 °C). At this time, though T_{chwl} was under control due to chiller CH#2 was working at full load, the effect of high T_{chwr} on T_{cdwl} was noticed (T_{cdwl} =29.61°C). However, simultaneously, the building load was low. Thus, the chiller adjusted its load to decrease to the building load in a very short time. When BAS sampled again at 10:15 on July 26, 2013, obvious changes of variables (E and T_{cdwl}) were noticed.

II. *Large building load and chiller load*

Building load is usually high in the afternoon. At 17:30 on July 26, 2013, high V_{chw} was noticed due to the large cooling load demand of building. As a result, the chiller worked at full load, and T_{chwl} deviated the setpoint a lot, though it was still within the measurement uncertainty of T_{chwl}. Chiller *COP* usually decreases slightly when the cooling load exceed a certainty region [112], which means chiller consumed more electricity to maintain T_{chwl} at the setpoint temperature. This condition was verified by the occurrence of peak of E, at the same time. Besides, the large T_{chwl} value propagated to other subsequential variables and might be with the time-lag effect. For example, T_{cdwl} peaked at 18:00:00 on July 26, 2013, two times intervals delay. The results of other studies support this phenomenon. In the work for chiller control optimization, simulation results showed an obvious delay effect between T_{chwl} and E [164]. Another study, based on TRANSYS program, revealed that low T_{chwl} usually lead to high T_{cdwl} for a water-cooled chiller, and the occurrence of T_{cdwl} peak fell behand the lowest T_{chwl} [165].

III. *Short-term malfunction of mechanical system or sensors.*

IV. *Prediction models: the ideal model does not exist* [166]. Though the proposed prediction models are accurate, errors still exist, which adds the variance to the residuals.

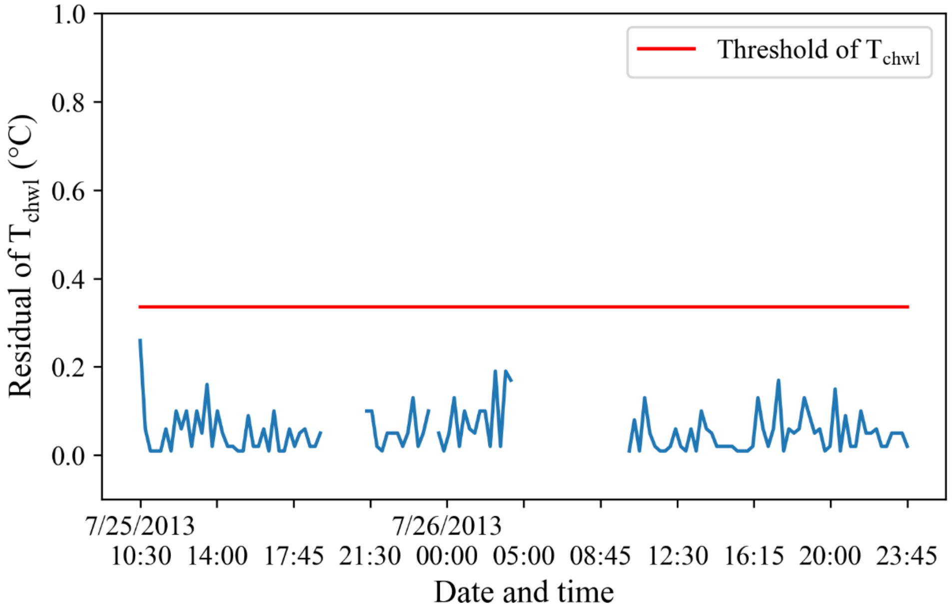

Figure 7-7. The comparison between the residual of T_{chwl} and the threshold of T_{chwl} over the testing dataset of July 2013 under normal operation conditions.

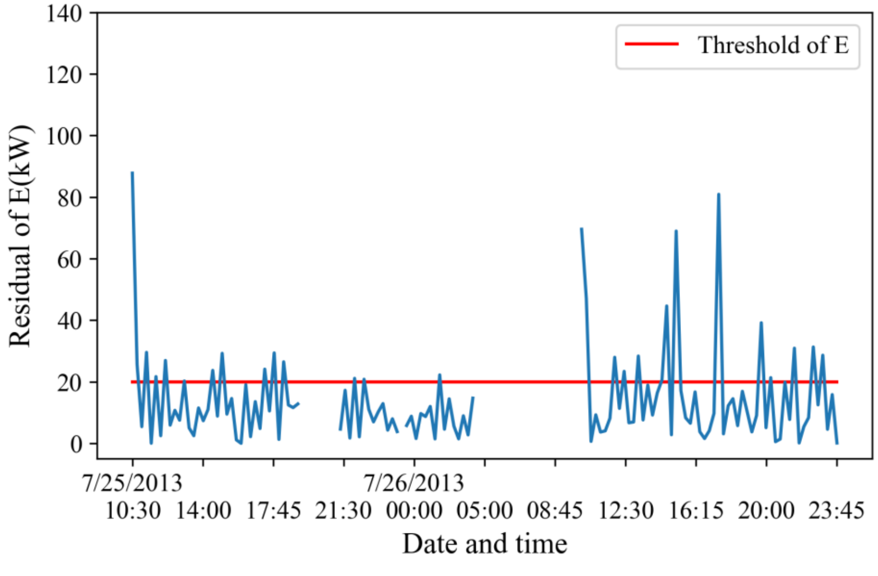

Figure 7-8. The comparison between the residual of E and the threshold of E over the testing dataset of July 2013 under normal operation conditions.

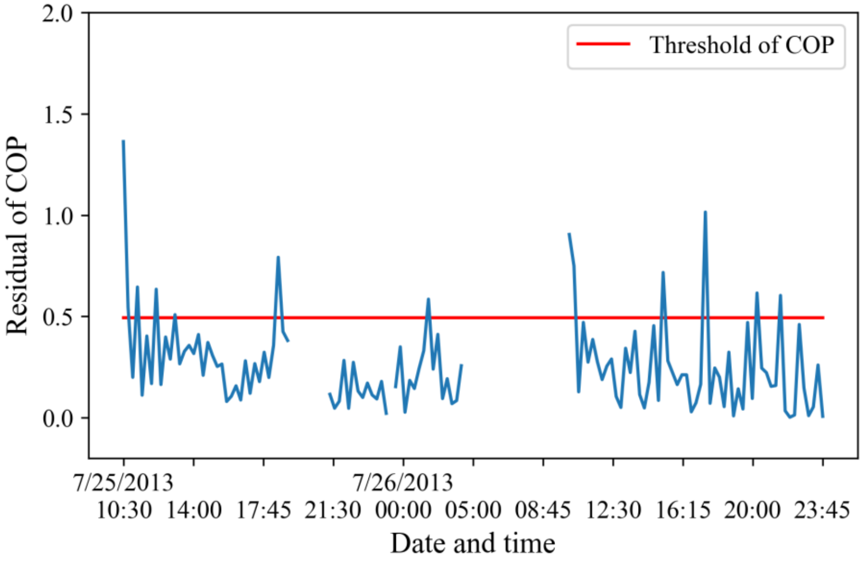

Figure 7-9. The comparison between the residual of *COP* and the threshold of *COP* over the testing dataset of July 2013 under normal operation conditions.

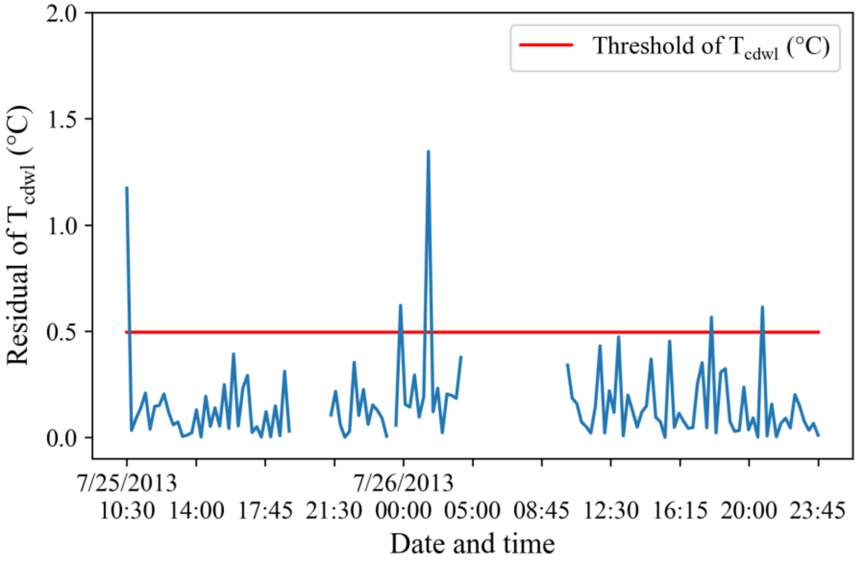

Figure 7-10. The comparison between the residual of T_{cdwl} and the threshold of T_{cdwl} over the testing dataset of July 2013 under normal operation conditions.

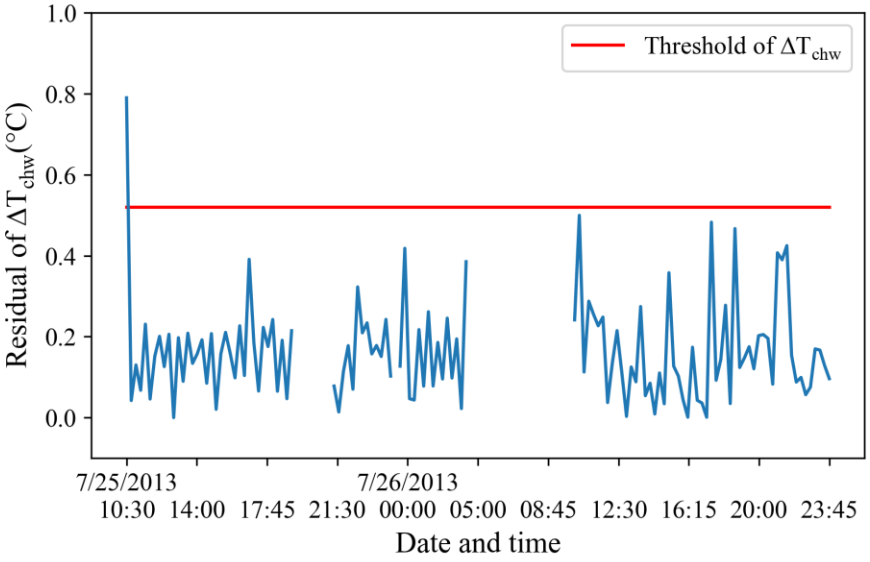

Figure 7-11. The comparison between the residual of ΔT_{chw} and the threshold of ΔT_{chw} over the testing dataset of July 2013 under normal operation conditions.

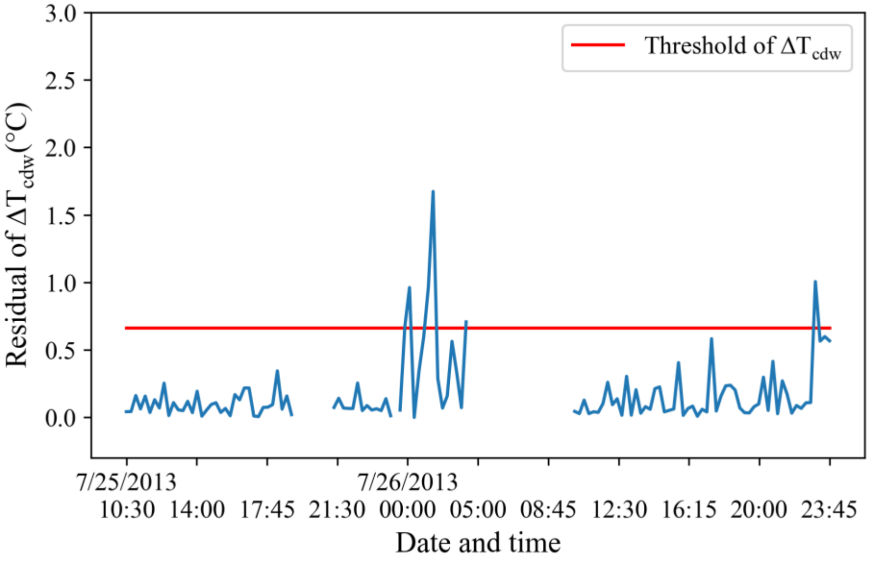

Figure 7-12. The comparison between the residual of ΔT_{cdw} and the threshold of ΔT_{cdw} over the testing dataset of July 2013 under normal operation conditions.

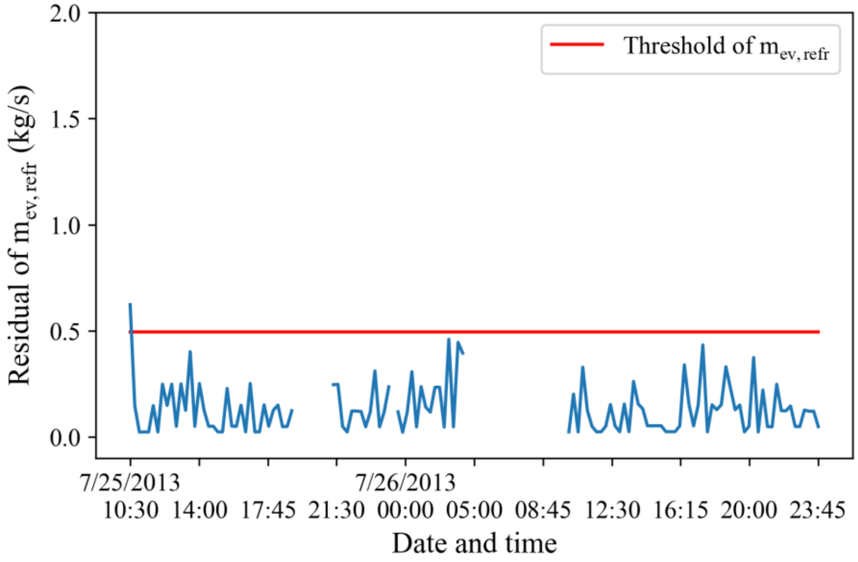

Figure 7-13. The comparison between the residual of $m_{ev,refr}$ and the threshold of $m_{ev,refr}$ over the testing dataset of July 2013 under normal operation conditions.

In summary, some singular points, exceeding the threshold, could occur when the cooling plant system operates under normal conditions. The variance of T_{chwl} can lead to instant impacts on certain variables (e.g., E), or very-shortly delay impacts on other variables (e.g., T_{cdwl}). Therefore, such irregular points are not regarded as faults and the collected trend data from BAS system are considered as fault-free. In this dissertation, only continuous points that are greater than threshold are considered as faults.

7.2. Grey-box models derived with dynamic window regarding the dataset of July 2013

The dataset of July 2013 is divided into five equal-size subsets, where each subset contains 89 data points. The start time and end time, and the number of data points of each subset is listed in Table 7-3, where Subset 5 is dedicated for the model testing. This division of the dataset of July 2013 is used for the model re-training and testing of five grey-box models (E_b, COP_b, $T_{cdwl,b}$, $\Delta T_{chw,b}$, and $\Delta T_{cdw,b}$) for the purpose of verification of model robustness over a month (July 2013).

Table 7-3. Information of the five subsets, during July 2013 (excluding weekends and holidays).

Dataset		Dataset Size	Start	End
Training dataset	Subset 1	89	23:00:00 July 11, 2013	21:00:00 July 12, 2013
	Subset 2	89	21:15:00 July 12, 2013	08:30:00 July 22, 2013
	Subset 3	89	08:45:00 July 22, 2013	06:45:00 July 23, 2013
	Subset 4	89	07:00:00 July 23, 2013	17:45:00 July 25, 2013
Testing dataset	Subset 5	89	18:00:00 July 25, 2013	23:45:00 July 26, 2013
In total		445	23:00:00 July 11, 2013	23:45:00 July 26, 2013

7.2.1. Results of augmented window approach with the dataset of July 2013

The augmented window approach (AWA) uses four augmented windows to retrain each of the five grey-box models (E_b, COP_b, $T_{cdwl,b}$, $\Delta T_{chw,b}$, and $\Delta T_{cdw,b}$), and the dataset of each augmented window is shown in Figure 7-14, where the information of subsets is listed in Table 7-3. AW1 (augmented window 1) means the training is conducted with the first subset (Subset 1) and tested with Subset 5, while AW2 means the model is trained again with the first two subsets (Subtest 1 and Subset 2) and tested again with Subset 5. The same method for model retaining and testing is applied to AW3 and AW4.

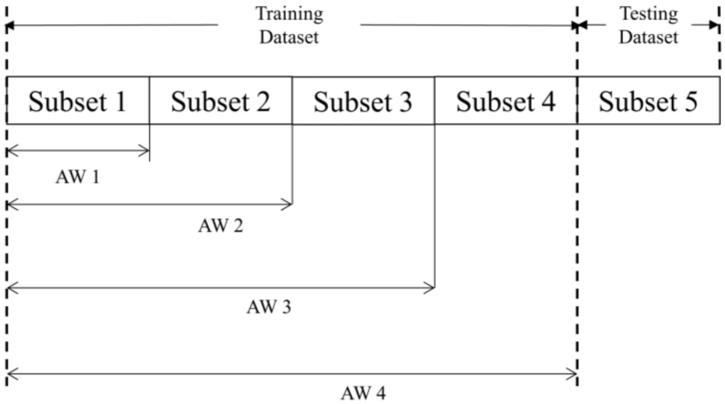

Figure 7-14. Schematic of augmented window approach.

Retrain the five grey-box models (E_b, COP_b, $T_{cdwl,b}$, $\Delta T_{chw,b}$, and $\Delta T_{cdw,b}$) with one AW each time, and test them with Subset 5. The parameters, derived with each AW of July 2013, are listed in Table C-1 of Appendix C. The average performance metrics values over both the training and testing datasets, resulting from the model retraining with four AWs, are listed in Table 7-4. The detailed performance metrics, over both the training and testing datasets, for each AW are listed in Table C-2 of Appendix C.

Table 7-4. Average performance metrics values for grey-box models derived from AWA, using measurements of July, 2013.

Model	Training dataset					Testing dataset				
	r	*RMSE*	*CV (%)*	*MBE*	*NMBE*	*r*	*RMSE*	*CV (%)*	*MBE*	*NMBE*
E (*kW*), Equation 5-4	0.99	18.42	5.58	0.03	0.00	0.98	20.64	6.04	6.90	0.02
COP (-), Equation 5-5	0.92	0.27	5.31	0.00	0.00	0.89	0.36	7.18	-0.12	-0.02
T_{cdwl}(°C), Equation 5-9	0.99	0.22	0.68	0.00	0.00	0.99	0.25	0.77	0.00	0.00
ΔT_{chw} (°C) Equation 5-12	1.00	0.19	4.31	-0.03	-0.01	0.99	0.20	4.39	-0.02	0.00
ΔT_{cdw} (°C) Equation 5-15	0.99	0.25	5.82	0.00	0.00	0.98	0.33	7.59	-0.01	0.00

Generally, each set of parameter values (Table C-1) of a grey-box model does not show significant difference against the augmented training dataset. Besides, the performance metrics values of each grey-box model against the augmented training dataset (Table C-2), over the testing dataset, also do not show significant difference. Table 7-4 indicates *RMSE* of each grey-box model over the testing dataset is less than the corresponding measurement uncertainty (Table 6-5) of variables except E_b, which is very close to the measurement uncertainty of *E*. Therefore, one can conclude the five grey-box models are robust against training dataset size.

7.2.2. Results of sliding window approach with the dataset of July 2013

The sliding window approach (SWA) uses four sliding windows to retrain each of five grey-box models, and the dataset of each sliding window is shown in Figure 7-15, where the information of each subset is listed in Table 7-3. The size of each sliding window (SW) is fixed at a constant: 89 data points. SW1 means the model is trained with the first subset (Subset 1) and tested with Subset 5, while SW2 means the model is trained with the next equal-sized subset (Subset 2) and tested with Subset 5. The same method for model retaining and testing is applied to SW3 and SW4.

Retrain the five grey-box models (E_b, COP_b, $T_{cdwl,b}$, $\Delta T_{chw,b}$, and $\Delta T_{cdw,b}$) with one subset each time and test them with Subset 5. Repeat this process until all sliding windows are used for model training. The parameters, derived with each SW of July 2013, are listed in Table C-3. The average performance metrics values over both the training and testing datasets, resulting from the model retraining with four SWs, are listed in Table 7-5. The detailed performance metrics, over both the training and testing datasets, derived from each SW, are listed in Table C-4 of Appendix C.

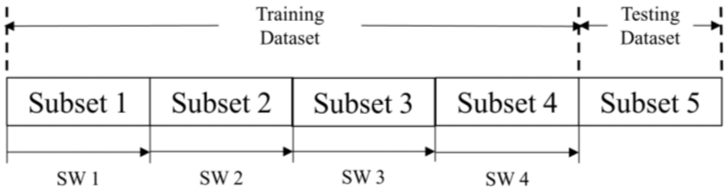

Figure 7-15. Schematic of sliding window approach.

Table 7-5. Average performance metrics values for grey-box models, derived from SWA.

Model	Training dataset					Testing dataset				
	r	*RMSE*	*CV (%)*	*MBE*	*NMBE*	*r*	*RMSE*	*CV (%)*	*MBE*	*NMBE*
E *(kW)*, Equation 5-4	0.98	17.75	5.66	0.01	0.00	0.98	20.74	6.07	3.98	0.01
COP *(-)*, Equation 5-5	0.87	0.26	5.24	0.00	0.00	0.88	0.39	7.85	-0.15	-0.03
T_{cdwl}(°C), Equation 5-9	0.99	0.21	0.65	0.00	0.00	0.98	0.28	0.85	-0.02	0.00
ΔT_{chw} (°C) Equation 5-12	0.99	0.17	4.07	-0.02	0.00	0.99	0.22	4.75	-0.01	0.00
ΔT_{cdw} (°C) Equation 5-15	0.98	0.26	6.72	0.00	0.00	0.97	0.36	8.25	0.00	0.00

Based on Table C-3, each set of parameters of a grey-box model, over the four sliding windows, have only slight variances. The performance metrics values of each grey-box model against the sliding training dataset (Table C-4), over the testing dataset, also do not show significant difference. Over the testing dataset (Table 7-5), all *RMSE* values of four grey-box models (*COP*, T_{cdwl}, ΔT_{chw}, and ΔT_{cdw}) are less than the corresponding measurement uncertainty (Table 6-5), except *RMSE* of the grey-box model for E_b, which is only slightly greater than the measurement uncertainty of *E*. Hence, one can conclude the five grey-box models (E_b, COP_b, $T_{cdwl,b}$, $\Delta T_{chw,b}$, and $\Delta T_{cdw,b}$) are robust over different chiller operation periods.

7.3. Conclusion of model development with measurements of July 2013

Based on the results of model training and testing with static window (SSA) and dynamic window (AWA and SWA) approaches over July 2013, the five grey-box models (E_b, COP_b, $T_{cdwl,b}$,

$\Delta T_{chw,b}$, and $\Delta T_{cdw,b}$) are reliable and robust. Thus, one can conclude the proposed five grey-box models can capture the monthly chiller operation characters well and can be regarded as benchmarking grey-box models.

As the dataset length of measurements of July 2013 is small, for safety, benchmarking grey-box models derived with static window (Equations 7-1 to 7-5) are selected to conduct the fault detection and diagnosis since they cover the most training data (most chiller operation characteristics).

7.4. Grey-box models derived with the dataset of 2016

The derived benchmarking grey-box models with respect to measurements of July 2013 represent the monthly trend of chiller operation. Though the model accuracy and robustness over a short period are validated by the static window approach and dynamic window approach, the model performance and robustness over a long term is worth exploring. Thus, this section presents the model validation over a whole cooling season with the measurements of 2016. The comparison of grey-box models, derived from a short-term dataset and a long-term dataset (measurements of 2013 and 2016), representing different operation characteristics of the chiller, is shown at the end of this section.

Three approaches, including one static window approach (SSA) and two dynamic window approaches (AWA and SWA), are used to train and test the five grey-box models (E_b, COP_b, $T_{cdwl,b}$, $\Delta T_{chw,b}$, and $\Delta T_{cdw,b}$.). As a model derived solely by SSA may lead to the biased model [148,149], the dynamic window approaches are needed to erase this concern and validate the model robustness over diverse chiller operation conditions. Augmented window and sliding window are two common dynamic model retraining approaches, models derived with them are generally more robust than that derived with SSA [167,168].

7.4.1. Grey-box models derived with static window regarding the dataset of 2016

As the dataset of CH#1 of 2016 under WD is selected for model development (Section 6.2, Chapter 6), it is separated into the training dataset and the testing dataset based on sequential splitting [147]. For the single split approach (SSA), the training dataset is composed of measurements during working days of the first 13 weeks (2198 data points), from 07:45 on May 25, 2016, to 23:45 on August 19, 2016, while the testing dataset is composed of measurements of the last two weeks (678 data points), from 0:00 on August 22, 2016, to 23:45:00 on September 2, 2016 (Table 6-2). Data recorded on weekends and holidays are excluded.

The five grey-box models (E_b, COP_b, $T_{cdwl,b}$, $\Delta T_{chw,b}$, and $\Delta T_{cdw,b}$) are developed from measurements of normal operation without known problems. Based on the measurements of 2016, the five grey-box models are derived with the training dataset of SSA, and parameters are identified by least-square algorithm.

Benchmarking model of the electric power input to the chiller

$$E_b = -39.86(T_{chwl} - \overline{T_{chwl}}) + 0.22\, V_{chw} + 22.16\, m_{ev,ref} + 32.65 \tag{7-9}$$

Benchmarking model of the coefficient of performance (COP)

$$COP_b = 0.85\, T_{chwl} + 0.03\, V_{chw} + 74.78\, PLR - 3.45 m_{ev,ref} - 5.59 \tag{7-10}$$

Benchmarking model of the condenser-water leaving temperature

$$T_{cdwl,b} = 0.37\,(T_{chwr} - T_{chwl}) + 0.01 V_{chw} - 0.05\, m_{ev,ref} + 0.01\, E + 0.89\, T_{cdwr} + 1.40 \tag{7-11}$$

Benchmarking model of Delta-T of chilled water

$$\Delta T_{chw,b} = (0.19 u_{norm} + 0.53)(T_{chwr} - T_{ev}) \tag{7-12}$$

Benchmarking model of Delta-T of condenser-water

$$\Delta T_{cdw,b} = 0.15 T_{dis} + 0.58 T_{cd} - 0.74 T_{cdwr} - 0.25 \tag{7-13}$$

Graphical relationships between predicted and measured values of the five selected target variables (Figures 7-16 to 7-20), and the performance metrics of grey-box models, over both the training and testing datasets, show good prediction performance (Table 7-6), where values of performance metrics are rounded.

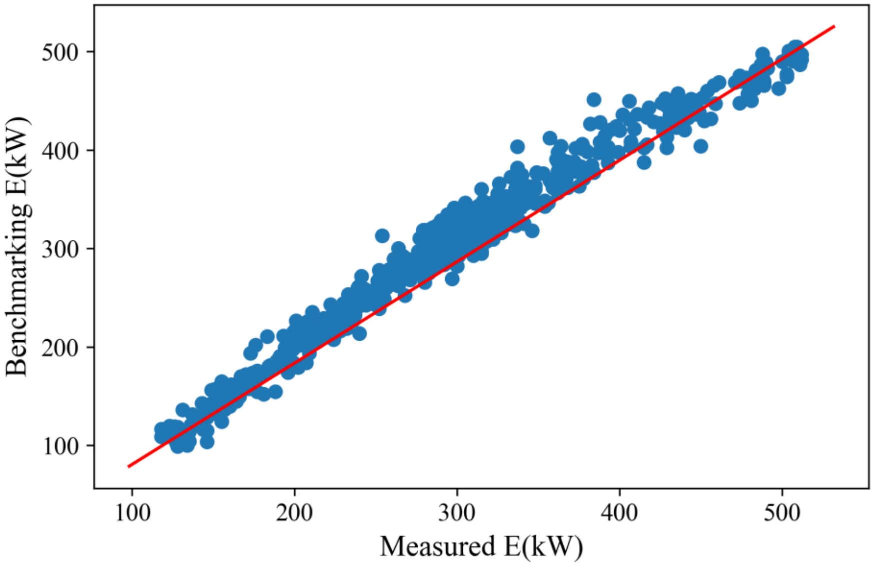

Figure 7-16. Benchmarking values of the electric power input *E* versus measured values over testing data under normal operation conditions of 2016.

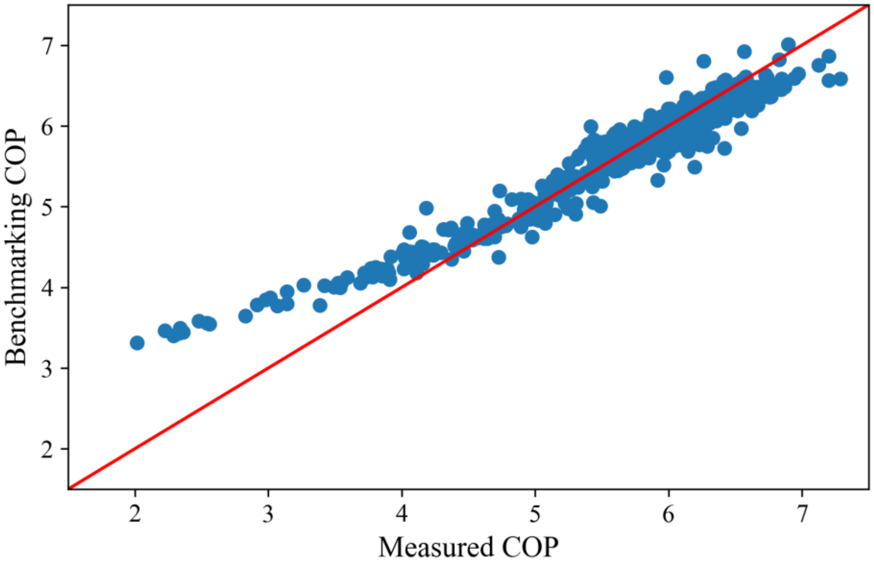

Figure 7-17. Benchmarking values of the coefficient of performance *COP* versus measured values over testing data under normal operation conditions of 2016.

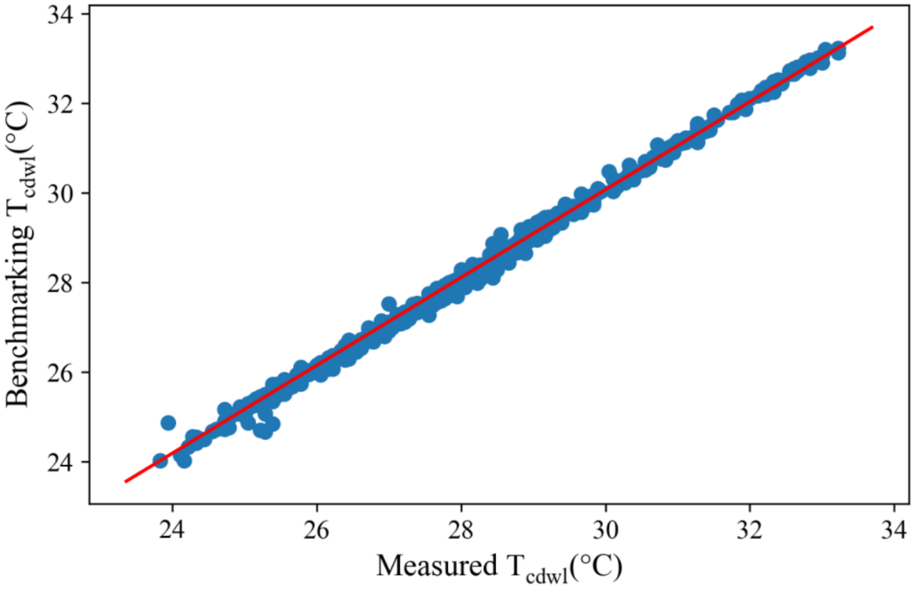

Figure 7-18. Benchmarking values of the condenser water leaving temperature T_{cdwl} versus measured values over testing data under normal operation conditions of 2016.

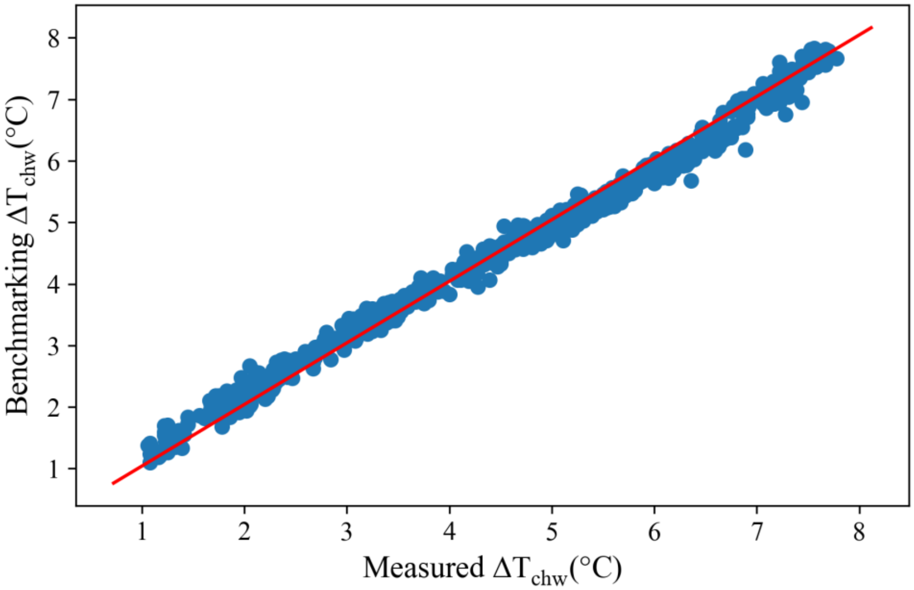

Figure 7-19. Benchmarking values of the delta-T of chilled water ΔT_{chw} versus measured values over testing data under normal operation conditions of 2016.

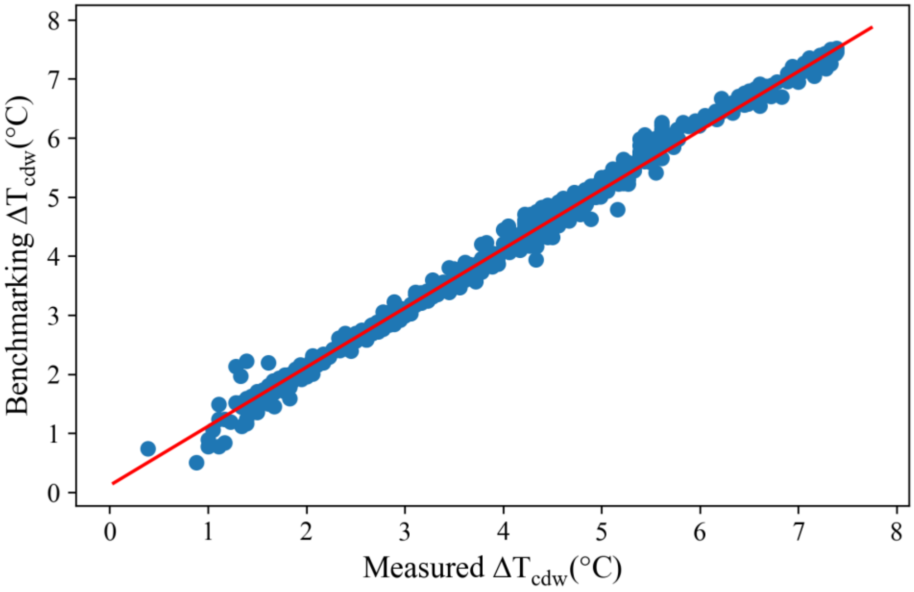

Figure 7-20. Benchmarking values of the delta-T of condenser water ΔT_{cdw} versus measured values over testing data under normal operation conditions of 2016.

Table 7-6. Performance metrics of grey-box models over both training and testing datasets, based on measurements of 2016.

Model	Training dataset					Testing dataset				
	r	*RMSE*	*CV(%)*	*MBE*	*NMBE*	*r*	*RMSE*	*CV(%)*	*MBE*	*NMBE*
E (kW), Equation 5-4	0.99	15.20	4.90	0.00	0.00	0.99	17.19	5.96	-3.82	-0.01
COP (-), Equation 5-5	0.95	0.21	3.68	0.00	0.00	0.97	0.26	4.55	-0.01	0.00
T_{cdwl}(°C), Equation 5-9	1.00	0.17	0.58	0.00	0.00	1.00	0.14	0.48	-0.06	0.00
ΔT_{chw} (°C) Equation 5-12	1.00	0.17	3.39	-0.02	0.00	1.00	0.20	4.35	-0.03	-0.01
ΔT_{cdw} (°C) Equation 5-15	0.99	0.26	5.68	0.00	0.00	1.00	0.20	4.73	-0.13	-0.03

Single split approach (SSA) is a static model training approach, the disadvantages for the application of SSA are (1) the user needs to have data over at least a few weeks for training before using, and (2) it might lead to biased model. The training dataset of SSA may cover only one certainty chiller operation character, other model retraining approaches, being able to represent diverse chiller operation characters, are needed to verify the model robustness.

7.4.2. Grey-box models derived with augmented window regarding the dataset of 2016

The augmented window approach (AWA) is used to explore the sensitivity of model performance against dataset size. Grey-box models can be retrained periodically by a set of augmented data when new measurements are available [169]. The application of AWA for model training has the obvious advantage of being able to validate whether the model predicts well over both the local (e.g., monthly) and the global (e.g., seasonal) trends of chiller operation [170]. Besides, augmented data can cover unexplored input space, prevent overfitting, and improve the generalization ability [171]. The disadvantage of AWA is the data accumulation, which might become too large to be manageable. Due to the quantity of recent addition of new data is less compared to the older data, it is also likely that the latest changes in the augmented training dataset have smaller impact on the model training.

Table 7-7. Duration and dataset size of each augmented window, from measurements of Chiller CH#1 of 2016.

Dataset	Training dataset		Testing dataset	
	Date	Dataset Size	Date	Dataset Size
AW1	05/23 – 07/03	546	07/04 – 07/10	330
AW2	05/23 – 07/10	876	07/11 – 07/24	454
AW3	05/23 – 07/17	1050	07/18 – 07/31	463
AW4	05/23 – 07/24	1330	07/25 – 08/07	353
AW5	05/23 – 07/31	1513	08/01 – 08/21	685
AW6	05/23 – 08/07	1683	08/08 – 08/28	780
AW7	05/23 – 08/14	1916	08/15 – 09/04	960

The chiller CH#1 works for 12 weeks during the whole cooling season of 2016. Totally, seven augmented windows are divided, and the duration of training dataset and testing dataset of each augmented window are listed in Table 7-7, where the ratio of training dataset size to testing dataset size in each augmented window is kept around 2. The first augmented window (marked as AW1 in Table 7-7) covers measurements of the first four weeks, where the training dataset of AW1 is composed of the first 546 data points and the testing dataset of AW1 is composed of the last 330 data points. The second augmented window (marked as AW2 in Table 7-7) spans from May 23 to July 24, where the first 876 data points are used for model training and the last 454 data points are used for model testing. As the size of augmented window increases successively, the last augmented window (marked as AW7 in Table 7-7) includes measurements of the whole cooling season, where the first 1,916 data points compose the training dataset of AW7, and the last 960 data points compose the testing dataset of AW7.

Retrain and testing the five grey-box models (E_b, COP_b, $T_{cdwl,b}$, $\Delta T_{chw,b}$, and $\Delta T_{cdw,b}$) with all the seven augmented windows (Table 7-7). The parameters of the five grey-box models, derived with the training dataset of each augmented window, are listed in Table C-5. The average performance metrics values over both the training and testing datasets, resulting from the retraining approaches of AWA, are listed in Table 7-8. The performance metrics of each AW, over both the training and testing datasets, are listed in Table C-6 of Appendix C.

Table 7-8. Average performance metrics values of grey-box models, derived from each augmented window with the measurements of the chiller CH#1 during the summer of 2016.

Model	Training dataset					Testing dataset				
	r	*RMSE*	*CV (%)*	*MBE*	*NMBE*	*r*	*RMSE*	*CV (%)*	*MBE*	*NMBE*
E (kW), Equation 5-4	0.99	15.78	5.19	0.00	0.00	0.99	15.57	5.04	-1.96	-0.01
COP (-), Equation 5-5	0.95	0.24	4.30	0.00	0.00	0.94	0.20	3.42	0.00	0.00
T_{cdwl}(°C), Equation 5-9	1.00	0.18	0.63	0.00	0.00	1.00	0.15	0.54	-0.05	0.00
ΔT_{chw} (°C) Equation 5-12	1.00	0.17	3.50	-0.03	-0.01	1.00	0.17	3.48	-0.03	-0.01
ΔT_{cdw} (°C) Equation 5-15	0.99	0.22	5.08	0.00	0.00	0.99	0.27	5.86	-0.16	-0.03

Generally, each set of parameters (Table C-5) of a grey-box model does not show significant difference as the training dataset increases. Performance metrics values of each grey-box model (Table C-6), over the testing dataset, also do not show significant difference as the training dataset increases. Table 7-8 indicates the average *RMSE* value of each grey-box model is less than the corresponding measurement uncertainty of a target variable. Thus, one can conclude the five grey-box models, derived with the measurements of whole cooling season of 2016, are accurate and robust against training dataset size.

7.4.3. Grey-box models derived with sliding window regarding the dataset of 2016

The sliding window approach (SWA) is used to explore the sensitivity of model performance against periodically updated measurements. SWA can be represented graphically as repeatedly sliding a time window across a time series dataset to choose the training data. SWA has the strength of keeping track of latest operation data, but it loses previous data. The prediction results may not well represent the annual or seasonal trend of chiller operation [169]. The advantages of SWA are performing model retraining is feasible with a relatively small and constant size of the training dataset. The application of SWA helps to verify the model robustness over diverse chiller operation conditions.

Six sliding windows (SW) are derived from the measurements of 2016, and each sliding window contains measurements of seven weeks, as listed in Table 7-9. The starting and ending dates of both the training and testing datasets of each SW are also listed in Table 7-9. For instance, the first sliding window (marked as SW1 in Table 7-9), includes the training dataset composed of 1050 data points (from May 23 to July 17, 2016) and testing dataset composed of 463 data points (from July 18 to July 31, 2016).

Table 7-9. Duration and dataset size of each sliding window, from measurements of Chiller CH#1 of 2016.

Dataset	Training dataset		Testing dataset	
	Date	Dataset Size	Date	Dataset Size
SW1	05/23 – 07/17	1050	07/18 – 07/31	463
SW2	06/20 – 07/24	1144	07/25 – 08/07	353
SW3	06/27 – 07/31	1189	08/01 – 08/14	403
SW4	07/04 – 08/07	1137	08/08 – 08/21	515
SW5	07/11 – 08/14	1040	08/15 – 08/28	547
SW6	07/18 – 08/21	1148	08/22 – 09/04	678

Retrain and test the five grey-box models (E_b, COP_b, $T_{cdwl,b}$, $\Delta T_{chw,b}$, and $\Delta T_{cdw,b}$) with all the six augmented windows (Table 7-9). The parameters of the five grey-box models, derived with training dataset of each SW of 2016, are listed in Table C-7. The average performance metrics values over both the training and testing datasets, resulting from the retraining approaches of SWA, are listed in Table 7-10. The performance metrics of each SW are listed in Table C-8 of Appendix C.

Based on Table C-7, there are only slight variances in terms of each set of parameter values of a grey-box model, in terms of all the six sliding windows. The performance metrics values of each grey-box model over each sliding window (Table C-8), on both training and testing datasets, also do not show significant difference. Over the testing dataset, all the average *RMSE* values of each of the five grey-box models (Table 7-10) are less than the corresponding measurement uncertainty (Table 6-6). Hence, one can conclude the five grey-box models are robust against the sliding dataset, which means the proposed models are not sensitive to the dataset that represents the chiller operating status at different periods. For instance, the training dataset of SW3 are mainly composed of measurements of July 2016 and the testing dataset of SW3 are mainly composed of measurements of the first two weeks of August, 2016, where [112] indicates the average chiller cooling load of July 2016 (1623.14kW) is about 225kW less than that of the first two weeks of August, 2016 (1845.74kW). Even though, performance metrics (Table C-8) of the five grey-box models over the testing dataset of SW3 still indicate these models are accurate. Thus, based on the results of measurements of 2016, the five grey-box models can extrapolate to operation conditions outside the range of training dataset.

Table 7-10. Average performance metrics values of grey-box models, derived from each sliding window with the measurements of the chiller CH#1 during the summer of 2016.

Model	Training dataset					Testing dataset				
	r	*RMSE*	*CV (%)*	*MBE*	*NMBE*	*r*	*RMSE*	*CV (%)*	*MBE*	*NMBE*
E (kW), Equation 5-4	0.99	14.27	4.63	0.00	0.00	0.99	15.09	4.87	0.83	0.00
COP (-), Equation 5-5	0.95	0.19	3.27	0.00	0.00	0.95	0.19	3.24	0.02	0.00
T_{cdwl} (°C), Equation 5-9	1.00	0.16	0.55	0.00	0.00	1.00	0.15	0.52	-0.05	0.00
ΔT_{chw} (°C) Equation 5-12	1.00	0.16	3.31	-0.02	0.00	1.00	0.17	3.49	-0.03	-0.01
ΔT_{cdw} (°C) Equation 5-15	0.99	0.18	3.95	0.00	0.00	0.99	0.27	5.86	-0.18	-0.04

7.4.4. Conclusion of model development with measurements of 2016

Based on the results of model training and testing with static window (SSA) and dynamic window (AWA and SWA) over the whole cooling season of 2016, the five grey-box models (E_b, COP_b, $T_{cdwl,b}$, $\Delta T_{chw,b}$, and $\Delta T_{cdw,b}$) are reliable and robust, as all the *RMSE* values are less than corresponding threshold values. Thus, one can conclude the five grey-box models can capture the seasonal chiller operation status well and can be regarded as benchmarking grey-box models. As the models (Equations 7-9 to 7-13) derived with SSA contain the most training data among the three model approaches, reflecting well the seasonal operation trend of a chiller, they are selected to proceed MDFDD.

7.5. Comparison of grey-box models derived with datasets of July 2013 and 2016.

The comparison of model training and testing results is conducted for the performance metrics and parameters of benchmarking grey-box models, derived with measurements of July 2013 and the whole cooling season of 2016, with respect to the three model training approaches (SSA, AWA, and SWA).

For the five performance metrics: *r, RMSE, CV, MBE, NMBE* (listed in in Table 7-1, Table 7-6, Table C-2, Table C-4, Table C-6, and Table C-8), there is no significant difference in terms of each benchmarking grey-box model over both the short dataset (measurements of July 2013) and the long dataset (whole cooling season of 2016), whatever model training approach (static window or dynamic window) is used.

The benchmarking grey-box models derived with the short dataset and the long dataset, describing the chiller monthly and the seasonal operation trends, show some similar behavior, while, in reality, there might be some different behaviors. For instance, a significant difference is noticed for the parameter (α_1) of the regressor $T_{chwl} - \overline{T_{chwl}}$ of the benchmarking grey-box model E_b regarding the dataset of July 2013 and the dataset of 2016. Though this difference might indicate different physical meanings, the value of the regressor $T_{chwl} - \overline{T_{chwl}}$ is very small. Thus, one can conclude the proposed five benchmarking grey-box models can represent well both the monthly trend and the seasonal trend of chiller operation, and are robust.

Chapter 8: Results of MDFDD using artificial faults

Detailed records of known equipment faults in existing HVAC system are usually unavailable for research purposes. The building operation team, due to potential disturbances in the operation and occupants' discomfort, does not easily accept the insertion of artificial physical faults in the operation of existing HVAC systems. Several publications present the insertion of numerical artificial faults in the computer simulation models. For instance, a fixed bias of 1°C was added to the chilled water return temperature sensor in TRANSYS simulator to generate data with a fault [91]. A bias fault of 10°C and a drifting fault of 0.9°C/h were injected into simulation results for fault detection using the neural network model [65].

Since there are no faults recorded by the BAS during the chiller operation of this case study, numerical artificial faults are inserted in the measurement data file: (i) the increase of bias error of the chilled water leaving temperature, and (ii) the reduction of refrigerant mass flow rate at the evaporator. The results of fault detection, in this chapter, are mainly derived with the threshold identification Method A (sole measurement uncertainty). Fault detection results based on threshold identification Method B, including both the measurement uncertainty and prediction uncertainty, are also presented for comparison purposes. The back ward fault diagnosis rules are also applied to isolate the fault source.

8.1. Results of inserting artificial faults with threshold identification Method A

8.1.1. Artificial fault of the measured chilled water leaving temperature

A bias of 5°C increase is inserted into the testing dataset for T_{chwl} over eight-time steps, starting at 13:15:00 on July 26, 2013 and ending at 15:00:00 on July 26, 2013 (Figure 8-1). The bias value of 5 °C is selected to exceed the measurement uncertainty of T_{chwl}.

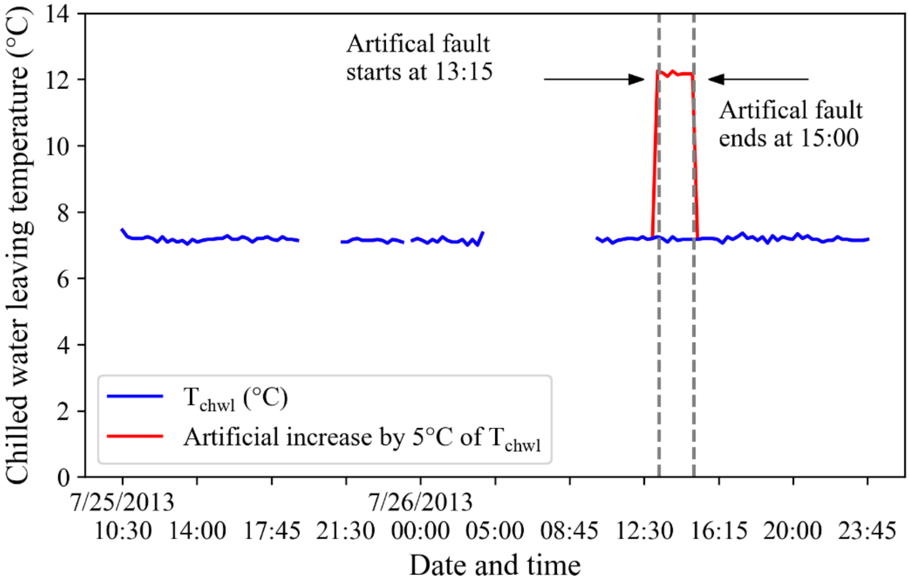

Figure 8-1. Artificial increase of 5°C for T_{chwl} over eight-time steps, starting at 13:15:00 on July 26, 2013 and ending at 15:00:00 on July 26, 2013.

Totally, six symptoms (*Symp*(T_{chwl}), *Symp(E)*, *Symp(COP)*, *Symp*(T_{cdwl}), *Symp*(ΔT_{chw}), and *Symp*($m_{ev,refr}$)) are successfully detected, and they are displayed from Figure 8-2 to Figure 8-7. The detected six symptoms all start from 13:15:00 on July 26, 2013, and end at 15:00:00 on July 26, 2013, which is the same time interval as the artificial T_{chwl} fault. The MDFDD model performance metrics are listed in Table 8-1.

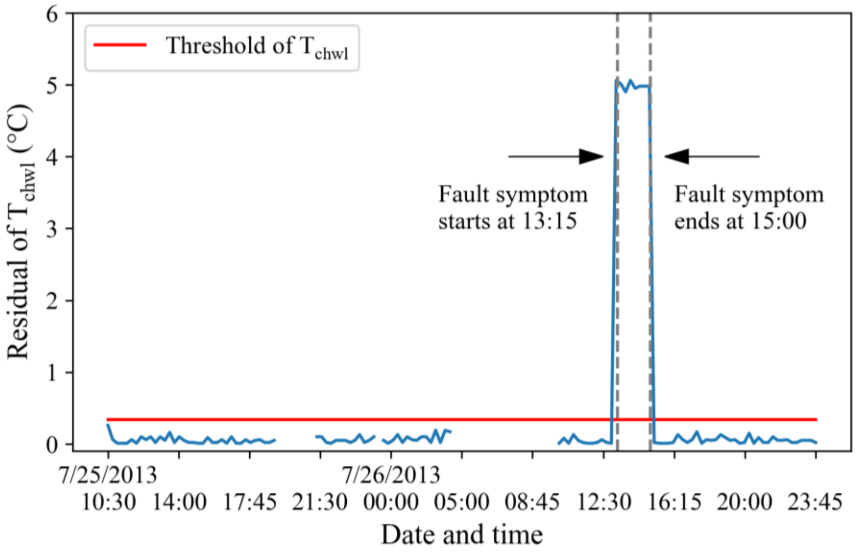

Figure 8-2. Impact of artificial fault of T_{chwl} on the fault symptom of T_{chwl}.

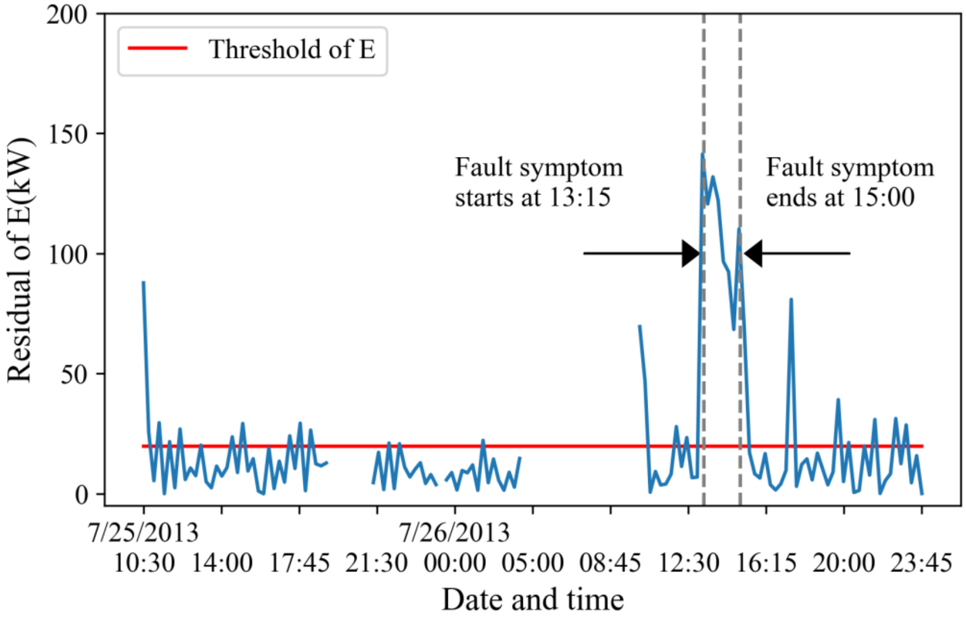

Figure 8-3. Impact of artificial fault of T_{chwl} on the fault symptom of E.

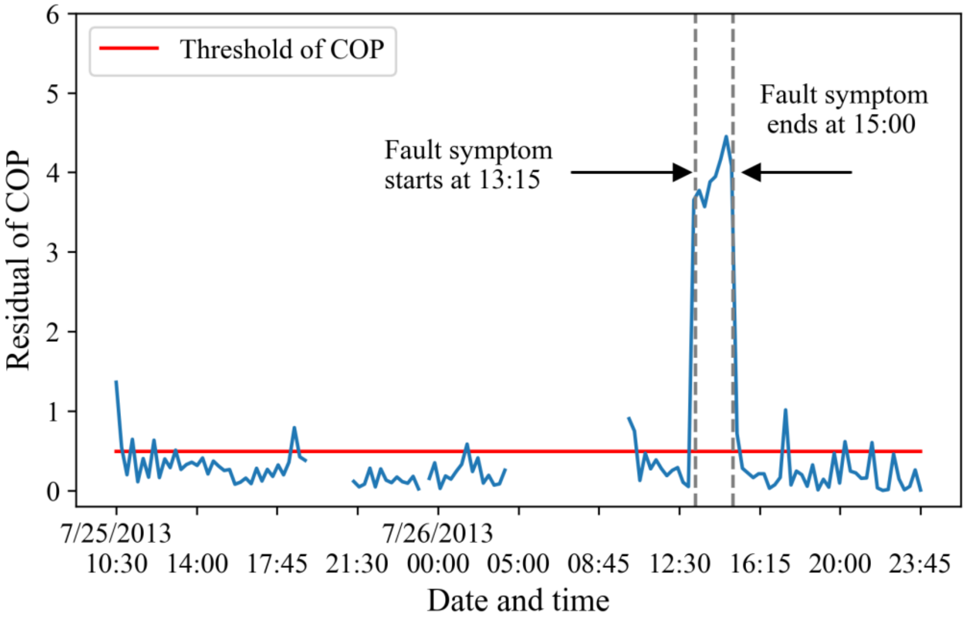

Figure 8-4. Impact of artificial fault of T_{chwl} on the fault symptom of COP.

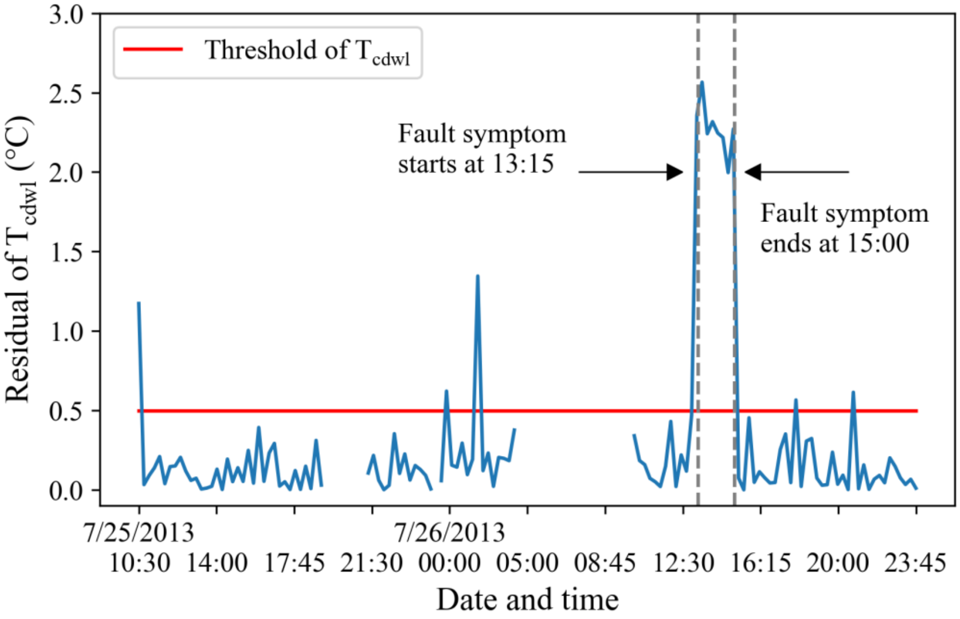

Figure 8-5. Impact of artificial fault of T_{chwl} on the fault symptom of T_{cdwl}.

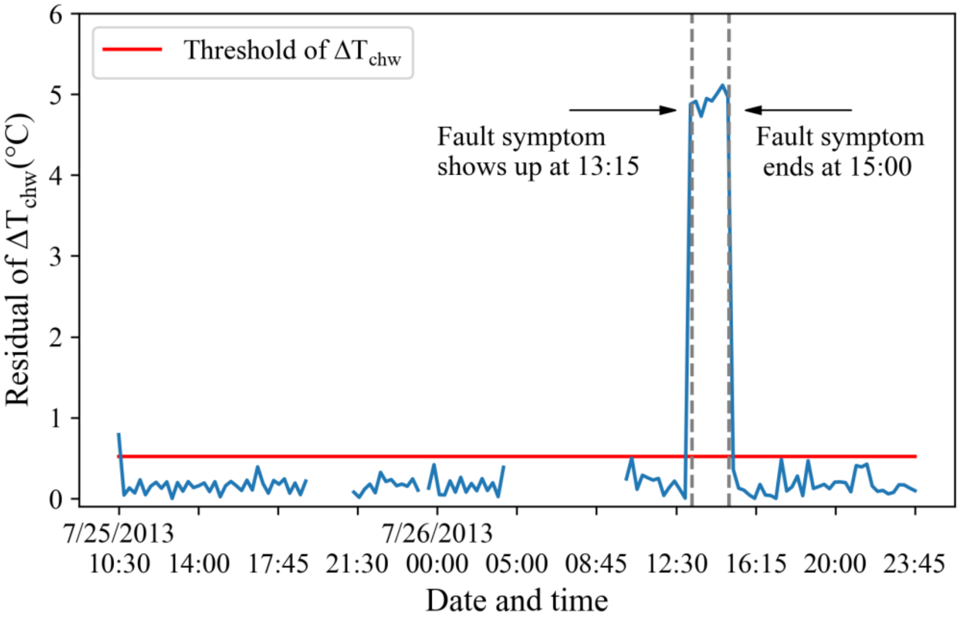

Figure 8-6. Impact of artificial fault of T_{chwl} on the fault symptom of ΔT_{chw}.

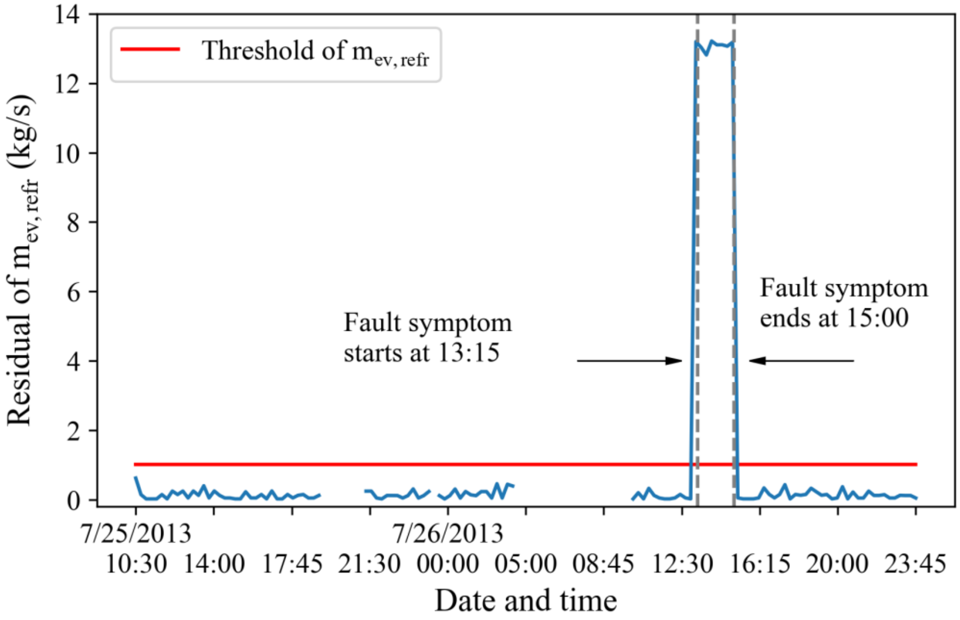

Figure 8-7. Impact of artificial fault of T_{chwl} on the fault symptom $m_{ev,refr}$.

Table 8-1. Model performance metrics for artificially inserted T_{chwl} fault, derived from test dataset from July 25, 2013, to July 26, 2013.

Assessment metrics	Symptoms					
	Symp(T_{chwl})	*Symp(E)*	*Symp(COP)*	*Symp(T_{cdwl})*	*Symp(ΔT_{chw})*	*Symp($m_{ev,refr}$)*
AC	100%	78.99%	89.08%	95.80%	99.16%	100%
HR	100%	100%	100%	100%	100%	100%
FAR	0.00%	22.52%	11.71%	4.50%	0.90%	0.00%

HR values for all the six symptoms (*Symp(T_{chwl})*, *Symp(E)*, *Symp(T_{cdwl})*, *Symp(COP)*, *Symp(ΔT_{chw}),* and *Symp($m_{ev,refr}$)*) are 100%. Thus, all the fault symptoms during the period of artificially inserted T_{chwl} fault, are successfully detected.

Some singular points, exceeding the threshold under fault-free time, are observed for *E,* T_{cdwl}, *COP*, and ΔT_{chw}, which results in the relative lower *AC* (e.g., *AC* value of *E* is 78.99%, Table 8-1). As explained in Chapter 7, they might be caused by the short-term malfunction of mechanical system or sensors, and are not continuous. Therefore, such abnormal measurements are not considered as fault symptoms. Similar conditions are also noticed in the case study of artificial $m_{ev,refr,ref}$ fault (e.g., Figure 8-9).

As *Symp(T_{chwl})*, *Symp(E)*, *Symp(COP)*, *Symp(T_{cdwl})*, *Symp(ΔT_{chw}),* and *Symp($m_{ev,refr}$)* are detected simultaneously, the variables T_{chwl}, E, COP, T_{cdwl}, ΔT_{chw}, and $m_{ev,refr,ref}$ appear to be faulty according to fault diagnosis rules. Additional investigation by the operation team is needed.

8.1.2. Artificial fault of the measured refrigerant mass flow rate

The refrigerant mass flow rate at the evaporator is reduced by 40% due to a fault starting at 13:15:00 on July 26, 2013 and ending at 15:00:00 on July 26, 2013 (Figure 8-8). The value of 40% is selected to exceed the measurement uncertainty of $m_{ev,refr,ref}$.

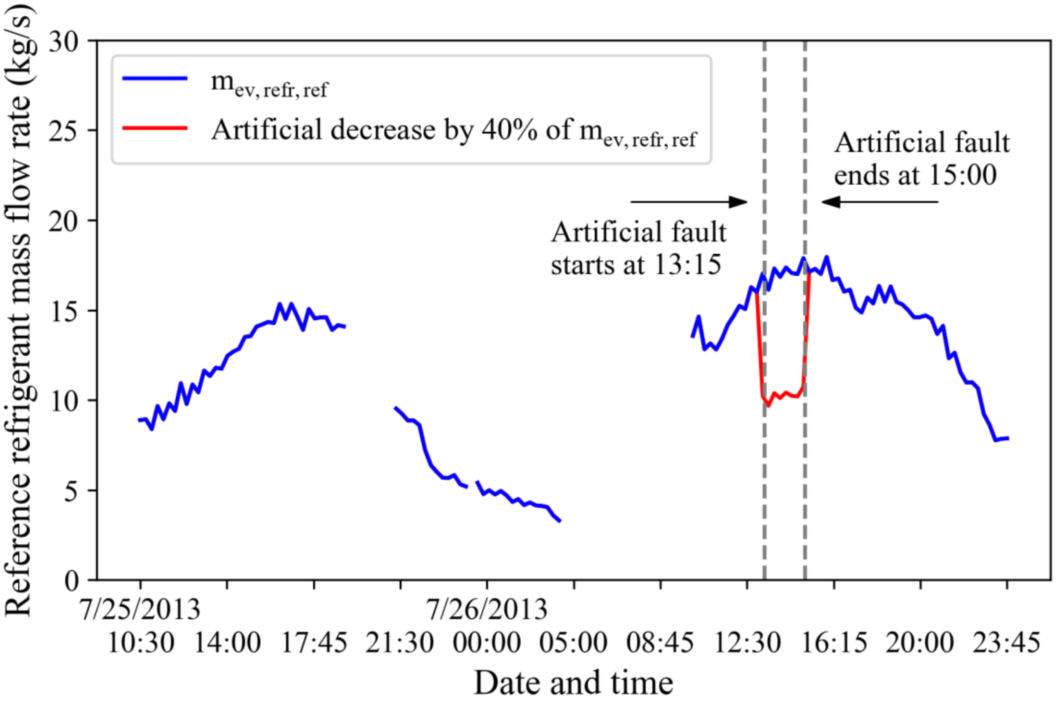

Figure 8-8. Artificial decrease by 40% of refrigerant mass flow rate starting at 13:15:00 on July 26, 2013 and ending at 15:00:00 on July 26, 2013.

Symp(E), *Symp(T_{cdwl})*, *Symp(COP)*, and *Symp($m_{ev,refr}$)* are successfully detected and they all start at 13:15:00 on July 26, 2013 and end at 15:00:00 on July 26, 2013 (Figure 8-9 to Figure 8-12), which is the same time period of artificial $m_{ev,refr,ref}$ fault. The MDFDD model performance metrics are listed in Table 8-2.

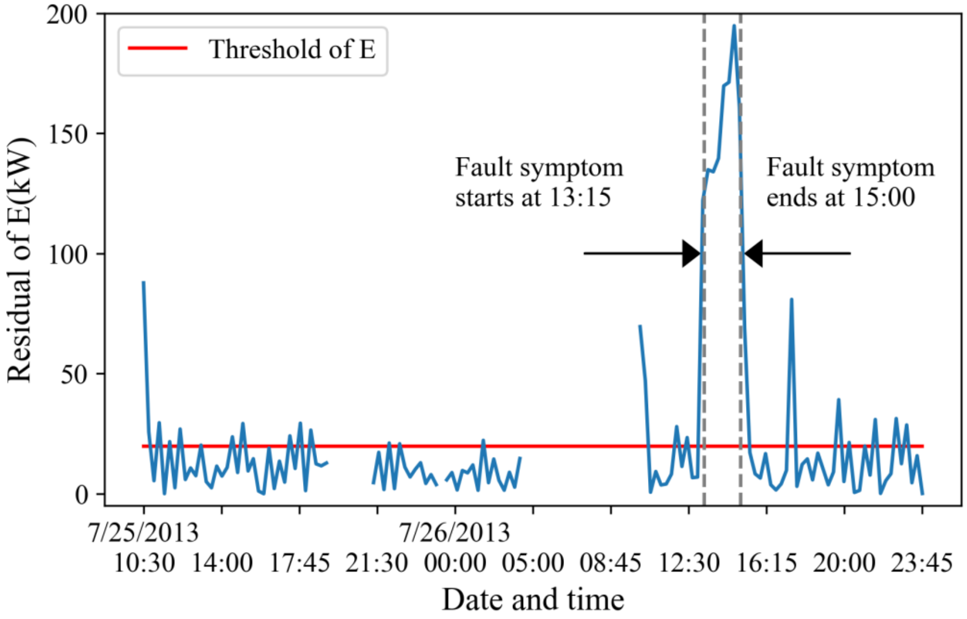

Figure 8-9. Impact of artificial fault of $m_{ev,refr,ref}$ on the fault symptom of E.

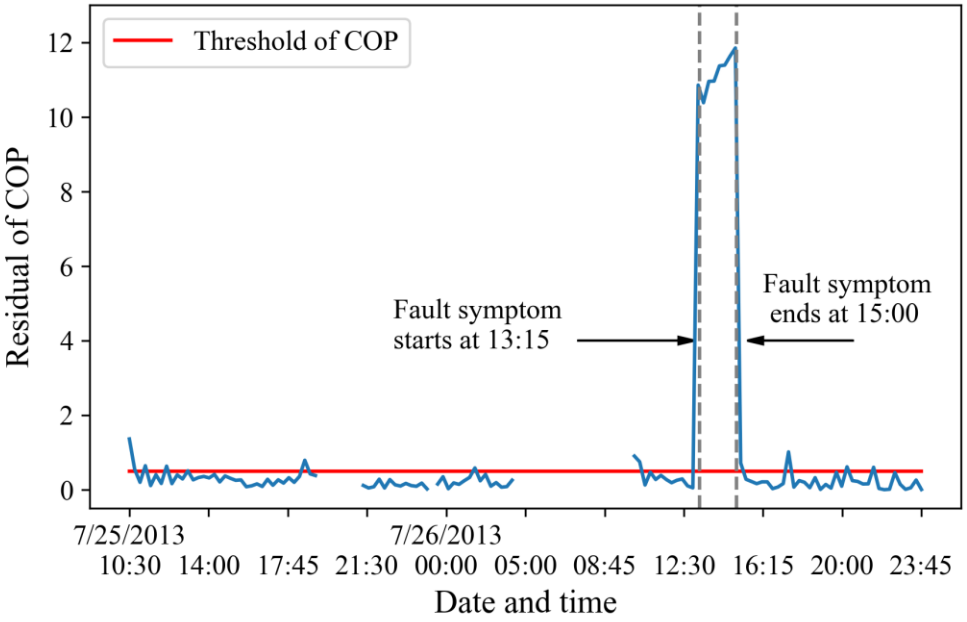

Figure 8-10. Impact of artificial fault of $m_{ev,refr,ref}$ on the fault symptom of COP.

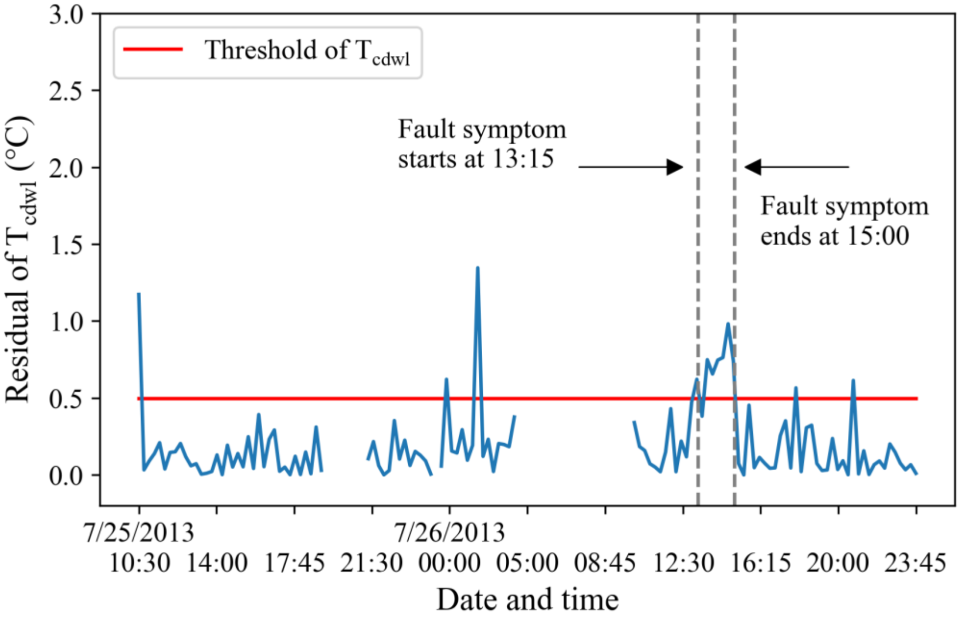

Figure 8-11. Impact of artificial fault of $m_{ev,refr,ref}$ on the fault symptom of T_{cdwl}.

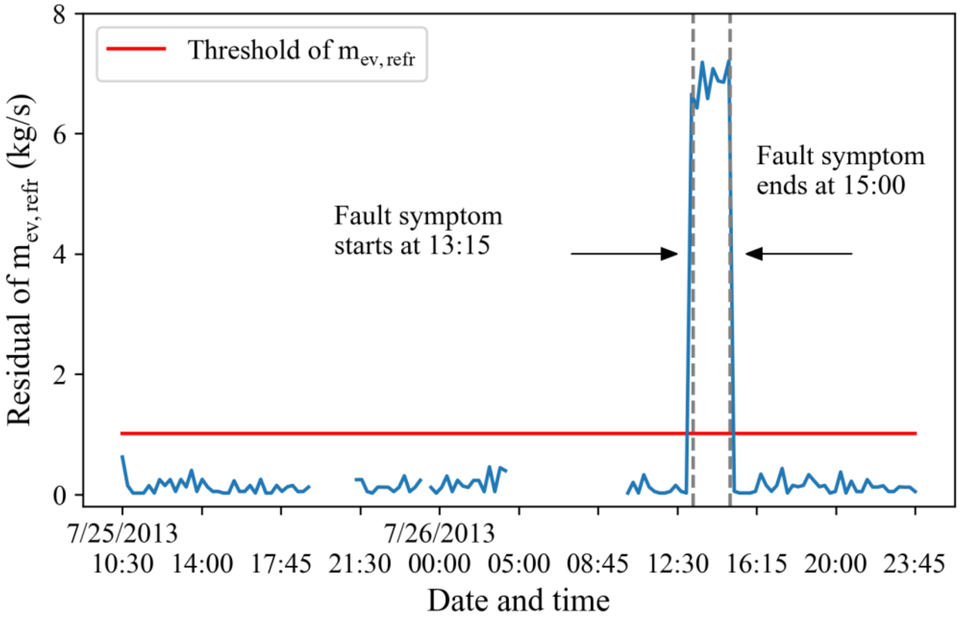

Figure 8-12. Impact of artificial fault of $m_{ev,refr,ref}$ on the fault symptom of $m_{ev,refr}$.

Table 8-2. Model performance metrics for artificially inserted $m_{ev,refr,ref}$ fault, derived from test dataset from July 25, 2013, to July 26, 2013.

Assessment metrics	*Symptoms*			
	$Symp(E)$	$Symp(COP)$	$Symp(T_{cdwl})$	$Symp(m_{ev,refr})$
89.08%	78.99%	89.08%	94.96%	100%
100%	100%	100%	87.50%	100%
11.71%	22.52%	11.71%	4.50%	0.00%

The impact of artificial fault of $m_{ev,refr}$ propagates to the three variables of E_b, COP_b and $T_{cdwl,b}$, which sequentially leads to the detection of $Symp(E)$, $Symp(COP)$, and $Symp(T_{cdwl})$. The impact of artificial $m_{ev,refr,ref}$ fault on itself is also identified as $Symp(m_{ev,refr})$ is detected.

In this example, the fault symptoms of E, COP, T_{cdwl}, and $m_{ev,refr}$ are detected. According to fault diagnosis rules, the three variables E, COP, T_{cdwl}, and $m_{ev,refr,ref}$ are faulty. Additional investigation by the operation team is needed.

8.1.3. Conclusion of case study with threshold identification Method A

The results, obtained from the case study with threshold identification Method A (sole measurement uncertainty), demonstrate that MDFDD model can detect and diagnose these dependent symptoms successfully. Due to some singular points occur during fault-free time, the accuracy of the proposed fault detection model is affected. Even though, the lowest AC for $Symp(E)$ of case study results can still reach to 78.99%. Faulty variables are also isolated by the fault diagnosis rules. Therefore, one can conclude that the proposed MDFDD model is reliable.

The proposed MDFDD model can detect and diagnose MDFs with high accuracy regarding the dataset of 2016. Due to the space limitation and for the purpose of simplification, corresponding results are not presented here.

8.2. Results of artificial faults with threshold identification Method B

Based on threshold identification Method B, including both the measurement uncertainty (U_m) and prediction uncertainty (U_p), in Chapter 5 and the benchmarking grey-box models derived with measurements of chiller CH#2 in July, 2013, the prediction uncertainty is calculated (Table 8-3). As U_p is not applicable to variables of T_{chwl}, and $m_{ev,refr,ref}$, corresponding cells are marked with NA in Table 8-3.

Table 8-3. Measurement uncertainty, prediction uncertainty, and threshold with respect to target variables, derived from the training dataset of 2013 of chiller CH#2.

Variables	Method A		Method B
	Measurement uncertainty (U_m)	Prediction uncertainty (U_p)	Overall uncertainty (OU)
E (kW)	19.02	11.98	23.22
COP	0.48	1.30	1.39
T_{cdwl} (℃)	0.49	0.17	0.52
T_{chwl} (℃)	0.34	NA	0.34
ΔT_{chw} (℃)	0.52	0.18	0.56
ΔT_{cdw} (℃)	0.66	0.13	0.68
$m_{ev,refr,ref}$ (kg/s)	0.68	NA	0.68

Based on Table 8-3, for the five target variables (E, COP, T_{cdwl}, ΔT_{chw}, and ΔT_{cdw}), it is noticed that (1) all the values of U_p are less than the values of U_m except for COP, and (2) threshold values identified by Method B are greater than the corresponding values identified by Method A. The prediction uncertainty for E, COP are very large, especially for COP with a U_p value of 1.30 that is greater than the measurement uncertainty of COP (U_m of COP is 0.48).

As described in Chapter 2, benchmarking grey-box models for E, COP, and T_{cdwl} are correlation-based grey-box models, and benchmarking grey-box models for ΔT_{chw} and ΔT_{cdw} are physical-based grey-box models. Results in Table 8-3 indicate the prediction uncertainty of physical-based grey-box models tends to be small. Compare performance metrics (Table 7-1) and U_p (Table 8-3) of five grey-box models, it is noticed that a model with a small CV usually has small prediction uncertainty (e.g., grey-box models for T_{cdwl} and ΔT_{chw}). Only based on the results of this case study, the author is not sure whether an intrinsic relation exists between model performance and model prediction uncertainty. But the results indicate a grey-box model with good performance tends to have small prediction uncertainty.

8.2.1. Fault detection and diagnosis with threshold identification Method B

The case study is conducted with benchmarking grey-box models derived with the dataset of July, 2013, and threshold identification Method B, including both the measurement uncertainty and prediction uncertainty. The artificial fault is inserted to the refrigerant mass flow rate at evaporator with a reduction of 40% starting at 13:15:00 on July 26, 2013 and ending at 15:00:00

on July 26, 2013, as listed in Figure 8-8. The residual value of each target variable is compared with the corresponding threshold, identified by Method B, for fault detection, and the results are displayed from Figure 8-13 to Figure 8-16. Performance metrics of fault detection are listed in Table 8-4.

Results indicate *Symp(E)*, *Symp(COP)*, *Symp(T_{cdwl})*, and *Symp($m_{ev,refr}$)* are successfully detected and they all start at 13:15:00 on July 26, 2013 and end at 15:00:00 on July 26, 2013 (Figure 8-13 to Figure 8-16), which is the same time interval of artificial $m_{ev,refr,ref}$ fault. Compared with the case and corresponding results presented in Section 8.1.2, the only change in this case study is threshold values, thus, the detected symptoms for the two case study are the same, which are as expected.

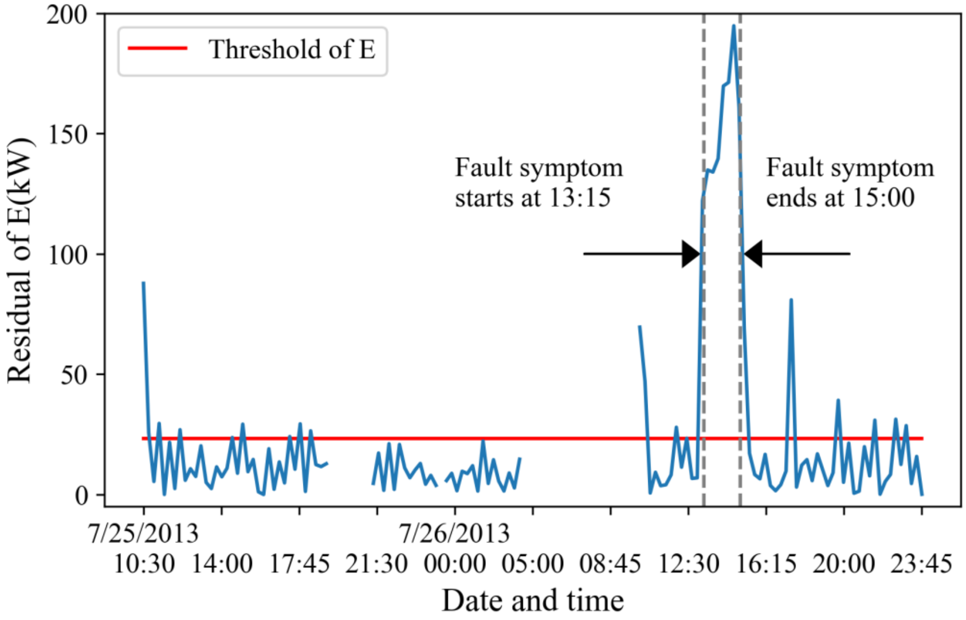

Figure 8-13. Impact of artificial fault of $m_{ev,refr,ref}$ on the fault symptom of *E*.

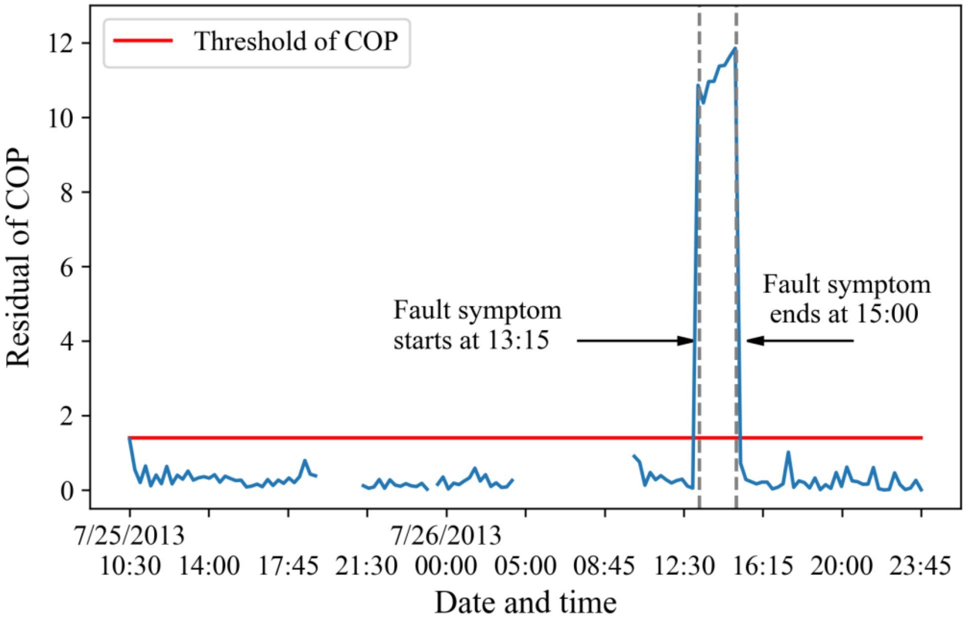

Figure 8-14. Impact of artificial fault of $m_{ev,refr,ref}$ on the fault symptom of COP.

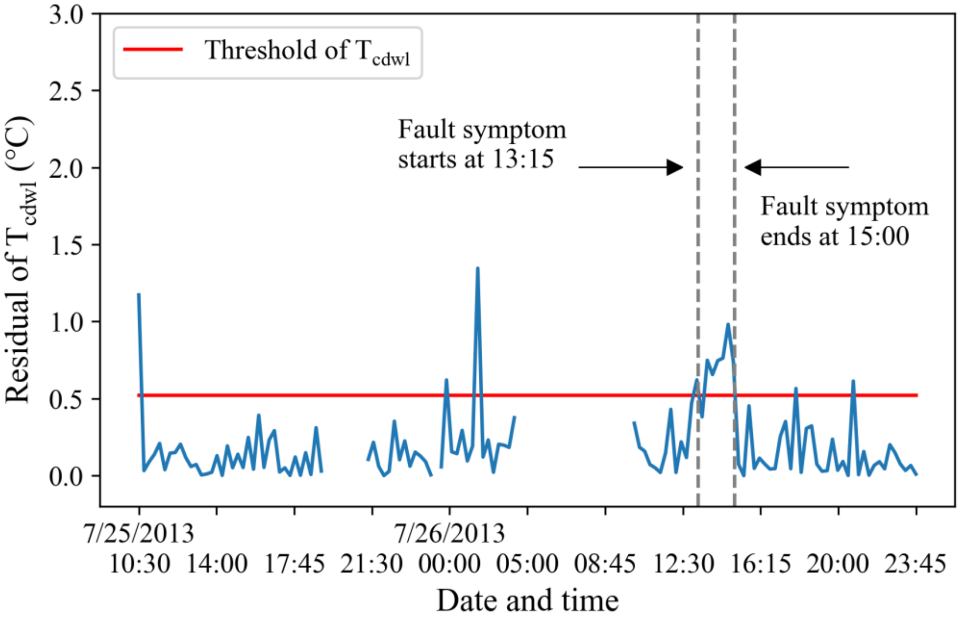

Figure 8-15. Impact of artificial fault of $m_{ev,refr,ref}$ on the fault symptom of T_{cdwl}.

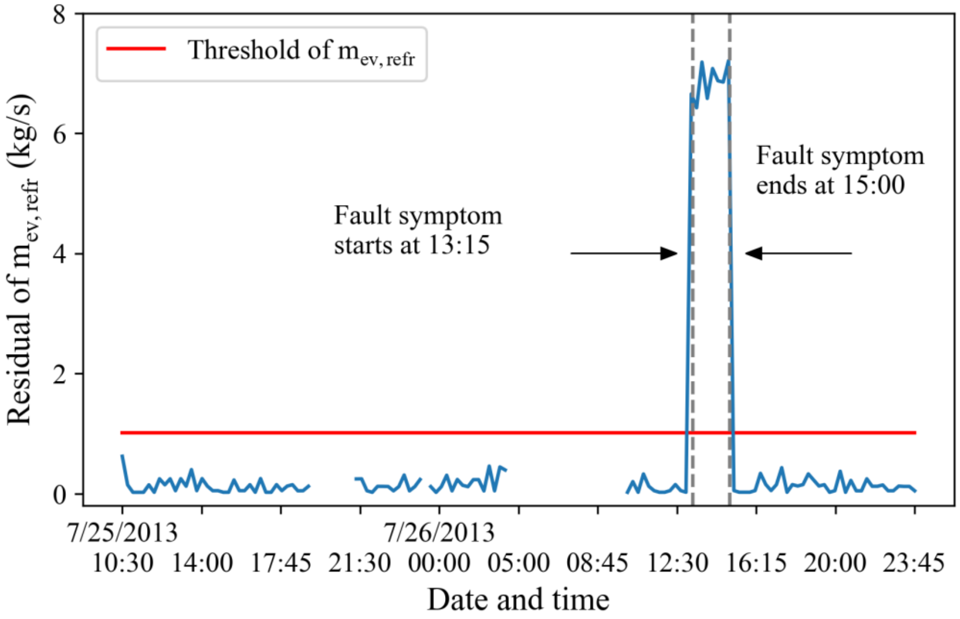

Figure 8-16. Impact of artificial fault of $m_{ev,refr,ref}$ on the fault symptom of $m_{ev,refr}$.

Table 8-4. Model performance metrics for artificially inserted $m_{ev,refr,ref}$ fault, derived from test dataset from July 25, 2013, to July 26, 2013, based on threshold identification Method B.

Assessment metrics	*Dependent symptoms*			
	Symp(E)	*Symp(COP)*	*Symp(T_{cdwl})*	*Symp($m_{ev,refr}$)*
AC	84.03%	100%	94.96%	100%
HR	100%	100%	87.50%	100%
FAR	17.12%	0.00%	4.50%	0.00%

Compare the performance metrics of MDFDD model, resulting from threshold identification Method A (Table 8-2) and Method B (Table 8-4), it is noticed that the fault detection performance regarding Method B improves for *Symp(E)* and *Symp(COP)* with the increase of *AC* and the decrease of *FAR*.

However, *AC* and *FAR* for *Symp(T_{cdwl})* don't show significant improvement. One possible reason is $\varepsilon(T_{cdwl})$ derived with Method *B* only increases very slightly as of $\varepsilon(T_{cdwl})$ derived with Method A, which is not enough to contribute a significant improvement. Another possible reason is the relatively small size of testing dataset with non-homogenous data distribution with respect to the dataset of July 2013.

8.2.2. Conclusion of case study with threshold Method B

In conclusion, the physical-based grey-box model and the grey-box model with good performance tend to have small prediction uncertainty. Apart from the threshold Method A, case study results of forward fault detection model with respect to the threshold Method B also show good performance. Thus, one can conclude that the threshold Method B can also be considered as an effective approach to identify the threshold for fault detection.

Chapter 9: Application of transfer learning

This chapter introduces the application of transfer learning approach to the prediction of target chiller variables (E, COP, T_{cdwl}, ΔT_{chw}, and ΔT_{cdw}), using deep neural network models. Transfer learning (TL) is applied by transferring a DNN model learnt from one chiller (called source chiller) to another chiller (called target chiller). The model performance is evaluated with the target chiller.

9.1. Transfer learning and deep learning

9.1.1. Introduction to transfer learning

Transfer learning (TL) can be defined as the ability of a system to recognize and apply knowledge and skills learned in previous tasks to novel tasks [125]. Motivated by satisfying the need for lifelong machine learning methods that retain and reuse previous learnt knowledge, the transfer learning methods aim to improve the performance of target learners to target models by transferring the knowledge identified in different but related models [172]. It contributes to solving the defects that can occur, such as lack of data for a model and/or the time required to train a new model. TL has been successfully used for regularization of learner's objective function [173,174], parameter sharing [175,176], parameter restriction [177], and model ensemble etc [178].

The application of transfer learning methods used in the building field was used for predicting building energy use [126–128]. An instance-based transfer learning strategy (e.g., instance-based TrAdaBoost) was applied to forecast the energy consumption of HVAC system [126]. The results indicated that the transfer learning strategy could improve the forecasting accuracy. Fan et al [127] transferred features of an ANN model (e.g., T_{oa}, RH_{oa}, etc.) to another one to predict the short-term building energy use. TL achieved a decrease of 67% in terms of *RMSE*. Yun and Cheol [128] transferred a pre-trained ANN model to estimate the target building properties, and fine tune the parameters with a training dataset from the target building. They reported that the TL strategy could improve the *CV(RMSE)* value by 10%, compared with the conventional ANN approach.

TL was also applied to study FDD in HVAC systems [129,179]. Chase and Baosen [179] used a transferable naïve Bayesian classifier, trained with the source HVAC system, to detect faults resulting from component degradation in the target HVAC system. For the chiller FDD, a domain adaptive model derived from a source chiller was migrated to a target chiller [129]. This work proved the feasibility of TL for FDD, by migrating existing models to a new chiller model without the time and resource requirements associated with the development of a new model.

In summary, as a time-efficient and source-efficient approach, transfer learning (TL) applies the knowledge learnt in previous tasks to new tasks.

9.1.2. Introduction to deep learning

Deep learning (DL) is a kind of machine learning method coupling the representation learning, aiming to solve a source of difficulty in the real-word applications of artificial intelligence, where many of the factors of variation influence every single piece of data that we are able to observe [180]. The quintessential example of a DL model is a multilayer perceptron, composed of a mathematical function (consist of many simpler function) mapping some set of input values to output values, where each application of a different mathematical function can be regarded as providing a new representation of the input.

DL, from the perspective of concept, refers to machine learning models that include multi-levels of nonlinear transformation; deep neural network (DNN) models are the application of such strategies to neural networks [150]. Apart from multiple layer perceptron, common DNN models may include convolutional neural networks (CNNs), Long-short term memory networks (LSTMs), etc.

To start a modelling project in the field of artificial neural networks (ANN), one of the first decisions is how to select the suitable model from diverse ANN models. Measurements of case study in this dissertation indicate the time leg effect is not significant. For this reason, the time-series model (e.g., LSTMs) is not selected, instead, multiple layer perceptron is selected as the DNN model to predict five chiller variables, including E, COP, T_{cdwl}, ΔT_{chw}, and ΔT_{cdw}.

Figure 9-1 shows a fully connected DNN model, as an example, for the prediction task with three sequential layers: (1) one input layer including n inputs, (2) three hidden layers, and (3) one output layer including m outputs. Each layer is composed of adjustable neurons, where the number of neurons of the input layer usually depends on the number of independent inputs and the number of neurons of the output layer depends on the target.

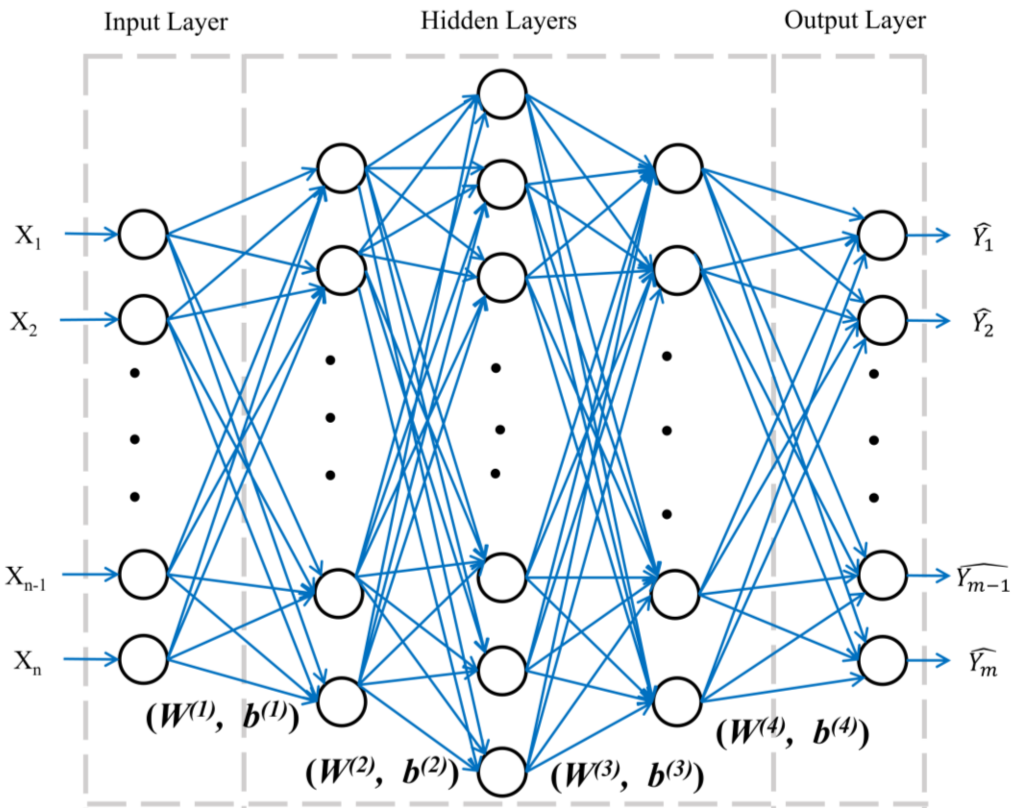

Figure 9-1. Deep neural network model architecture.

DNN is a type of feed-forward neural network, the summation of inputs with corresponding weights and bias (e.g., $W^{(1)}$ and $b^{(1)}$ in Figure 9-1) is sent to the first hidden layer and goes through a non-linear transformation, complying with the activation function applied. Sequentially, the information of the first hidden layer is sent to the next hidden layer for another non-linear transformation along with corresponding weights and bias, following the feedforward process. Equation 9-1, Equation 9-2, and Equation 9-3 are listed here to show, as an example, the governing equations of a DNN model in Figure 9-1.

$$h^{(1)} = g^{(1)}\left(W^{(1)}X + b^{(1)}\right) \tag{9-1}$$

$$h^{(2)} = g^{(2)}\left(W^{(2)}h^{(1)} + b^{(2)}\right) \tag{9-2}$$

$$\hat{Y} = W^{(4)}h^{(3)} + b^{(4)} \tag{9-3}$$

where $h^{(1)}$ and $h^{(2)}$ are the outputs of the first and second hidden layers, g is the activation function, $\hat{Y}$ is the output of the output layer, $W^{(2)}$ and $b^{(2)}$, for instance, are weights and bias of the second hidden layer.

A short critical literature review is conducted focusing on DNN application in the field of HVAC, and covers the publications in recent years (from 2015 to 2022), which are listed in a chronological order in Table 9-1. These papers are focusing on either the prediction task or the classification task. One of the most important hyperparameters of a DNN model is the configurations of hidden layers, including the number of hidden layers and the number of neurons in each hidden layer. A DNN model with more hidden layers usually outperforms the one with only a single hidden layer in some aspects like more accurate, avoiding overfitting, etc. Results of literature review might support this point as all the reviewed papers use at least two hidden layers. Literature review finds 4 out of the 11 reviewed papers utilize three hidden layers, which takes the most in terms of hidden layer numbers of a DNN model. However, based on Table 9-1, there is not a general rule to set the number of hidden layers except one proposed in reference [181]. As for the neuron numbers of a hidden layer, both the uniform and the non-uniform neuron numbers of each hidden layer are observed. The activation function of the rectified linear unit (ReLU) is used by seven papers; four other papers omit this information (marked as NA in Table 9-1).

Table 9-1. Architecture of deep neural network in the literature review.

Neuron number of input layer	Number of hidden layers/neurons	Neuron number of output layer	Activation function	Year	Ref.
4	2/18, 9	1	NA	2015	[181]
6	5/ 200 each layer	6	ReLU	2019	[182]
8	3/ 5, 1, 8	2	NA	2019	[183]
6	2/ 8, 8	4	ReLU	2019	[184]
9	6/ 20, 100, 100, 100, 100, 100	2	ReLU	2019	[185]
43	2/ 50, 50	4	NA	2020	[186]
12	3/ 100, 80, 50	1	ReLU	2021	[187]
4	2/ 65, 256	1	ReLU	2021	[188]
8	5/ 20 each	2	NA	2021	[189]
9	3/ 64, 64, 64	1	ReLU	2022	[190]
78	3/ 128 each	1	ReLU	2022	[191]

Note*: The column of *Number of hidden layers/neurons* shows the number of hidden layers and the number of neurons of each layer. For instance, 2/18,9 indicates a DNN model with two hidden layers, the first hidden layer with 18 neurons and the second hidden layer with nine neurons.

Miriam et al. [181] proposed a method to create a suitable structure of a DNN model based on the number of neurons of the input layer. The study compared three structures, with different numbers of hidden layers and the number of neurons, to predict the electric energy consumptions of real buildings. Results indicated that the DNN model with the configurations of (1) two hidden layers, (2) the number of neurons in the first hidden layer of $2\times(2\times n+1)$, and (3) the number of neurons in the second hidden layer of $2\times n+1$, achieved the best performance and is the most robust. Here, n is the number of neurons of the input layer.

9.2. Methodology of the application of transfer learning

9.2.1. Transfer learning strategies

Transfer learning usually includes the transfer of information between two domains: (1) the source domain (SD) that contains data of previous tasks, which can be used for the model pre-training and testing, and (2) the target domain (TD) that contains data of the new task, which is used for the fine-tuning of a model (e.g., in the case of DNN model, the weights are changed), and the testing of updated model. This dissertation introduced three transfer leaning strategies: TLS0, TLS1, and TLS2:

1. TLS0: The DNN model is trained and tested with the dataset of SD, and then used directly with the dataset of TD, without changes of initial model weights. The DNN model performance is evaluated with the testing dataset of TD. TLS0 is also called direct TL.
2. TLS1: The DNN model is first pre-trained and tested with the dataset of SD, and then it is updated by using the dataset of TD. The weights of all DNN model layers are fine-tuned with the training dataset of TD. Finally, the updated DNN model is evaluated with the testing dataset of TD.
3. TLS2: The DNN model is first pre-trained and tested with the dataset of SD, and then it is updated with the dataset of TD. Only the weights of the output layer are updated. Finally, the updated DNN model is evaluated with the testing dataset of TD.

In addition to the above three transfer learning strategies, another DNN model is developed by using the so-called self-learning (SelfL) strategy. This model is trained and tested only with the dataset of TD.

9.2.2. Deep-neural network model structure and evaluation

This dissertation used DNNs as a tool to conduct TL. Five DNN models were built and each one was used to predict one selected target variable. The input variables and the output variable of a DNN model are selected as the corresponding regressor variables and the target variable of a benchmarking grey-box model (Chapter 5). For instance, the benchmarking grey-box model of Equation 5-4 for E includes three regressor variables: T_{chwl}, V_{chw}, and $m_{ev,refr,ref}$, which are selected as the inputs of the DNN model of E. The structure of each DNN model, including hidden layer number and corresponding number of neurons, refers to the guide of [181], as listed in Table 9-2.

Table 9-2. Architecture of each deep neural network model.

DNN model	Input layer		Hidden layer (HL)		Output layer	Target variable
	Input variables	Input neurons	HL1 neurons	HL2 neurons	Output neurons	
DNN1	T_{chwl}, V_{chw}, $m_{ev,refr,ref}$	3	14	7	1	E
DNN2	T_{chwl}, V_{chw}, PLR, $m_{ev,refr,ref}$	4	18	9	1	COP
DNN3	T_{chwr}, T_{chwl}, V_{chw}, $m_{ev,refr,ref}$, E, T_{cdwr}	6	26	13	1	T_{cdwl}
DNN4	V_{chw}, T_{chwl}, T_{ev}	3	14	7	1	ΔT_{chw}
DNN5	T_{dis}, T_{cd} T_{cdwr}	3	14	7	1	ΔT_{cdw}

As the scale of diverse variables differs a lot, data normalization is required. Otherwise, such condition might lead to weights of a DNN model that are too small and/or too large, which in turn affects the model performance. The min-max normalization method is used in this dissertation, as it was suitable for data with known bounds and without many outliers [192]. The equation for the min-max normalization of each variable is provided in Equation 9-4:

$$X_{i,norm} = \frac{X_i - X_{min}}{X_{max} - X_{min}} \tag{9-4}$$

Where $X_{i,norm}$ is the normalized value of X_i, X_i is a data point of a variable within measurements, X_{min} is the minimum value, and X_{max} is the maximum value. The min-max normalization method adjusts values of a variable to a range of 0 and 1.

The five DNN models are developed using Python (version 3.9.12) [160] with open libraries like TensorFlow (version 2.10.0) [193]. The trial-and-error method is applied to identify the optimum hyper-parameters of five DNN models, i.e., the activation function and learning rate. For each DNN model, the iteration is set for 10,000 epochs, and the optimum activation function (Table 9-3) is selected from the following list: 'relu' [194], 'elu', 'gelu' [195], 'selu' [196,197], 'sigmoid', 'tanh' (Equations 9-5 to 9-10). The optimum learning rate (Table 9-3) is selected from the following list: 0.001, 0.01, 0.1, 0.2, 0.4, 0.6, 1.

Table 9-3. The selected activation function and learning rate for each DNN model.

DNN model		Optimum activation function and learning rate		Criterion to stop model training
Model number	Output variable	Activation function	Learning Rate	
DNN1	E	ReLU	0.1	1.4×10^{-3}
DNN2	COP	SeLU	0.01	3.7×10^{-3}
DNN3	T_{cdwl}	GeLU	0.1	1.2×10^{-3}
DNN4	ΔT_{chw}	GeLU	0.2	1.3×10^{-4}
DNN5	ΔT_{cdw}	SeLU	0.01	1.4×10^{-3}

1. Rectified Linear Unit (ReLU)

$$f(x) = \max(0, x) = \begin{cases} x, x > 0 \\ 0, x \leq 0 \end{cases} \tag{9-5}$$

2. Exponential Linear Unit (ELU)

$$f(x) = \begin{cases} EXP(x) - 1, x < 0 \\ x, x \geq 0 \end{cases} \tag{9-6}$$

3. Gaussian Error Linear Unit (GeLU)

$$f(x) = 0.5x\left[1 + tanh\left(\sqrt{\frac{2}{\pi}}(x + 0.044715x^3)\right)\right] \tag{9-7}$$

4. Scaled Exponential Linear Unit (SeLU)

$$f(x) = \lambda \begin{cases} \alpha(e^x - 1)x, x > 0 \\ x, x \leq 0 \end{cases} \tag{9-8}$$

with $\alpha \approx 1.6733$ and $\lambda \approx 1.0507$ [196].

5. Sigmoid function

$$f(x) = \frac{1}{1+e^{-x}} \tag{9-9}$$

6. Tangent function (tanh)

$$f(x) = \frac{e^x - e^{-x}}{e^x + e^{-x}} \tag{9-10}$$

Within this work, the algorithm of stochastic gradient descent with momentum [198,199] (Equations 9-11 to 9-12) is applied to tune the weights of DNN models. The loss function (Equation 9-13) is used to estimate the loss of the model over the training dataset so that the weights can be updated iteratively to reduce the loss [200].

$$M^t = M^{t-1} - lv^t \tag{9-11}$$

Where:

$$v^t = \beta v_{t-1} + (1-\beta)\nabla_M L \tag{9-12}$$

$$L = \sum_{j=1}^{n}(\hat{y_j} - y_j) \tag{9-13}$$

Where M represents weights, l is the learning rate, β is the momentum constant, $\nabla_M L$ is the gradient, n equals to the length of training dataset, j is indicator.

The model training stops once one of the two criteria has been met: (1) the mean square error of the output (target) variable over the training dataset has fallen under the value listed in Table 9-3 (identified by trial-and-error method), or (2) the maximum number of iterations of 10,000 epochs has been reached.

The prediction results are compared with measurements, and the model performance is evaluated with three performance metrics (*r, RMSE,* and *CV*) that are introduced in Chapter 5. In addition, mean absolute deviation (*MAD*) [117] is presented as another performance metric to evaluate DNN models, as shown in Equation 9-14.

$$MAD = \frac{\sum_{i=1}^{n}|\hat{y_i} - y_i|}{n} \tag{9-14}$$

According to ASHRAE Guideline 14 [201], the calibration of a computer model is acceptable if the *CV* between the predictions and measurements of prediction of the whole building energy use is smaller than 30%, when using hourly data, or smaller 15% when using monthly data. The author estimated, with measurements of 15-minute time, the acceptable *CV* value should be greater than 30% due to larger variation of measurements.

By extension of such recommended values of *CV*, some authors have applied the recommendations to other variables of HVAC systems. Reference [202] reported a range between 19.09% and 19.40%, reference [203] reported 5.58%, and reference [204] reported 15%. Another study reported an acceptable prediction of the ventilation temperature of a nearly zero energy building when *CV* was 20% [205].

This dissertation evaluates the model by comparison with the measurement uncertainty, and with the metrics presented above.

9.3. Two case studies

9.3.1. Case study #1

The implementation of TL within this dissertation is to verify whether a DNN model learnt from a SD of a chiller (source chiller) performs well for the prediction of another chiller (target chiller). For this purpose, measurements of chiller CH#2 (source chiller) in July 2013 are used as SD. Three target domains are extracted from measurements of chiller CH#1 (target chiller) in 2016 (Table 6-2, Chapter 6). The information of training dataset and testing dataset of SD and three TDs is listed in Table 9-4. The five DNN models were first pre-trained with the training dataset of source chiller (CH#2, 2013) and, then, transferred to the target chiller (CH#1, 2016).

Table 9-4. Information of source domain and target domain for case study #1.

Datasets		Source domain (CH#2, 2013)	Target domain (CH#1, 2016)		
			TD1	TD2	TD3
Training dataset	Duration	7/11-7/24	6/22 - 6/23	7/4 – 7/8	8/1 – 8/4
	Dataset size	326	138	330	170
Testing dataset	Duration	7/25-7/26	6/27 - 6/30	7/11 -7/15	8/8 – 8/12
	Dataset size	119	222	174	233

The training dataset of SD under normal operation, composed of first 326 measurements (73%

of the whole data set) was recorded by BAS every 15 minutes, from July 11, 2013 to July 24, 2013, is used for the identification of model weights. The remaining 119 measurement data (27% of the whole dataset), from July 25, 2013 to July 26, 2013, are used for the model testing.

It is worth noticing that, in TD1 and TD3, the length of the training dataset is smaller than the testing dataset. This is especially valid for TD1, were the training set consists of 138 data points while the testing set consists of 222 data points.

Measurements indicate that the main characteristic of case study #1 contains diverse chiller operation conditions (loads) over three target domains (TD1, TD2, and TD3). The average values of *E* over the training datasets of TD2 and TD3 are 315.11kW and 328.24kW (Figure 9-2), which are greater than that of TD1 (253.41kW).

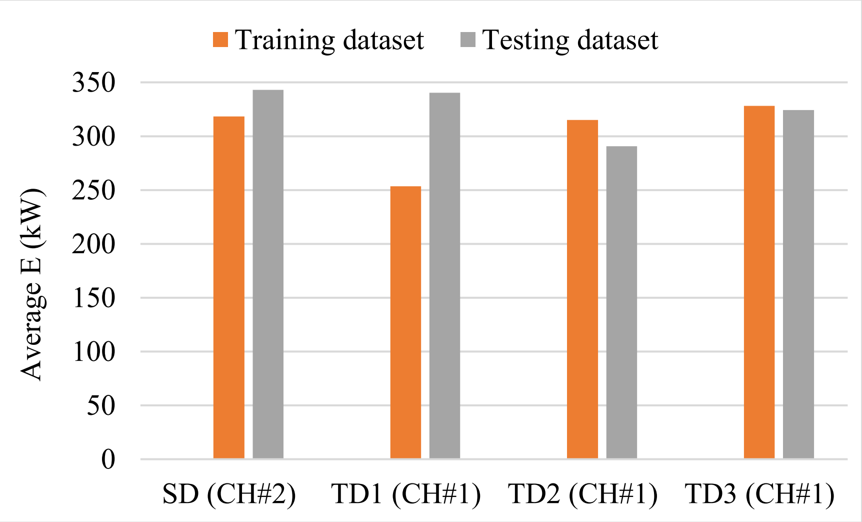

Figure 9-2. Average values of measured *E* over the training dataset and the testing dataset of SD and three TDs in case study #1.

9.3.2. Case study #2

The source domain of case study #2 is the same as that of case study #1 (Table 9-4); however, the three TDs are different. They were also extracted from measurements of chiller CH#1 (target chiller) in 2016 (Table 6-2, Chapter 6), but the testing dataset of each TD contains almost the rest of the summer for 2016. The three TDs of case study #2 are marked with TD4, TD5, and TD6 (Table 9-5), respectively. Case study #2 represents the condition when only very limited data (training dataset) of TD are available for updating weights of a DNN model by using TL to improve model performance over the rest of data of a summer.

Table 9-5. Information of source domain and target domain for case study #2.

Datasets		Source domain (CH#2, 2013)	Target domain (CH#1, 2016)		
			TD4	TD5	TD6
Training dataset	Duration	7/11-7/24	6/22 - 6/23	7/4 – 7/8	7/11 – 7/13
	Dataset size	326	138	330	144
Testing dataset	Duration	7/25-7/26	6/27-8/12	7/11-8/12	7/15-8/12
	Dataset size	119	1592	1040	896

Based on the approach to calculate measurement uncertainty (Chapter 5), Table 9-6 presents the values (mean ± uncertainty) of directly measured and derived variables with respect to training datasets of six target domains (TD1 to TD6). The chiller operation characteristics with respect to SD and TDs are compared in Table 9-6.

Table 9-6. Mean and measurement uncertainty of directly measured and derived variables identified with the training datasets of source domain and target domains.

Variables	Source domain (CH#2, 2013)	Target domains (CH1, 2016)			
	SD	TD1(TD4)	TD2(TD5)	TD3	TD6
E (kW)	324.67±19.02	253.41±16.50	315.11±20.36	328.24±21.81	273.28±23.49
COP (-)	5.02±0.48	5.54±0.57	5.84±0.59	5.96±0.61	5.56±0.67
T_{cdwl} (°C)	32.70±0.49	27.13±0.48	28.56±0.52	28.80±0.54	27.67±0.60
ΔT_{chw} (°C)	4.31±0.52	3.99±0.54	5.04±0.54	5.28±0.54	4.31±0.59
ΔT_{cdw} (°C)	4.07±0.66	3.61±0.64	4.65±0.67	4.83±0.69	3.91±0.73
V_{chw} (L/s)	91.15±4.56	86.31±4.33	88.47±4.43	88.90±4.46	87.56±4.42
PLR (-)	0.52±0.04	0.45±0.04	0.59±0.05	0.62±0.05	0.50±0.04
T_{ev} (°C)	4.91±0.33	5.06±0.44	4.79±0.33	4.78±0.33	5.02±0.34
T_{cd} (°C)	33.59±0.53	27.99±0.51	29.52±0.55	30.20±0.58	28.50±0.65
T_{cdwr} (°C)	28.62±0.44	23.52±0.42	23.90±0.43	23.96±0.43	23.76±0.43
T_{chwr} (°C)	11.50±0.40	10.81±0.42	11.93±0.42	12.22±0.43	11.16±0.49
T_{chwl} (°C)	7.19±0.34	6.82±0.33	6.89±0.34	6.94±0.34	6.86±0.34
$m_{ev,refr,ref}$ (kg/s)	10.83±0.68	9.09±0.73	11.97±0.94	12.59±0.98	10.12±0.84

9.3. Results

9.3.1. DNN model training and testing results regarding the source domain

The five DNN models are trained and tested with the optimum hyperparameters, including activation function and learning rate, using measurements of SD (chiller CH#2 of July 2013). The performance metrics of the DNN models, calculated over both the training and the testing datasets, are listed in Table 9-7, where the measurement uncertainty (U_m) of five target variables is also included.

Table 9-7. Performance metrics of five DNN models and measurement uncertainty with respect to SD (CH#2, 2013).

Target variables	Training dataset					Testing dataset			
	r	*RMSE*	*CV (%)*	*MAD*	U_m	*r*	*RMSE*	*CV (%)*	*MAD*
E (kW)	0.99	16.93	5.31	16.39	19.02	0.98	23.48	6.89	12.45
COP (-)	0.96	0.21	4.16	0.19	0.48	0.92	0.26	5.17	0.15
T_{cdwl} (°C)	0.99	0.25	0.76	0.21	0.49	0.99	0.28	0.84	0.19
ΔT_{chw} (°C)	1.00	0.08	1.75	0.07	0.52	1.00	0.08	1.76	0.06
ΔT_{cdw} (°C)	0.99	0.23	5.62	0.17	0.66	0.98	0.27	6.16	0.15

It is noticed that *RMSE* values (Table 9-7) of four DNN models (*COP*, T_{cdwl}, ΔT_{chw}, and ΔT_{cdw}) over the testing dataset are smaller than corresponding measurement uncertainty. Furthermore, the *RMSE* of the DNN model predicting the target variable *E* is 23.48kW over the testing dataset; which is only slightly greater than the measurement uncertainty of *E* (19.02kW). One possible reason for the result of *E* is the average chiller load of the testing dataset is greater than that of the training dataset (Figure 9-2). The DNN model of *E*, derived with the training dataset of SD, may miss some high-load chiller operational conditions.

Overall, the evaluation metrics (Table 9-7) indicate the five DNN models derived with SD perform well.

9.3.2. Self-learning results based on case study #1 and case study #2

The five DNN models are pre-trained and tested with the optimum hyperparameters, including the activation function and the learning rate, on six target domains (TD1 to TD6). The performance metrics of DNN models, calculated over TD1, TD2, and TD3 (case study #1), are listed in Appendix D (Table D-1). Results with respect to TD4, TD5, and TD6 (case study #2) are listed in Appendix D (Table D-2).

For the results of case study #1 (Table D-1), all *RMSE* values of five DNN models over the testing dataset of TD2 are less than the corresponding measurement uncertainties. However, *RMSE* values over testing datasets of TD1 and TD3 show different results. For instance, over the testing datasets of TD3, the *RMSE* value for *E* is significantly greater than the measurement uncertainty of *E*. *RMSE* values of three DNN models (*E*, *COP*, and ΔT_{cdw}) over the testing dataset of TD1 are greater than corresponding measurement uncertainties.

For the results of case study #2 (Table D-2), all *RMSE* values of five DNN models over the testing dataset of TD5/TD6 are less than the corresponding measurement uncertainties. However, *RMSE* values of four DNN models (*E*, *COP*, T_{cdwl}, and ΔT_{cdw}) in TD4 are greater than the corresponding measurement uncertainties.

9.3.3. Results of transfer learning with respect to case study #1

The five DNN models (*E*, *COP*, T_{cdwl}, ΔT_{chw}, and ΔT_{cdw}), derived with the training dataset of SD, are transferred to the target chiller with three TDs (TD1, TD2, and TD3) by using three TL strategies (TLS0, TLS1, and TLS2). TLS0 directly transfers the five DNN models, trained on SD, to the target chiller (CH#1, 2016) and the model performance is evaluated with testing datasets of three TDs (TD1, TD2, and TD3), as shown in Table D-3. Both TLS1 and TLS2 transfer the five DNN models, pre-trained on SD, to the target chiller (CH#1, 2016) and, then, fine-tune weights with the training dataset of three TDs (TD1, TD2, and TD3). The difference is TLS1 updated the weights of all the layers of a DNN model, while TLS2 only updated the weights of the output layer of a DNN model. Then, the model performance is evaluated with testing datasets of three TDs (TD1, TD2, and TD3), as shown in Table D-4 and Table D-5.

The *RMSE* values obtained by the four strategies (SelfL, TLS0, TLS1, and TLS2) are compared in Table 9-8. *RMSE* of SelfL for *E* in TD1, *COP* in TD1, and *E* in TD3 are significantly greater than corresponding measurement uncertainty. Over the six *RMSE* values of TLS0 (Table 9-8), three of them are greater than their corresponding measurement uncertainty (e.g., *E* in TD1). Thus, TLS1 and TLS2 perform better than TLS0 and SelfL, as all *RMSE* of TLS1 and TLS2 are smaller than corresponding measurement uncertainty, except for the case of *E* in TD1. One possible explanation for this result with respect to TD1 is the average *E* over the training dataset is a small value (Figure 9-2), which leads to a small value of measurement uncertainty of *E*.

Table 9-8. RMSE of SelfL, TLS0, TLS1, and TLS2 over the testing dataset of three TDs (TD1, TD2, and TD3).

Strategy	Target dataset					
	TD1		TD2		TD3	
	E (*kW*)	*COP* (-)	*E* (*kW*)	*COP* (-)	*E* (*kW*)	*COP* (-)
SelfL	69.71	0.94	19.19	0.37	30.47	0.58
TLS0	23.46	0.54	22.45	0.63	20.87	0.48
TLS1	21.05	0.33	11.82	0.42	11.34	0.28
TLS2	21.06	0.33	11.88	0.41	12.61	0.24
Measurement uncertainty (U_m)	16.50	0.57	20.36	0.59	21.81	0.61

Table 9-9. *CV* of SelfL, TLS0, TLS1, and TLS2 over the testing dataset of three TDs (TD1, TD2, and TD3).

Strategy	Target dataset					
	TD1		TD2		TD3	
	E (%)	*COP*(%)	*E* (%)	*COP*(%)	*E* (%)	*COP*(%)
SelfL	20.48	15.83	6.60	6.51	9.39	9.90
TLS0	6.89	9.11	7.72	11.07	6.43	8.26
TLS1	6.18	5.50	4.07	7.35	3.50	4.76
TLS2	6.35	5.48	4.08	7.18	3.89	4.12

Table 9-10. MAD of SelfL, TLS0, TLS1, and TLS2 over the testing dataset of three TDs (TD1, TD2, and TD3).

Strategy	Target dataset					
	TD1		TD2		TD3	
	E (*kW*)	*COP* (-)	*E* (*kW*)	*COP* (-)	*E* (*kW*)	*COP* (-)
SelfL	49.11	0.69	13.97	0.25	26.65	0.16
TLS0	19.34	0.43	16.22	0.52	15.15	0.41
TLS1	16.13	0.26	8.69	0.29	9.00	0.22
TLS2	16.51	0.25	8.80	0.28	9.56	0.19
Measurement uncertainty (U_m)	16.50	0.57	20.36	0.59	21.81	0.61

The *CV* and *MAD* values obtained by the four strategies (SelfL, TLS0, TLS1, and TLS2) with respect to three target domains (TD1 to TD3) are compared in Table 9-9 and Table 9-10, respectively. Table 9-9 indicates all *CV* values of the four strategies (SelfL, TLS0, TLS1, and TLS2) with respect to three target domains (TD1 to TD3) are far less than the recommended 30% [201]. Besides, *CV* values with respect to TLS1 and TLS2 over three target domains (TD1 to TD3) are less than corresponding values with respect to SelfL and TLS0. The trend observed on Table 9-8 and Table 9-9 is also noticed in Table 9-10. Thus, TLS1 and TLS2 perform better than SelfL and

TLS0 in general in case study #1.

Table 9-11. Summary of comparison of each performance metrics with respect to case study #1.

Performance metrics	Condition		
	TLS1 > TLS2	TLS1 = TLS2	TLS1 < TLS2
RMSE	3	5	7
CV	6	1	8
MAD	5	4	6
Total	14	10	21

Table 9-11 is derived with the comparison of performance metrics (*RMSE*, *CV*, and *MAD*) on three target domains (TD1, TD2, and TD3), resulting from TLS1 and TLS2. For instance, 3 in the second column means three *RMSE* values of DNN models with the application of TLS1 over three TDs of case study #1 are greater than corresponding *RMSE* values with TLS2. Usually, a DNN model with a smaller *RMSE* or *CV* or *MAD* indicates the model performance is better. Therefore, if the condition of TLS1<TLS2 (or TLS1>TLS2) has the largest number in the row of total in Table 9-11, it represents TLS1 (or TLS2) performs better than TLS2 (or TLS1) in general.

The largest number in Table 9-11 is twenty-one with the condition of TLS1<TLS2, which indicates twenty-one *RMSE*, *CV*, and *MAD* values of DNN models applying TLS1 over three target domains (TD1, TD2, and TD3) are smaller than that with respect to TLS2. Thus, TLS1 performs better than TLS2 over case study #2.

9.3.4. Results of transfer learning with respect to case study #2

The five DNN models (*E*, *COP*, T_{cdwl}, ΔT_{chw}, and ΔT_{cdw}), derived with the training dataset of SD, are transferred to the target chiller with three TDs (TD4, TD5, and TD6) by using three TL strategies (TLS0, TLS1, and TLS2). TLS0 directly transfers the five DNN models, trained on SD, to the target chiller (CH#1, 2016) and the model performance is evaluated with testing datasets of three TDs (TD4, TD5, and TD6), as shown in Table D-6. TLS1 and TLS2 transfer the five DNN models, pre-trained on SD, to the target chiller (CH#1, 2016) and, then, fine-tune weights with the training dataset of three TDs (TD4, TD5, and TD6). The difference is TLS1 updated weights of all layers of a DNN model, while TLS2 only updated weights of the output layer of a DNN model. Then, the model performance is evaluated with testing datasets of three TDs (TD4, TD5, and TD6), as shown in Table D-7 and Table D-8.

The *RMSE* values obtained by the four strategies (SelfL, TLS0, TLS1, and TLS2) are compared in Table 9-12. *RMSE* of SelfL for *E* in TD4 and *COP* in TD4 are significantly greater than corresponding measurement uncertainty. Over the six *RMSE* values of TLS0 (Table 9-12), two of them are greater than corresponding measurement uncertainty (e.g., *E* in TD4). For the results of TLS1 or TLS2, only the *RMSE* of *E* in TD4 is greater than the corresponding measurement uncertainty throughout the three target domains (TD4, TD5, and TD6). Thus, TLS1 and TLS2 perform better than TLS0 and SelfL in terms of *RMSE* in case study #2.

Table 9-12. *RMSE* of SelfL, TLS0, TLS1, and TLS2 over the testing datasets of three TDs (TD4, TD5, and TD6) with respect to DNN models of *E* and *COP*.

Strategy	Target dataset					
	TD4		TD5		TD6	
	E (*kW*)	*COP* (-)	*E* (*kW*)	*COP* (-)	*E* (*kW*)	*COP* (-)
SelfL	69.45	0.91	13.92	0.30	20.55	0.34
TLS0	20.81	0.69	19.65	0.69	19.36	0.66
TLS1	18.06	0.39	18.57	0.31	15.67	0.31
TLS2	29.00	0.40	25.77	0.41	16.52	0.29
Measurement uncertainty (U_m)	16.50	0.57	20.36	0.59	23.49	0.67

Table 9-13. *CV* of SelfL, TLS0, TLS1, and TLS2 over the testing datasets of three TDs (TD4, TD5, and TD6) with respect to DNN models of *E* and *COP*.

Strategy	Target dataset					
	TD4		TD5		TD6	
	E (%)	*COP*(%)	*E* (%)	*COP*(%)	*E* (%)	*COP*(%)
SelfL	22.03	15.51	4.49	5.16	6.50	5.78
TLS0	6.60	11.82	6.34	11.81	6.13	11.30
TLS1	5.73	6.70	5.99	5.32	4.96	5.21
TLS2	9.20	6.88	8.31	6.97	5.23	4.94

The *CV* and *MAD* values obtained by the four strategies (SelfL, TLS0, TLS1, and TLS2) with respect to three target domains (TD4 to TD6) are compared in Table 9-13 and Table 9-14, respectively. Table 9-13 indicates all *CV* values of the four strategies (SelfL, TLS0, TLS1, and TLS2) with respect to three target domains (TD4 to TD6) are far less than the recommend 30% [201]. Besides, *CV* values with respect to TLS1 and TLS2 over three target domains (TD1 to TD3) are less than corresponding values with respect to SelfL and TLS0 (Table 9-13). The trend observed on Table 9-12 and Table 9-13 is also noticed in Table 9-14. Thus, TLS1 and TLS2 perform better than SelfL and TLS0 in general in case study #2.

Table 9-14. *MAD* of SelfL, TLS0, TLS1, and TLS2 over the testing datasets of three TDs (TD4, TD5, and TD6) with respect to DNN models of *E* and *COP*.

Strategy	Target dataset					
	TD4		TD5		TD6	
	E (*kW*)	*COP* (-)	*E* (*kW*)	*COP* (-)	*E* (*kW*)	*COP* (-)
SelfL	43.45	0.60	10.23	0.24	15.40	0.27
TLS0	15.85	0.56	14.66	0.56	14.53	0.54
TLS1	16.50	0.57	20.36	0.59	23.49	0.67
TLS2	25.99	0.32	22.91	0.33	11.64	0.23
Measurement uncertainty (U_m)	16.50	0.57	20.36	0.59	23.49	0.67

Table 9-15 is derived with the comparison of performance metrics (*RMSE*, *CV*, and *MAD*) on three target domains (TD4, TD5, and TD6), resulting from TLS1 and TLS2. The largest number in Table 9-15 is twenty-nine with the condition of TLS1<TLS2, which is significantly greater than that with the condition of TLS1>TLS2. The number twenty-nine indicates there are twenty-nine *RMSE*, *CV*, and *MAD* values of DNN models with respect to TLS1 over three target domains (TD1, TD2, and TD3) are smaller than that with respect to TLS2. Therefore, TLS1 performs better than TLS2 over case study #2.

Table 9-15. Summary of comparison of each performance metrics with respect to case study #2.

Performance metrics	Condition		
	TLS1 > TLS2	TLS1 = TLS2	TLS1 < TLS2
RMSE	4	1	10
CV	5	0	10
MAD	4	2	9
Total	13	3	29

9.4. Conclusions of transfer learning

Based on the results of case study #1 and case study #2, one can conclude:

1. TLS1 or TLS2 performs better than TLS0 or SelfL in both case study #1 and case study #2. Updating weights of DNN models with the information of new task helps to improve performance of DNN models over testing dataset of TD.
2. TLS1 (fine-tune weights of all DNN model layers) is the best strategy to conduct TL.
3. Results with respect to case study #2 indicate updating model weights with even very limited data of new task, TL can help to improve the DNN model performance over almost the whole summer.

Such kind of model with TL shows great potentials and feasibility to conduct fault detection.

10. Main contributions and recommendations

10.1. Summary of contributions

This dissertation is a contribution to multiple-dependent faults detection and diagnosis chillers using benchmarking grey-box models along with measurements from a real building. The benchmarking grey-box models for three system-level target variables (E_b, COP_b, and $T_{cdwl.b}$), and two component-level target variables (ΔT_{chw} and ΔT_{cdw}) perform well:

1. Accurately and robustly predict target variables under normal conditions over a short dataset (July 2013) and a long dataset (whole cooling season of 2016),
2. Propagate impacts to target variables due to regressor variables faults, when artificial faults are injected into the dataset. Case study results verify the effectiveness of the forward fault detection approach and the backward fault diagnosis approach.

This dissertation also studied the effectiveness of different transfer learning strategies in improving the performance of DNN models for the prediction of target variables.

Towards the goal of this dissertation, the main contributions are:

1. Present a classification scheme to distinguish individual faults and dependent faults. This classification scheme indicates the intrinsic relationship between regressor variables, and between regressor variable(s) and target variable(s).
2. Present five benchmarking grey-box models to predict target variables with respect to chiller operation. Three grey-box models in simple format, instead of state equations with a complex format, are developed to estimate refrigerant enthalpy with high accuracy at three key positions of a refrigerant cycle.
3. Present a forward fault detection model to detect chiller MDFs, using measurements from BAS of a real building.
4. Present a backward fault diagnosis model to decouple the dependency relationship of target variables and regressor variables, and isolate the fault source successfully.
5. Present a new approach to estimate the prediction uncertainty of a model. Correspondingly, a new method is developed to identify threshold for fault detection, which covers the uncertainty information from both the measurement side and the prediction side.

6. The transfer learning strategy is proved to be a feasible and efficient approach to develop an accurate DNN model for a new task. Initializing the weights of the a new model, based on a previous site, and then update the all the weights based on the secondary site is the best strategy to conduct transfer learning.

10.2. Recommendations for future work

This section summarizes the limitations of MDFDD model, based on which the recommendations for future work are presented.

1. Benchmarking grey-box models, under normal conditions, are verified by measurements, which supports a solid conclusion of accurate and robust models. Though MDFs are detected successfully, whether the model complies well with chiller real responses under faulty conditions is not verified, as measurement data with faults are not available. Future work should focus on designing and conducting chiller experiments with physical faults as recognised by BAS, for the purpose of verifying existing chiller FDD models or developing new models based on needs.
2. The relationship between proper model training and the subsequential application in FDD should be well studied. If a model is underfit or overfit, its performance on detecting or diagnosing faults would be highly affected. Different from prediction/forecasting models dealing with only normal conditions, a reliable model used for FDD should perform well under both the normal condition and the faulty condition (able to generate significant impact on target variables). Further, a perfect model should comply well with the real chiller response to a fault.
3. Although one regressor variable fault (e.g., T_{chwl}) might have impact on other regressors such as V_{chw} or/and $m_{ev,refr,ref}$, this dissertation considers only the significant impact on the target variable (e.g., E). The impact on other regressor variables is neglected. Future work should consider the combined effects.
4. The time interval of BAS recordings is 15 minutes, which is not enough for the fault detection under transient regimes. Thus, the proposed method could miss the impact of shorter-time disturbances. The advanced monitoring system with shorter time steps could be able to capture transient operation characteristics of a chiller. Data collected by such advanced monitoring system could be used to develop FDD models under chiller transient

operations or starting-up/shutting-down periods. The cost-effectiveness of installing a dedicated monitoring system should be compared with the BAS.

5. Literature review finds only one study, ASHRAE project 1043-RP [107], that used data from laboratory experiments of a chiller with faults. However, corresponding experiments were conducted more than twenty years ago, and only limited fault types were investigated. The lack of database with faults is the main barrier restricting the FDD study for HVAC systems. Along with the recent development of intelligent buildings, more faults of new types have emerged. State-of-the-art models should meet new challenges, as a results, more open databases with HVAC system faults are expected in the future work.
6. Benchmarking grey-box models, presented in this dissertation, are easy to be deployed, as they need less data to derive an accurate model (resource-efficient) and are fast to be trained (time-efficient), compared with other general black box models (e.g., deep learning models). As grey-box models usually have a simple format, they are easily to be accepted by the building facility management team. Thus, such models show great potentials to realize the automation of FDD and commercialization of related product/software. Future work can focus on upgrading BAS, by integrating a program with MDFDD model, to realize automatic online FDD.

References

[1] B. Dudley, Spencer Dale, BP statistical review of world energy, 2018.

[2] Statista, (2021). https://www.statista.com/statistics/263455/primary-energy-consumption-of-selected-countries/ (accessed October 7, 2021).

[3] Natural Resources Canada, (2021). https://oee.nrcan.gc.ca/corporate/statistics/neud/dpa/showTable.cfm?type=HB&sector=aaa&juris=ca&rn=2&page=0 (accessed October 6, 2021).

[4] J. Whitmore, P.O. Pineau, The State of Energy in Quebec, Montreal, 2019. https://energie.hec.ca/ (accessed January 28, 2023).

[5] S. Deshmukh, L. Glicksman, L. Norford, Case study results: Fault detection in air-handling units in buildings, Advances in Building Energy Research. 14 (2020) 305–321.

[6] L. Pe, A review on buildings energy consumption information, Energy Build. 40 (2008) 394–398. https://doi.org/10.1016/j.enbuild.2007.03.007.

[7] K.W. Roth, D. Westphalen, P. Llana, M. Feng, The energy impact of faults in US commercial buildings, in: International Refrigeration and Air Conditioning Conference, West Lafayette, USA, 2004.

[8] A.P. Rogers, F. Guo, B.P. Rasmussen, A review of fault detection and diagnosis methods for residential air conditioning systems, Build Environ. 161 (2019) 106236. https://doi.org/10.1016/j.buildenv.2019.106236.

[9] L. Li, H. Luo, S.X. Ding, Y. Yang, K. Peng, Performance-based fault detection and fault-tolerant control for automatic control systems, Automatica. 99 (2019) 308–316.

[10] J. Qu, H. Zhang, G. Zhang, H. Chen, Incipient fault detection of chiller based on improved CVA, in: E3S Web of Conferences, 2021.

[11] R. Suttell, Preventive HVAC maintenance is a good investment, Buildings. 100 (2006) 50–52.

[12] H.B. Gunay, W. Shen, C. Yang, Text-mining building maintenance work orders for component fault frequency, Building Research & Information. 47 (2019) 518–533.

[13] M.C. Comstock, J.E. Braun, E.A. Groll, R. Danks, A survey of common faults for chillers, ASHRAE Trans. 108 PART 1 (2002) 819–825.

[14] S.H. Rich, V. Venkatasubramanian, Causality-based failure-driven learning in diagnostic

expert systems, AIChE Journal. 35 (1989) 943–950. https://doi.org/10.1002/aic.690350607.

[15] V.E. Silva Souza, J. Mylopoulos, Monitoring and diagnosing malicious attacks with autonomic software, Lecture Notes in Computer Science (Including Subseries Lecture Notes in Artificial Intelligence and Lecture Notes in Bioinformatics). 5829 LNCS (2009) 84–98. https://doi.org/10.1007/978-3-642-04840-1_9.

[16] C.P. Atthapol Ngaopitakkul, Chaowat Apisit, Sulee Bunjongjit, Identifying types of simultaneous fault in transmission line using discrete wavelet transform and fuzzy logic algorithm, International Journal of Innovative Computing, Information and Control. 9 (2013) 2701–2712.

[17] S.H. Cho, Y.J. Hong, W.T. Kim, M. Zaheer-Uddin, Multi-fault detection and diagnosis of HVAC systems: An experimental study, Int J Energy Res. 29 (2005) 471–483. https://doi.org/10.1002/er.1065.

[18] William Collins, Collins Online Dictionary, Harper Collins Publishers. (2021). https://www.collinsdictionary.com/.

[19] G. Lee, B. Lee, E.S. Yoon, C. Han, Multiple-fault diagnosis under uncertain conditions by the quantification of qualitative relations, Ind Eng Chem Res. 38 (1999) 988–998. https://doi.org/10.1021/ie980359k.

[20] J. Qin, S. Wang, A fault detection and diagnosis strategy of VAV air-conditioning systems for improved energy and control performances, Energy Build. 37 (2005) 1035–1048. https://doi.org/10.1016/j.enbuild.2004.12.011.

[21] Z. Du, X. Jin, Detection and diagnosis for multiple faults in VAV systems, Energy Build. 39 (2007) 923–934. https://doi.org/10.1016/j.enbuild.2006.09.015.

[22] X. Zhao, Lab test of three fault detection and diagnostic methods’ capability of diagnosing multiple simultaneous faults in chillers, Energy Build. 94 (2015) 43–51. https://doi.org/10.1016/j.enbuild.2015.02.039.

[23] M.S. Breuker, J.E. Braun, Common Faults and Their Impacts for Rooftop Air Conditioners, HVAC&R Res. 4 (1998) 303–318. https://doi.org/10.1080/10789669.1998.10391406.

[24] S. Katipamula, M.R. Brambley, Methods for fault detection, diagnostics, and prognostics for building systems—a review, part I, HVAC and R Research. 11 (2005) 3–25. https://doi.org/10.1080/10789669.2005.10391133.

[25] M.C. Keir, A.G. Alleyne, Dynamic Modeling, Control, and Fault Detection in Vapor

Compression Systems, 61801 (2006). https://www.energy.gov/ (accessed February 2, 2022).

[26] J. Weimer, S.A. Ahmadi, J. Araujo, F.M. Mele, D. Papale, I. Shames, H. Sandberg, K.H. Johansson, Active actuator fault detection and diagnostics in HVAC systems, in: Proceedings of the Fourth ACM Workshop on Embedded Sensing Systems for Energy-Efficiency in Buildings, Toronto Ontario Canada, 2012: pp. 107–114.

[27] Michael G. Mckellar, David R. Tree, Steady State Characteristics of Failures of a Household Refrigerator, in: International Refrigeration and Air Conditioning Conference, West Lafayette, USA, 1988.

[28] N. Fernandez, M.R. Brambley, S. Katipamula, H. Cho, J. Goddard, L. Dinh, Self-Correcting HVAC Controls Project Final Report, 2009.

[29] M.R. Brambley, N. Fernandez, W. Wang, K.A. Cort, H. Cho, H. Ngo, J.K. Goddard, Final Project Report : Self-Correcting Controls for VAV System Faults Filter / Fan / Coil and VAV Box Sections, 2011.

[30] K. Bruton, P. Raftery, P. O’Donovan, N. Aughney, M.M. Keane, D.T.J. O’Sullivan, Development and alpha testing of a cloud based automated fault detection and diagnosis tool for Air Handling Units, Autom Constr. 39 (2014) 70–83.

[31] W. Kim, S. Katipamula, A review of fault detection and diagnostics methods for building systems, Sci Technol Built Environ. 24 (2018) 3–21. https://doi.org/10.1080/23744731.2017.1318008.

[32] ASHRAE, ASHRAE fundamentals (SI), 2017.

[33] D. Zogg, E. Shafai, H.P. Geering, Fault diagnosis for heat pumps with parameter identification and clustering, Control Eng Pract. 14 (2006) 1435–1444. https://doi.org/10.1016/j.conengprac.2005.11.002.

[34] D. Yu, H. Li, Y. Yu, A gray-box based virtual scfm meter in rooftop air-conditioning units, J Therm Sci Eng Appl. 3 (2011) 1–7. https://doi.org/10.1115/1.4003702.

[35] B. Sun, P.B. Luh, Q.S. Jia, Z. O’Neill, F. Song, Building energy doctors: An SPC and Kalman Filter-based method for system-level fault detection in HVAC systems, IEEE Transactions on Automation Science and Engineering. 11 (2014) 215–229. https://doi.org/10.1109/TASE.2012.2226155.

[36] N. Ren, J. Liang, B. Gu, H. Han, Fault diagnosis strategy for incompletely described samples and its application to refrigeration system, Mech Syst Signal Process. 22 (2008)

436–450. https://doi.org/10.1016/j.ymssp.2007.08.004.

[37] B. Chen, J.E. Braun, Simple rule-based methods for fault detection and diagnostics applied to packaged air conditioners/Discussion, ASHRAE Trans. 107 (2001) 847.

[38] N.S. Castro, Performance evaluation of a reciprocating chiller using experimental data and model predictions for fault detection and diagnosis/Discussion, ASHRAE Trans. 108 (2002) 889.

[39] Y. Chen, L. Lan, A fault detection technique for air-source heat pump water chiller/heaters, Energy Build. 41 (2009) 881–887.

[40] O. Morisot, D. Marchio, Fault Detection and Diagnosis on HVAC Variable Air Volume System Using Artificial Neural Networks, in: IBPSA Building Simulation, 1999: p. 1087. http://www.ibpsa.org/proceedings/bs1999/bs99_pb-09.pdf.

[41] M. Kim, S.H. Yoon, W.V. Payne, P.A. Domanski, Cooling mode fault detection and diagnosis method for a residential heat pump, NIST Special Publication. 1087 (2008).

[42] G. Mavromatidis, S. Acha, N. Shah, Diagnostic tools of energy performance for supermarkets using Artificial Neural Network algorithms, Energy Build. 62 (2013) 304–314. https://doi.org/10.1016/j.enbuild.2013.03.020.

[43] Y. Zhao, C. Zhang, Y. Zhang, Z. Wang, J. Li, A review of data mining technologies in building energy systems: Load prediction, pattern identification, fault detection and diagnosis, Energy and Built Environment. 1 (2020) 149–164. https://doi.org/10.1016/j.enbenv.2019.11.003.

[44] Y.J. Park, S.K.S. Fan, C.Y. Hsu, A review on fault detection and process diagnostics in industrial processes, Processes. 8 (2020). https://doi.org/10.3390/PR8091123.

[45] J. Huang, T. Fukuda, T. Matsuno, Model-based intelligent fault detection and diagnosis for mating electric connectors in robotic wiring harness assembly systems, IEEE/ASME Transactions on Mechatronics. 13 (2008) 86–94.

[46] J. Ma, J. Jiang, Applications of fault detection and diagnosis methods in nuclear power plants: A review, Progress in Nuclear Energy. 53 (2011) 255–266.

[47] Y. Yu, D. Woradechjumroen, D. Yu, A review of fault detection and diagnosis methodologies on air-handling units, Energy Build. 82 (2014) 550–562. https://doi.org/10.1016/j.enbuild.2014.06.042.

[48] H. Li, J.E. Braun, A Methodology for Diagnosing Multiple- Simultaneous Faults in Rooftop

Air Conditioners, in: International Refrigeration and Air Conditioning Conference, 2004.

[49] H. Li, A decoupling-based unified fault detection and diagnosis approach for packaged air conditioners, Purdue University, 2004.

[50] H. Li, J.E. Braun, Decoupling features and virtual sensors for diagnosis of faults in vapor compression air conditioners, International Journal of Refrigeration. 30 (2007) 546–564. https://doi.org/10.1016/j.ijrefrig.2006.07.024.

[51] H. Li, J.E. Braun, A methodology for diagnosing multiple simultaneous faults in vapor-compression air conditioners, HVAC&R Res. 13 (2007) 369–395. https://doi.org/10.1080/10789669.2007.10390959.

[52] B.T. Thumati, M.A. Feinstein, J.W. Fonda, A. Turnbull, F.J. Weaver, M.E. Calkins, S. Jagannathan, An online model-based fault diagnosis scheme for HVAC systems, in: Proceedings of the IEEE International Conference on Control Applications, IEEE, 2011: pp. 70–75. https://doi.org/10.1109/CCA.2011.6044486.

[53] B. Argüello-Serrano, M. Vélez-Reyes, Nonlinear control of a heating, ventilating, and air conditioning system with thermal load estimation, IEEE Transactions on Control Systems Technology. 7 (1999) 56–63. https://doi.org/10.1109/87.736752.

[54] B.T. Thumati, S. Jagannathan, A model based fault detection and accommodation scheme for nonlinear discrete-time systems with asymptotic stability guarantee, in: 2009 American Control Conference, 2009: pp. 4988–4993.

[55] A.M. Subramaniam, T. Jain, J.J. Yam, Bilinear model-based diagnosis of lock-in-place failures of variable-air-volume HVAC systems of multizone buildings, Journal of Building Engineering. 28 (2020). https://doi.org/10.1016/j.jobe.2019.101023.

[56] D. Jreijiry, A. Husaunndee, C. Inard, J.G. Villenave, Control of ventilation in buildings using SIMBAD building and HVAC toolbox, in: Proceedings of Building Simulation, 2003: pp. 591–598.

[57] W. Kim, J.E. Braun, Development, implementation, and evaluation of a fault detection and diagnostics system based on integrated virtual sensors and fault impact models, Energy Build. 228 (2020) 110368. https://doi.org/10.1016/j.enbuild.2020.110368.

[58] H. Wang, Y. Chen, A robust fault detection and diagnosis strategy for multiple faults of VAV air handling units, Energy Build. 127 (2016) 442–451. https://doi.org/10.1016/j.enbuild.2016.06.013.

[59] Z. Du, X. Jin, Multiple faults diagnosis for sensors in air handling unit using Fisher discriminant analysis, Energy Convers Manag. 49 (2008) 3654–3665. https://doi.org/10.1016/j.enconman.2008.06.032.

[60] Z. Du, X. Jin, X. Yang, A robot fault diagnostic tool for flow rate sensors in air dampers and VAV terminals, Energy Build. 41 (2009) 279–286. https://doi.org/10.1016/j.enbuild.2008.09.007.

[61] R. Yan, Z. Ma, G. Kokogiannakis, Y. Zhao, A sensor fault detection strategy for air handling units using cluster analysis, Autom Constr. 70 (2016) 77–88.

[62] H. Han, B. Gu, Y. Hong, J. Kang, Automated FDD of multiple-simultaneous faults (MSF) and the application to building chillers, Energy Build. 43 (2011) 2524–2532. https://doi.org/10.1016/j.enbuild.2011.06.011.

[63] H. Han, B. Gu, T. Wang, Z.R. Li, Important sensors for chiller fault detection and diagnosis (FDD) from the perspective of feature selection and machine learning, International Journal of Refrigeration. 34 (2011) 586–599.

[64] H. Shahnazari, P. Mhaskar, J.M. House, T.I. Salsbury, Modeling and fault diagnosis design for HVAC systems using recurrent neural networks, Comput Chem Eng. 126 (2019) 189–203. https://doi.org/10.1016/j.compchemeng.2019.04.011.

[65] M. Elnour, N. Meskin, M. Al-naemi, Sensor data validation and fault diagnosis using Auto-Associative Neural Network for HVAC systems, Journal of Building Engineering. 27 (2020).

[66] H. Wang, Y. Chen, A robust fault detection and diagnosis strategy for multiple faults of VAV air handling units, Energy Build. 127 (2016) 442–451. https://doi.org/10.1016/J.ENBUILD.2016.06.013.

[67] H. Li, J.E. Braun, Decoupling features for diagnosis of reversing and check valve faults in heat pumps, International Journal of Refrigeration. 32 (2009) 316–326.

[68] H.B. Gunay, Z. Shi, G. Newsham, R. Moromisato, Detection of zone sensor and actuator faults through inverse greybox modelling, Build Environ. 171 (2020) 106659. https://doi.org/10.1016/j.buildenv.2020.106659.

[69] J.M. Gordon, K.C. Ng, Thermodynamic modeling of reciprocating chillers, J Appl Phys. 75 (1994) 2769–2774. https://doi.org/10.1063/1.356215.

[70] J.M. Gordon, K.C. Ng, H.T. Chua, Centrifugal chillers: Thermodynamic modelling and a diagnostic case study, International Journal of Refrigeration. 18 (1995) 253–257.

https://doi.org/10.1016/0140-7007(95)96863-2.

[71] T.S. Lee, Thermodynamic modeling and experimental validation of screw liquid chillers, 2004 Winter Meeting - Technical and Symposium Papers, American Society of Heating, Refrigerating and Air-Conditioning Engineers. (2004) 213–222.

[72] J. Saththasivam, K.C. Ng, Predictive and diagnostic methods for centrifugal chillers, ASHRAE Trans. 114 PART 1 (2008) 282–287.

[73] DOE, DOE-2 Reference Manual, Part 1 (Version 2.1A), Group WX-4, Program Support Los Alamos Scientific Laboratory Los Alamos, New Mexico. (1980) 772.

[74] Braun James Edward, Methodologies for the Design and Control of Chilled Water Systems, Doctorial Thesis, University of Wisconsin - Madison, 1988.

[75] F.W.H. Yik, V.K.C. Lam, Chiller models for plant design studies, Building Services Engineering Research and Technology. 19 (1998) 233–241. https://doi.org/10.1177/014362449801900407.

[76] D.J. Swider, A comparison of empirically based steady-state models for vapor-compression liquid chillers, Appl Therm Eng. 23 (2003) 539–556. https://doi.org/10.1016/S1359-4311(02)00242-9.

[77] C.W.H. Chan, Optimizing chiller plant control logic, ASHRAE J. 48 (2006) 38–42.

[78] Engineering Reference — EnergyPlus 8.6, (2011). https://bigladdersoftware.com/epx/docs/8-6/engineering-reference/chillers.html#electric-chiller-model-based-on-fluid-temperature-differences.

[79] D. Monfet, R. Zmeureanu, Ongoing commissioning of water-cooled electric chillers using benchmarking models, Appl Energy. 92 (2012) 99–108. https://doi.org/10.1016/j.apenergy.2011.10.019.

[80] T. Zhao, J. Wang, M. Xu, K. Li, An online predictive control method with the temperature based multi-variable linear regression model for a typical chiller plant system, Build Simul. 12 (2020) 335–348. https://doi.org/10.1007/978-981-13-9524-6_26.

[81] J.M. Gordon, K.C. Ng, Cool thermodynamics: the engineering and physics of predictive, diagnostic and optimization methods for cooling system, Cambridge International Science Publishing, Great Abington, Cambridge, UK, 2001.

[82] K.M. Powell, W.J. Cole, U.F. Ekarika, T.F. Edgar, Optimal chiller loading in a district cooling system with thermal energy storage, Energy. 50 (2013) 445–453.

https://doi.org/10.1016/j.energy.2012.10.058.

[83] W. Gang, J. Wang, Predictive ANN models of ground heat exchanger for the control of hybrid ground source heat pump systems, Appl Energy. 112 (2013) 1146–1153. https://doi.org/10.1016/j.apenergy.2012.12.031.

[84] K.M. Powell, J.S. Kim, W.J. Cole, K. Kapoor, J.L. Mojica, J.D. Hedengren, T.F. Edgar, Thermal energy storage to minimize cost and improve efficiency of a polygeneration district energy system in a real-time electricity market, Energy. 113 (2016) 52–63. https://doi.org/10.1016/j.energy.2016.07.009.

[85] Z. Liu, H. Tan, D. Luo, G. Yu, J. Li, Z. Li, Optimal chiller sequencing control in an office building considering the variation of chiller maximum cooling capacity, Energy Build. 140 (2017) 430–442.

[86] A. Bejan, Advanced engineering thermodynamics, 2nd ed., John Wiley & Sons, Inc., New York, 1998.

[87] Som Shrestha Sagar, Empirical validation of building energy simulation software: EnergyPlus, Master Thesis, Iowa State University, 2006.

[88] M. Padilla, D. Choinière, J.A. Candanedo, D. Choini`, C. Ere, J. Jos´, E.A. Candanedo, A model-based strategy for self-correction of sensor faults in variable air volume air handling units, Sci Technol Built Environ. 21 (2015) 1018–1032. https://doi.org/10.1080/23744731.2015.1025682.

[89] A. Ranade, G. Provan, A. El-Din Mady, D. O'Sullivan, A computationally efficient method for fault diagnosis of fan-coil unit terminals in building Heating Ventilation and Air Conditioning systems, Journal of Building Engineering. 27 (2020) 100955. https://doi.org/10.1016/J.JOBE.2019.100955.

[90] Z. Shi, W. O'Brien, B. Gunay, Building Zone Fault Detection with Kalman Filter based Methods, in: Proceedings of ESim 2016: 9th Conference of IBPSA-Canada, IBPSA Publications, Hamilton, Canada, 2016.

[91] Z. Du, B. Fan, X. Jin, J. Chi, Fault detection and diagnosis for buildings and HVAC systems using combined neural networks and subtractive clustering analysis, Build Environ. 73 (2014) 1–11.

[92] F. Boem, R. Reci, A. Cenedese, T. Parisini, Distributed Clustering-based Sensor Fault Diagnosis for HVAC Systems, IFAC-PapersOnLine. 50 (2017) 4197–4202.

https://doi.org/10.1016/J.IFACOL.2017.08.811.

[93] Z. Hou, Z. Lian, Y. Yao, X. Yuan, Data mining based sensor fault diagnosis and validation for building air conditioning system, Energy Convers Manag. 47 (2006) 2479–2490. https://doi.org/10.1016/J.ENCONMAN.2005.11.010.

[94] P.M. Papadopoulos, V. Reppa, Distributed Adaptive Estimation Scheme for Isolation of Sensor Faults in Multi- zone HVAC Systems Distributed Adaptive Estimation Scheme for Isolation of Sensor Faults in Multi-zone HVAC Systems, IFAC-Papers OnLine. 48 (2015) 1146–1151. https://doi.org/10.1016/j.ifacol.2015.09.681.

[95] X. Zhao, M. Yang, H. Li, Decoupling features for fault detection and diagnosis on centrifugal chillers (1486-RP), HVAC&R Res. 17 (2011) 86–106. https://doi.org/10.1080/10789669.2011.543254.

[96] H. Han, B. Gu, Y. Hong, J. Kang, Automated FDD of multiple-simultaneous faults (MSF) and the application to building chillers, Energy Build. 43 (2011) 2524–2532. https://doi.org/10.1016/J.ENBUILD.2011.06.011.

[97] Y. Zhao, F. Xiao, S. Wang, An intelligent chiller fault detection and diagnosis methodology using Bayesian belief network, Energy Build. 57 (2013) 278–288. https://doi.org/10.1016/J.ENBUILD.2012.11.007.

[98] Y. Fan, X. Cui, H. Han, H. Lu, Chiller fault diagnosis with field sensors using the technology of imbalanced data, Appl Therm Eng. 159 (2019) 113933. https://doi.org/10.1016/J.APPLTHERMALENG.2019.113933.

[99] W. Yao, D. Li, L. Gao, Fault detection and diagnosis using tree-based ensemble learning methods and multivariate control charts for centrifugal chillers, Journal of Building Engineering. 51 (2022) 104243. https://doi.org/10.1016/J.JOBE.2022.104243.

[100] M. Bonvini, M.D. Sohn, J. Granderson, M. Wetter, M.A. Piette, Robust on-line fault detection diagnosis for HVAC components based on nonlinear state estimation techniques, Appl Energy. 124 (2014) 156–166. https://doi.org/10.1016/J.APENERGY.2014.03.009.

[101] A. Beghi, R. Brignoli, L. Cecchinato, G. Menegazzo, M. Rampazzo, A data-driven approach for fault diagnosis in HVAC chiller systems, 2015 IEEE Conference on Control and Applications, CCA 2015 - Proceedings. (2015) 966–971. https://doi.org/10.1109/CCA.2015.7320737.

[102] A. Beghi, R. Brignoli, L. Cecchinato, G. Menegazzo, M. Rampazzo, F. Simmini, Data-

driven Fault Detection and Diagnosis for HVAC water chillers, Control Eng Pract. 53 (2016) 79–91. https://doi.org/10.1016/J.CONENGPRAC.2016.04.018.

[103] B. Sun, P.B. Luh, Q.S. Jia, Z. O'Neill, F. Song, Building energy doctors: An SPC and Kalman Filter-based method for system-level fault detection in HVAC systems, IEEE Transactions on Automation Science and Engineering. 11 (2014) 215–229. https://doi.org/10.1109/TASE.2012.2226155.

[104] J. Huang, H. Yoon, O. Pradhan, T. Wu, J. Wen, Z. O'Neill, K.S. Candan, A Cosine-based Correlation Information Entropy Approach for Building Automatic Fault Detection Baseline Construction, Sci Technol Built Environ. (2022) 1–16. https://doi.org/10.1080/23744731.2022.2080110.

[105] T. Mulumba, A. Afshari, K. Yan, W. Shen, L.K. Norford, Robust model-based fault diagnosis for air handling units, Energy Build. 86 (2015) 698–707. https://doi.org/10.1016/J.ENBUILD.2014.10.069.

[106] B. Bezyan, R. Zmeureanu, Detection and Diagnosis of Dependent Faults That Trigger False Symptoms of Heating and Mechanical Ventilation Systems Using Combined Machine Learning and Rule-Based Techniques, Energies 2022, Vol. 15, Page 1691. 15 (2022) 1691. https://doi.org/10.3390/EN15051691.

[107] B. Satyam, James E. Rraun, DEVELOPMENT AND VALIDATION OF A MECHANISTIC, DYNAMIC MODEL FOR A VAPOR COMPRESSION CENTRIFUGAL LIQUID CHILLER (ASHRAE Project 1043-RP), 2002.

[108] Behrad Bezyan, Detection and diagnosis of multiple dependent faults in HVAC systems using machine learning techniques, Concordia University, 2022.

[109] K.H. Ng, F.W.H. Yik, P. Lee, K.K.Y. Lee, D.C.H. Chan, Bayesian method for HVAC plant sensor fault detection and diagnosis, Energy Build. 228 (2020). https://doi.org/10.1016/j.enbuild.2020.110476.

[110] C. Matthew, E.B. James, A.F. Eckhard, A survey of common faults for chillers, ASHRAE Trans. 108 (2002) 819–825.

[111] J. Chen, L. Zhang, Y. Li, Y. Shi, X. Gao, Y.H.-R. and Sustainable, undefined 2022, A review of computing-based automated fault detection and diagnosis of heating, ventilation and air conditioning systems, Elsevier. (n.d.). https://www.sciencedirect.com/science/article/pii/S1364032122003057 (accessed June 15,

2022).

[112] H. Dou, R. Zmeureanu, Evidence-based assessment of energy performance of two large centrifugal chillers over nine cooling seasons, Sci Technol Built Environ. 27 (2021) 1243–1255. https://doi.org/10.1080/23744731.2021.1931437.

[113] R. and A.E. American Society of Heating, ASHRAE Handbook - HVAC Applications, chapter 38, Atlanta, USA, 2019.

[114] D.E. Blahnik, R.F. Klein, Aging Assessment of Essential HVAC Chillers Used in Nuclear Power Plants, Office of Nuclear Regulatory Research, U.S. Nuclear Regulatory Commission. 1 (1993).

[115] D. Monfet, R. Zmeureanu, Ongoing commissioning approach for a central cooling and heating plant, ASHRAE Trans. 117 (2011) 908–924.

[116] Guideline 2-2010: Engineering Analysis of Experimental Data, American Society of Heating, Refrigerating and Air-Conditioning Engineers, Inc.: Atlanta, GA, USA. (2010).

[117] T.A. Reddy, Applied Data Analysis and Modeling for Energy Engineers and Scientists, Springer, New York, USA, 2011.

[118] Ronald E. Walpole, Raymond H. Myers, Sharon L. Myers, Keying Ye, Probability & Statistics for Engineers & Scientists, 9th ed., Pearson Education, Inc., Boston, 2010.

[119] F.W. Yu, W.T. Ho, Assessing operating statuses for chiller system with Cox regression, International Journal of Refrigeration. 98 (2019) 182–193. https://doi.org/10.1016/j.ijrefrig.2018.10.028.

[120] F.W.H. Yik, S.H. Lee, J.H.K. Lai, K.T. Chan, Experience of using a chilled water circuit design to expedite in site chiller performance measurement, Building Services Engineering Research and Technology. 31 (2010) 279–300. https://doi.org/10.1177/0143624410370171.

[121] E. Fabrizio, M. Filippi, J. Virgone, An hourly modelling framework for the assessment of energy sources exploitation and energy converters selection and sizing in buildings, Energy Build. 41 (2009) 1037–1050. https://doi.org/10.1016/j.enbuild.2009.05.005.

[122] ACRG, (2021). http://www.air-conditioning-and-refrigeration-guide.com/ (accessed September 6, 2021).

[123] CheckMyChiller.com, (2021). https://checkmychiller.com/content/public/help.php (accessed September 6, 2021).

[124] D. Monfet, R. Zmeureanu, CALIBRATION OF AN ENERGYPLUS CENTRAL

COOLING PLANT MODEL WITH MEASUREMENTS AND INTER-PROGRAM COMPARISON, in: Proceedings of BS2013: 13th Conference of International Building Performance Simulation Association, IBPSA publications, Chambery, France, 2013. https://www.simeb.ca:8443/index_fr.jsp.

[125] S.J. Pan, Q. Yang, A survey on transfer learning, IEEE Trans Knowl Data Eng. 22 (2009) 1345–1359.

[126] F. Qian, W. Gao, Y. Yang, D. Yu, Potential analysis of the transfer learning model in short and medium-term forecasting of building HVAC energy consumption, Energy. 193 (2020).

[127] C. Fan, Y. Sun, F. Xiao, J. Ma, D. Lee, J. Wang, Y.C. Tseng, Statistical investigations of transfer learning-based methodology for short-term building energy predictions, Appl Energy. 262 (2020) 114499.

[128] Y.-D. Ko, C.-S. Park, Parameter estimation of unknown properties using transfer learning from virtual to existing buildings, J Build Perform Simul. 14 (2021) 503–514.

[129] X. Zhu, K. Chen, B. Anduv, X. Jin, Z. Du, Transfer learning based methodology for migration and application of fault detection and diagnosis between building chillers for improving energy efficiency, Build Environ. 200 (2021) 107957.

[130] J. Han, J. Pei, M. Kamber, Data mining: concepts and techniques, Elsevier, 2011.

[131] Environment Canada, (2021). https://weather.gc.ca/canada_e.html (accessed March 20, 2021).

[132] J. Runge, Short-term forecasting for the electrical demand of Heating , Ventilation , and Air Conditioning systems, 2021.

[133] H. Li, D. Yu, J.E. Braun, A review of virtual sensing technology and application in building systems, HVAC&R Res. 17 (2011) 619–645. https://doi.org/10.1080/10789669.2011.573051.

[134] Woohyun Kim, Fault Detection and Diagnosis for Air Conditioners and Heat Pumps based on Virtual Sensors, Doctorial thesis, Purdue University, 2013.

[135] Jebaraj Vasudevan, TRAINING AND EVALUATION OF VIRTUAL SENSORS FOR ROOFTOP UNITS, Master thesis, Purdue University, 2015.

[136] W. Kim, J.E. Braun, Development and evaluation of virtual refrigerant mass flow sensors for fault detection and diagnostics, 2015. http://www.elsevier.com/open-access/userlicense/1.0/.

[137] 2016 ASHRARE Handbook- HVAC system and Equipment (SI Edition), 2016.

[138] M.C. Comstock, J.E. Braun, E.A. Groll, The sensitivity of chiller performance to common faults, HVAC and R Research. 7 (2001) 263–279. https://doi.org/10.1080/10789669.2001.10391274.

[139] T.L. Bergman, F.P. Incropera, D.P. DeWitt, A.S. Lavine, Fundamentals of heat and mass transfer, Sixth edit, John Wiley \& Sons, 2006.

[140] M. Kind, H. Martin, P. Stephan, W. Roetzel, B. Spang, H. Müller-Steinhagen, others, VDI Heat Atlas, Second edi, Springer, 2010.

[141] E. Mcdonald, R. Zmeureanu, Virtual flow meter for chilled and condenser water for chillers: Estimates versus measurements, Sci Technol Built Environ. 22 (2016) 178–188. https://doi.org/10.1080/23744731.2015.1085279.

[142] E. McDonald, R. Zmeureanu, Virtual flow meter to estimate the water flow rates in chillers, ASHRAE Conference-Papers. 120 (2014) 200–208.

[143] B.A. Younglove, M.O. Mclinden, An International Standard Equation of State for the Thermodynamic Properties of Refrigerant 123 (2,2-Dichloro-1,1,1-Trifluoroethane), J Phys Chem Ref Data. 23 (1994) 731–779. https://doi.org/10.1063/1.555950.

[144] National Institute of Standards and Technology, NIST Chemistry WebBook, SRD 69, (2021). https://webbook.nist.gov/ (accessed May 22, 2021).

[145] Reference Fluid Thermodynamic and Transport Properties Database (REFPROP), (2022). https://www.nist.gov/programs-projects/reference-fluid-thermodynamic-and-transport-properties-database-refprop#:~:text=The%20NIST%20REFPROP%20database%20provides,fluid%20mixtures%2C%20including%20accepted%20standards. (accessed February 7, 2022).

[146] M. D. McKay, Evaluating prediction uncertainty NUREG/CR - 6311, Santa Fe, New Mexico, USA, 1995. https://inis.iaea.org/search/search.aspx?orig_q=RN:26051087 (accessed August 2, 2022).

[147] M. Kuhn, K. Johnson, Feature Engineering and Selection, 2019. https://doi.org/10.1201/9781315108230.

[148] P. de B. Harrington, Multiple Versus Single Set Validation of Multivariate Models to Avoid Mistakes, Crit Rev Anal Chem. 48 (2018) 33–46. https://doi.org/10.1080/10408347.2017.1361314/SUPPL_FILE/BATC_A_1361314_SM74

05.DOCX.

[149] M.D.S. Ahamed, R. Zmeureanu, N. Cortrufo, J. Candanedo, Gray-box virtual sensor of the supply air temperature of air handling units, Sci Technol Built Environ. 26 (2020) 1151–1162.

[150] Jason Runge, Short-term forecasting for the electrical demand of Heating, Ventilation, and Air Conditioning systems, Doctorial Thesis, Concordia University, 2021.

[151] B. Villadsen, M.J. Vilbert, D. Harris, A. Lawrence Kolbe, Financial Asset Pricing Principles, Risk and Return for Regulated Industries. (2017) 35–50. https://doi.org/10.1016/B978-0-12-812587-8.00003-4.

[152] Will Kenton, Robust, (2022). https://www.investopedia.com/terms/r/robust.asp#:~:text=A%20model%20is%20considered%20to,changed%20due%20to%20unforeseen%20circumstances. (accessed May 15, 2022).

[153] Christopher. Chatfield, Time-series forecasting, Chapman & Hall/CRC, 2001.

[154] Vijay Kotu, Bala Deshpande, Data Science Concepts and Practice, Second, ELSEVIER, 2019.

[155] H. Han, B. Gu, J. Kang, Z.R. Li, Study on a hybrid SVM model for chiller FDD applications, Appl Therm Eng. 31 (2011) 582–592.

[156] W.S. Yun, W.H. Hong, H. Seo, A data-driven fault detection and diagnosis scheme for air handling units in building HVAC systems considering undefined states, Journal of Building Engineering. 35 (2021) 102111. https://doi.org/10.1016/J.JOBE.2020.102111.

[157] R. Rabbany, Applied Machine Learning Some core concepts, Montreal, Canada, 2021. http://www.reirab.com/Teaching/AML21/coreConcepts.pdf (accessed January 22, 2022).

[158] H. Han, B. Gu, T. Wang, Z.R. Li, Important sensors for chiller fault detection and diagnosis (FDD) from the perspective of feature selection and machine learning, International Journal of Refrigeration. 34 (2011) 586–599. https://doi.org/10.1016/J.IJREFRIG.2010.08.011.

[159] D. Lee, C.W. Lai, K.K. Liao, J.W. Chang, Artificial intelligence assisted false alarm detection and diagnosis system development for reducing maintenance cost of chillers at the data centre, Journal of Building Engineering. 36 (2021) 102110. https://doi.org/10.1016/J.JOBE.2020.102110.

[160] Guido van Rossum, Python Release Python 3.9.12 | Python.org, (2022).

https://www.python.org/ (accessed August 31, 2022).

[161] Scikit-Learn machine learning in Python - Scikit-Learn 1.1.2 Documentation, (2022). https://scikit-learn.org/stable/ (accessed January 28, 2023).

[162] D.L.J. Alexander, A. Tropsha, D.A. Winkler, Beware of R2: simple, unambiguous assessment of the prediction accuracy of QSAR and QSPR models, J Chem Inf Model. 55 (2015) 1316–1322.

[163] Y. Sun, H. Xue, W. Wang, S. Wu, Y. Wu, Y. Hong, S. Deng, Development of an optimal control method of chilled water temperature for constant-speed air-cooled water chiller air conditioning systems, Appl Therm Eng. 180 (2020) 115802. https://doi.org/10.1016/J.APPLTHERMALENG.2020.115802.

[164] B.C. Ahn, J.W. Mitchell, Optimal control development for chilled water plants using a quadratic representation, Energy Build. 33 (2001) 371–378. https://doi.org/10.1016/S0378-7788(00)00119-5.

[165] L. Wang, E.W.M. Lee, R.K.K. Yuen, A practical approach to chiller plants' optimisation, Energy Build. 169 (2018) 332–343. https://doi.org/10.1016/J.ENBUILD.2018.03.076.

[166] R. MacCallum, Specification Searches in Covariance Structure Modeling, Psychol Bull. 100 (1986) 107–120. https://doi.org/10.1037/0033-2909.100.1.107.

[167] Y.T. Chae, R. Horesh, Y. Hwang, Y.M. Lee, Artificial neural network model for forecasting sub-hourly electricity usage in commercial buildings, Energy Build. 111 (2016) 184–194. https://doi.org/10.1016/J.ENBUILD.2015.11.045.

[168] Vijay Kotu, Bala Deshpande, Data Science Concepts and Practice, Second, ELSEVIER， Morgan Kaufmann, Cambridge, MA 02139, United States, 2019.

[169] J. Yang, H. Rivard, R. Zmeureanu, On-line building energy prediction using adaptive artificial neural networks, Energy Build. 37 (2005) 1250–1259. https://doi.org/10.1016/j.enbuild.2005.02.005.

[170] J. Yang, H. Rivard, R. Zmeureanu, BUILDING ENERGY PREDICTION WITH ADAPTIVE ARTIFICIAL NEURAL NETWORKS, in: Ninth International IBPSA Conference, Montreal, 2005. https://citeseerx.ist.psu.edu/viewdoc/download?doi=10.1.1.545.5698&rep=rep1&type=pdf (accessed August 9, 2022).

[171] Y. Li, H. Hu, G. Zhou, Using Data Augmentation in Continuous Authentication on

Smartphones, IEEE Internet Things J. 6 (2019) 628–640. https://doi.org/10.1109/JIOT.2018.2851185.

[172] F. Zhuang, Z. Qi, K. Duan, D. Xi, Y. Zhu, H. Zhu, H. Xiong, Q. He, A comprehensive survey on transfer learning, Proceedings of the IEEE. 109 (2020) 43–76.

[173] F. Zhuang, P. Luo, S.J. Pan, H. Xiong, Q. He, Ensemble of anchor adapters for transfer learning, in: Proceedings of the 25th ACM International on Conference on Information and Knowledge Management, 2016: pp. 2335–2340.

[174] F. Zhuang, X. Cheng, P. Luo, S.J. Pan, Q. He, Supervised representation learning with double encoding-layer autoencoder for transfer learning, ACM Transactions on Intelligent Systems and Technology (TIST). 9 (2017) 1–17.

[175] F. Zhuang, P. Luo, H. Xiong, Q. He, Y. Xiong, Z. Shi, Exploiting associations between word clusters and document classes for cross-domain text categorization, Statistical Analysis and Data Mining: The ASA Data Science Journal. 4 (2011) 100–114.

[176] F. Zhuang, P. Luo, C. Du, Q. He, Z. Shi, H. Xiong, Triplex transfer learning: Exploiting both shared and distinct concepts for text classification, IEEE Trans Cybern. 44 (2013) 1191–1203.

[177] T. Tommasi, B. Caputo, The more you know, the less you learn: from knowledge transfer to one-shot learning of object categories, in: BMVC, 2009.

[178] J. Gao, W. Fan, J. Jiang, J. Han, Knowledge transfer via multiple model local structure mapping, in: Proceedings of the 14th ACM SIGKDD International Conference on Knowledge Discovery and Data Mining, 2008: pp. 283–291.

[179] C.P. Dowling, B. Zhang, Transfer Learning for HVAC System Fault Detection, Proceedings of the American Control Conference. 2020-July (2020) 3879–3885. https://doi.org/10.23919/ACC45564.2020.9147772.

[180] I. Goodfellow, Y. Bengio, A. Courville, Deep Learning, MIT press, 2016.

[181] M. Benedetti, V. Cesarotti, V. Introna, J. Serranti, Energy consumption control automation using Artificial Neural Networks and adaptive algorithms: Proposal of a new methodology and case study, Appl Energy. 165 (2016) 60–71. https://doi.org/10.1016/j.apenergy.2015.12.066.

[182] K.-P. Lee, B.-H. Wu, S.-L. Peng, Deep-learning-based fault detection and diagnosis of air-handling units, Build Environ. 157 (2019) 24–33.

[183] A.J. Khalil, A.M. Barhoom, B.S. Abu-Nasser, M.M. Musleh, S.S. Abu-Naser, Energy Efficiency Prediction using Artificial Neural Network, International Journal of Academic Pedagogical Research. 3 (2019) 1–7. https://philpapers.org/rec/KHAEEP (accessed October 31, 2022).

[184] Mohamed Issam Ayadi, Abderrahim Maizate, Mohamed Ouzzif, Charif Mahmoudi, Deep Learning in Building Management Systems over NDN: use case of Forwarding & HVAC Control, in: 2019 International Conference on Internet of Things (iThings) and IEEE Green Computing and Communications (GreenCom) and IEEE Cyber, Physical and Social Computing (CPSCom) and IEEE Smart Data (SmartData), 2019: pp. 1192–1198. https://ieeexplore.ieee.org/stamp/stamp.jsp?tp=&arnumber=8875410 (accessed October 31, 2022).

[185] Y. Chen, Z. Tong, Y. Zheng, H. Samuelson, L. Norford, Transfer learning with deep neural networks for model predictive control of HVAC and natural ventilation in smart buildings, J Clean Prod. 254 (2020) 119866. https://doi.org/10.1016/J.JCLEPRO.2019.119866.

[186] U. Ali, M.H. Shamsi, M. Bohacek, K. Purcell, C. Hoare, E. Mangina, J. O'Donnell, A data-driven approach for multi-scale GIS-based building energy modeling for analysis, planning and support decision making, Appl Energy. 279 (2020) 115834. https://doi.org/10.1016/J.APENERGY.2020.115834.

[187] H. Park, D.Y. Park, Comparative analysis on predictability of natural ventilation rate based on machine learning algorithms, Build Environ. 195 (2021) 107744. https://doi.org/10.1016/J.BUILDENV.2021.107744.

[188] M. Esrafilian-Najafabadi, F. Haghighat, Occupancy-based HVAC control using deep learning algorithms for estimating online preconditioning time in residential buildings, Energy Build. 252 (2021) 111377. https://doi.org/10.1016/J.ENBUILD.2021.111377.

[189] A.A. Al-Shargabi, A. Almhafdy, D.M. Ibrahim, M. Alghieth, F. Chiclana, Tuning Deep Neural Networks for Predicting Energy Consumption in Arid Climate Based on Buildings Characteristics, Sustainability 2021, Vol. 13, Page 12442. 13 (2021) 12442. https://doi.org/10.3390/SU132212442.

[190] R. Olu-Ajayi, H. Alaka, I. Sulaimon, F. Sunmola, S. Ajayi, Building energy consumption prediction for residential buildings using deep learning and other machine learning techniques, Journal of Building Engineering. 45 (2022) 103406.

https://doi.org/10.1016/J.JOBE.2021.103406.

[191] M. Wang, Z. Wang, Y. Geng, B. Lin, Interpreting the neural network model for HVAC system energy data mining, Build Environ. 209 (2022) 108449. https://doi.org/10.1016/J.BUILDENV.2021.108449.

[192] Laurene Fausett, Fundamentals of Neural Networks: Architectures, Algorithms and Applications, 1st ed., Pearson, 1993.

[193] Google, TensorFlow, (2022). https://www.tensorflow.org/ (accessed December 1, 2022).

[194] V. Nair, G.E. Hinton, Rectified Linear Units Improve Restricted Boltzmann Machines, in: The 27th International Conference on Machine Learning, Haifa, Israel, 2010. file:///C:/Users/umroot/OneDrive%20-%20Concordia%20University%20-%20Canada/Desktop/432.pdf (accessed January 19, 2023).

[195] D. Hendrycks, K. Gimpel, Gaussian Error Linear Units (GELUs), 2016. http://arxiv.org/abs/1606.08415.

[196] P. Ramachandran, B. Zoph, Q. Le, Searching for Activation Functions, 2017. https://doi.org/https://doi.org/10.48550/arXiv.1710.05941.

[197] G. Klambauer, T. Unterthiner, A. Mayr, S. Hochreiter, Self-Normalizing Neural Networks, in: 31st Conference on Neural Information Processing Systems, Long Beach, CA, USA, 2017.

[198] S.I. Amari, Backpropagation and stochastic gradient descent method, Neurocomputing. 5 (1993) 185–196.

[199] I. Sutskever, J. Martens, G. Dahl, G. Hinton, On the importance of initialization and momentum in deep learning, in: Proceedings of the 30th International Conference on Machine Learning, Atlanta, Georgia, USA, 2013.

[200] Jason Brownlee, Machine Learning Mastery - Deep Learning Performance, (2019). https://machinelearningmastery.com/how-to-choose-loss-functions-when-training-deep-learning-neural-networks/#:~:text=This%20requires%20the%20choice%20of,loss%20on%20the%20next%20evaluation. (accessed January 20, 2023).

[201] Guideline 14-2014: measurement of energy and demand savings, American Society of Heating, Refrigerating and Air-Conditioning Engineers. (2014).

[202] L.G.R. Santos, A. Afshari, L.K. Norford, J. Mao, Evaluating approaches for district-wide

energy model calibration considering the Urban Heat Island effect, Appl Energy. 215 (2018) 31–40. https://doi.org/10.1016/j.apenergy.2018.01.089.

[203] R.E. Hedegaard, M.H. Kristensen, T.H. Pedersen, A. Brun, S. Petersen, Bottom-up modelling methodology for urban-scale analysis of residential space heating demand response, Appl Energy. 242 (2019) 181–204. https://doi.org/10.1016/J.APENERGY.2019.03.063.

[204] Y.Q. Ang, Z.M. Berzolla, C.F. Reinhart, From concept to application: A review of use cases in urban building energy modeling, Appl Energy. 279 (2020) 115738. https://doi.org/10.1016/J.APENERGY.2020.115738.

[205] A. O' Donovan, P.D. O' Sullivan, M.D. Murphy, Predicting air temperatures in a naturally ventilated nearly zero energy building: Calibration, validation, analysis and approaches, Appl Energy. 250 (2019) 991–1010. https://doi.org/10.1016/j.apenergy.2019.04.082.

Appendix A: Uncertainty estimation of direct and derived measurements

For the measurement uncertainty of derived variables and direct variables in this dissertation, they are listed here:

$$BU_E = \bar{E} \times 0.05 \tag{A14}$$

$$BU_{T_{ev}} = \overline{T_{ev}} \times 0.005 + 0.3 \tag{A15}$$

$$BU_{T_{cd}} = \overline{T_{cd}} \times 0.005 + 0.3 \tag{A16}$$

$$U_{T_{suc}} = U_{T_{ev}} \tag{A17}$$

$$\frac{U_{T_{dis}}}{\overline{T_{dis}}} = \sqrt{(\frac{U_{T_{suc}}}{\overline{T_{suc}}})^2 + (\frac{U_{P_{ev}}}{\overline{P_{ev}}})^2 + (\frac{U_{P_{cd}}}{\overline{P_{cd}}})^2} \tag{A18}$$

$$U_{T_{ll}} = U_{T_{cd}} \tag{A19}$$

$$\frac{U_{Q_{ev,chw}}}{\overline{Q_{ev,chw}}} = \sqrt{(\frac{U_{T_{chwr}}}{\overline{T_{chwr}}})^2 + (\frac{U_{T_{chwl}}}{\overline{T_{chwl}}})^2 + (\frac{U_{V_{chw}}}{\overline{V_{chw}}})^2} \tag{A20}$$

$$\frac{U_{COP}}{\overline{COP}} = \sqrt{(\frac{U_{Q_{ev,chw}}}{\overline{Q_{ev,chw}}})^2 + (\frac{U_E}{\bar{E}})^2} \tag{A21}$$

$$\frac{U_{h_{suc}}}{\overline{h_{suc}}} = \sqrt{(\frac{U_{T_{suc}}}{\overline{T_{suc}}})^2 + (\frac{U_{P_{ev}}}{\overline{P_{ev}}})^2} \tag{A22}$$

$$\frac{U_{h_{dis}}}{\overline{h_{dis}}} = \sqrt{(\frac{U_{T_{dis}}}{\overline{T_{dis}}})^2 + (\frac{U_{P_{cd}}}{\overline{P_{cd}}})^2} \tag{A23}$$

$$\frac{U_{h_{ll}}}{\overline{h_{ll}}} = \sqrt{(\frac{U_{T_{ll}}}{\overline{T_{ll}}})^2 + (\frac{U_{P_{cd}}}{\overline{P_{cd}}})^2} \tag{A24}$$

$$\frac{U_{T_{dis}}}{\overline{T_{dis}}} = \sqrt{(\frac{U_{T_{suc}}}{\overline{T_{suc}}})^2 + (\frac{U_{P_{ev}}}{\overline{P_{ev}}})^2 + (\frac{U_{P_{cd}}}{\overline{P_{cd}}})^2} \tag{A25}$$

$$U_{\Delta T_{cdw}} = \sqrt{(U_{T_{cdwr}})^2 + (U_{T_{cdwl}})^2} \tag{A26}$$

$$U_{T_{cd,appr}} = \sqrt{(U_{T_{cd}})^2 + (U_{T_{cdwl}})^2} \tag{A27}$$

$$U_{T_{ev,appr}} = \sqrt{(U_{T_{ev}})^2 + (U_{T_{chwl}})^2} \tag{A28}$$

Where the symbol with '‾', above a variable, represents the mean value if this variable.

Appendix B: Direct and derived measurements with measurement uncertainty of summers of 2009 to 2017 under the three scenarios

Table B1. Weakly values (mean ± uncertainty) of direct and derived measurements from the operation of chiller CH#1 (scenario 1) over 10 weeks, from June 22 to August 28, 2016

Week	T_{chwl}, ℃	T_{chwr}, ℃	V_{chw}, *L/s*	*E*, *kW*	$Q_{ev,chw}$, *kW*	*COP*
4	6.88±0.33	11.28±0.39	86.52±4.33	276.5±16.1	1589.7±123.8	5.75±0.56
5	6.88±0.33	11.28±0.39	87.25±4.37	277.4±16.2	1607.5±125.0	5.79±0.56
6	6.87±0.33	11.33±0.39	87.96±4.40	281.49±16.4	1638.8±127.4	5.82±0.57
7	6.86±0.33	11.53±0.39	87.32±4.37	286.2±16.4	1700.7±131.9	5.94±0.57
8	6.85±0.33	11.47±0.39	87.88±4.40	280.1±16.7	1691.4±131.5	5.87±0.57
9	6.88±0.33	11.79±0.38	87.68±4.39	303.1±17.1	1792.1±138.0	5.91±0.56
10	6.91±0.34	11.94±0.39	88.14±4.41	310.3±17.5	1842.1±141.5	5.94±0.57
11	6.88±0.33	11.94±0.40	87.81±4.39	314.9±18.4	1849.4±142.8	5.87±0.57
12	6.92±0.34	12.08±0.40	89.00±4.46	330.7±19.7	1916.0±147.9	5.79±0.60
13	6.86±0.33	11.29±0.39	87.62±4.39	278.0±16.0	1621.6±126.2	5.83±0.60

Table B2. Direct and derived measurements of summers of 2009 to 2017 from the operation of chiller CH#1 (scenario 1)

Year	T_{chwl}, ℃	T_{chwr}, ℃	V_{chw}, *L/s*	*E*, *kW*	$Q_{ev,chw}$, *kW*	*COP*
2009	7.07±0.34	11.84±0.39	82.58±4.15	324.1±18.6	1658.0±126.7	5.09±0.49
2010	6.99±0.34	11.5±0.39	84.91±4.25	303.1±17.2	1591.6±122.4	5.22±0.5
2011	N/A	N/A	N/A	N/A	N/A	N/A
2012	6.86±0.33	11.6±0.4	87.78±4.39	325.1±19.1	1733.1±135.0	5.33±0.52
2013	6.84±0.34	10.92±0.4	88.31±4.42	290.0±17.7	1505.7±119.2	5.15±0.51
2014	6.83±0.33	10.99±0.39	88.72±4.44	299.8±17.3	1540.3±120.5	5.12±0.50
2015	7.12±0.34	12.31±0.42	89.68±4.49	340.1±20.5	1948.5±150.5	5.71±0.56
2016	6.88±0.33	11.56±0.39	87.7±4.39	293.1±17.0	1714.5±132.8	5.85±0.57
2017	6.69±0.33	10.77±0.39	85.79±4.3	255.0±15.4	1468.2±116.8	5.75±0.57

Table B3. Direct and derived measurements of summers of 2009 to 2017 from the operation of chiller CH#2 (scenario 2)

Year	T_{chwl}, ℃	T_{chwr}, ℃	V_{chw}, L/s	E, kW	$Q_{ev,chw}$, kW	COP
2009	7.22±0.34	11.30±0.38	84.66±4.27	300.0±17.6	1460.0±111.7	4.83±0.47
2010	7.16±0.34	11.32±0.38	87.47±4.38	297.9±16.9	1521.6±116.2	5.09±0.49
2011	7.02±0.34	11.36±0.38	88.46±4.43	294.4±16.5	1530.2±116.4	5.19±0.49
2012	7.26±0.34	11.63±0.04	90.83±4.55	311.4±18.3	1657.6±126.5	5.32±0.51
2013	7.19±0.34	11.37±0.39	91.60±4.59	309.5±18.3	1597.9±122.4	5.16±0.50
2014	7.21±0.34	11.83±0.39	92.70±4.64	341.4±19.4	1787.6±135.5	5.23±0.50
2015	7.25±0.34	11.44±0.39	92.72±4.66	316.1±18.5	1619.4±124.3	5.11±0.49
2016	7.12±0.34	11.31±0.40	89.93±4.51	293.9±17.3	1581.9±123.1	5.36±0.52
2017	7.22±0.34	11.30±0.38	90.44±4.53	312.0±17.4	1696.2±136.0	5.43±0.53

Table B4. Direct and derived measurements of summers of 2009 to 2017 from the simultaneous operation of chillers CH#1+CH#2 (scenario 3)

Year	T_{chwl}, ℃	T_{chwr}, ℃	V_{chw}, L/s	E, kW	$Q_{ev,chw}$, kW	COP
2009	7.05±0.34	11.77±0.37	146.54±7.40	581.4±31.8	2882.8±219.8	4.96±0.46
2010	7.01±0.34	12.09±0.37	144.85±7.29	588.0±31.6	3078.0±233.7	5.23±0.49
2011	6.97±0.34	11.71±0.39	145.37±7.48	559.9±34.1	2877.5±224.2	5.12±0.51
2012	6.97±0.33	11.95±0.38	154.65±7.76	603.5±33.4	3207.8±245.3	5.31±0.50
2013	6.96±0.34	12.33±0.39	157.19±7.87	646.9±35.6	3517.8±268.0	5.43±0.51
2014	6.94±0.33	11.89±0.39	157.94±7.92	619.3±35.6	3256.2±250.9	5.25±0.51
2015	6.95±0.34	12.32±0.40	156.99±7.88	654.8±38.0	3511.7±269.6	5.36±0.52
2016	6.62±0.33	12.02±0.39	156.37±7.84	622.9±35.1	3517.7±274.8	5.65±0.54
2017	6.03±0.33	11.73±0.38	153.41±7.74	613.9±34.0	3477.5±277.3	5.66±0.55

Appendix C: Performance metrics of model training and testing using measurements of July 2013 and the cooling season of 2016.

Table C-1. Parameters of grey-box models identified from each augmented window, using measurements of July, 2013.

Model		Parameters					
$E(kW)$, Equation 5-4		α_1	α_2	α_3	α_0		
	AW1	20.44	-0.74	22.03	146.96		
	AW2	29.83	-1.53	22.26	214.48		
	AW3	33.37	-1.86	22.72	239.93		
	AW4	29.50	-1.50	22.31	212.11		
COP, Equation 5-5		β_1	β_2	β_3	β_4	β_0	
	AW1	1.00	0.08	77.30	-3.49	-11.85	
	AW2	0.68	0.02	33.49	-1.44	-3.76	
	AW3	0.52	0.03	44.22	-1.95	-3.61	
	AW4	0.51	0.03	39.86	-1.74	-3.47	
$T_{cdwl}(°C)$, Equation 5-9		δ_1	δ_2	δ_3	δ_4	δ_5	δ_0
	AW1	0.31	0.02	-0.04	0.01	1.01	-2.22
	AW2	0.43	0.02	-0.07	0.01	0.91	0.78
	AW3	0.46	0.02	-0.08	0.01	0.92	0.36
	AW4	0.39	0.02	-0.08	0.01	0.90	0.91
$\Delta T_{chw}(°C)$, Equation 5-12		ϵ_1	ϵ_2				
	AW1	1.28	-0.52				
	AW2	0.60	0.10				
	AW3	0.56	0.14				
	AW4	0.70	0.02				
$\Delta T_{cdw}(°C)$, Equation 5-15		θ_1	θ_2	θ_3	θ_0		
	AW1	0.19	0.49	-0.28	-12.26		
	AW2	0.10	0.60	-0.41	-8.16		
	AW3	0.12	0.56	-0.41	-7.88		
	AW4	0.18	0.49	-0.46	-6.55		

Table C-2. Performance metric values based on each augmented window for each grey-box model, using measurements of July 2013.

Model		Training dataset					Testing dataset				
		r	*RMSE*	*CV (%)*	*MBE*	*NMBE*	*r*	*RMSE*	*CV (%)*	*MBE*	*NMBE*
E(kW), Equation 5-4	AW1	0.99	15.18	4.49	0.03	0.00	0.98	20.20	5.91	5.90	0.02
	AW2	0.98	20.68	6.38	0.03	0.00	0.98	21.00	6.14	7.89	0.02
	AW3	0.98	19.24	5.66	0.03	0.00	0.98	20.83	6.09	7.26	0.02
	AW4	0.98	18.59	5.80	0.03	0.00	0.98	20.52	6.00	6.57	0.02
COP, Equation 5-5	AW1	0.96	0.19	3.77	0.00	0.00	0.86	0.47	9.45	-0.17	-0.03
	AW2	0.91	0.31	6.07	0.00	0.00	0.91	0.31	6.19	-0.09	-0.02
	AW3	0.90	0.28	5.45	0.00	0.00	0.90	0.33	6.71	-0.12	-0.02
	AW4	0.91	0.30	5.94	0.00	0.00	0.91	0.32	6.37	-0.10	-0.02
T_{cdwl}(°C), Equation 5-9	AW1	0.99	0.17	0.50	0.00	0.00	0.99	0.26	0.78	0.00	0.00
	AW2	0.99	0.26	0.81	0.00	0.00	0.99	0.25	0.76	0.01	0.00
	AW3	0.99	0.23	0.70	0.00	0.00	0.99	0.25	0.76	0.00	0.00
	AW4	0.99	0.23	0.70	0.00	0.00	0.99	0.25	0.77	0.00	0.00
ΔT_{chw}(°C), Equation 5-12	AW1	1.00	0.16	3.48	-0.02	-0.01	0.99	0.21	4.60	-0.06	-0.01
	AW2	0.99	0.22	5.00	-0.04	-0.01	0.99	0.20	4.36	0.01	0.00
	AW3	0.99	0.20	4.21	-0.03	-0.01	1.00	0.20	4.29	-0.02	0.00
	AW4	1.00	0.20	4.56	-0.03	-0.01	0.99	0.20	4.29	0.00	0.00
ΔT_{cdw} (°C) Equation 5-15	AW1	0.99	0.20	4.52	0.00	0.00	0.97	0.35	7.97	-0.01	0.00
	AW2	0.99	0.27	6.59	0.00	0.00	0.98	0.32	7.30	-0.02	0.00
	AW3	0.99	0.24	5.36	0.00	0.00	0.98	0.33	7.39	-0.02	0.00
	AW4	0.98	0.28	6.80	0.00	0.00	0.98	0.34	7.72	0.00	0.00

Table C-3. Parameters of grey-box models identified from each sliding window, using measurements of July 2013.

Model	Parameters						
		α_1	α_2	α_3	α_0		
$E(kW)$, Equation 5-4	SW1	20.44	-0.74	22.03	146.96		
	SW2	27.15	-1.31	22.04	195.21		
	SW3	14.77	-0.58	23.97	106.20		
	SW4	18.70	-0.53	21.32	134.45		
		β_1	β_2	β_3	β_4	β_0	
COP, Equation 5-5	SW1	1.00	0.08	77.30	-3.49	-11.85	
	SW2	0.63	0.01	21.99	-0.91	-2.31	
	SW3	-0.04	0.05	55.87	-2.51	-1.14	
	SW4	0.65	0.12	3.09	-0.04	-12.21	
		δ_1	δ_2	δ_3	δ_4	δ_5	δ_0
$T_{cdwl}(°C)$, Equation 5-9	SW1	0.31	0.02	-0.04	0.01	1.01	-2.22
	SW2	0.43	0.02	-0.07	0.01	0.88	1.01
	SW3	-0.16	-0.04	0.16	0.01	1.09	0.81
	SW4	-0.01	0.02	-0.03	0.02	0.88	0.79
		ϵ_1	ϵ_0				
$\Delta T_{chw}(°C)$, Equation 5-12	SW1	1.28	-0.52				
	SW2	0.64	0.06				
	SW3	0.35	0.34				
	SW4	1.70	-0.92				
		θ_1	θ_2	θ_3	θ_0		
$\Delta T_{cdw}(°C)$, Equation 5-15	SW1	0.19	0.49	-0.28	-12.26		
	SW2	0.02	0.67	-0.44	-6.95		
	SW3	0.20	0.45	-0.56	-2.96		
	SW4	0.39	0.24	-0.50	-5.12		

Table C-4. Performance metric values based on each sliding window for each grey-box model, using measurements of July 2013.

Model		Training dataset					Testing dataset				
		r	*RMSE*	*CV (%)*	*MBE*	*NMBE*	*r*	*RMSE*	*CV (%)*	*MBE*	*NMBE*
E(kW), Equation 5-4	AW1	0.99	15.18	4.49	0.03	0.00	0.98	20.20	5.91	5.90	0.02
	AW2	0.98	24.90	8.02	0.01	0.00	0.98	21.61	6.32	9.40	0.03
	AW3	0.98	15.00	4.05	0.00	0.00	0.98	22.85	6.68	8.71	0.03
	AW4	0.98	15.93	6.08	0.01	0.00	0.98	20.82	6.09	6.99	0.02
COP, Equation 5-5	AW1	0.96	0.19	3.77	0.00	0.00	0.86	0.47	9.45	-0.17	-0.03
	AW2	0.88	0.36	7.28	0.00	0.00	0.92	0.30	6.08	-0.08	-0.02
	AW3	0.74	0.18	3.34	0.00	0.00	0.87	0.40	8.05	-0.20	-0.04
	AW4	0.92	0.30	6.56	0.00	0.00	0.89	0.39	7.80	-0.15	-0.03
T_{cdwl}(°C), Equation 5-9	AW1	0.99	0.17	0.50	0.00	0.00	0.99	0.26	0.78	0.00	0.00
	AW2	0.98	0.33	1.03	0.00	0.00	0.99	0.25	0.77	0.02	0.00
	AW3	0.99	0.13	0.40	0.00	0.00	0.98	0.32	0.96	-0.06	0.00
	AW4	0.99	0.21	0.66	0.00	0.00	0.98	0.29	0.89	-0.04	0.00
ΔT_{chw}(°C), Equation 5-12	AW1	1.00	0.16	3.48	-0.02	-0.01	0.99	0.21	4.60	-0.06	-0.01
	AW2	0.99	0.23	5.63	-0.03	-0.01	0.99	0.23	5.01	0.09	0.02
	AW3	0.99	0.13	2.43	-0.01	0.00	1.00	0.21	4.43	-0.06	-0.01
	AW4	0.99	0.16	4.77	-0.01	0.00	0.99	0.23	4.95	0.00	0.00
ΔT_{cdw} (°C) Equation 5-15	AW1	0.99	0.20	4.52	0.00	0.00	0.97	0.35	7.97	-0.01	0.00
	AW2	0.98	0.33	8.36	0.00	0.00	0.98	0.32	7.17	-0.03	-0.01
	AW3	0.99	0.12	2.51	0.00	0.00	0.97	0.35	7.94	-0.03	-0.01
	AW4	0.96	0.37	11.48	0.00	0.00	0.96	0.44	9.94	0.07	0.02

Table C-5. Parameters of grey-box models identified from each augmented window, using the measurements from the chiller CH#1 during the summer of 2016.

Model	Dataset	Parameters					
$E(kW)$, Equation 5-4		α_1	α_2	α_3	α_0		
	AW1	-68.22	-0.04	21.76	63.07		
	AW2	-53.74	-0.05	22.07	59.30		
	AW3	-52.83	-0.46	22.26	91.83		
	AW4	-51.83	-0.17	22.00	68.29		
	AW5	-49.55	-0.08	22.05	59.97		
	AW6	-44.34	0.12	22.00	42.25		
	AW7	-44.32	-0.06	22.19	56.35		
COP, Equation 5-5		β_1	β_2	β_3	β_4	β_0	
	AW1	0.59	0.02	67.01	-3.06	-2.47	
	AW2	0.68	0.01	71.16	-3.27	-2.81	
	AW3	0.69	0.02	74.31	-3.42	-3.75	
	AW4	0.79	0.03	73.92	-3.41	-4.85	
	AW5	0.82	0.03	74.02	-3.41	-5.21	
	AW6	0.78	0.03	74.71	-3.45	-4.97	
	AW7	0.82	0.03	75.02	-3.47	-5.43	
$T_{cdwl}(°C)$, Equation 5-9		δ_1	δ_2	δ_3	δ_4	δ_5	δ_0
	AW1	0.38	0.03	-0.07	0.01	0.88	0.07
	AW2	0.36	0.02	-0.06	0.01	0.88	0.52
	AW3	0.39	0.02	-0.07	0.01	0.89	0.45
	AW4	0.39	0.02	-0.06	0.01	0.89	0.80
	AW5	0.39	0.02	-0.06	0.01	0.89	0.78
	AW6	0.38	0.01	-0.06	0.01	0.89	0.98
	AW7	0.37	0.01	-0.05	0.01	0.89	1.02
$\Delta T_{chw}(°C)$, Equation 5-12		ϵ_1	ϵ_0				
	AW1	0.30	0.43				
	AW2	0.25	0.47				
	AW3	0.25	0.47				
	AW4	0.28	0.45				
	AW5	0.25	0.48				
	AW6	0.21	0.52				
	AW7	0.22	0.50				
$\Delta T_{cdw}(°C)$, Equation 5-15		θ_1	θ_2	θ_3	θ_0		
	AW1	0.12	0.65	-0.82	0.77		
	AW2	0.07	0.71	-0.84	0.94		
	AW3	0.08	0.71	-0.84	0.90		
	AW4	0.09	0.69	-0.83	0.76		
	AW5	0.11	0.66	-0.80	0.51		
	AW6	0.10	0.66	-0.79	0.37		
	AW7	0.11	0.65	-0.78	0.25		

Table C-6. Performance metric values based on each augmented window for each grey-box model, using measurements of the whole cooling season of 2016.

Model		Training dataset					Testing dataset				
		r	*RMSE*	*CV(%)*	*MBE*	*NMBE*	*r*	*RMSE*	*CV(%)*	*MBE*	*NMBE*
E (kW), Equation 5-4	AW1	0.99	16.27	5.41	0.00	0.00	0.99	17.34	5.50	-4.84	-0.02
	AW2	0.99	16.28	5.32	0.00	0.00	0.99	14.52	5.07	-6.15	-0.02
	AW3	0.99	16.18	5.33	0.00	0.00	0.99	14.56	4.80	-4.60	-0.02
	AW4	0.99	15.55	5.19	0.00	0.00	0.99	15.40	4.66	-1.97	-0.01
	AW5	0.99	15.63	5.15	0.00	0.00	0.99	14.92	4.59	2.13	0.01
	AW6	0.99	15.43	5.04	0.00	0.00	0.99	15.51	5.03	2.35	0.01
	AW7	0.99	15.12	4.90	0.00	0.00	0.99	16.75	5.61	-0.63	0.00
T_{cdwl}*(°C),* Equation 5-5	AW1	1.00	0.20	0.70	0.00	0.00	1.00	0.15	0.51	-0.01	0.00
	AW2	1.00	0.18	0.64	0.00	0.00	1.00	0.16	0.58	-0.01	0.00
	AW3	1.00	0.18	0.63	0.00	0.00	1.00	0.16	0.55	-0.02	0.00
	AW4	1.00	0.18	0.62	0.00	0.00	1.00	0.15	0.52	-0.04	0.00
	AW5	1.00	0.17	0.61	0.00	0.00	1.00	0.16	0.55	-0.07	0.00
	AW6	1.00	0.17	0.60	0.00	0.00	1.00	0.15	0.53	-0.08	0.00
	AW7	1.00	0.17	0.59	0.00	0.00	1.00	0.15	0.55	-0.10	0.00
COP, Equation 5-9	AW1	0.94	0.28	5.02	0.00	0.00	0.92	0.24	4.04	-0.01	0.00
	AW2	0.94	0.25	4.50	0.00	0.00	0.95	0.23	3.96	-0.01	0.00
	AW3	0.95	0.25	4.50	0.00	0.00	0.95	0.18	3.08	0.00	0.00
	AW4	0.95	0.24	4.28	0.00	0.00	0.92	0.14	2.27	0.04	0.01
	AW5	0.95	0.23	4.08	0.00	0.00	0.94	0.16	2.67	0.01	0.00
	AW6	0.95	0.22	3.91	0.00	0.00	0.96	0.21	3.71	-0.01	0.00
	AW7	0.95	0.22	3.77	0.00	0.00	0.97	0.24	4.18	0.01	0.00
ΔT_{chw}*(°C),* Equation 5-12	AW1	1.00	0.17	3.71	-0.03	-0.01	1.00	0.16	3.12	-0.04	-0.01
	AW2	1.00	0.17	3.47	-0.03	-0.01	1.00	0.17	3.78	-0.02	0.00
	AW3	1.00	0.17	3.49	-0.02	-0.01	1.00	0.17	3.49	-0.01	0.00
	AW4	1.00	0.17	3.57	-0.03	-0.01	0.99	0.15	2.87	0.00	0.00
	AW5	1.00	0.17	3.49	-0.03	-0.01	1.00	0.17	3.23	-0.04	-0.01
	AW6	1.00	0.17	3.41	-0.02	0.00	1.00	0.18	3.71	-0.04	-0.01
	AW7	1.00	0.16	3.36	-0.02	0.00	1.00	0.19	4.14	-0.04	-0.01
ΔT_{cdw}*(°C),* Equation 5-15	AW1	0.99	0.27	6.39	0.00	0.00	1.00	0.15	3.20	0.07	0.01
	AW2	0.99	0.23	5.26	0.00	0.00	1.00	0.11	2.64	-0.02	-0.01
	AW3	0.99	0.22	4.96	0.00	0.00	0.99	0.23	5.15	-0.12	-0.03
	AW4	0.99	0.20	4.59	0.00	0.00	0.99	0.31	6.40	-0.25	-0.05
	AW5	0.99	0.22	4.87	0.00	0.00	0.99	0.38	7.99	-0.28	-0.06
	AW6	0.99	0.22	4.88	0.00	0.00	0.99	0.34	7.65	-0.23	-0.05
	AW7	0.99	0.21	4.64	0.00	0.00	0.99	0.34	8.03	-0.26	-0.06

Table C-7. Parameters of grey-box models identified from training dataset of each sliding window, using the measurements from the chiller CH#1 during the summer of 2016.

Model	Dataset	Parameters					
$E(kW)$, Equation 5-4		α_1	α_2	α_3	α_0		
	SW1	-52.83	-0.46	22.26	91.84		
	SW2	-39.85	0.63	21.70	-0.68		
	SW3	-38.32	1.38	21.72	-67.70		
	SW4	-35.77	1.43	21.71	-72.74		
	SW5	-35.43	0.40	22.14	13.49		
	SW6	-35.91	2.20	21.81	-139.61		
COP, Equation 5-5		β_1	β_2	β_3	β_4	β_0	
	SW1	0.69	0.02	74.31	-3.42	-3.75	
	SW2	1.13	0.04	85.84	-3.99	-8.60	
	SW3	1.07	0.04	81.51	-3.78	-7.48	
	SW4	0.96	0.04	81.95	-3.80	-7.27	
	SW5	0.97	0.06	82.41	-3.83	-8.68	
	SW6	0.99	0.04	76.54	-3.55	-7.19	
$T_{cdwl}(°C)$, Equation 5-9		δ_1	δ_2	δ_3	δ_4	δ_5	δ_0
	SW1	0.39	0.02	-0.07	0.01	0.89	0.45
	SW2	0.37	0.01	-0.05	0.01	0.85	2.25
	SW3	0.35	0.01	-0.04	0.01	0.85	2.46
	SW4	0.33	0.00	-0.03	0.01	0.86	2.45
	SW5	0.34	0.00	-0.03	0.01	0.86	2.40
	SW6	0.21	-0.02	0.02	0.01	0.83	5.27
$\Delta T_{chw}(°C)$, Equation 5-12		ϵ_1	ϵ_0				
	SW1	0.25	0.47				
	SW2	0.24	0.48				
	SW3	0.17	0.55				
	SW4	0.16	0.56				
	SW5	0.19	0.53				
	SW6	0.13	0.59				
$\Delta T_{cdw}(°C)$, Equation 5-15		θ_1	θ_2	θ_3	θ_0		
	SW1	0.08	0.71	-0.84	0.90		
	SW2	0.09	0.69	-0.73	-1.33		
	SW3	0.15	0.59	-0.68	-1.87		
	SW4	0.13	0.60	-0.65	-2.11		
	SW5	0.12	0.60	-0.66	-1.65		
	SW6	0.12	0.58	-0.67	-1.16		

Table C-8. Performance metric values based on each sliding window for each grey-box model, using measurements of the whole cooling season of 2016.

Model		Training dataset					Testing dataset				
		r	*RMSE*	*CV(%)*	*MBE*	*NMBE*	*r*	*RMSE*	*CV(%)*	*MBE*	*NMBE*
E (kW), Equation 5-4	SW1	0.99	16.18	5.33	0.00	0.00	0.99	14.56	4.80	-4.60	-0.02
	SW2	0.99	14.38	4.77	0.00	0.00	0.99	14.25	4.31	-0.27	0.00
	SW3	0.99	14.31	4.59	0.00	0.00	0.99	12.55	3.85	1.92	0.01
	SW4	0.99	13.80	4.47	0.00	0.00	0.99	14.82	4.58	5.57	0.02
	SW5	0.99	13.45	4.34	0.00	0.00	0.99	16.78	5.57	5.13	0.02
	SW6	0.99	13.51	4.27	0.00	0.00	0.99	17.56	6.09	-2.75	-0.01
T_{cdwl}*(°C),* Equation 5-5	SW1	1.00	0.18	0.63	0.00	0.00	1.00	0.16	0.55	-0.02	0.00
	SW2	1.00	0.15	0.54	0.00	0.00	1.00	0.15	0.53	-0.04	0.00
	SW3	1.00	0.15	0.53	0.00	0.00	1.00	0.15	0.51	-0.03	0.00
	SW4	1.00	0.15	0.53	0.00	0.00	1.00	0.16	0.56	-0.08	0.00
	SW5	1.00	0.15	0.53	0.00	0.00	1.00	0.14	0.50	-0.08	0.00
	SW6	1.00	0.15	0.51	0.00	0.00	1.00	0.13	0.47	-0.04	0.00
COP, Equation 5-9	SW1	0.95	0.25	4.50	0.00	0.00	0.95	0.18	3.08	0.00	0.00
	SW2	0.96	0.19	3.34	0.00	0.00	0.90	0.16	2.74	0.07	0.01
	SW3	0.95	0.18	3.17	0.00	0.00	0.95	0.13	2.27	0.01	0.00
	SW4	0.95	0.18	3.05	0.00	0.00	0.95	0.17	2.88	0.04	0.01
	SW5	0.96	0.17	2.87	0.00	0.00	0.96	0.22	3.95	0.00	0.00
	SW6	0.95	0.16	2.72	0.00	0.00	0.97	0.26	4.55	-0.02	0.00
ΔT_{chw}*(°C),* Equation 5-12	SW1	1.00	0.17	3.49	-0.02	-0.01	1.00	0.17	3.49	-0.01	0.00
	SW2	1.00	0.16	3.34	-0.02	0.00	0.99	0.15	2.83	0.00	0.00
	SW3	1.00	0.16	3.20	-0.02	0.00	1.00	0.15	2.88	-0.02	0.00
	SW4	1.00	0.16	3.25	-0.02	0.00	1.00	0.17	3.36	-0.04	-0.01
	SW5	1.00	0.16	3.25	-0.02	0.00	1.00	0.19	4.04	-0.06	-0.01
	SW6	1.00	0.17	3.30	-0.02	0.00	1.00	0.20	4.37	-0.03	-0.01
ΔT_{cdw}*(°C),* Equation 5-15	SW1	0.99	0.22	4.96	0.00	0.00	0.99	0.23	5.15	-0.12	-0.03
	SW2	1.00	0.13	3.01	0.00	0.00	0.99	0.33	6.73	-0.26	-0.05
	SW3	0.99	0.16	3.55	0.00	0.00	1.00	0.20	4.21	-0.15	-0.03
	SW4	0.99	0.18	3.88	0.00	0.00	0.99	0.37	7.85	-0.25	-0.05
	SW5	1.00	0.16	3.41	0.00	0.00	0.99	0.34	7.87	-0.26	-0.06
	SW6	0.99	0.23	4.90	0.00	0.00	1.00	0.14	3.37	-0.05	-0.01

Appendix D: Measurement uncertainty and performance metrics of DNN models with respect to transfer learning

Table D-1. Measurement uncertainty of target variables and performance metrics of five DNN models over three target domains (TD1, TD2, and TD3) based on self-learning.

Target variables	Training dataset					Testing dataset			
	r	*RMSE*	*CV (%)*	*MAD*	U_m	*r*	*RMSE*	*CV (%)*	*MAD*
					TD1				
E (kW)	0.97	12.93	5.10	10.30	16.5	0.90	69.71	20.48	49.11
COP (-)	0.94	0.29	5.31	0.23	0.57	0.64	0.94	15.83	0.69
T_{cdwl} (°C)	0.96	0.27	1.01	0.22	0.48	0.98	0.42	1.45	0.31
ΔT_{chw} (°C)	1.00	0.07	1.83	0.06	0.54	1.00	0.15	2.81	0.12
ΔT_{cdw} (°C)	0.98	0.23	6.35	0.18	0.64	0.97	0.89	17.33	0.69
					TD2				
E (kW)	0.99	13.91	4.42	9.79	20.36	0.99	19.19	6.60	13.97
COP (-)	0.90	0.24	4.10	0.18	0.59	0.93	0.37	6.51	0.25
T_{cdwl} (°C)	0.99	0.25	0.88	0.20	0.52	0.99	0.28	1.00	0.22
ΔT_{chw} (°C)	1.00	0.08	1.58	0.06	0.54	1.00	0.10	2.24	0.08
ΔT_{cdw} (°C)	1.00	0.17	3.65	0.13	0.67	0.99	0.30	7.19	0.23
					TD3				
E (kW)	0.99	12.29	3.74	9.88	21.81	0.98	30.47	9.39	26.65
COP (-)	0.84	0.58	9.65	0.12	0.61	0.92	0.58	9.90	0.16
T_{cdwl} (°C)	0.99	0.32	1.11	0.18	0.54	0.98	0.50	1.75	0.47
ΔT_{chw} (°C)	1.00	0.16	2.95	0.09	0.54	1.00	0.20	3.91	0.13
ΔT_{cdw} (°C)	0.99	0.20	4.10	0.14	0.69	0.99	0.43	8.96	0.38

Table D-2. Measurements uncertainty of target variables and performance metrics of five DNN models over three target domains (TD4, TD5, and TD6) based on self-learning.

Target variables	Training dataset					Testing dataset			
	r	*RMSE*	*CV (%)*	*MAD*	U_m	*r*	*RMSE*	*CV (%)*	*MAD*
				TD4					
E (kW)	0.97	15.8	6.24	12.06	16.5	0.90	69.45	22.03	43.45
COP (-)	0.94	0.29	5.39	0.23	0.57	0.71	0.91	15.51	0.60
T_{cdwl} (°C)	0.96	0.35	1.30	0.28	0.48	0.98	0.57	2.01	0.39
ΔT_{chw} (°C)	1.00	0.14	3.56	0.12	0.54	1.00	0.22	4.33	0.18
ΔT_{cdw} (°C)	0.98	0.61	17.03	0.56	0.64	0.99	1.01	21.90	0.92
				TD5					
E (kW)	0.99	13.60	4.32	9.74	20.36	0.99	13.92	4.49	10.23
COP (-)	0.91	0.28	4.77	0.22	0.59	0.92	0.30	5.16	0.24
T_{cdwl} (°C)	0.99	0.30	1.05	0.24	0.52	0.99	0.30	1.06	0.23
ΔT_{chw} (°C)	1.00	0.10	2.07	0.09	0.54	1.00	0.11	2.27	0.09
ΔT_{cdw} (°C)	1.00	0.40	8.66	0.38	0.67	0.99	0.31	6.82	0.27
				TD6					
E (kW)	0.99	14.01	5.13	10.03	23.49	0.98	20.55	6.50	15.40
COP (-)	0.93	0.33	5.93	0.24	0.67	0.74	0.34	5.78	0.27
T_{cdwl} (°C)	0.99	0.33	1.18	0.25	0.60	0.98	0.43	1.51	0.29
ΔT_{chw} (°C)	1.00	0.09	2.08	0.07	0.59	1.00	0.09	1.85	0.08
ΔT_{cdw} (°C)	0.99	0.24	6.13	0.18	0.73	0.99	0.25	5.41	0.21

Table D-3. Measurements uncertainty of target variables and performance metrics of five DNN models over testing dataset of three target domains (TD1, TD2, and TD3) based on TLS0.

Target variable	*r*	*RMSE*	*CV (%)*	*MAD*	U_m
TD1					
E (kW)	0.98	23.46	6.89	19.34	16.5
COP (-)	0.76	0.54	9.11	0.43	0.57
T_{cdwl} (°C)	0.99	0.43	1.48	0.39	0.48
ΔT_{chw} (°C)	1.00	0.32	5.84	0.28	0.54
ΔT_{cdw} (°C)	0.98	0.51	10.07	0.43	0.64
TD2					
E (kW)	0.99	22.45	7.72	16.22	20.36
COP (-)	0.88	0.63	11.07	0.52	0.59
T_{cdwl} (°C)	0.99	0.42	1.51	0.38	0.52
ΔT_{chw} (°C)	1.00	0.30	6.54	0.25	0.54
ΔT_{cdw} (°C)	0.95	0.60	14.28	0.49	0.67
TD3					
E (kW)	0.99	20.87	6.43	15.15	21.81
COP (-)	0.86	0.48	8.26	0.41	0.61
T_{cdwl} (°C)	0.99	0.49	1.73	0.44	0.54
ΔT_{chw} (°C)	1.00	0.38	7.28	0.31	0.54
ΔT_{cdw} (°C)	0.98	0.48	10.11	0.39	0.69

Table D-4. Measurements uncertainty of target variables and performance metrics of five DNN models over testing datasets of three target domains (TD1, TD2, and TD3) based on TLS1.

Target variables	*r*	*RMSE*	*CV (%)*	*MAD*	U_m
TD1					
E (kW)	0.98	21.05	6.18	16.13	16.5
COP (-)	0.80	0.33	5.50	0.26	0.57
T_{cdwl} (°C)	0.99	0.42	1.44	0.34	0.48
ΔT_{chw} (°C)	1.00	0.17	3.03	0.12	0.54
ΔT_{cdw} (°C)	0.96	0.51	9.94	0.34	0.64
TD2					
E (kW)	0.99	11.82	4.07	8.69	20.36
COP (-)	0.92	0.42	7.35	0.29	0.59
T_{cdwl} (°C)	0.99	0.30	1.08	0.25	0.52
ΔT_{chw} (°C)	1.00	0.11	2.46	0.09	0.54
ΔT_{cdw} (°C)	0.97	0.51	12.17	0.38	0.67
TD3					
E (kW)	0.99	11.34	3.50	9.0	21.81
COP (-)	0.91	0.28	4.76	0.22	0.61
T_{cdwl} (°C)	0.99	0.28	0.98	0.23	0.54
ΔT_{chw} (°C)	1.00	0.10	1.87	0.08	0.54
ΔT_{cdw} (°C)	0.98	0.44	9.19	0.33	0.69

Table D-5. Measurements uncertainty of target variables and performance metrics of five DNN models over testing datasets of three target domains (TD1, TD2, and TD3) based on TLS2.

Target variables	*r*	*RMSE*	*CV (%)*	*MAD*	U_m
			TD1		
E (kW)	0.98	21.60	6.35	16.51	16.5
COP (-)	0.79	0.33	5.48	0.25	0.57
T_{cdwl} (°C)	0.99	0.42	1.44	0.34	0.48
ΔT_{chw} (°C)	1.00	0.18	3.24	0.13	0.54
ΔT_{cdw} (°C)	0.96	0.52	10.17	0.32	0.64
			TD2		
E (kW)	0.99	11.88	4.08	8.80	20.36
COP (-)	0.92	0.41	7.18	0.28	0.59
T_{cdwl} (°C)	0.99	0.29	1.02	0.24	0.52
ΔT_{chw} (°C)	1.00	0.11	2.38	0.09	0.54
ΔT_{cdw} (°C)	0.97	0.52	12.44	0.38	0.67
			TD3		
E (kW)	0.99	12.61	3.89	9.56	21.81
COP (-)	0.92	0.24	4.12	0.19	0.61
T_{cdwl} (°C)	0.99	0.28	0.99	0.24	0.54
ΔT_{chw} (°C)	1.00	0.10	1.97	0.08	0.54
ΔT_{cdw} (°C)	0.98	0.45	9.32	0.35	0.69

Table D-6. Measurements uncertainty of target variables and performance metrics of five DNN models over testing datasets of three target domains (TD4, TD5, and TD6) based on TLS0.

Target variables	*r*	*RMSE*	*CV (%)*	*MAD*	U_m
			TD4		
E (kW)	0.99	20.81	6.60	15.85	16.5
COP (-)	0.83	0.69	11.82	0.56	0.57
T_{cdwl} (°C)	1.00	0.45	1.56	0.39	0.48
ΔT_{chw} (°C)	1.00	0.37	7.29	0.31	0.54
ΔT_{cdw} (°C)	0.98	0.74	15.88	0.69	0.64
			TD5		
E (kW)	0.99	19.65	6.34	14.66	20.36
COP (-)	0.85	0.69	11.81	0.56	0.59
T_{cdwl} (°C)	0.99	0.45	1.57	0.39	0.52
ΔT_{chw} (°C)	1.00	0.36	7.17	0.30	0.54
ΔT_{cdw} (°C)	0.98	0.69	15.14	0.64	0.67
			TD6		
E (kW)	0.99	19.36	6.13	14.53	23.49
COP (-)	0.83	0.66	11.30	0.54	0.67
T_{cdwl} (°C)	0.99	0.44	1.55	0.38	0.60
ΔT_{chw} (°C)	1.00	0.36	7.11	0.30	0.59
ΔT_{cdw} (°C)	0.99	0.68	14.51	0.63	0.73

Table D-7. Measurements uncertainty of target variables and performance metrics of five DNN models over testing datasets of three target domains (TD4, TD5, and TD6) based on TLS1.

Target variables	*r*	*RMSE*	*CV (%)*	*MAD*	U_m
TD4					
E (kW)	0.99	18.06	5.73	14.80	16.5
COP (-)	0.87	0.39	6.70	0.32	0.57
T_{cdwl} *(°C)*	1.00	0.53	1.87	0.49	0.48
ΔT_{chw} (°C)	1.00	0.11	2.19	0.09	0.54
ΔT_{cdw} (°C)	0.93	2.29	49.16	2.19	0.64
TD5					
E (kW)	0.99	18.57	5.99	15.17	20.36
COP (-)	0.88	0.31	5.32	0.24	0.59
T_{cdwl} *(°C)*	0.99	0.49	1.72	0.35	0.52
ΔT_{chw} (°C)	1.00	0.10	2.05	0.08	0.54
ΔT_{cdw} (°C)	0.99	0.38	8.32	0.31	0.67
TD6					
E (kW)	0.99	15.67	4.96	11.06	23.49
COP (-)	0.82	0.31	5.21	0.24	0.67
T_{cdwl} *(°C)*	0.99	0.22	0.79	0.17	0.60
ΔT_{chw} (°C)	1.00	0.10	1.93	0.08	0.59
ΔT_{cdw} (°C)	0.99	0.26	5.52	0.20	0.73

Table D-8. Measurements uncertainty of target variables and performance metrics of five DNN models over testing datasets of three target domains (TD4, TD5, and TD6) based on TLS2.

Target variables	*r*	*RMSE*	*CV (%)*	*MAD*	U_m
			TD4		
E (kW)	0.99	29.00	9.20	25.99	16.5
COP (-)	0.87	0.40	6.88	0.32	0.57
T_{cdwl} (°C)	1.00	0.61	2.15	0.57	0.48
ΔT_{chw} (°C)	1.00	0.12	2.36	0.09	0.54
ΔT_{cdw} (°C)	0.93	2.24	48.07	2.14	0.64
			TD5		
E (kW)	0.99	25.77	8.31	22.91	20.36
COP (-)	0.88	0.41	6.97	0.33	0.59
T_{cdwl} (°C)	1.00	0.45	1.59	0.38	0.52
ΔT_{chw} (°C)	1.00	0.12	2.49	0.10	0.54
ΔT_{cdw} (°C)	0.88	2.43	53.37	2.29	0.67
			TD6		
E (kW)	0.99	16.52	5.23	11.64	23.49
COP (-)	0.82	0.29	4.94	0.23	0.67
T_{cdwl} (°C)	0.99	0.22	0.76	0.16	0.60
ΔT_{chw} (°C)	1.00	0.09	1.85	0.07	0.59
ΔT_{cdw} (°C)	0.99	0.27	5.84	0.21	0.73